ESTABLISHING CLEAR-SKY MEAN SIGNAL LEVELS ON GEOSTATIONARY SATELLITE LINKS

by

Noraisyah Mohamed Shah
A Dissertation
Submitted to the
Graduate Faculty
of
George Mason University
in Partial Fulfillment of
The Requirements for the Degree
of
Doctor of Philosophy
Electrical and Computer Engineering

Committee:

_____	Dr. Jeremy E. Allnutt, Dissertation Co-Director
_____	Dr. Peter Paris, Dissertation Co-Director
_____	Dr. Bijan Jabbari, Committee Member
_____	Dr. Pelin Kurtay, Committee Member
_____	Dr. Diana Wang, Committee Member
_____	Dr. Monson H. Hayes, Department Chair
_____	Dr. Kenneth S. Ball, Dean, Volgenau School of Engineering
Date:_____	Fall Semester 2014 George Mason University Fairfax, VA

Establishing Clear-Sky Mean Signal Levels on Geostationary Satellite Links

A Dissertation submitted in partial fulfillment of the requirements for the degree of Doctor of Philosophy at George Mason University

by

Noraisyah Mohamed Shah
Master of Engineering
Oita University, Japan, 2003

Co-Directors:
Jeremy E. Allnutt, Professor
Department of Electrical and Computer Engineering
Peter Paris, Professor
Department of Electrical and Computer Engineering

Fall Semester 2014
George Mason University
Fairfax, VA

DEDICATION

This is dedicated to my family, relatives and friends who were constantly there for me. There is no doubt in my mind that without their continued support and counsel, I could not have completed this process. Thank you very much. Words cannot express how much I love you all.

ACKNOWLEDGEMENTS

This work would not have been possible without the financial support of University Malaya, Malaysia and the generous scholarship from the Society of Satellite Professionals International (SSPI) Mid-Atlantic Regional Chapter. Thank you very much.

I would like to express my deepest gratitude to my advisor, Dr. Jeremy Allnutt, for his excellent guidance, patience and for assisting me in my search for propagation data. I would like to thank Dr. Peter Paris for his attentiveness and suggestions that ultimately improved the quality of my research. I am very grateful that he agreed to co-advise this dissertation. To all my committee members, Dr. Bijan Jabbari, Dr. Pelin Kurtay and Dr. Diana Wang, thank you for letting my defense be an enjoyable moment, and for your brilliant comments and suggestions.

I would also like to thank Dr. Kathleen Wage and Dr. Jill Nelson for guiding my understanding of digital signal processing, and to Dr. Robert Weigel for his feedback and suggestions in performing the statistical analysis for the spectrum estimation. To all dedicated faculty and staffs of the Volgenau School of Engineering, thank you for making this a rewarding experience.

Special thanks goes out to NASA for access to the ACTS data, Dr. Dennis Sweeney of Virginia Tech. for Olympus data, Dr. Wolfhard Vogel of Texas A&M University for Texas data, Dr. Luiz da Silva Mello of Pontifical Catholic University of Rio de Janeiro together with Dr. Martha Pudwell and Dr. Marcio Rodrigues for Brazil data, Dr. Qing Wei Pan and Mr. Charles Tsui, both of Manukau Institute of Technology, for Papua New Guinea data, and for generously sharing the DFT source code that they used in their Atmospheric Tides analysis. Also, my thanks to Dr. Carlo Riva of Politecnico de Milano in Italy, for insights into some of their satellite data analyses, and all who communicated during the initial search for propagation data.

Last but not least, to Jumsairi, for without his IT expertise I would still be working on data extraction.

TABLE OF CONTENTS

LIST OF TABLES

LIST OF FIGURES

LIST OF ABBREVIATIONS

ACTS Propagation Terminal ..... APT
Advanced Communication Technology Satellite ..... ACTS
Alaska ..... AK
British Columbia ..... BC
Colorado ..... CO
Confidence Interval CI
Complementary cumulative distribution function ..... CCDF
Discrete Fourier Transform ..... DFT
Fast Fourier Transform ..... FFT
Florida ..... FL
International Telecommunication Union ..... ITU
ITU-Radiocommunications ..... ITU-R
Low noise amplifier ..... LNA
National Aeronautics and Space Administration ..... NASA
National Oceanic and Atmospheric Administration ..... NOAA
New Mexico ..... NM
Oklahoma ..... OK
Phase locked loop ..... PLL
Root mean squared error ..... RMSE
Texas ..... TX
Virginia Polytechnic Institute and State University ..... VTECH
Welch's Overlapped Segment Averaging ..... WOSA

ABSTRACT

ESTABLISHING CLEAR-SKY MEAN SIGNAL LEVELS ON GEOSTATIONARY SATELLITE LINKS

Noraisyah Mohamed Shah, Ph.D.

George Mason University, 2014

Dissertation Co-Directors: Dr. Jeremy E. Allnutt and Dr. Peter Paris

Diurnal variations observed on satellite beacon experiments were often ascribed to changes in satellite antenna beam pointing due to the satellite not being in a truly geostationary orbit, or to variations in pointing due to diurnal heating effects on the satellite antenna. However, experiments in Papua New Guinea which used co-located radiometer and satellite beacon receivers, detected diurnal and seasonal variations in the received satellite beacon signal level during clear sky that suggested the atmosphere played a role in the signal variation. These effects were termed as atmospheric tides, and could significantly affect the fade margin calculations in low margin systems. Additional evidence supporting the existence of atmospheric tides were found in several time series satellite propagation data collected from sites in North America and in Brazil. This showed that the atmospheric tides phenomenon also affects communications satellite links to temperate regions as well. Factors that contribute to the existence of atmospheric

tides as well as procedures that can help limit these effects in measuring clear-sky mean levels were proposed. The result of this research presents evidence that a 24 hour diurnal variations seen is due to atmospheric effects, and not due to satellite payload or orbital instabilities. It is recommended that the seasonal and diurnal variation of the mean clear-sky level is considered in determining link budget for low margin systems, and the sinusoidal nature of the variation augment the function of radiometers in evaluating the true rain fade level.

CHAPTER 1: INTRODUCTION

With the improved price and performance of today's satellite-based solutions as well as the introduction of K-band for satellite services, Very Small Aperture Terminals (VSAT) systems have seen rapid growth in data networking services, both in commercial and consumer markets. However, due to the need for small antennas and relatively low power transmit amplifiers for VSAT systems, operating margins are limited. The availability is consequently reduced to 99% of the time or even less, as a basic countermeasure to reduce costs [1].

This small margin makes it crucial to have an accurate fade margin description to establish performance and availability criteria. Conventionally, attenuation and depolarization are the key parameters used in establishing fade margins, together with information on fade duration and intervals, site diversity, and fade rates. The mean clear sky level used in determining link budgets had always been taken to be a constant value, but experiments in Papua New Guinea [2] indicated this was not always true.

1.1 Problem statement and research approach

The goals of this dissertation are listed as follows:

I. Search for evidence of *atmospheric tides* in propagation data collected from sites in other climate zones, different to the warm climate of Papua New Guinea where it was first identified.

II. Detect any significant seasonal and diurnal variations, as well as use spectral estimation methods to establish the periodicity of any variation.

III. Identify and quantify the mechanisms involved in the attenuation experienced by the satellite signal and identify variations in the sites that might lead to different characteristics of the atmospheric tides being apparent.

IV. Suggest a method to extract the diurnal signal variation due to atmospheric tides from propagation measurements via a modeling procedure.

In an attempt to investigate if the diurnal variation in clear sky level can be seen in other geographical areas and climate zones, evidence of atmospheric tides were searched for in other data sources taken from propagation experiments that utilized co-located radiometer and geostationary satellite beacons directed along the same path. These databases are:

1. 20.2 GHz and 27.5 GHz beacon and radiometer attenuation data collected from 7 sites in North America in an experiment conducted by National Aeronautics and Space Administration's (NASA) Advanced Communications Technology Satellite (ACTS).
2. 11.2 GHz INTELSAT beacon experiment observed by Texas A&M University in Austin, Texas.
3. 11.45 GHz INTELSAT 705 beacon experiment observed in Mosqueiro Brazil, by the Center of Telecommunications Studies of Pontifical Catholic University of Rio de Janeiro, Brazil

4. Propagation measurements using the Olympus satellite beacons at the frequencies of 12.5, 20 and 30 GHz, observed in Blacksburg VA by the Virginia Polytechnic Institute and State University (Virginia Tech).

The extracted time series data are then plotted to visually detect any seasonal or diurnal variation in the data. Three different spectral estimation techniques; the raw periodogram, Method1 and Method2; were then used to identify any periodicities in the data. Statistical analysis using the Bootstrap block resampling method was performed onto the spectral peaks to verify the significance of the diurnal periodicities detected.

Several probable causes of atmospheric tides were presented and the most probable explanation identified. Based on the result, the mechanism involved in the seasonal and diurnal variations in the attenuation experienced by the satellite signal during clear sky are then modeled, with recommendations on how these variations can be extracted to obtain true mean clear-sky levels.

1.2 Contribution and dissertation outline

From the results, it is confirmed that the diurnal variations seen in both satellite beacon and their co-located radiometer data have a period of 24 hours, and is due to atmospheric effects, and not due to satellite payload or orbital instabilities. It was shown that the seasonal/diurnal affects communications satellite links to temperate regions as well, and were not limited to tropical sites or of any particular elevation angle. However, there is a trend of decreasing diurnal effect as the average climate becomes less warm and humid. The presence of a sidereal and anti-sidereal peak was also detected to the right and left of the solar peak, respectively, in some of the result. These side peaks can be

generated when a daily solar variation is amplitude modulated by a seasonal variation of one cycle/year, producing sidebands at the sidereal and anti-sidereal frequencies.

The seasonal variation detected in propagation signal variations was successfully estimated using the gaseous attenuation model provided in the ITU recommendation P676-9. It was also possible to model the mean clear-sky level using a cosine formula, with a period of 24 hours and its other parameters such as amplitude, vertical and horizontal shift estimated from the meteorological data together with the observed average beacon attenuation. Compared to a constant mean clear-sky level, the cosine clear-sky model performed better in sites that are warmer, and can be used to predict the next couple of days with reasonable accuracy.

It is appreciated that many of these clear sky variations are relatively small, and are normally taken account of in a typical link budget by allocating an implementation margin. However, on some links, the seasonal and annual variations can be significant, possibly approaching half of the attenuation margin for small terminals. Thus considering the diurnal and seasonal variation of the mean clear sky level in determining link budget would provide a more accurate fade margin description in low margin systems, with limited link operating margins. Diurnal variations of the clear sky level are possible source of errors in assessing the true rain fade level. The cosine clear-sky model generated could assist in evaluating the true rain fade level as the radiometer will not be able to assist in the removal of any signal variations due to the atmosphere.

This dissertation is structured as follows. Chapter 2 gives a general introduction to satellite communication by taking a brief look at the history of satellite communication in

terms of its advancement, advantages and limitations. In Chapter 3 the role of propagation measurement campaign, its equipment and types of data collected are given. The types of propagation impairments are discussed, together with the use of radiometer and fade mitigation techniques to counter these effects. In the following Chapter 4, the time series plot of the extracted beacon and co-located radiometer data from four databases are given. The various spectrum estimation methods used to establish any periodicity in the data are presented, together with their result. In Chapter 5, two statistical analyses will be given. One tests the significance of any diurnal periodicity peak detected in Chapter 4. Another in the complementary cumulative distribution function (CCDF) of attenuation in clear sky conditioned to different time and season. This provides quantitative information to evaluate the impact on low margin systems, of changes in clear sky level. Chapter 6 investigates all possible source of seasonal/diurnal variation detected, and identifies the most probable cause. Seasonal and diurnal variation detected in the mean clear sky beacon attenuation is modelled in Chapter 7. The closing chapter, Chapter 8 contains a summary of the study and suggestions for future work.

CHAPTER 2: SATELLITE COMMUNICATIONS

Commercial satellite communications was first introduced in 1965, when the first geosynchronous satellite for international communication, INTELSAT 1, was launched in 1965. Since then, improvements in satellite launch technology have enabled heavier satellites to be put in orbit. Advancement in microwave techniques and power transmission amplifiers has increased the number of channels and services offered by satellites. With higher capacity per launch, satellite services are now offered at a lower cost per telephone or video channel than in the past.

The increase in size and power of satellites directly enabled the reduction in size and cost of earth stations receivers. The cost of earth station ownership has been brought down considerably and the number of Earth satellite receivers has increased. As a consequence of this, the broadcast capability of satellites can be fully exploited. Such applications include service provision directly to customers using small, low-cost earth stations; mobile communication to ships, aircraft, land vehicles and individuals; and direct-to-public television/sound broadcasts and data distribution/gathering from widely distributed terminals. Multipoint data transmission networks and data collection networks have been developed under the name of VSAT (very small aperture terminals) networks. VSATs however operates on a limited link margin. Link margin, measured in dB, is the

difference between the receiver's threshold sensitivity and the actual received power. If the link margin is exceeded, the receiver will not work according to its specification.

2.1 Frequency Bands

Regulations are needed to ensure the efficient use of the radio-frequency spectrum. In the USA, these regulations are managed by the Federal Communications Committee (FCC). The International Telecommunications Union (ITU) is the agency responsible for coordinating the shared global use of the radio spectrum, and the FCC is the United State's representative at the ITU for such coordination. The ITU also promotes international cooperation in assigning satellite orbits, and orbital slots, establishes worldwide standards and assists in improving telecommunication infrastructure in the developing world. The following Table 2.1 from [3] summarizes the frequency band allocations to radio-communication services.

Table 2.1: Summary of frequency bands allocation to radio-communication service

Radiocommunication service	**Typical frequency bands for uplink/downlink**	**Usual terminology**
Fixed satellite service (FSS)	6/4 GHz 8/7 GHz 14/12-11 GHz 30/20 GHz 50/40 GHz	C band X band Ku band Ka band V band
Mobile satellite service (MSS)	1.6/1.5 GHz 30/20 GHz	L band Ka band
Broadcasting satellite service (BSS)	2/2.2 GHz 2.6/2.5 GHz 12 GHz	S band S band Ku band

In the fixed satellite services (FSS), the X-band is reserved for military and government use, while the C-bands are occupied by the oldest systems and are currently saturated. The K-bands (Ku- and Ka-band) are therefore of rising interest due to their large available bandwidth and present relatively little use.

The original C-band satellites were power limited and so required large earth station antennas. The initial standard-A antennas designed for use in the INTELSAT system were 30 m in diameter, a major cost factor in building an earth station. However with the launch of more sophisticated higher power satellites, later INTELSAT VII series, and subsequent, satellites were designed with the new Standard –A and Standard-C earth station, with antenna diameters on the order of 15m, as well as with even smaller earth stations (Standard-F3 at 6/4 GHz and Standard-E3 at 14/11 GHz), with antenna diameters on the order of 10m [4], [5], [6]. As compared with the less occupied K band signals, the C-band frequencies are low enough that they are not appreciably attenuated by rainfall, a principal cause of signal degradation in the atmosphere. Cosmic noise is also at its lowest levels in the range of 1-10 GHz.

The most significant disadvantage of C-band is that it is already saturated, and coordinating the earth station antenna location to avoid receiving or generating interference to other terrestrial microwave radio relay links or other satellite communications link using the same frequency has become increasingly difficult. This has led to the investigation of utilizing the next band of higher band of frequencies above the Ku-band, the Ka-band, for satellite communication. Ka-band also has an available bandwidth in excess of 1000 MHz, much wider than the conventional C-band.

The frequency range of Ku- and Ka-band is defined as 12.5 GHz to 18 GHz and 26.5 GHz to 40 GHz respectively. However, in satellite communication, Ku-band is conventionally referred to as 14/11 GHz and Ka-band is 30/20 GHz. The convention is to give the uplink frequency before the downlink frequency. The main disadvantage for Ka-band is that it is more severely affected by tropospheric impairments than lower frequencies. Rain attenuation depends on rain rate, rain-path length and the drop-size distribution. At Ka-band (1 to 1.5 cm wavelength), the drop size, even in moderate rain events, is comparable to the wavelength which is about 1 to 1.5 cm, causing severe attenuation and inevitable communication–link outages [7]. This has given rise to a worldwide propagation measurement campaign to collect propagation data, so as to characterize the rain medium, as well as to develop effective rain-fade counter measure techniques. Table 2.2 [8], gives a summary of relevant propagation impairments, the physical cause of each, and the major importance for current satellite systems.

Table 2.2: Propagation Impairments

Propagation Impairment	**Physical cause**	**Prime Importance**
Attenuation and sky noise increases	Atmospheric gases, cloud, rain	Frequencies above about 10 GHz
Signal depolarization	Rain, ice crystals	Prime importance for C-band; less important for Ku-band; even less for Ka-band
Refraction, atmospheric multipath	Atmospheric gases	Communication and tracking at low elevation angles
Signal scintillations	Tropospheric and Ionospheric refractivity fluctuations	Tropospheric at frequencies above 10GHz and low angles; Ionospheric at frequencies below 10 GHz
Reflection multipath, blockage	Earth's surface, objects on surface	Mobile-satellite services
Propagation delays, variations	Troposphere, ionosphere	Precise timing and location systems; time division multiple access (TDMA) systems
Intersystem interference	Ducting, scatter, diffraction	Mainly C-band at present; rain scatter may be significant at higher frequencies

CHAPTER 3: PROPAGATION MEASUREMENTS CAMPAIGN

Studies on wave propagation on earth-space paths have a long history starting with NASA's ATS-5 spacecraft in 1969, and were mainly carried out in North America, Europe, and Japan with some significant experiments in Brazil recently. The International Telecommunications Satellite Organization (INTELSAT) conducted a world-wide propagation measurement campaign [9] over two decades. To supplement these, the International Telecommunication Union (ITU) has also made a resolution [Resolution 5 (Rev.WRC-2000)] to offer assistance to developing countries in tropical areas to carry out national propagation studies. Table 3 below gives a concise history of wave propagation measurements obtained from [10], [11], [12], [13] and [14].

Table 3.1: History of wave propagation

System	**Launch date**	**Frequency (GHz)**
NASA ATS-5 (US)	1969	15.4
NASA ATS-6 (US)	1974	20/30
CTS (Canada/US)	1976	11.7
COMSTAR Series (COMSAT/AT&T)	1976-81	19/28
SIRIO (Europe)	1977	20/30
ETS Series (Japan)	Since 1970s	20/30 (40 in ETS-6)
Olympus (Europe)	1989	12.5/20/30
ACTS (US)	1993	20.2/27.5
EUTELSAT HOTBIRD 6 (Europe)	2002	19.7
TELESAT ANIK F2 (Canada)	2004	20.2

The purpose of measuring wave propagation is mainly to collect adequate data for developing accurate prediction method for most regions of the world. Currently the interest lies in the Ku- and Ka-band frequencies. During the course of these experiments, continuous and simultaneous propagation and meteorological data are collected for a long period of time. Measured data were needed for periods of at least a year due to the cyclo-stationary characteristics of the weather that produces the attenuating events. For the purpose of collecting data, the sites selected were equipped with co-located beacon receivers and radiometers at approximately the same frequency, a rain gauge, and humidity and temperature sensors. The collection of rainfall rate data is for the development of a statistical relationship between the path attenuation and point rainfall rate. This also requires collecting long-term data.

The geosynchronous earth orbit (GSO) is the preferred orbit for communication satellite due to having the advantage of remaining permanently in the same area of the sky, viewed from a particular location on Earth. It is constantly within view of a given ground station, enabling continuous communication with the satellite. In addition, if the orbit is circular (eccentricity = 0), and the orbit is in the equatorial plane (inclination angle = 0), the satellite will appear to hover motionless above the earth at the subsatellite point above the equator. This important special orbit is the geostationary earth orbit (GEO). Unlike geostationary satellites, geosynchronous satellites do not hover motionlessly, but over the course of a day, traces out a path in the sky that is typically a lissajous "figure of 8" as drawn in Figure 3.1, for orbits with zero eccentricity. As the

eccentricity increases, the shape changes, appearing as a teardrop or a tilted ellipse. It is noted however that the 'real world' GEO orbit in use today would have an inclination angle slightly greater than 0 and possibly an eccentricity that also exceeds 0 [7].

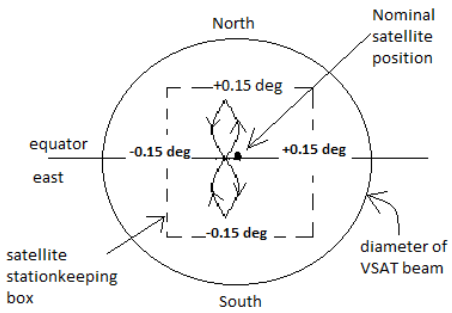

Figure 3.1: Variation caused by an inclined orbit

All of the early experimental satellites used for propagation research were in geosynchronous orbits with inclinations of usually at least 1 degree. This coupled with the use of non-tracking antennas on the ground for propagation measurements, produced data in the absence of any path attenuation similar to that shown in Figure 3.2, a schematic of the received signal levels during clear sky, for two days. The vertical scale is the relative change in dB of the signal level from the mean level measured at the earth terminal.

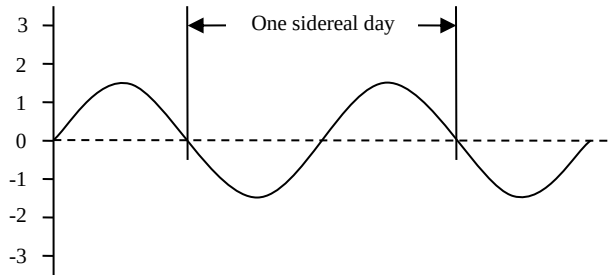

Figure 3.2: Received signal variation in clear sky over a two day period.

Given the cyclical changes in clear-sky level due to satellite payload and orbital instabilities, when a rain attenuating event occurred, it was very difficult to measure the actual change in signal level due only to the rain, as can be seen in Figure 3.3, where the same attenuating event is shown at two different times, A and B, in the diurnal cycle. If only the signal level reached is recorded, a value of about -3 dB would be the value in event A while, in event B, the value would be about -1dB.

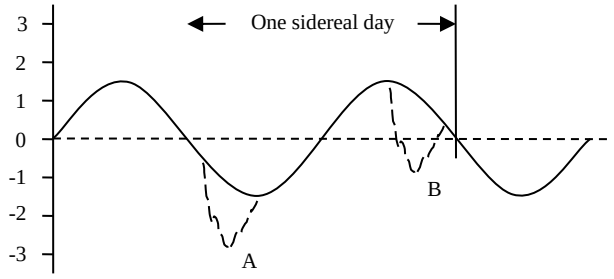

Figure 3.3: Received signal variation when a rain attenuating event occurs at two different parts of the day

To overcome the lack of a constant signal level in clear sky due to orbital and satellite stability effects, collocated radiometers were directed along the same look angle as the earth terminal receiving antenna. A radiometer detects changes in sky-noise temperature, from which path attenuation can be inferred. Any signal level changes due to orbital or satellite payload instabilities will not be detected by the radiometer, and so only effects due to constituents in the path will cause changes in sky-noise temperature. Radiometer data were therefore used to remove satellite signal level instabilities, and it was therefore assumed that what was left was the true path attenuation. See for example [15], [16], [17] and [18].

In beacon measurements, the strength of a satellite-borne beacon signal is monitored on the ground and the variations of the signal level are interpreted as propagation impairments. However, only a relative measure of the propagation impairments can be obtained. This is due to a lack of an absolute calibration of the measurement system and signal variation induced by the hardware associated with the beacon source, as well as the receiving equipment on the ground. Satellites that are not strictly geostationary, will have a small inclination angle with respect to the equator. Most of the available beacon data have been analyzed with reference to clear-sky conditions, and this process essentially removes the bulk of the low-attenuation producing phenomena.

Radiometers rely on sky noise temperature variations to estimate propagation impairments. Although the technique provide an absolute measure of the impairment level, only absorptive phenomena due to particulate matter and gases can be measured. In

addition there are several limitations to radiometer observations, including restricted dynamic range and the sensitivity to thermal emission from regions outside those that affect a satellite link at the same look angle as the radiometer. In order to capture all propagation phenomena a combination of beacon and radiometer measurements are normally required. Some of the more recent data collected using the INTELSAT system, the European Space Agency (ESA) Olympus satellite, and the National Aeronautics and Space Administration (NASA) Advanced Communications Technology Satellite (ACTS) are of this type and provide a useful database to enable the evaluation of propagation data [19].

From the collected data, the analysis and modeling of various factors impairing propagation, such as atmospheric and rain attenuation, depolarization, scintillation, and rain scattering, have been carried out. Impairment countermeasures by means of site diversity and uplink power control have also been developed. As a result of these propagation campaigns, the experimenters were able to develop a number of reliable prediction methods of the various factors impairing propagation on a worldwide scale, that were then adopted as formal recommendation by the ITU Radiocommunication Sector (ITU-R) [14]. The communications system providers are then able to design means to mitigate such propagation impairments, more commonly referred to as fade mitigation techniques (FMT).

3.1 Satellite Beacon Measurement

A beacon is a fixed-frequency unmodulated carrier transmitted by the satellite for reception on the ground. Given a satellite beacon in geostationary orbit, the direct

detection of the received signal will permit the excess attenuation along the path to be readily observed. Excess attenuation refers to attenuation from a mean value established in clear sky conditions. Transmission measurements using an available satellite beacon signal offer a wide dynamic range and are the most popular [20]. Good quality measured data can usually be extrapolated to other elevation angles and frequencies using approved ITU-R procedures. However, beacon measurements contain uncertainties [7]. The uncertainties can be grouped into two main causes; satellite induced errors and earth station induced errors.

Satellite induced errors include antenna pointing errors and transponder loading effects. Pointing errors are caused by the movement of satellites. The errors are small, change slowly and are not of major concern as important rain effects can be readily identified and extracted from the signal. Pointing errors are caused by nutation (wobble) in spin-stabilized satellites and by the pointing control algorithm used in body-stabilized satellite. Spin-stabilized satellites are cylindrical in shape and are stabilized in orbit by spinning on their North-South axis. Although spinning control and nutation correction are implemented [21], nutation effects still remains albeit very slightly. Spin-stabilized satellites rotate at rates on the order of 90 revolutions per minute, and unless rapid sampling is being employed, any changes in received signal level due to nutation will go undetected [7].

A body-stabilized satellite is maintained in space using the stabilizing element of each of the three axes; roll, yaw and pitch. Unlike spin-stabilized spacecraft, the entire body remains fixed in space, relative to earth and requires active attitude control.

However the pointing control algorithm causes nutation when it drifts between the two extremes of the control limits, before pointing corrections are applied [7]. The nutation period for 3-axis stabilized satellites is on the order of 90 seconds.

In some satellite propagation measurements, the satellite is not in a truly geostationary orbit but has a non-zero inclination angle with respect to the equatorial plane. This produces a cyclic variation in its position in the orbit. This cyclic variation has a known period of one sidereal day (approximately 23 hours 56 minutes and 4 seconds) and can be easily removed using a co-located radiometer. A co-located radiometer operating at the beacon frequency can be used to set the mean level for the beacon data [22], [23] and [24] since it is not subject to spacecraft-induced diurnal signal variations. In the ACTS experiment, radiometrically inferred attenuation was used to determine the path attenuation during periods with low attenuation values. In one experiment a prediction scheme using a fourth-order harmonic fit to the diurnal variations of the previous unattenuated beacon signal was used during periods with high attenuation [23]. A radiometer can usually provide a good estimate of the beacon attenuation except during the onset or cessation of a rain event. Difficulties, as well as a solution, to reference level estimation scheme during solar eclipse periods and during sun intrusion were also discussed in [23]. In an experiment in Papua New Guinea [2], evidence of diurnal, seasonal and annual variations were found in the received satellite beacon signal as well as in the data collected from a co-located radiometer. This phenomenon was given the term atmospheric tides by the authors. The variation of the signal was also found to have a periodic variation of a solar day and not a sidereal day. The existence of

this variation in the radiometer data as well as its periodic solar day variation proves that the diurnal variations observed in signal level were due to the atmosphere and not due to changes in satellite antenna beam pointing caused by orbital motion, and/or variations in pointing due to diurnal heating effects on the satellite antenna. The atmospheric tide phenomenon was generally ignored by propagation experimenters as it seems to be probably a tropical phenomenon of little relevance to temperate climates. However, similar observations were observed on analyzing the ACTS data collected in the temperate regions of North America [25]. For propagation measurements, no formal procedure has been adopted yet that permits the removal of diurnal variations due to atmospheric tides, although the use of radiometers to remove diurnal effects due to satellite motion of beam coverage changes is well established.

Transponder loading is another possible source of error. A transponder is usually a simple repeater which gathers signal over a range of uplink frequencies and re-transmit them on a different set of downlink frequencies to receivers on Earth. This is also known as a frequency translation transponder. However the distribution of power amongst the signals that it carries depends on the number of signals being supported. If the beacon signal can be modulated, the application of the modulation will also reduce the power in the carrier. Thus serious errors can occur when measurement of the beacon signal is done without knowledge of its modulation state, or the loading of the transponder. These changes can go unnoticed if occurring during a severe precipitation event.

The second major cause of beacon measurement error happens at the earth station. Some satellite beacon receivers use the phased locked loop (PLL) technique to track

variation in the beacon frequency. Errors can occur when the signal is lost. The bandwidth of the loop is a compromise between the fade margin required and recovery of the lock. A smaller bandwidth of the loop enables lower signal level to be detected, but it will take longer for the signal to be re-acquired when lost. However the bandwidths of the PLL are now automatically switchable. The bandwidth is relatively narrow when the signal is locked, and can be extended to permit relatively fast re-acquisition when the signal is lost [7]. A frequency locked loop (FLL) was used instead in the Olympus propagation measurement program conducted at Virginia Tech [22]. Frequency information was derived from the 12 GHz downlink frequency, the lowest of the three experiment frequencies. The Olympus experiment carried three different beacon frequencies; 12 GHz, 20 GHz and 30 GHz. A lower frequency experiences smaller fading, ensuring that frequency lock was maintained in all but the most severe fades. The 12 GHz FLL also permitted rapid reacquisition after loss of lock since the 12 GHz signal returned to the acquisition threshold level before the 20 and 30 GHz signals.

Earth station equipment is also another source of error. Proper equipment testing as well as constant calibration is needed to ensure any undue experimental errors are detected and accounted for. In the ACTS experiment, higher than usual attenuation values were recorded due to the existence of a crinkled plastic coating over the conducting surface of the antenna reflector, which prevented water from flowing quickly off the antenna. Water on the feed window also produces a mismatch between the antenna and receiver LNA design [23]. These problems however were successfully resolved. Constant calibration is also needed to ensure correct measurement. In [24] beacon receiver

calibrations were performed approximately every 15 minutes by the signal injection method to allow for the characterization in the enhancement region and to avoid having to rely on rare periods with low scintillations for a constant reference signal. [20] has a waveguide switch in the RF section of each receiver for injection of a calibration signal into the beacon path and a motorized step attenuator to aid in system calibration. It was possible to minimize data loss through equipment malfunction by careful system design, built-in redundancy, and daily operator inspection [24].

3.2 Radiometer

A radiometer is a device for measuring the variation in noise power or brightness temperature of a source. Low level rain attenuation (up to 10dB) can also be inferred from the sky-brightness temperature measurement. This provides a means to cross check on the beacon-attenuation measurements. The radiometrically derived attenuation (A_{RD}) can be obtained from the following formula:

$$A_{RD} = 10log\frac{(T_m - T_c)}{(T_m - T_{sky})} \tag{3.1}$$

Where T_m is medium temperature, $T_c = 2 \text{ to } 3\ K$ is the cosmic background temperature and T_{sky} is sky-brightness temperature measured by the radiometer, which is assumed to be the radiated temperature of the medium.

When properly calibrated [22], [23], the radiometer measures gaseous attenuation in clear-sky conditions, in an absolute sense. During rain, attenuation derived from the radiometer contains the contribution due to both gaseous and rain attenuation. The hydrometeor effect (attenuation due to rain) can be separated from the gaseous attenuation when the inferred path attenuation exceeds a threshold set for the clear-sky condition.

Radiometer data are also used to establish an absolute reference level for beacon data, since it is not subject to spacecraft-induced diurnal signal variations. The spacecraft platform will have some proper motion in its geostationary orbit. This motion interacts with the earth-terminal antenna pattern that leads to a diurnal fluctuation in the received beacon signal. The radiometrically predicted attenuation, however, only contains effects from oxygen, water vapor, and hydrometeors, plus a constant low value due to the cosmic background temperature. This bias removal method is widespread: for example, the European Space Agency uses an established ‘template’ from clear-weather data, obtained from averaging 15 min average data point values at the same time over the four previous days [26]. [24] uses six minutes averaged data points to establish the diurnal variation by averaging values in a day with those at the same time on the previous three and following three days. [27] uses a sixth-order polynomial interpolation to approximate the daily diurnal variation curve, allowing them to handle most rainy periods without using previous- or following-day data.

There are two types of radiometric measurements from which slant path attenuation can be derived; active measurements and passive measurements. Active

measurement uses the Sun as a natural radio source to measure attenuation through the atmosphere. Radiometers that are designed specifically to follow the motion of the Sun are called Sun-tracking radiometers. However Sun-tracking radiometer data are not easily transferable to satellite communications due to the fact that the Sun is not a stationary source. To keep track with the Sun's movement, the attenuation statistics will have to be for a multitude of different elevation angles and azimuths, and no night-time data will be obtainable. The tracking of the Sun will also conceal diurnal characteristics of weather patterns and their preferred orientations. To overcome these deficiencies, passive radiometer measurements were introduced that used fixed-pointing radiometers.

There are two main types of passive radiometers; total power and Dicke radiometers. Total power radiometers are designed to share the same antenna and RF hardware with the beacon receiver. It is susceptible to gain changes in the receiving equipment, but the signal path through the receiver from the antenna is not interrupted, permitting simultaneous radiometric and satellite beacon measurements. This combined system is cheaper to build than two individual units, as well as being easier to correlate as both have the same antenna pattern.

A Dicke radiometer offers a more accurate method of measuring sky noise temperature than a total power radiometer as it eliminates all errors due to gain changes in the receiver. However it does not allow any satellite beacon signal to be measured accurately using the same antenna and receiver. This standalone equipment is usually co-located with the beacon receiver during propagation measurement.

Measurements taken at Virginia Tech under the Olympus satellite measurement program used both a total power radiometer integrated with the satellite beacon receiver, as well as a co-located NOAA Dicke switched radiometer. The experimenters found that the Dicke switched radiometers offered a more accurate method of measuring sky noise temperature than total power radiometers. However, the total power radiometer used in the Virginia Tech experiment was found to provide sufficient accuracy when predicting low-level atmospheric attenuation, and was a cheaper alternative [28].

As with any measuring equipment, passive radiometers are prone to potential errors, causing changes in the perceived brightness temperature. The averaging effect of the radiometer antenna pattern, the location of the radiometer antenna away from the rain cell, radiation from the ground detected by the antenna side lobes and scattering by the attenuation medium may cause an underestimation of the actual brightness temperature measured. However, despite all of the inherent errors possible, the results provided by passive radiometers are rather good [7].

Potential errors can be minimized by repeated calibration and careful control. In [22], to improve the ability of the total power radiometer to distinguish between changes in the antenna noise temperature (or sky noise temperature) and variation in the gain of the receiver or its noise temperature, three measures were implemented. First, the physical temperature of the receiver stages are kept at a constant elevated temperature of 50°C in the RF front-end and 40°C in the radiometer IF enclosure. This minimized the variations in receiver gain and noise temperature. Second, at periodic intervals, a calibrated amount of noise from a noise diode was injected to extract gain fluctuations.

At a longer interval a waveguide switch transferred the input of each receiver from the antenna feed output port to a waveguide load that was kept at a constant known temperature. The switching to an ambient temperature matched load was to determine system noise temperature. Radiometer data were then processed to remove the effects of gain and system noise temperature changes before the calculation of radiometric attenuation.

The ACTS experiment used wide-bandwidth, high gain total power radiometers with a digital beacon receiver. The use of a digital receiver provides precise measurement of relative changes in beacon level that extends the dynamic range of the radiometer observation. However wide-bandwidth, high gain total power radiometer systems are prone to slow changes in time that is related to the electronic circuits between the radiometer detector and the analog-digital converter used to record the data. To provide a stable system, every 15 minutes, two known power level changes are inserted into the radiometer receiver and the receiver output was corrected to match these changes. Overall radiometer system calibration is then needed to provide an accurate relationship between the calculated radiometric attenuation and the measured sky brightness temperature as the power detected by the radiometer is not only from noise power incident on the antenna but from noise power generated by losses in the switch and waveguide. The components of the waveguide switch which connects the radiometer to the antenna were thermally coupled to the outside air temperature. The system calibration was established by comparing the sky brightness temperature observed by the radiometer

to those predicted theoretically based on simultaneously measured vertical profiles of atmospheric temperature and relative humidity [23].

3.3 Propagation Impairments

Propagation impairments include rain attenuation, gaseous attenuation, cloud attenuation, rain and ice depolarization, and scintillation. As the focus of this research effort is on line-of-site link impairments during apparent clear sky; hydrometeor effects, such as rain attenuation, cloud attenuation, rain and ice depolarization are discussed in appendix A. Other effects such as shadowing, blockage, and multipath scintillation, which may be present on satellite links involving mobile terminals, are not considered here.

The impact of propagation impairments causes uncontrolled variations in signal amplitude, phase, polarization, and angle of arrival. This results in a reduction in the quality of analog transmission and an increase in the error rate of digital transmission.

Attenuation is a reduction in the transmitted signal amplitude, which can degrade the reliability and performance of the communication links. It can be caused by atmospheric gasses (mainly oxygen and water vapor), by clouds which contain liquid water and ice particles, and precipitations such as rain, snow and hail.

Scintillation is the rapid fluctuations of the signal parameters or radiowave such as amplitude, phase, angle of arrival, and polarization. For frequencies above 3 GHz, refractive index irregularities occurring in the troposphere are the main cause of tropospheric scintillation.

Depolarization causes energy from one polarization state to transfer to another undesired orthogonally polarized state. This results in crosstalk or interference between

two orthogonally polarized channels. Depolarization is caused by non-symmetrical particles such as raindrops, snowflakes and ice particles; as well as by multipath propagation.

The random nature and general unpredictability of the phenomena that produce the propagation effects add further dimensions of complexity and uncertainty in the evaluation of transmission impairments on satellite communications. Consequently, statistical analyses techniques are generally most useful for the evaluation of transmission impairments on communication links.

3.3.1 Gaseous Attenuation

A radiowave propagating through the earth's atmosphere will experience a reduction in signal level due to interaction with the gaseous components in the transmission path, mainly oxygen and water vapor. The principal interaction mechanism is molecular absorption, which results in a reduction in signal amplitude (attenuation) of the signal. The absorption of the radiowave results from a quantum level change in the rotational energy of the molecule, and occurs at a specific resonant frequency or narrow band of frequencies. Oxygen has a series of very close absorption lines near 60 GHz and an isolated absorption line at 118.74. Water vapor has lines at 22.3 GHz, 183.3 GHz and 323.8 GHz.

Signal degradation can be minor or severe, depending on frequency, temperature, pressure, and water vapor concentration. Atmospheric gases also affect radio communications by adding atmospheric noise to the link. A complete method for calculating gaseous attenuation is given in Rec. ITU-R P. 676 [29].

3.3.2 Tropospheric Scintillation

Refractive index fluctuations in the first few kilometers of altitude, causes rapid signal fluctuations known as tropospheric scintillation. Signal parameters affected include amplitude, phase, angle of arrival and polarization. At above 10 GHz tropospheric scintillation is the sole cause of rapid signal fluctuations as ionospheric scintillation decreases with frequency. On satellite links, the significant scintillation effects are mainly attributed to strong turbulence in clouds and can appear in both essentially clear sky and bad weather condition. The effects are seasonally dependent, and vary day to day with the local climate [21]. Models estimating the effects of scintillations on the received signal can be found in [30], [31].

Scintillation fades could have a major impact on the performance of low margin systems (above 10 GHz) [31], for which the long-term availability is sometimes predominantly governed by scintillation effects rather than by rain. In Ka- or V-bands, where compensation techniques have to be designed, the dynamics of the scintillating signal may interfere with tracking system or FMT [32].

3.3.3 Sky noise increase

Any natural absorbing medium in the atmosphere that interacts with the transmitted radiowave will not only produce a reduction in the signal amplitude, but will also be a source of thermal noise radiation. The noise associated with these sources, referred to as radio noise or sky noise, will directly add to the system noise through an increase in the antenna temperature of the receiver. For very low noise communication receivers, radio

noise can be the limiting factor in the design and performance of the system. Radio noise is emitted from many resources, both natural and human made.

3.4 Use of radiometer data to correct beacon data

This section describe how a radiometer operating at a frequency close to that of the beacon receiver is used both to remove diurnal spacecraft-induced fluctuations, and to set an absolute reference level for the beacon data. As beacon measurements are relative rather than absolute, it is impossible to set a reference level without an auxiliary measurement. By having a reference level, any other uncertainties that are unrelated to an attenuation event can be removed. These uncertainties are identified as the diurnal variation due to spacecraft fluctuations, and clear air absorption [27].

In order to collect attenuation statistics from propagation experiments, two attenuation outputs need to be extracted from beacon measurements, both with any diurnal spacecraft fluctuations removed. These are attenuation relative to free space (A_{fs}) (or total attenuation) and attenuation relative to clear air (A_{ca}).

Attenuation relative to free space is the difference in decibels, between instantaneous signal (S_i) and the free space signal (S_{fs}) that the receiver would receive, if the propagation medium is a vacuum. A_{fs} includes all propagation impairments, i.e. fading due to gaseous absorption, clouds, scintillation and rain. Its value is normally positive, indicating a loss, but can be negative when the enhancement due to multipath propagation or tropospheric scintillation exceeds losses due to gases during clear weather.

$$A_{fs} = S_{fs} - S_i \tag{3.2}$$

Attenuation relative to clear air is the difference in decibels, between the instantaneous signal (S_i) and the signal that the receiving terminal would receive in clear weather (S_{ca})

$$A_{ca} = S_{ca} - S_i \tag{3.3}$$

A_{ca} includes scintillation, rain and cloud effects, but excludes gaseous absorption. S_{ca} is the clear-air reference level. It is determined from the free-space reference level and radiometer data.

In setting the beacon reference level process, several general steps were implemented by the propagation experiment in Olympus [22] and [27], Texas [24] and [33], Brazil [34] and ACTS [23].

In the initial step, data that may contain rain attenuation is avoided by considering data for which the sky temperature T_{sky} is less than a threshold. For Olympus, the threshold is 60K for the 12 GHz or 110K for 20 and 30 GHz. For Texas, T_{sky} has to be less than 90K for the 11.2 GHz received beacon frequency.

Scintillation effect is first removed using an averaging process. Both Olympus and Texas used a consecutive 6 minute interval averaging, a 1 minute interval for ACTS, while in Brazil, 2 seconds averaging was used.

The radiometer provides sky noise temperature data, T_{sky}, that is used to obtain gaseous attenuation (A_{ga}) values, using Equation (3.1). Any hydrometeor effects in addition to gaseous attenuation can be removed by limiting the T_{sky} values used in the equation. These threshold values were determined by trial and error from several days of data during the calibration process. By removing A_{gas} from the averaged measured beacon signal, the remaining attenuation is ascribed to spacecraft motion, A_{mot}. The symbol < > is used to denote the measured beacon signal after completing the averaging process.

$$\langle A_{meas} \rangle - A_{gas} = A_{mot} \tag{3.4}$$

Several different techniques have been proposed for the removal of the spacecraft induced diurnal variation from the beacon signal. The Olympus experiment at Virginia Tech used a sixth-order polynomial interpolation to approximate the diurnal variation curve, A_{mot}. This was because the Olympus satellite was in an inclined geosynchronous orbit with significant changes in signal level in clear sky. In the Texas experiment, a seasonal decomposition algorithm is used to remove this variation, which involves average values collected at 10 min intervals from three previous and following three days, all at the same local time. In the ACTS set-of experiments, the reference level is obtained from a fourth order harmonic fit to the attenuation corrected beacon power levels (after the removal of inferred gaseous attenuation from the radiometer data) from the previous day, with an additional diurnal variation correction to compensate for day-

to-day variations in satellite radiated power. This additional diurnal correction is computed at the end of each hour and applied to predict the correction for the next hour.

Thus after A_{mot} is estimated, the attenuation relative to clear air and attenuation relative to free space are obtained as follows:

$$A_{ca} = A_{meas} - A_{mot} \tag{3.5}$$

$$A_{fs} = A_{ca} - A_{gas} \tag{3.6}$$

The ACTS database provided values of attenuation relative to free space, while the data form the Olympus and Texas experiments as the measured relative beacon signal level in dB. The database from the experiment in Brazil was given in dBm. Thus data from Olympus, Texas and Brazil consist of raw data measured at the receiver, based on an arbitrary scale.

3.5 Clear air effects on fade mitigation techniques and low margin systems

Satellite communication links operating at frequencies above 10 GHz are greatly affected by propagation impairments such as attenuation, scintillation and depolarization [35]. There is also an increasing demand in domestic satellite services for corporations and small businesses that utilizes very small aperture terminals (VSATs) [4] for data application in the point-to-point and point-to-multipoint services. In view of the spectral congestion of the conventional frequency bands (C and Ku) allocated for satellite services, the next generation of communication satellites will exploit the outstanding

potential offered by Ka-band, including large available bandwidth and spacecraft with high-gain spot beam antennas that will be able to support smaller user terminals [36].

The advantage of smaller antenna size is that it reduces the cost of an earth station significantly. It does not require tracking, and the requirement for its location and system power is substantially reduced. However antenna size reduction also reduces the achievable forward gain and increases the beam widths, making them more susceptible to signal loss and interference.

Common counter measures to compensate for gain deficiencies include increasing the transmit power of the satellite or the coding gain. These are not always possible solutions due to power-flux density restrictions and economics in satellite transmission, as well as bandwidth and a round-trip delay limitation in increasing the coding gain. These problems are aggravated by the increased rain attenuation in bands above 10 GHz, as well as in sites with low elevation angles, which experience a higher likelihood of propagation impairments due to the longer path through the lower atmosphere. Availabilities better than 99.9% or 99.5% are difficult to achieve with low fade margin systems such as VSAT, with only 1 to 3 dB of available margin [35].

The standards for VSAT operations are not governed by the same strict performance requirements of public-switched telephone networks (PSTNs), and the availability requirements are substantially less. The user can specify requirements consistent with a particular application [4]. However the need to provide open VSAT networks requires that their links meet agreed international standards. These standards can be grouped into two objectives: performance and availability [37]. Performance

objectives define the requirements for connection during most of its time in service. This refers to operation during generally clear sky. Availability objectives define signal threshold during which an outage is expected. This happens during an onslaught of s major propagation impairment such as precipitation.

Fade margin is the system gain needed to insure the necessary Quality of Service recommended by the ITU-R against various transmission and other impairments. Traditionally for C-band services, the fade margins are increased to combat propagation effects. However, as frequencies above 10 GHz experience more severe signal fading, the larger fade margins required are not usually feasible either technically or economically. This requires the link fading to be compensated by other means in order to increase system availability. Fade mitigation techniques (FMT), are techniques that overcome fading without the use of large fixed margins. FMT can be divided into three categories: power control techniques, adaptive transmission techniques and diversity protection schemes. With the implementation of FMT it is possible to design VSAT systems with a reduced fixed margin that corresponds to the worst case of fading achievable in clear-sky conditions [32].

To maximize the link availability, the FMT system performs the following series of common functions; (a) observe/monitor link quality, (b) do short-term estimation/prediction of the behavior and the relevant duration of the next state of the channel, and (c) set/change the parameters of the system based on the above short-term estimate. To provide an accurate prediction, the design of the FMT requires an exact knowledge of the dynamics of the propagation channel. Conventionally the mean signal

level is determined based on attenuation and depolarization statistics, together with data on fade duration and intervals, site diversity and fade rates. The mean clear sky has always been taken as a constant value, but experiments in Papua New Guinea showed evidence of variation of clear sky level as high as 3dB peak to peak. A 3 dB rain attenuation event could therefore lead to a VSAT system in this region dropping below performance margins at times, even though there is an apparent 7 dB performance margin.

CHAPTER 4: INVESTIGATION AND ANALYSIS

This investigation began by searching for evidence of concurrent periodic variations in radiometer and satellite beacon attenuation data under clear sky conditions. These data can be obtained from propagation experiments that used co-located radiometer and satellite beacons directed along the same path. A long-term, time series or sampled data would potentially provide additional information of the existence, or lack of existence, of cyclical changes in the sky-noise temperature and path attenuation measured over daily, monthly, and annual periods.

Several contacts were made with research institutions and organizations to gain access to their data bank: NASA, Dr. Carlo Riva of Politecnico de Milano in Italy, EchoStar Satellite Services, Dr. Wolf Vogel of Texas A&M University, Dr. Luiz da Silva Mello of Pontifical Catholic University of Rio de Janeiro in Brazil, and Dr. Dennis Sweeney of Virginia Tech for the Olympus experiment data.

Data analysis begins with reviewing the variations seen in the satellite beacon received level and the path attenuation derived from the radiometer. Satellite beacon measurements give the attenuation of the signal that is received by the ground receiver, while a radiometer provides a measure of the inferred attenuation of the signal that is obtained based on the noise temperature that is detected along the path. If an attenuation effect has been caused by satellite and/or earth station tracking errors, then the radiometer

will not have observed any changes in sky noise along the path. Conversely, if an attenuation event is observed simultaneously by the radiometer and beacon receiver, then the effect must have been due to changes in the atmosphere along the slant-path.

Spectral estimation method is then used to gain insight into the frequency content of the time series.

4.1 Preliminary examination of the time series data

Investigation began with the ACTS database. This database contains 1-minute averaged beacon attenuation (dB) and radiometer-derived attenuation (dB) for two frequencies, 20.2 GHz and 27.5 GHz. It also stores various meteorological data collected every minute. The ACTS propagation experiment was conducted for five consecutive years (1994 to 1998), and from 6 sites in North America, collecting more than 2 million data points for each site. The sites span many rain-climate zones, and path elevation angles to the satellite vary from 8° to 52°. This is summarized in Table 4.1

Table 4.1: ACTS propagation terminal (APT) locations and their path characteristics

Location	**Coordinates (N lat. W long.)**	**Path Elevation and Azimuth angle (Clock-Wise from North)**	**Station Height (m)**	**Missing data file replaced**
Fairbanks, Alaska	64.85°, 147.82°	8.1° / 129.3°	180	0.2%
Vancouver, BC	49.25°, 123.22°	29.3° / 150.5°	110	0.1%
Greely, Colorado	40.33°,104.61°	43.1° / 172.8°	1900	5.8%
Tampa, Florida	28.06°, 82.42°	52.0° / 214.0°	50	3.0%
White Sands, New Mexico	32.54°, 106.61°	51.5° / 167.8°	1460	11.9%
Norman, Oklahoma	35.21°, 97.44°	49.1° / 184.4°	420	1.8%
Reston, Virginia	38.95°, 77.33°	39.2° / 213.3°	80	0.2%

The chart in Figure 4.1 gives the percentages of the ratio between actual recorded data to total time for the ACTS propagation data collected in 5 years. The ratio was assessed according to month. High data rate (above 90%) can be seen in the majority of the sites except for New Mexico, where available recorded data is below 80% for the month of Jul till Dec. There is also below 80% data from Florida in the month of October.

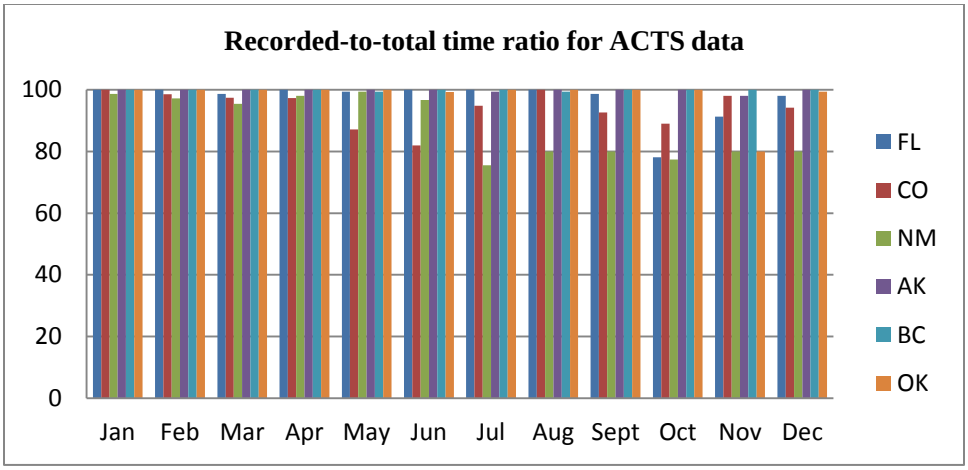

Figure 4.1: Recorded-to-total time ratio for ACTS data

Data collected in each day is stored separately in a file. Figure 4.2 is the data plot for the 20.2 GHz beacon attenuation data, after lost data files were replaced with similar dates of other years, from the same site. Inside available files, any unreadable data point values were also replaced with linear interpolated values. These extracted time series data are referred to as **raw data**.

Large changes in attenuation (shown in the vertical axis) are due to major rain events. The plot for Tampa, Florida shows significant rain effects throughout the year while that for Fairbanks, Alaska shows far fewer significant attenuation effects outside of the summer period.

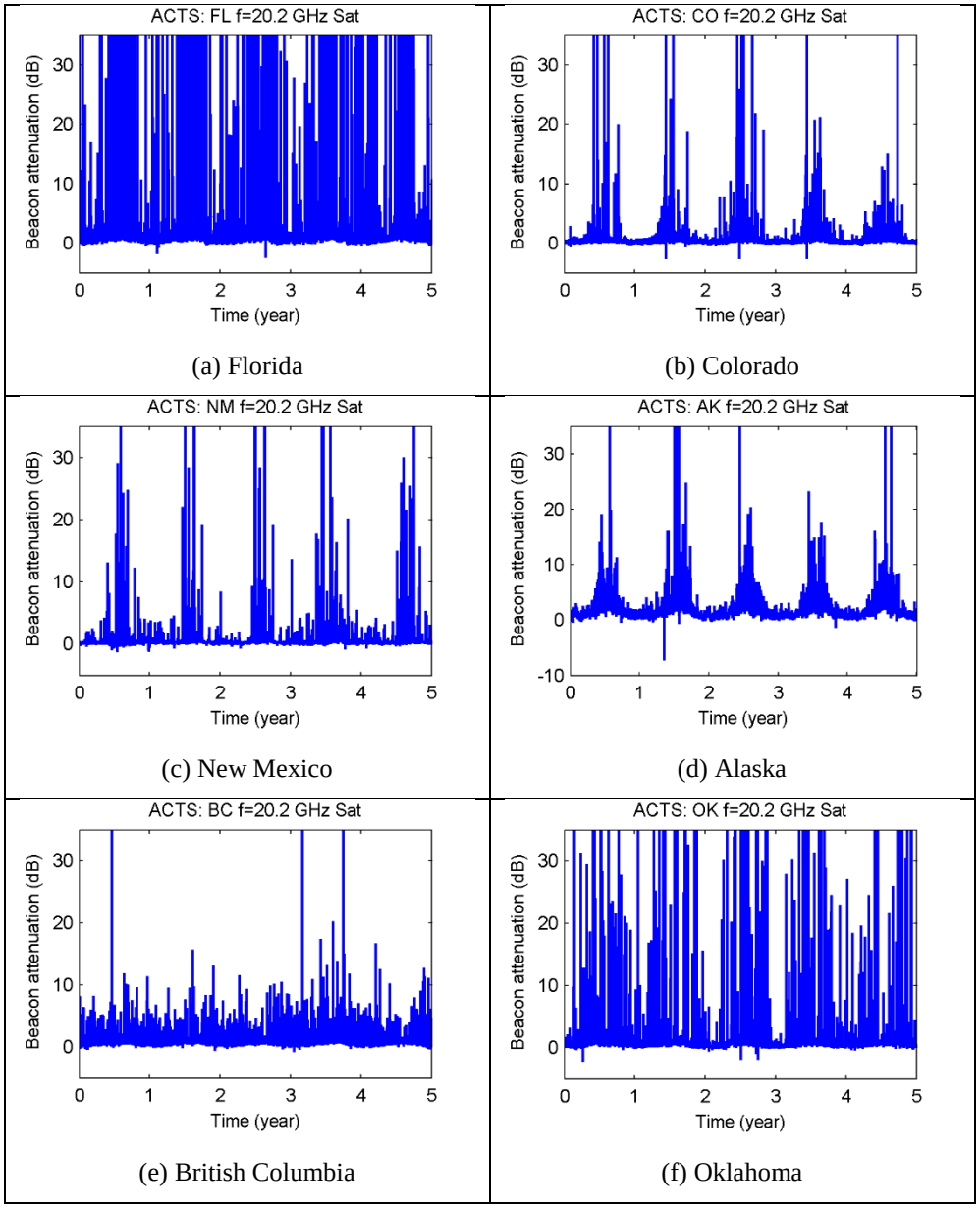

Figure 4.2: ACTS 20.2 GHz beacon attenuation data

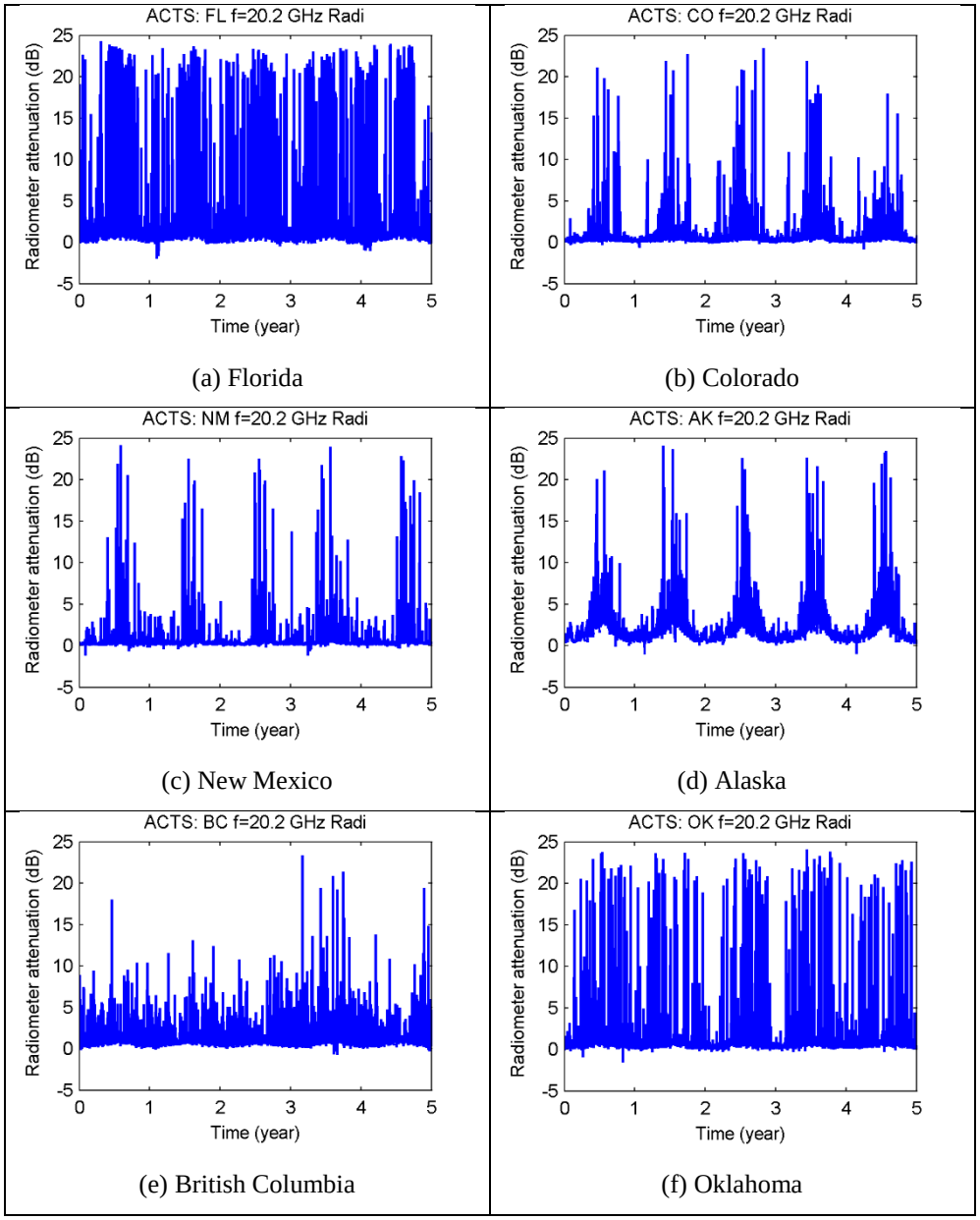

Figure 4.3: ACTS 20.2 GHz radiometer attenuation data

The 20 GHz radiometer and satellite beacon attenuation data were plotted simultaneously and evidence of concurrent periodic variations was then searched for within the plots. Figure 4.4 shows a one week-long sample of the beacon and radiometer attenuation signal variations, taken from a selected period at four different sites, which

had among the clearest periodic variation in the beacon and radiometer attenuation values. The dual plots of beacon and radiometer data are for (a) June 5th to 13th 1996 in Florida, (b) March 14th to 21st 1994 in Colorado, (c) October 12th to 19th 1995 in New Mexico and (d) 9th November to 16th 1995 in Alaska. A distinct periodic variation can be seen here in all sites except Fairbanks, Alaska. Note the time concurrence in the periodic variations in attenuation between the radiometer and satellite beacon traces of Figure 4.4. If the changes in beacon level had been due to satellite pointing errors, there would have been no change in the inferred path attenuation observed by the radiometer. There were some small, scattered rain events within the weeks' worth of data, but the period was mainly characterized by clear weather.

Spectral analysis is then used to assess whether there is a strong cyclic component in a time series.

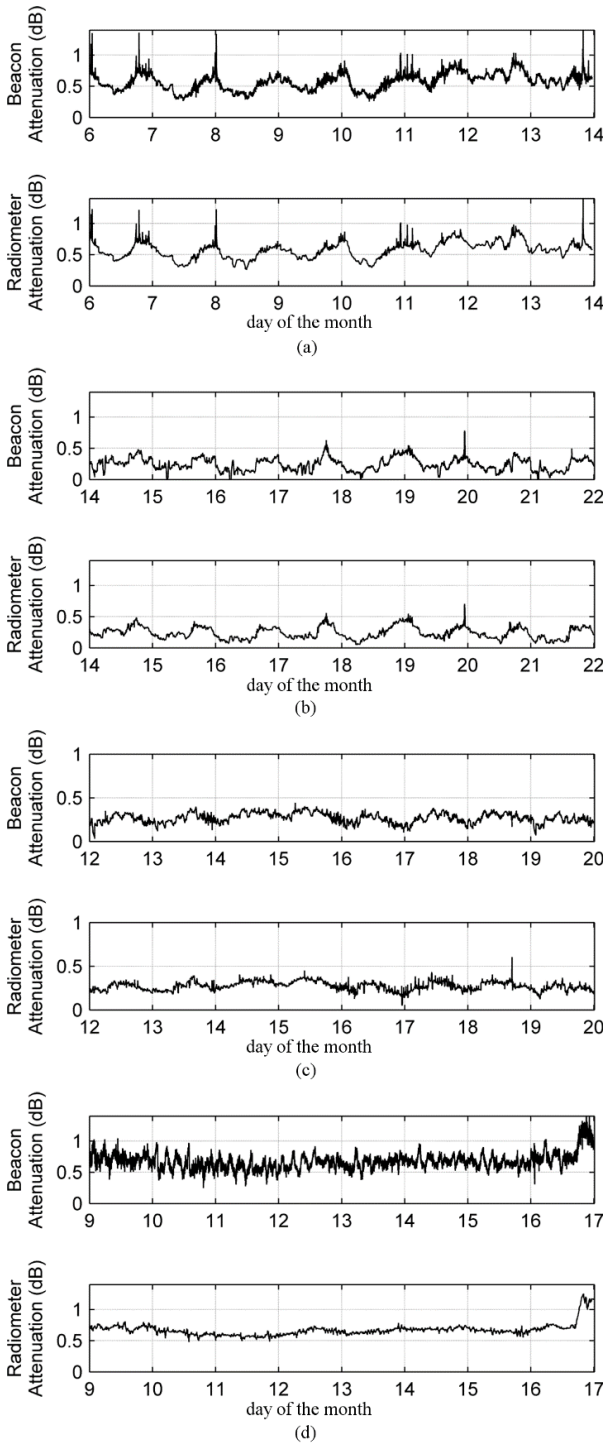

Figure 4.4: The dual plots of beacon and radiometer data for (a) June 5th to 13th 1996 in Florida, (b) March 14th to 21st 1994 in Colorado, (c) October 12th to 19th 1995 in New Mexico and (d) 9th November to 16th 1995 in Alaska

4.2 Spectral analysis

Spectral analysis is a name given to methods of estimating the strength of different frequency components of a time-domain signal. It can be used to gauge the periodicity of a signal variation. The performance of the spectrum estimate depends on:

- Resolution
- Variance
- Bias

A periodogram is an estimate of the spectral power of a signal. It is based on the squared magnitude of the discrete Fourier transform (DFT), a mathematical procedure to determine the frequency of a discrete signal sequence [38]. If a time series has a strong sinusoidal signal for some frequency, then there will be a peak in the periodogram at that frequency. If a time series has a strong nonsinusoidal signal for some frequency, then there will be a peak in the periodogram at that frequency but also peaks at some multiples of that frequency. The first frequency is called the fundamental frequency and its multiples, harmonics. The periodogram $I(f_i)$ equation is as follows:

$$I(f_i) = \frac{N}{2}(a_i^2 + b_i^2) \tag{4.1}$$

$$a_i = \frac{2}{N}\sum_{n=1}^{N} x_t[\cos(2\pi f_i t)] \tag{4.2}$$

$$b_i = \frac{2}{N}\sum_{n=1}^{N} x_t[\sin(2\pi f_i t)] \tag{4.3}$$

Where

$f_i = \frac{i}{N}$, with $i = 1,2,3..until\ \frac{N-1}{2}(if\ N\ is\ odd), or\ \frac{N}{2}\ (if\ N\ is\ even)$

N = the number of samples of the input sequence

x_t= the sequence of input samples, $x_0, x_1, x_2, \dots, x_N$

The Fast Fourier Transform (FFT) is the mathematical tool used to expedite computing of the DFT, and subsequently the periodogram spectral estimate. If the data segment consists of *N* points, then an *N*-point FFT produces *N* samples of the corresponding Fourier transform, limiting its resolution (bin size) to

$$resolution = \frac{sampling\ frequency, f_s}{N} \tag{4.4}$$

However the raw periodogram does not provide a good spectral estimate because of spectral bias and variance [39]. Raw periodogram are periodogram without any smoothing mechanism applied. The spectral bias is caused by a sharp truncation of the sequence, as the time series data has a limit and does not go to infinity, while the variance of the periodogram at a given frequency does not decrease with greater duration of data collection. The Welch's overlapped segment averaging (WOSA) procedure [40] is a

method of combined windowing and averaging, one of the smoothing method used to improve the basic periodogram estimate. Windowing is a method of multiplying the finite sequence with a window function which truncates the sequence gradually rather than abruptly. This reduces the spectral bias. In averaging, the finite samples are divided into K sets of 50% overlapping samples, find the periodogram of each set, and compute the average of the resulting periodograms. The averaged periodogram is a smoothed periodogram, while the raw periodogram is without any smoothing algorithm applied.

In the mathematical formulation of the Welch method, if $x^{(k)}[n]$ represents the k^{th} data segment (of length N) and a normalized window $v[n]$ is applied to this data, then the modified periodograms are defined as

$$\hat{P}'^{(k)}_{x}\left(e^{j\omega}\right) = \frac{1}{N}\left|\sum_{n=1}^{N-1} v[n]x^{(k)}[n]e^{-j\omega n}\right|^2 \tag{4.5}$$

where v has the property

$$\frac{1}{N}\sum_{n=0}^{N-1} v^2[n] = 1 \tag{4.6}$$

This spectral estimate is then taken as

$$\hat{S}_W\left(e^{j\omega}\right) = \frac{1}{K}\sum_{k=1}^{K} \hat{P}_x'^{(k)}\left(e^{j\omega}\right) \tag{4.7}$$

There are many types of different windows that have been proposed over time, each with its own advantage and disadvantage relative to the others [41]. The trade-off is between main-lobe width and side lobe level. A narrower main-lobe gives a better resolution especially with closely spaced frequency peaks, while a lower side lobe reduces side lobe leakages. The Hamming window is selected for use here due to its moderate tradeoff between frequency resolution and spectral leakage, and its common use in narrowband application [42].

The performance of the spectral density of a signal also depends on its resolution; the ability to discriminate spectral features. In order to resolve two peaks that are relatively close together in frequency, it is necessary for the difference between the two frequencies to be greater than the width of the main lobe. For Hamming window, the width of the main lobe is 4 bins. An example is given in Figure 4.5 below copied from [43].

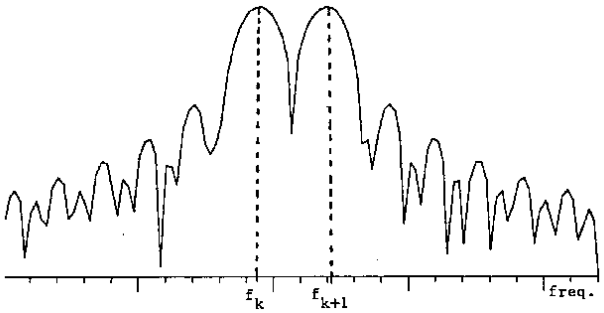

Figure 4.5 Spectrum of two clearly separated sinusoids

Thus to obtain the separation shown in the example, we require the two frequencies to be separated by

$$f_{k+1} - f_k > 4 \times \frac{sampling\ frequency, f_s}{N} \qquad (4.8)$$

Before implementing any spectral analysis procedure onto the time series data, any known trend or seasonal variation needs to be removed in order that the spectrum output is not dominated by known obvious features. The Fourier transform used for generating spectra treats the finite length data as though they are repeated indefinitely. A progressively increasing or decreasing mean signal level (trend) in the data will emerge in the spectrum as a cycle with a length equal to the length of the data. The process or removing trend is called *detrending*.

Any outliers or extreme observations which are inconsistent with the rest of the data are taken out as it may be an error due to a faulty device [44], [45]. In the beacon

attenuation data, outliers are caused by an extreme rain event which generates very high attenuation levels, as seen in Figure 4.2. Outliers in the form of very large or small (negative) could cause spurious background to the spectrum [46].

The following Section 4.2.1 describes the method used to remove outliers and Section 4.2.2 the removal of any seasonal trend.

4.2.1 Removing outliers from data

To identify outliers in the data, the mean signal level, as well as its maximum and minimum are estimated. For that, days that have attenuation values that are within a threshold value (*threshold A*), were preselected. *Threshold A* was set to exclude the top 1% of the data. The mean data was generated by resampling every 9600s in each preselected day (akin to taking 9 samples a day), and then using a 100 point moving average onto it. The 100 point moving average is equal to a minimum of an 11 day average, if the 100 points were taken on successive days. Of the preselected days, the maximum and minimum of each day were selected. A 30 point moving average (a minimum of 30 day averaging) was then used on the maximum and minimum data sets.

Figure 4.6 and Figure 4.7 gives the mean, minimum and maximum line generated for the beacon and radiometer data using the above procedures. The mean line is shown by the red line, while the maximum and minimum are given by the top and bottom blue lines. The raw data is shown in turquoise, and large changes in attenuation (shown on the vertical axis) seen in the figures are due to major rain events.

The plot for Tampa, Florida shows significant rain effects throughout the year while that for Fairbanks, Alaska shows far fewer significant attenuation effects outside of

the summer period. By removing the top 1% of the high attenuation values, attenuation caused by extreme rain events are excluded from the mean, maximum and minimum data sets. This gives a variation of the attenuation levels during clear sky.

The variations in the mean clear sky level (red) depict a seasonal variation, with high attenuation during the hot summer months and lower attenuation during the colder seasons. This seasonal change is similar in both beacon and radiometer data. The upper and lower solid blue lines are the maximum and minimum attenuation detected on a particular clear day respectively. The presence of a seasonal variation is significant, except for the particularities seen for British Columbia, which as can be seen later, are probably a feature of the equipment at the site. The biggest annual and seasonal variation of attenuation levels at all of the sites was found in Fairbanks Alaska. It has the largest changes from winter to summer of the six sites, and the elevation angle is believed to contribute to the large seasonal variations, in addition to having the coldest climate of the ACTS sites.

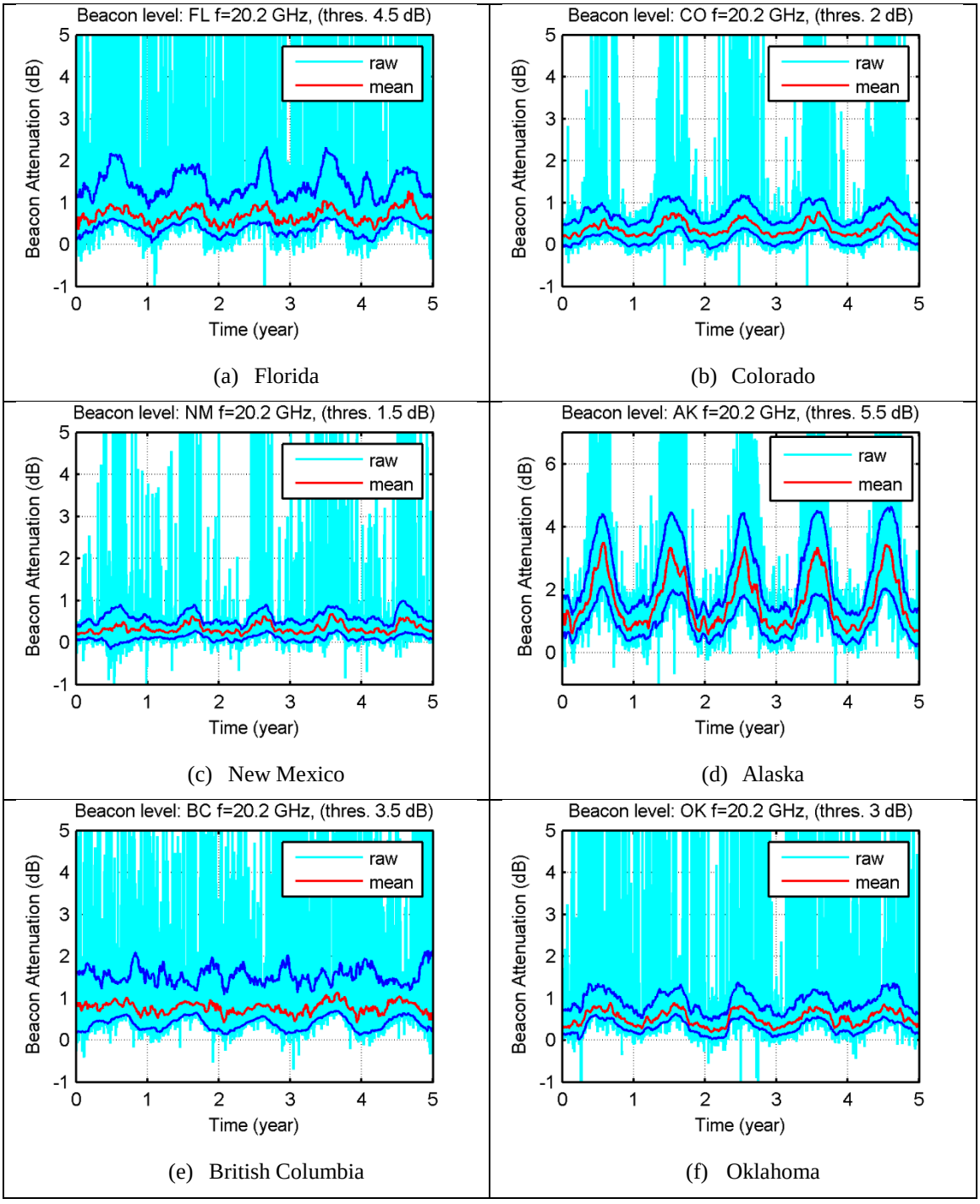

Figure 4.6: The max, min and mean line for ACTS 20.2 GHz beacon attenuation

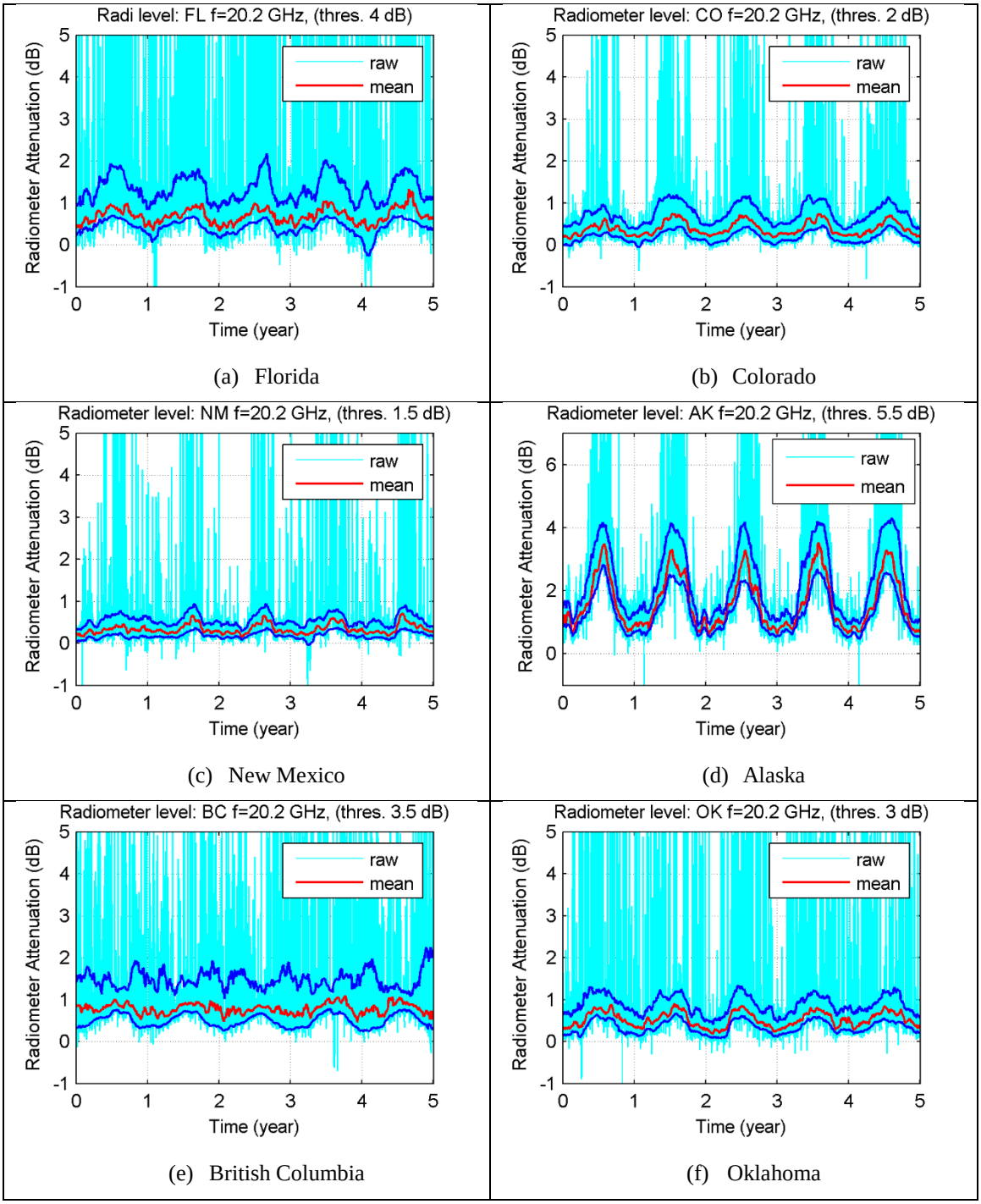

Figure 4.7: The max, min and mean line for ACTS 20.2 GHz radiometer attenuation

To remove the outliers, the mean is then subtracted from the raw data to obtain the differences. From the distribution of the absolute differences, values that exceed the top 2% (*threshold B*) are replaced with their respective values from the minimum (if the difference is negative) or maximum (positive difference) data set.

As most of the outliers appear at higher amplitudes, the above procedure fail to remove attenuation values that dropped extremely below the minimum line. Thus raw beacon data that are below -0.5 dB, and raw radiometer data below -0.2 dB are replaced with respective values from the minimum data set. The resulting time series data after removing outliers are given in Figure 4.8 for beacon and Figure 4.9 for radiometer data. These data are referred to as **capped** data. Figure 4.10 is the flow chart of the above procedure, and *Threshold A* and *B* used for each site is listed in Table 4.2 below. In the table, Subscript 1 refers to the threshold for the beacon data while 2 is for the radiometer data.

Table 4.2: Threshold values for removing outliers in 20.2GHz ACTS data

Site	Florida	Colorado	New Mexico	Alaska	British Columbia	Oklahoma
Threshold A_1	4.5	2.0	1.5	5.5	3.5	3.0
Threshold B_1	1.86	0.7	0.6	1.5	2.2	1.4
Threshold A_2	4	2.0	1.5	5.5	3.5	3.0
Threshold B_2	1.86	0.7	0.6	1.5	2.2	1.4

The removal of the top 2% of the absolute differences (*Threshold B*) was selected as this resulted (Figure 4.8) in data values that are between the maximum and minimum

data set generated earlier (Figure 4.6). From the result in Figure 4.8, most of the extreme values have been removed.

In all subsequent entries, capped data refers to data that has undergone this outlier removal process. In the next section, seasonal variation removal procedures are implemented.

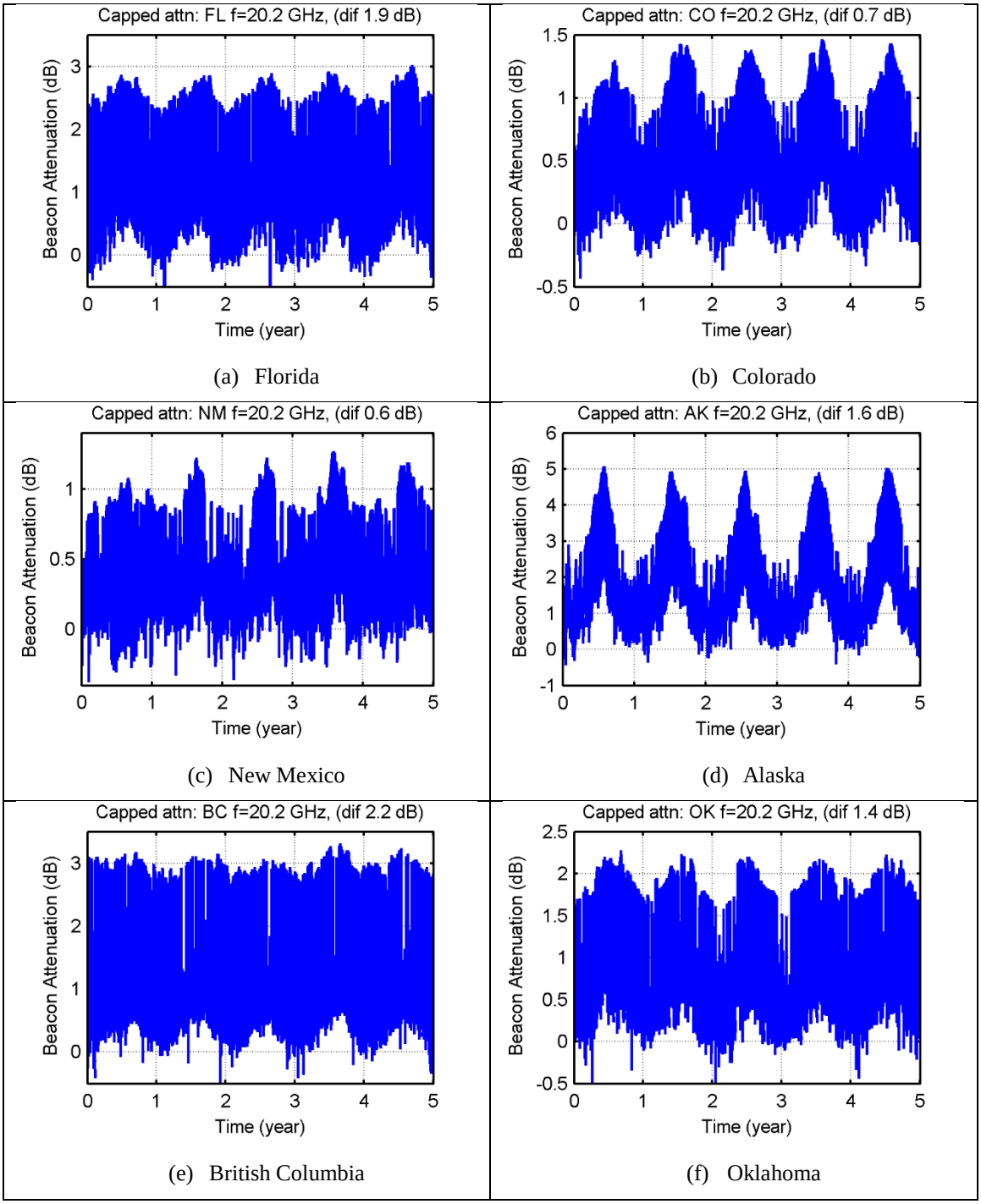

Figure 4.8: ACTS 20.2 GHz beacon attenuation after outliers removal (capped data)

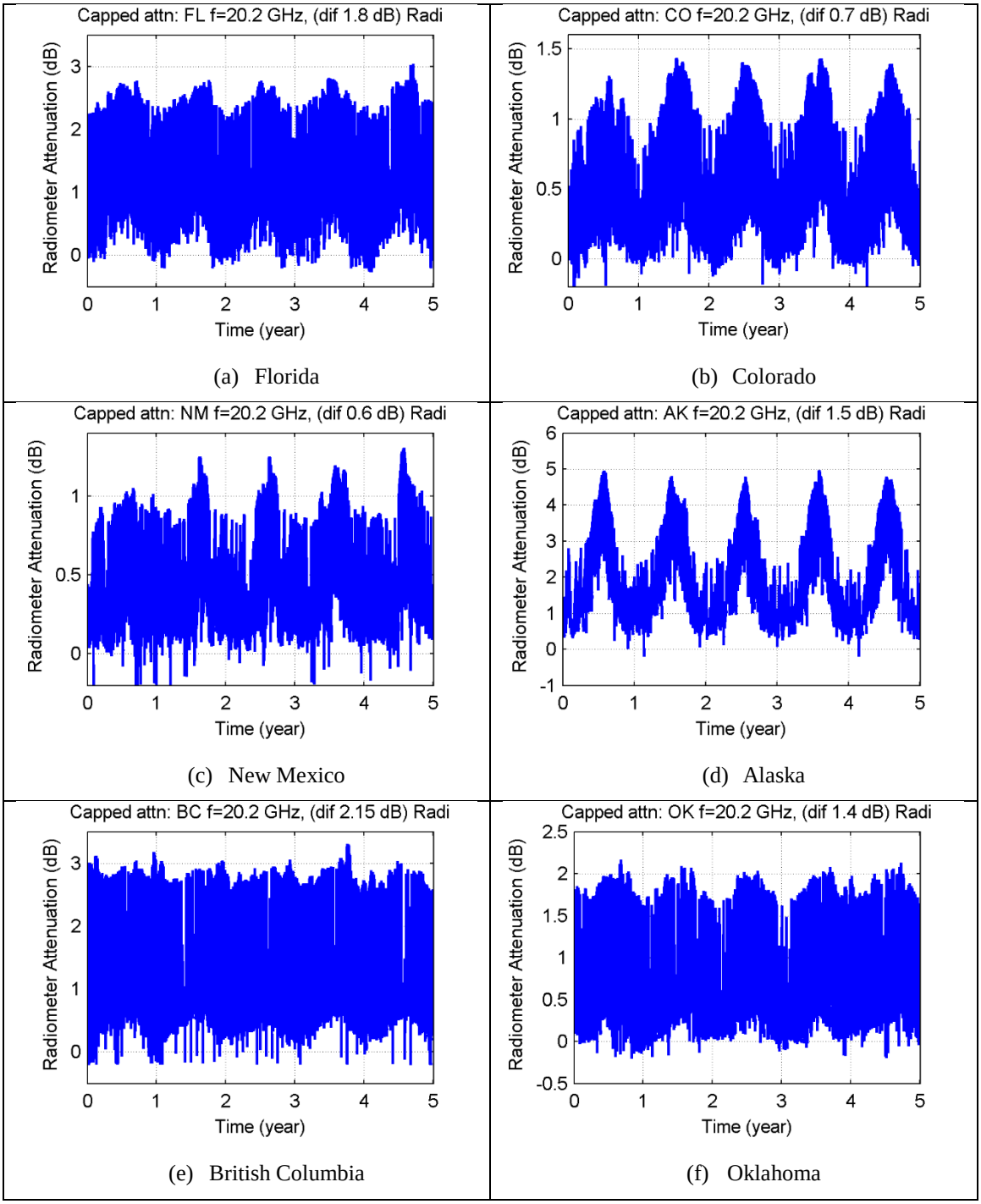

Figure 4.9: ACTS 20.2 GHz radiometer attenuation after outliers removal (capped data)

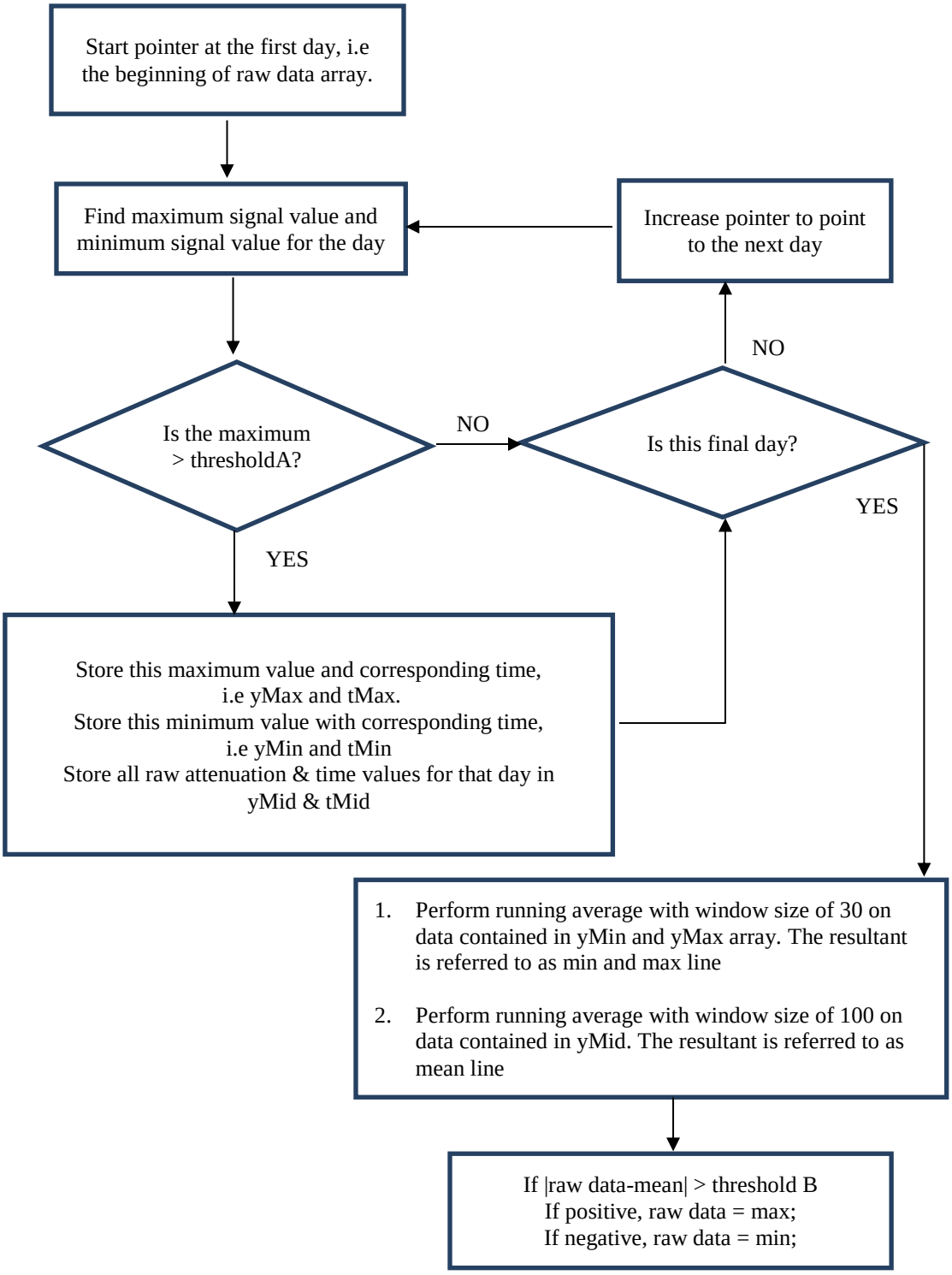

Figure 4.10: Flow chart for removing outliers

4.2.2 Removing seasonal effects

Spectral analysis describes the average distribution of power as a function of frequency, for the whole time series. It is constructed mathematically as though the time series is unchanging or stationary. For a spectrum to produce a useful description of the time series, it is usually required that the mean and variance of the data remain essentially constant (‘weak stationarity’, [47]).

Many atmospheric processes however, are distinctly not stationary, for example those exhibiting annual or diurnal cycles. There are two approaches for dealing with nonstationary series. Both aim to process the data in a way that will subsequently allow stationarity to be reasonably assumed. The first approach is to mathematically transform the nonstationary data to approximate stationarity (later referred to as Method 1). One of the procedures is to measure the trend and remove it from the data to produce a deseasonalized set of data

The second method is to stratify the data, which involves conducting separate analyses onto subsets of the data record that are short enough to be regarded as nearly stationary (Method 2). Both approaches were investigated by adopting two methods outlined in [48], as follows:

Method 1

Mathematically transform the data by computing the 12 monthly mean and standard deviation values. Equation (4.9) is then applied using the means and standard deviations for the appropriate calendar month.

$$z = \frac{x - \bar{x}}{s_x} \tag{4.9}$$

x is the capped time series data, while $\bar{x}$ and s_x are the corresponding mean and standard deviation of the each respective 30 day group. This transformation is also known as the *normalization* process, and the result, as **normalized** data. WOSA is then applied onto z to obtain a smoothed periodogram.

Method 2

Divide the capped time series data into segments of 30 days and compute the raw periodogram for each segment using Equation (4.1). The smoothed periodogram is then the average of the raw non-overlapping periodogram.

The following section contains the spectral estimation result of each available database, using three different methods, where possible. They are the result of the raw periodogram, Method 1 and Method 2. The raw periodogram implements Equation (4.1) using raw data as input, and without any smoothing procedure applied, i.e. without any windowing, averaging or zero padding. This give insight into the frequency content of the time series data prior to any preprocessing applied.

4.3 ACTS 20.2 GHz database

The following section gives the result of spectrum estimation onto ACTS 20.2 GHz beacon and radiometer data. Result for its counterpart in the 27.5 GHz frequency are given in Section 4.4

4.3.1 Raw periodogram

The input data for the raw periodogram was shown previously in Figure 4.2 (beacon data) and Figure 4.3 (radiometer data). The spectral estimation generated by the raw periodograms for each ACTS site is given in Figure 4.11 to Figure 4.16.

The spectrum estimation result is mostly concentrated in the area from 0 Hz to the vicinity of 1 cycle/solar day, which is $\frac{1}{24\times60\times60} = 1.1574 \times 10^{-5}$ Hz. Thus for easy viewing, all results from a particular site are depicted in three subfigures (a) to (c), of the following frequency regions:

(a) At the frequency of 0 Hz to the vicinity of 4 $cycles/solar\ day$ (the 3rd harmonics, $4.6 \times 10^{-5}\ Hz$). The location of the frequency of 1 cycle/solar day is highlighted by the left vertical gray line, and the 2nd harmonic, on the right. By highlighting this section of the output, the height of any solar frequency component and its harmonics can be compared to other peaks.

(b) In the frequency vicinity of $1\ cycle/year = 3.2 \times 10^{-7}$. Two vertical red dotted lines mark the location of 1 cycle/year and 2 cycle/year, from left to right, respectively. This helps to assess any frequency component that suggests the existence of a seasonal component. A green line marks the frequency of the lunar cycle, which is every 28 days.

(c) At the frequency vicinity of 1 cycle/day. Three vertical dotted lines were used to indicate the location of the solar, sidereal and anti-sidereal frequencies. Sidereal and anti-sidereal frequencies are detected in some sites. The definitions of sidereal and anti-sidereal are given in Section 6.3. The sidereal period is about 4 minutes less than a solar day, while anti-sidereal period is about 4 minutes more than a solar day.

Each subfigure contains both spectrum estimation result using the beacon (top) and radiometer data (below).

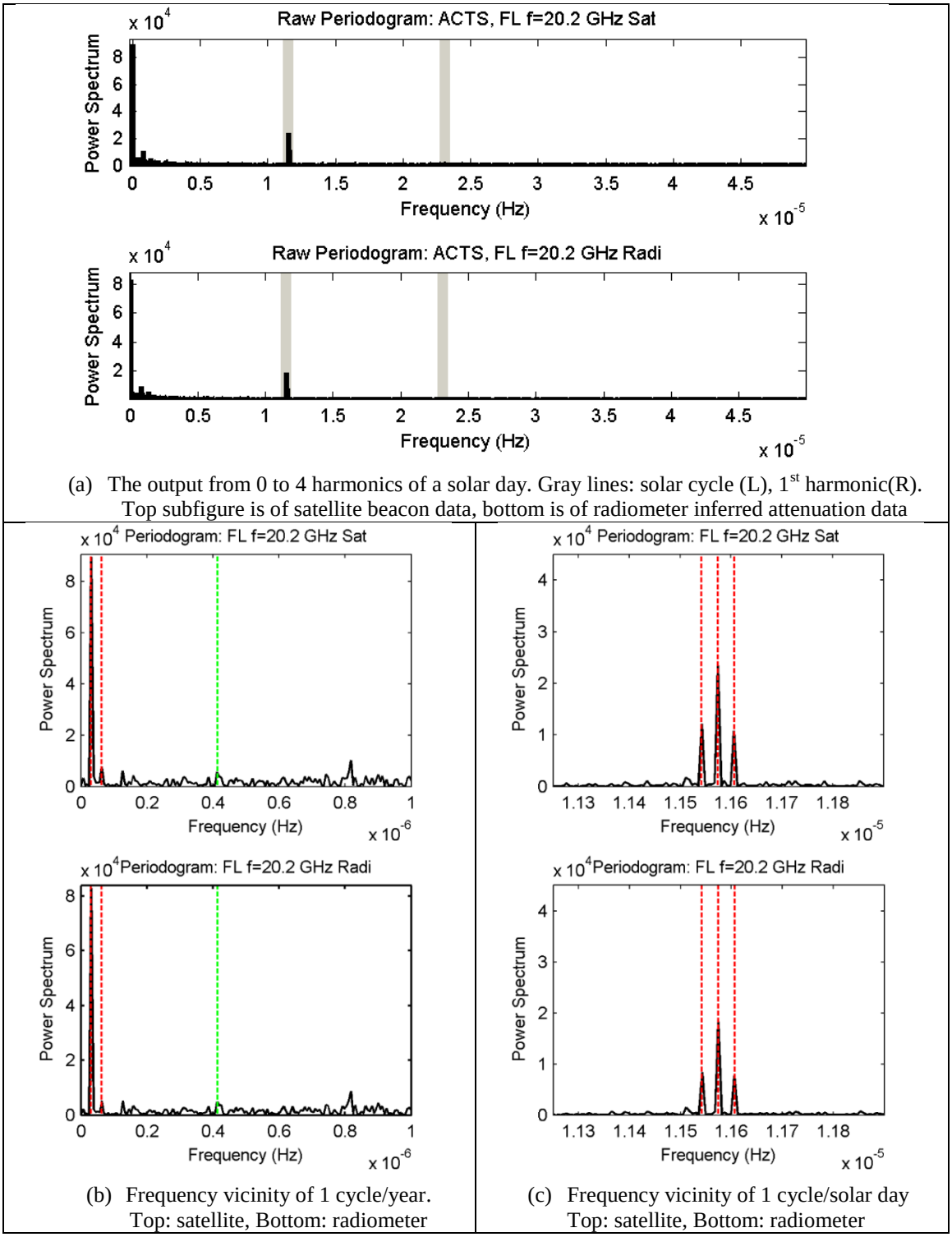

(a) The output from 0 to 4 harmonics of a solar day. Gray lines: solar cycle (L), 1st harmonic(R). Top subfigure is of satellite beacon data, bottom is of radiometer inferred attenuation data

(b) Frequency vicinity of 1 cycle/year. Top: satellite, Bottom: radiometer

(c) Frequency vicinity of 1 cycle/solar day Top: satellite, Bottom: radiometer

Figure 4.11: Raw periodogram: ACTS 20.2GHz data in Florida

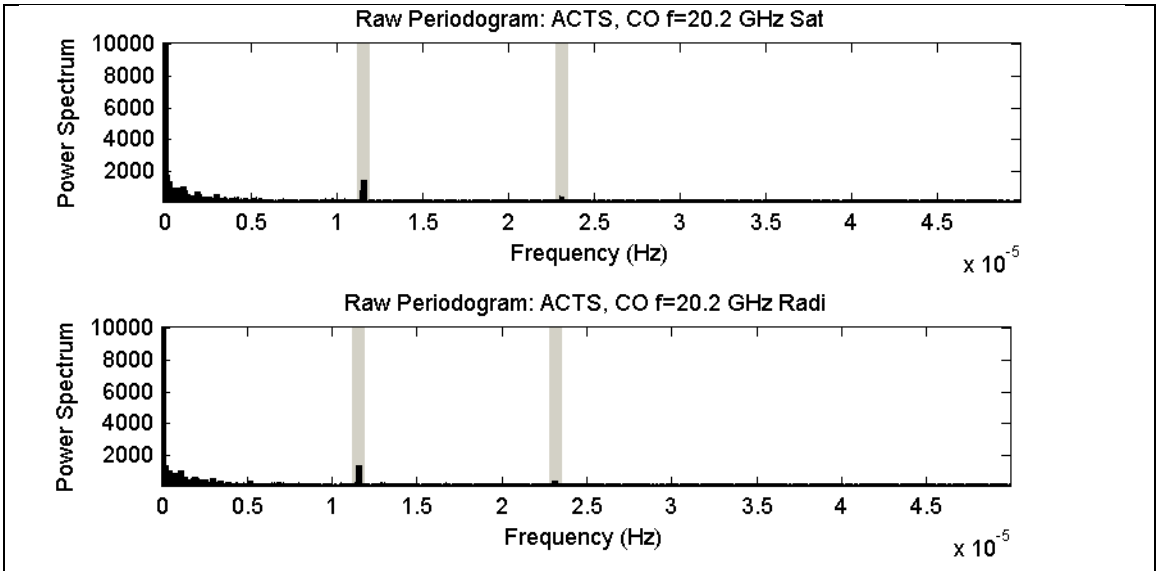

(a) The output from 0 to 4 harmonics of a solar day. Gray lines: solar cycle (L), 1st harmonic(R)

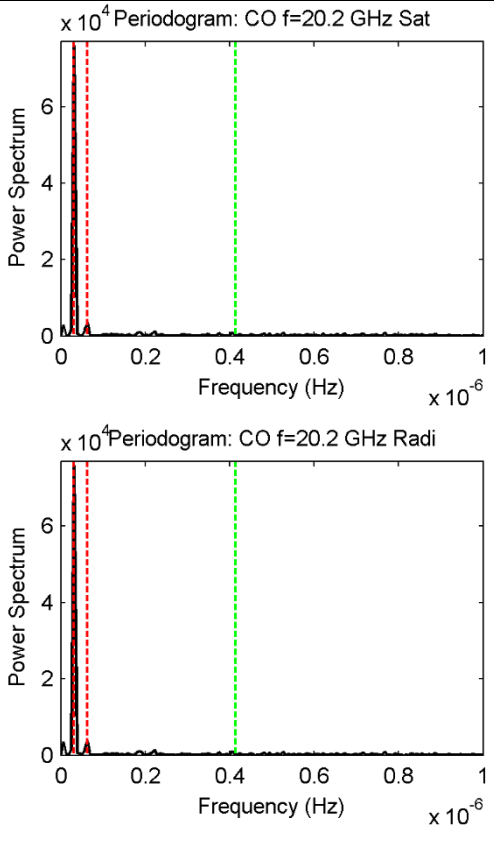

(b) Frequency vicinity of 1 cycle/year

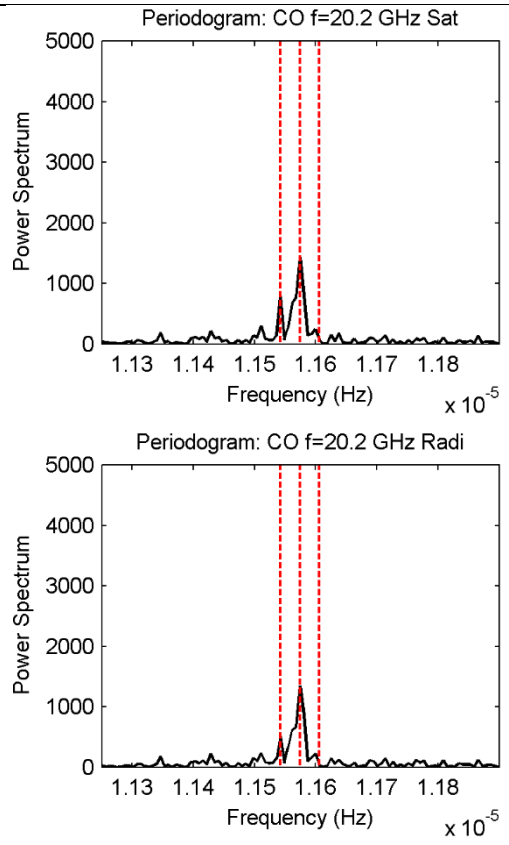

(c) Frequency vicinity of 1 cycle/solar day

Figure 4.12: Raw periodogram: ACTS 20.2GHz data in Colorado

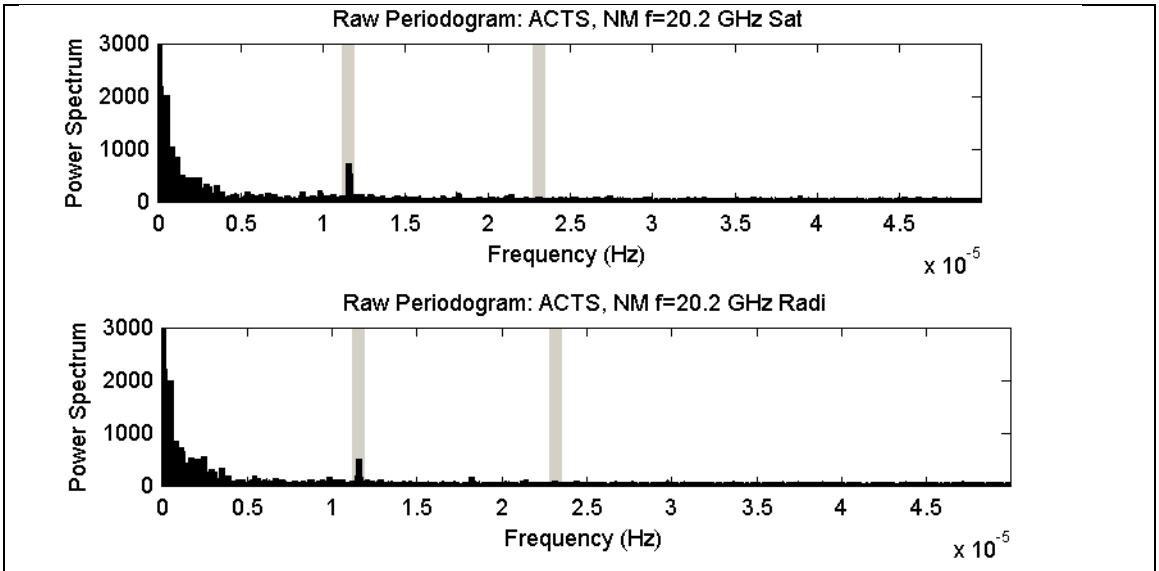

(a) The output from 0 to 4 harmonics of a solar day. Gray lines: solar cycle (L), 1st harmonic(R)

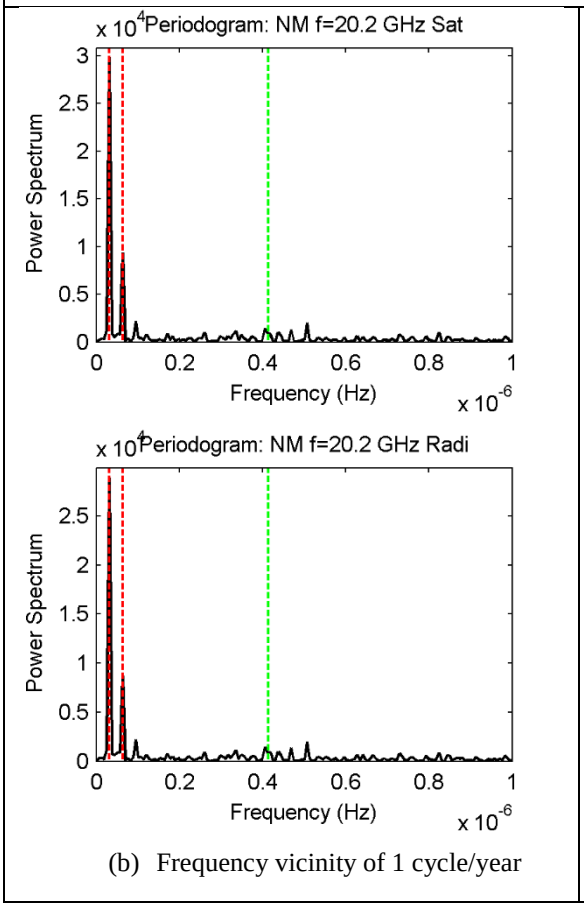

(b) Frequency vicinity of 1 cycle/year

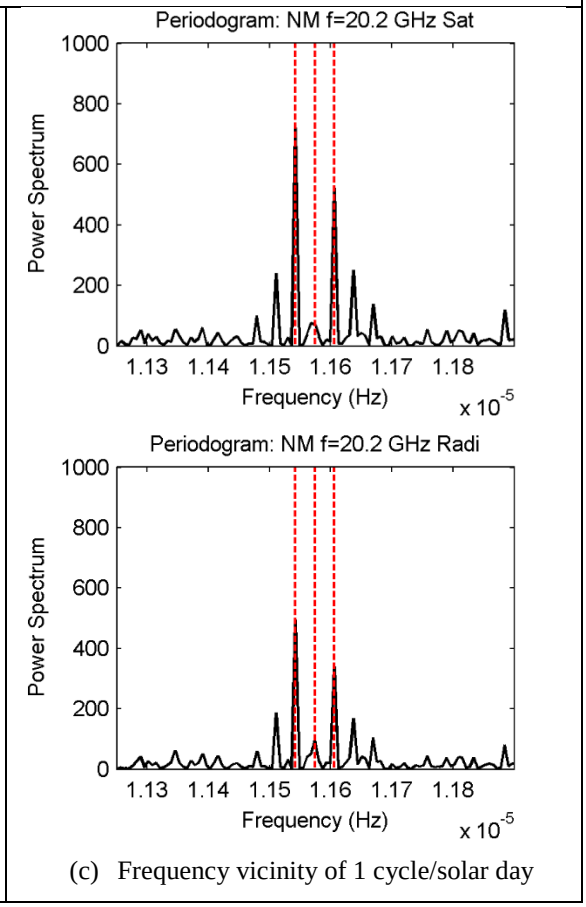

(c) Frequency vicinity of 1 cycle/solar day

Figure 4.13: Raw periodogram: ACTS 20.2GHz data in New Mexico

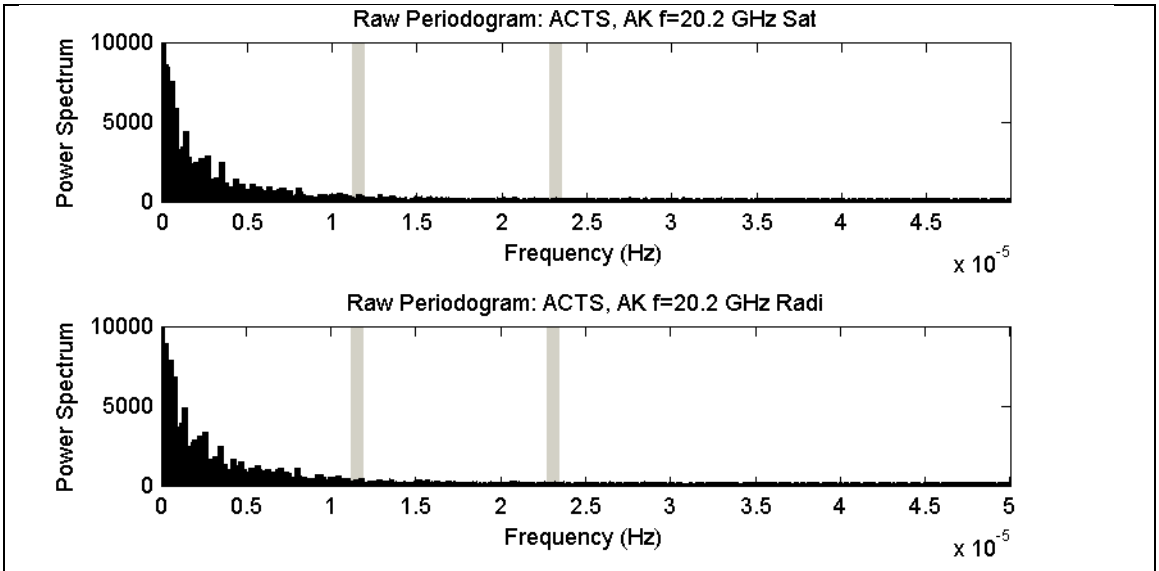

(a) The output from 0 to 4 harmonics of a solar day. Gray lines: solar cycle (L), 1st harmonic(R)

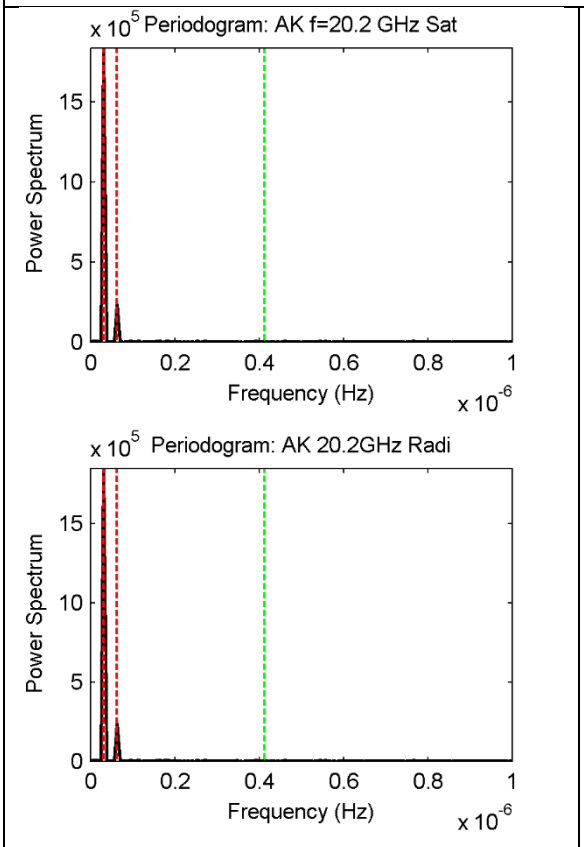

(b) Frequency vicinity of 1 cycle/year

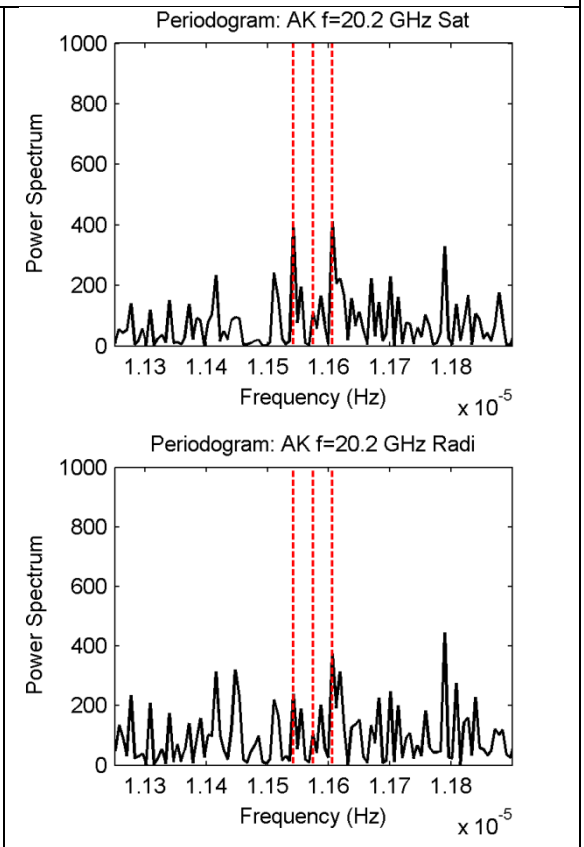

(c) Frequency vicinity of 1 cycle/solar day

Figure 4.14: Raw periodogram: ACTS 20.2GHz data in Alaska

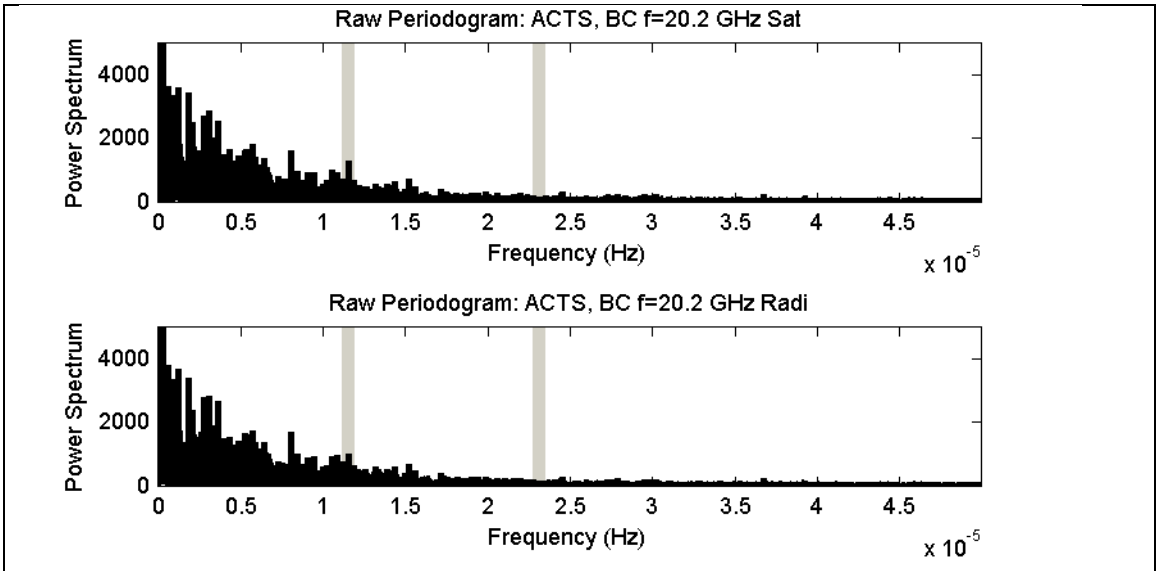

(a) The output from 0 to 4 harmonics of a solar day. Gray lines: solar cycle (L), 1st harmonic(R)

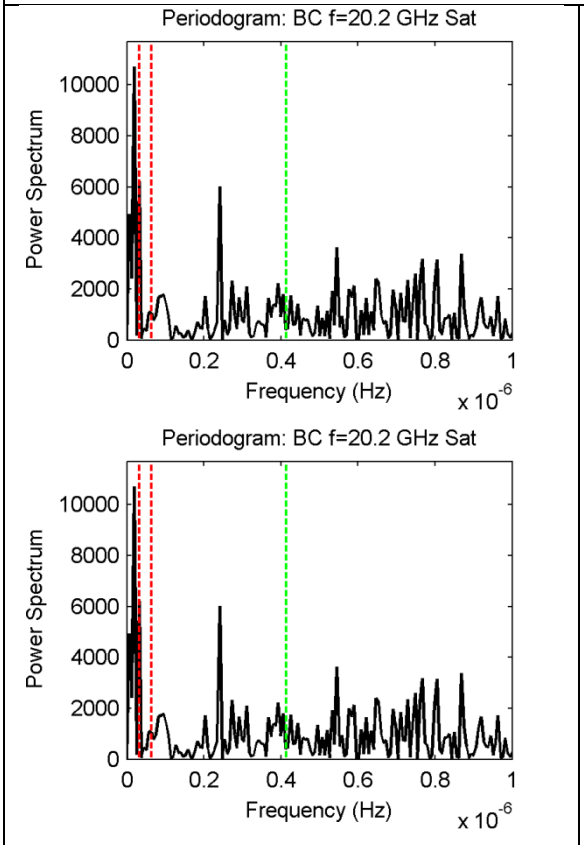

(b) Frequency vicinity of 1 cycle/year

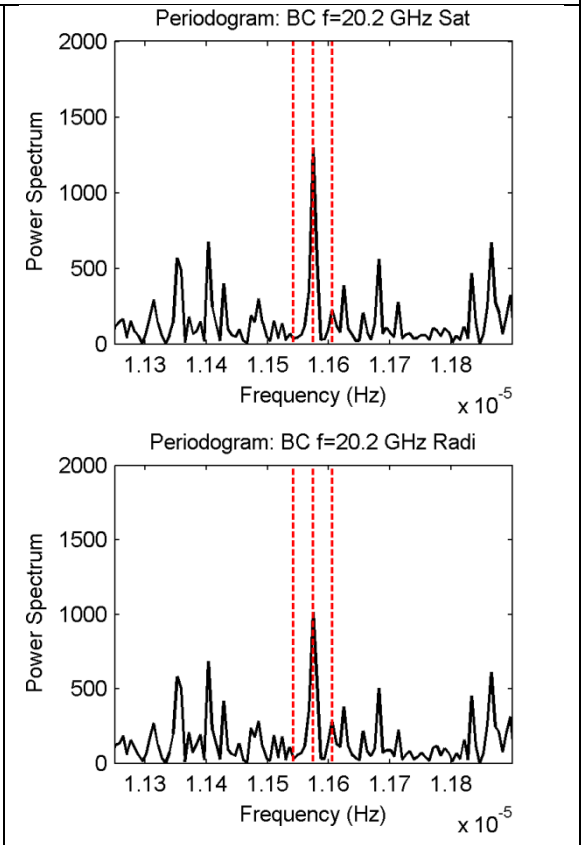

(c) Frequency vicinity of 1 cycle/solar day

Figure 4.15: Raw periodogram: ACTS 20.2GHz data in British Columbia

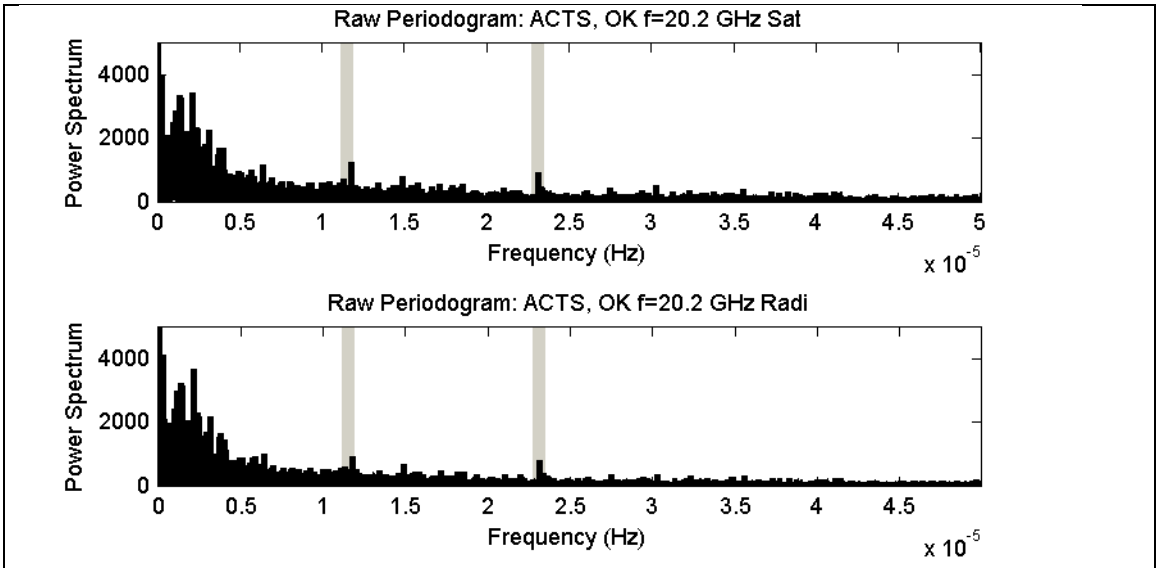

(a) The output from 0 to 4 harmonics of a solar day. Gray lines: solar cycle (L), 1st harmonic(R)

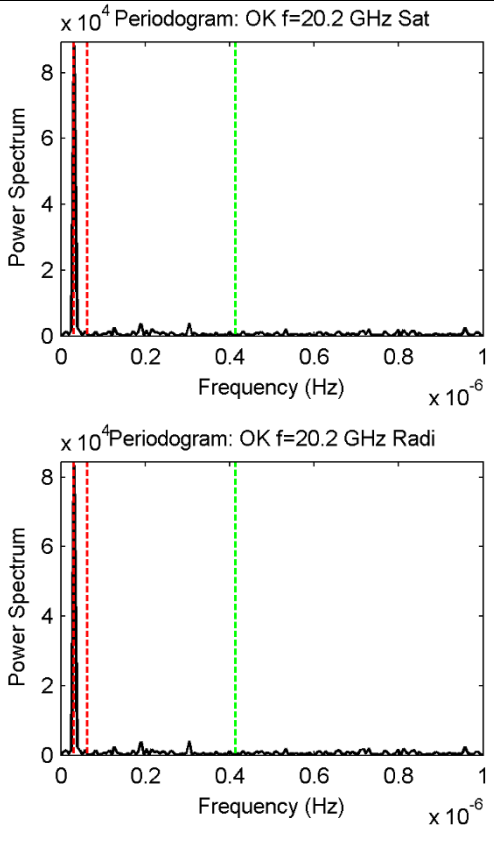

(b) Frequency vicinity of 1 cycle/year

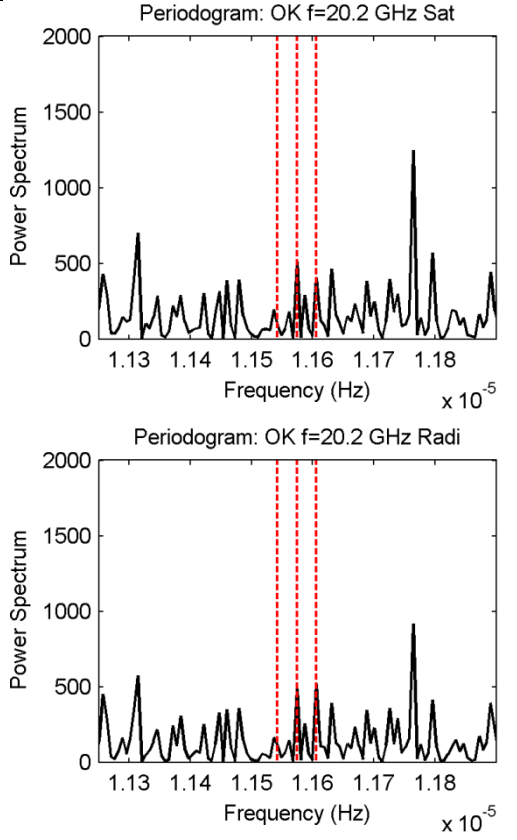

(c) Frequency vicinity of 1 cycle/solar day

Figure 4.16: Raw periodogram: ACTS 20.2GHz data in Oklahoma

There is a dominant presence of a seasonal periodicity with a frequency of 1 cycle per year shown in each subfigure (b), in all except for British Columbia (Figure 4.15). Here a peak appears slightly to the right, and not exactly on the frequency of the 1 cycle per year. The output for British Columbia has a significant amount of noise, compared to results from other sites. This could be due to calibration errors reported in [49]. Their analysis in attenuation distribution observation and model comparison had excluded the result obtained in British Columbia due to this error.

The presence of a solar day periodicity in subfigure (c) is strongest in Florida (Figure 4.11), then Colorado (Figure 4.12) and British Columbia. No significant solar peak is detected in New Mexico (Figure 4.13), Alaska (Figure 4.14) and Oklahoma (Figure 4.16). In Florida, the solar day peak is flanked by a strong anti-sidereal and sidereal peak, to its left and right, respectively. The presence of an anti-sidereal and sidereal peak is not as strong in Colorado; however it can be clearly seen in New Mexico, albeit without a solar day peak in the middle.

4.3.2 Result with method 1

In implementing WOSA, various segment sizes were tested to find the most suitable, as it is a tradeoff between the resulting frequency spectrum resolution and the number of possible averaging. A smaller segment size provides a higher number of averaging but produces a lower resolution output. A higher resolution gives more insight into the frequency content, while a large number of averaging reduces the variance in the output.

Referring to Figure 4.11(c), the side peaks were found to correspond to a cycle per sidereal day, and a cycle per anti-sidereal day.[50], to the right and left of a cycle per solar day respectively. The frequencies of these three peaks are:

- A cycle per sidereal day = 1.1606×10^{-5} Hz
- A cycle per solar day = 1.1574×10^{-5} Hz
- A cycle per anti-sidereal day =1.1542×10^{-5} Hz

These sidebands are not visible for segments that are sized less than 2 years. This is due to the resulting resolution of the spectrum output. The sidebands are so closed together that in order to differentiate the two successive peaks, they should be at least 2 bins away, requiring a resolution of at least $\frac{1.1574\times10^{-5}-1.1542\times10^{-5}}{2} = 1.6 \times 10^{-8}\ Hz$. With 2 years of data, a resolution of $\frac{1/60}{2\times365\times1440} = 1.58 \times 10^{-8}\ Hz$ is obtained. It is also reported in [51] that with a data period larger than one calendar year, the frequency resolution is sufficient to resolve the sidereal and diurnal frequencies.

Zero padding can be used to increase the spectrum resolution by appending the end of the time data sequence with zeros. This is a method used to improve the DFT spectral estimation. Frequencies in the discrete Fourier transform (DFT) are spaced at

intervals of Fs/N where Fs is the sampling frequency and N is the length of the input time series. Attempting to estimate the amplitude of a sinusoid with a frequency that does not correspond to a DFT bin can result in an inaccurate estimate. Therefore, zero padding the data before executing the DFT can often increase the frequency resolution and thus improve the amplitude estimate. In the ACTS and Texas data analysis (discussed in Section 4.4), zero padding was used to increase the segment size so that the number of samples N, is increased to N = 2628000. With N = 2628000, the sidereal and the solar peak will be $\frac{1.1574\times10^{-5}-1.1542\times10^{-5}}{(1/60)} \times 2628000 = 5$ bins apart, more than the minimum 4 for two peaks to be resolved using a Hamming window, as discussed in Section 4.1. Zero padding however does not improve the ability to resolve, to distinguish between, two closely spaced signals in the frequency domain, as shown in Figure 4.17(b). To improve true spectral resolution of two signals, more non-zero time samples are needed.

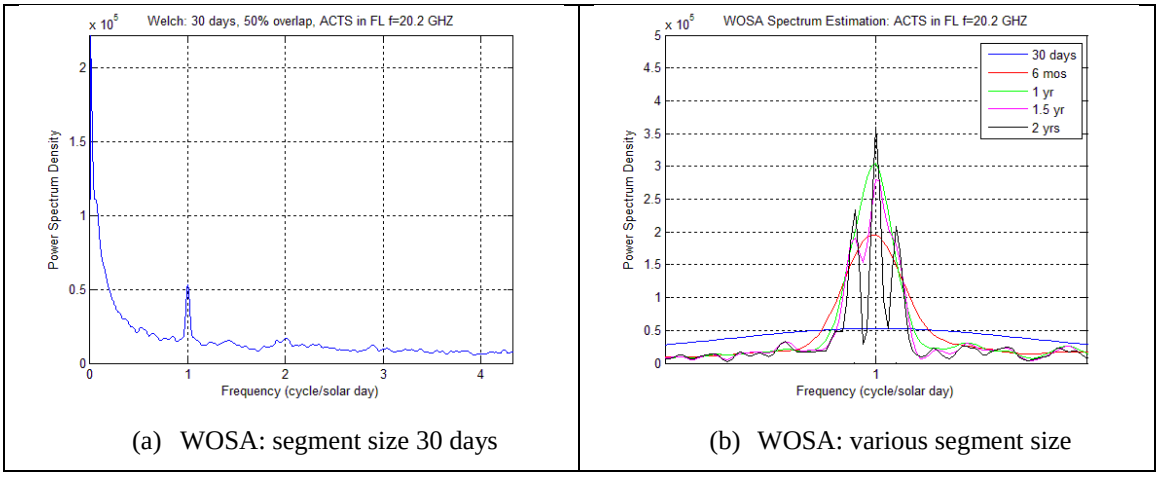

(a) WOSA: segment size 30 days

(b) WOSA: various segment size

Figure 4.17: Effect of segment size on WOSA output

A summary of the method 1 used is as follows:

Step 1: Obtained normalized data using equation (4.9)

Step 2: Implement WOSA with a segment size of 2×365 days and zero padded till 2628000 with an overlap of 50%. This results in 4 segments.

Figure 4.18 and Figure 4.19 gives the normalized beacon and radiometer data input used, while Figure 4.20 to Figure 4.25 gives the output for each ACTS site.

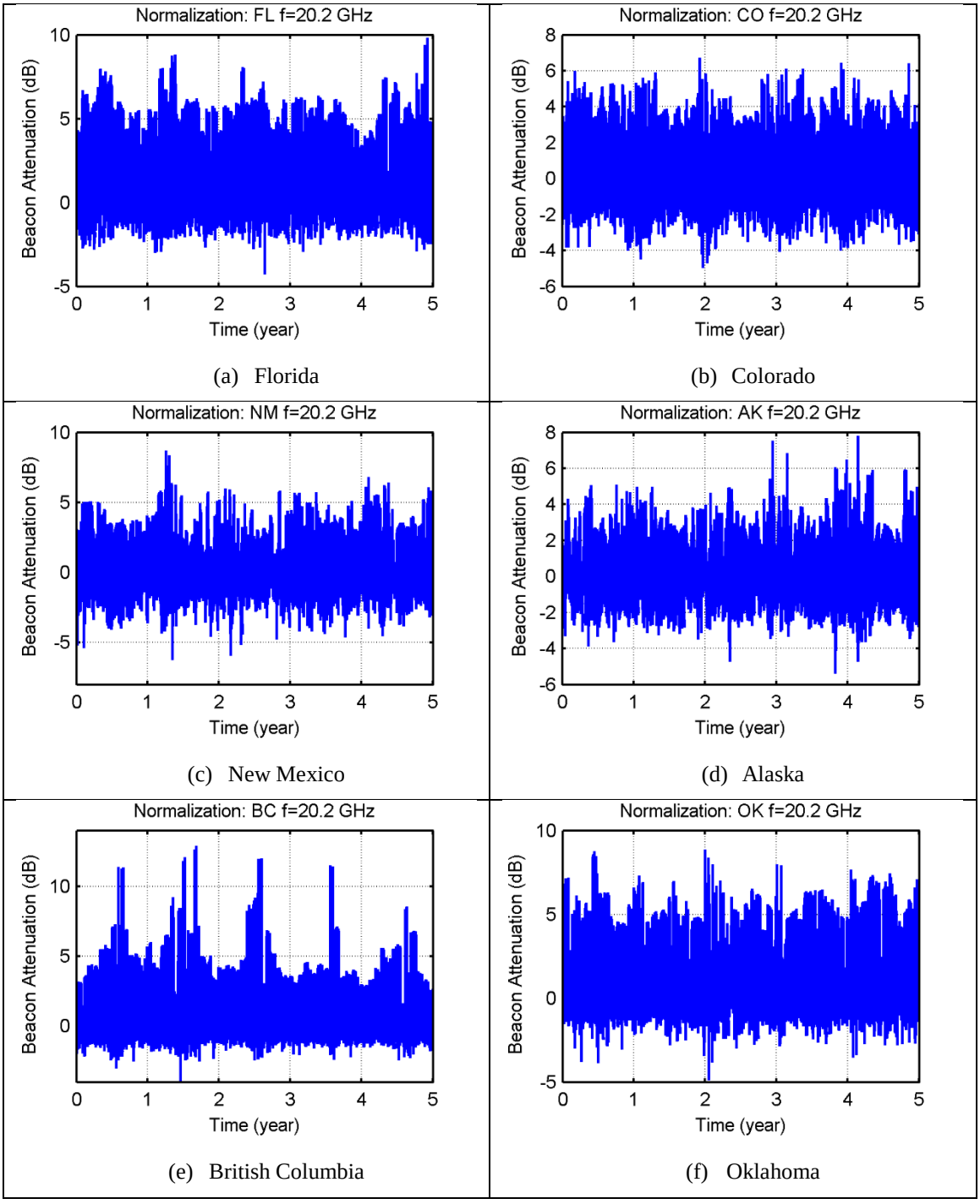

Figure 4.18: Normalized ACTS 20.2GHz beacon data

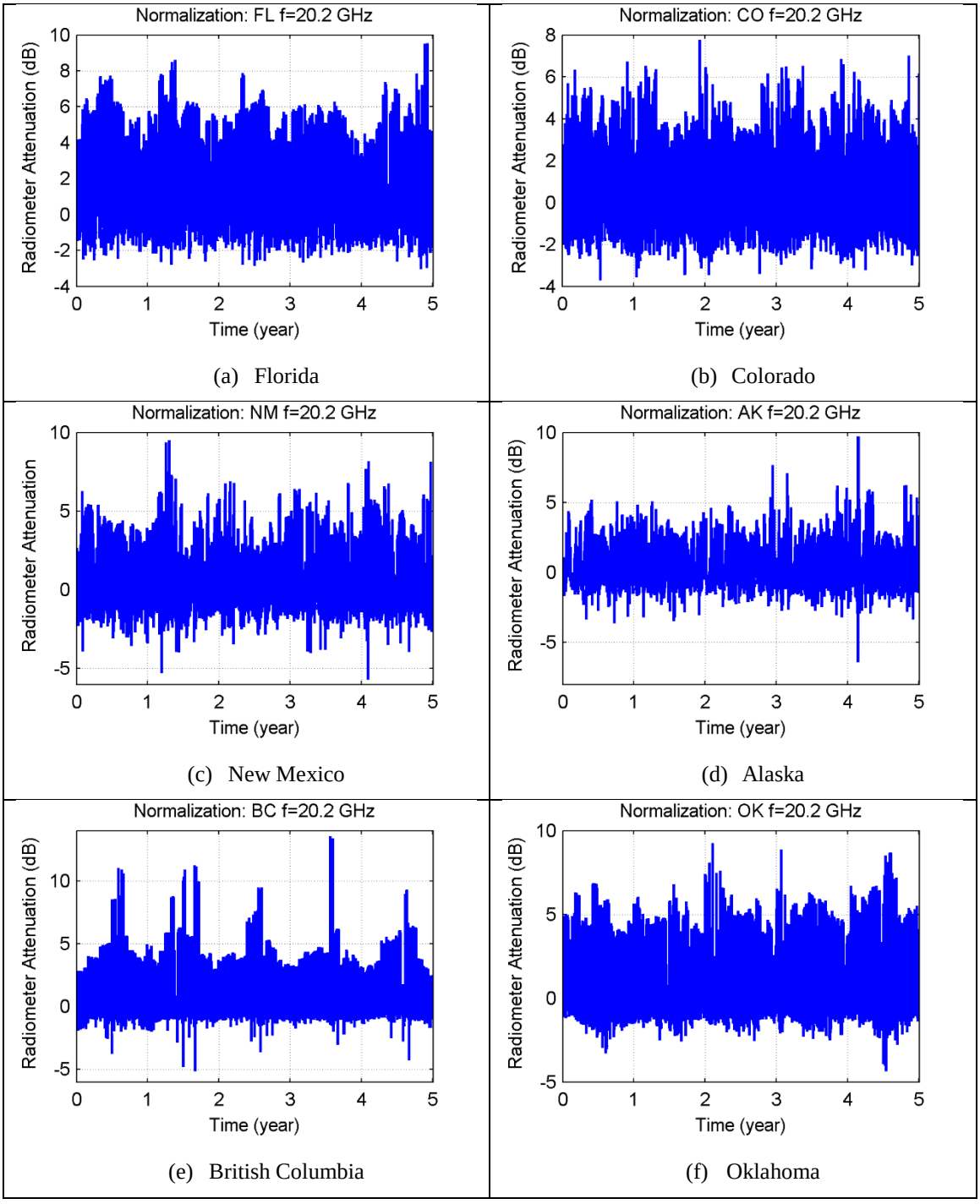

Figure 4.19: Normalized ACTS 20.2GHz radiometer data

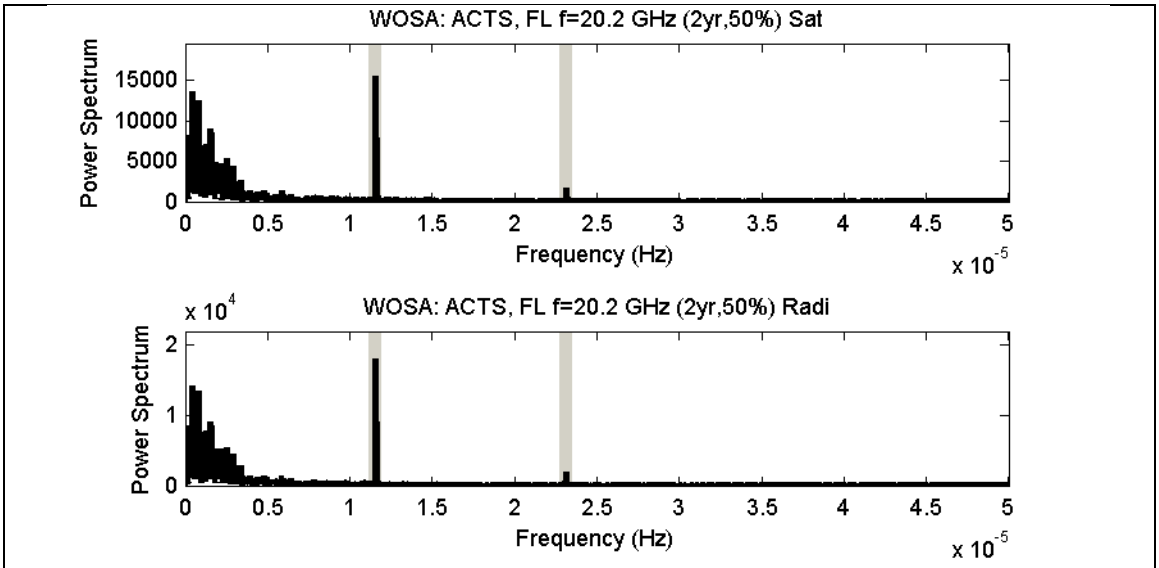

(a) The output from 0 to 4 harmonics of a solar day. Gray lines: solar cycle (L), 1st harmonic(R)

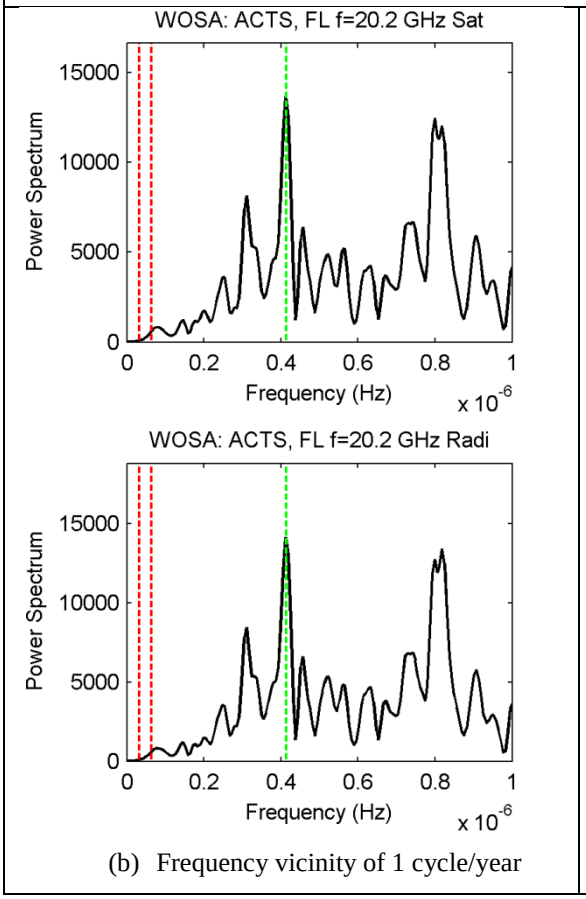

(b) Frequency vicinity of 1 cycle/year

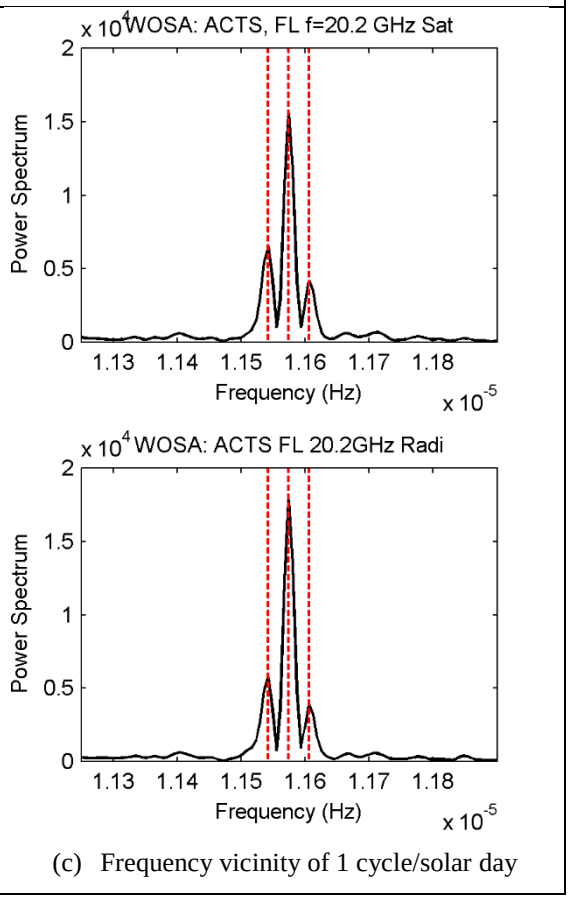

(c) Frequency vicinity of 1 cycle/solar day

Figure 4.20: Method 1 for ACTS 20.2GHz data in Florida

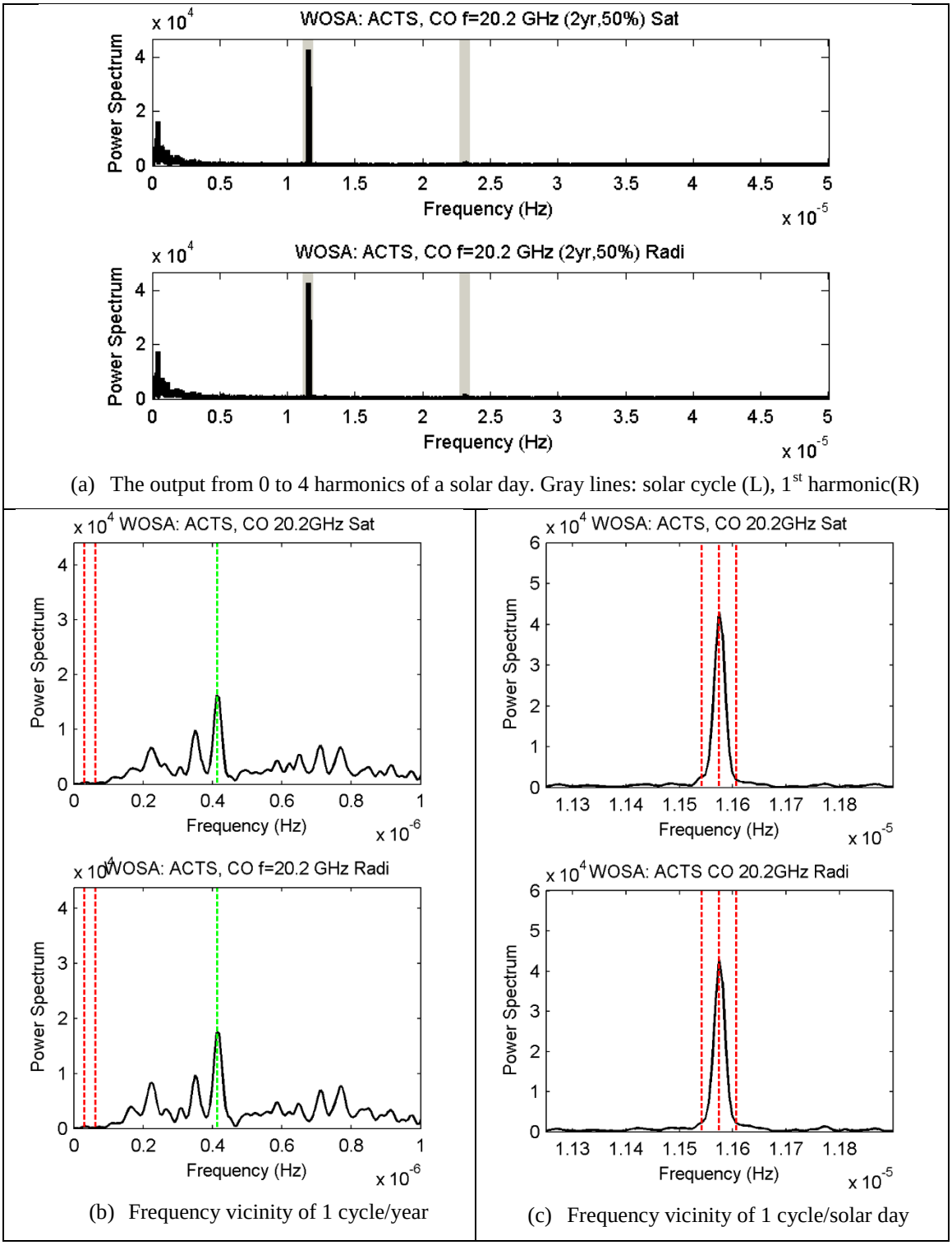

(a) The output from 0 to 4 harmonics of a solar day. Gray lines: solar cycle (L), 1st harmonic(R)

(b) Frequency vicinity of 1 cycle/year

(c) Frequency vicinity of 1 cycle/solar day

Figure 4.21: Method 1 for ACTS 20.2GHz data in Colorado

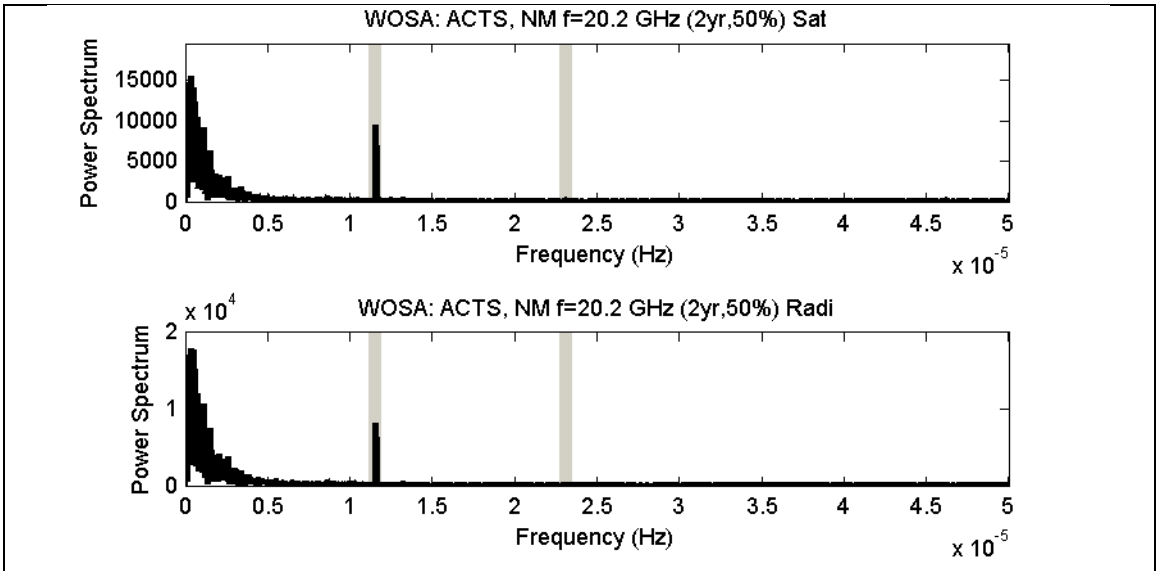

(a) The output from 0 to 4 harmonics of a solar day. Gray lines: solar cycle (L), 1st harmonic(R)

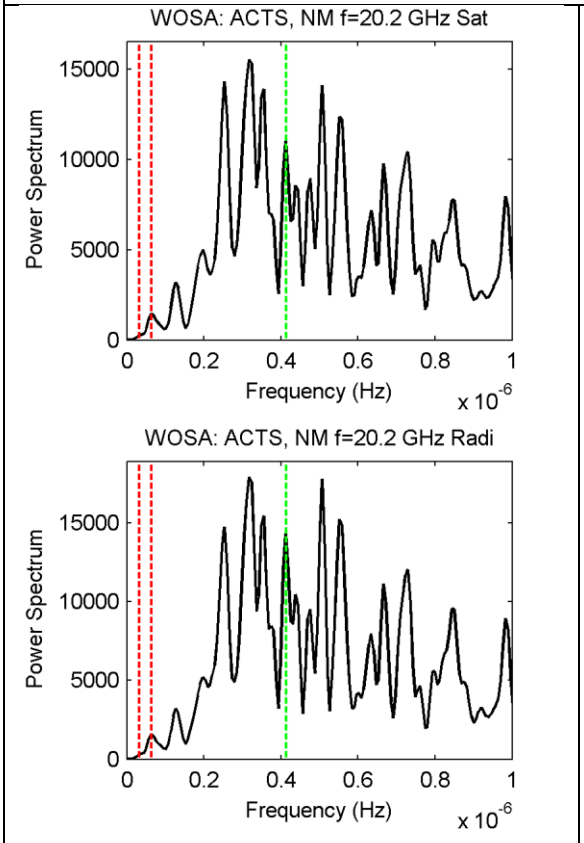

(b) Frequency vicinity of 1 cycle/year

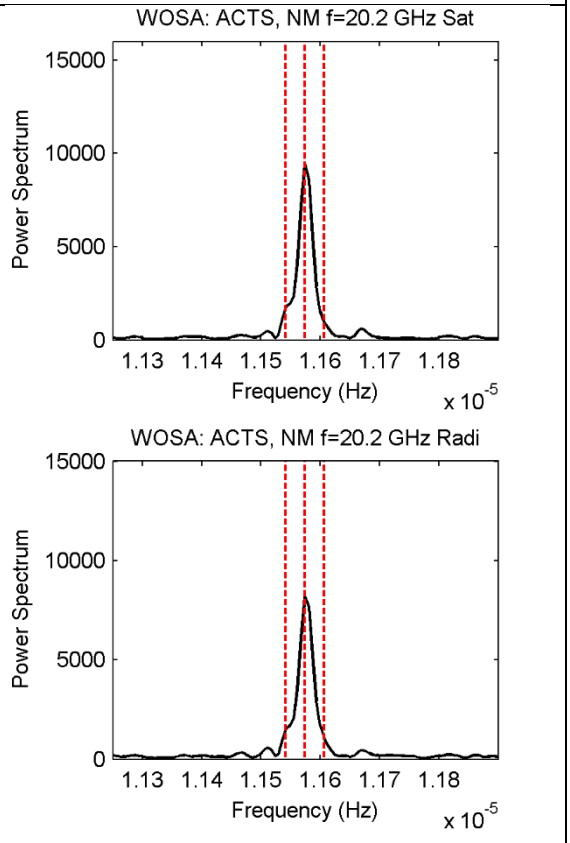

(c) Frequency vicinity of 1 cycle/solar day

Figure 4.22: Method 1 for ACTS 20.2GHz data in New Mexico

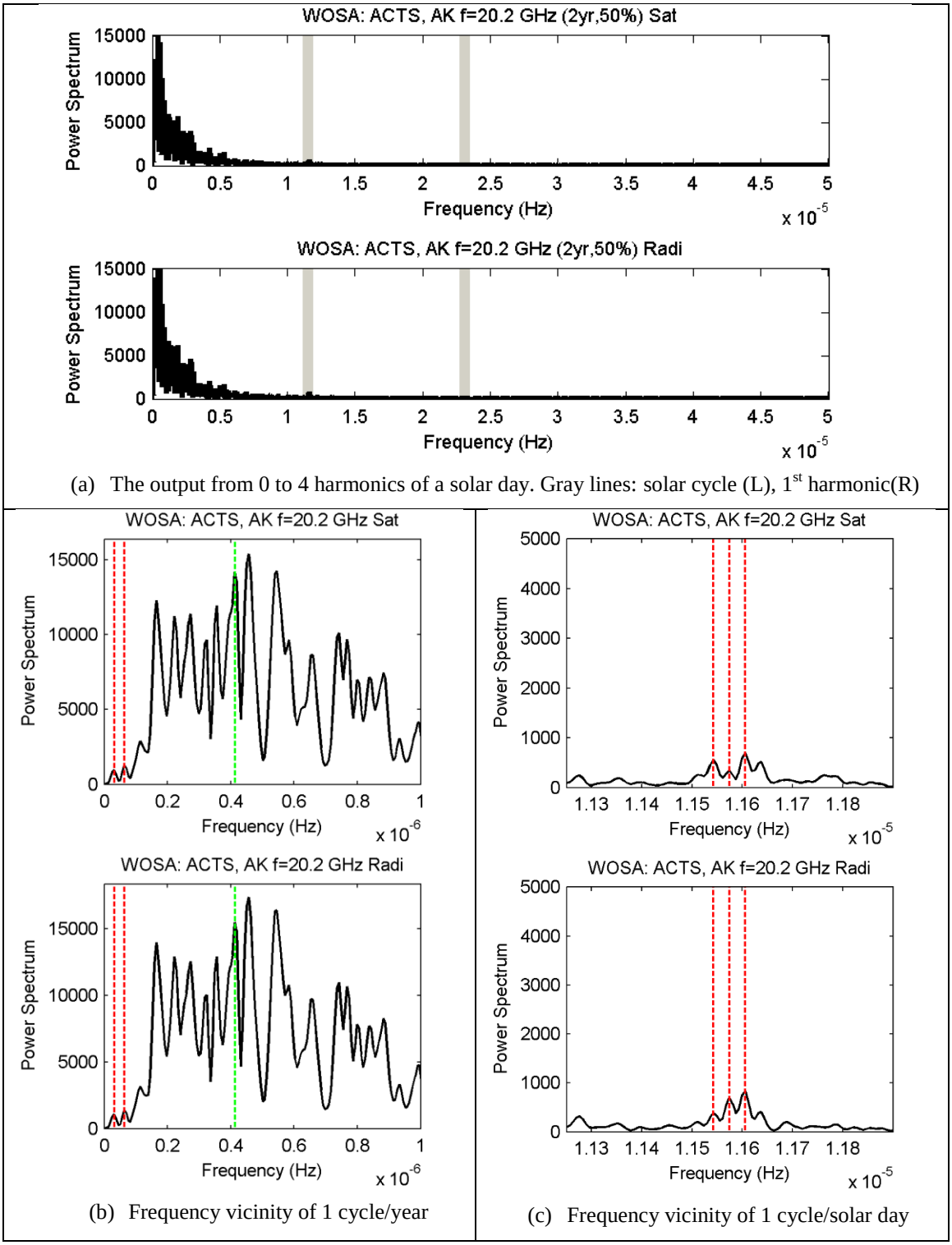

(a) The output from 0 to 4 harmonics of a solar day. Gray lines: solar cycle (L), 1st harmonic(R)

(b) Frequency vicinity of 1 cycle/year

(c) Frequency vicinity of 1 cycle/solar day

Figure 4.23: Method 1 for ACTS 20.2GHz data in Alaska

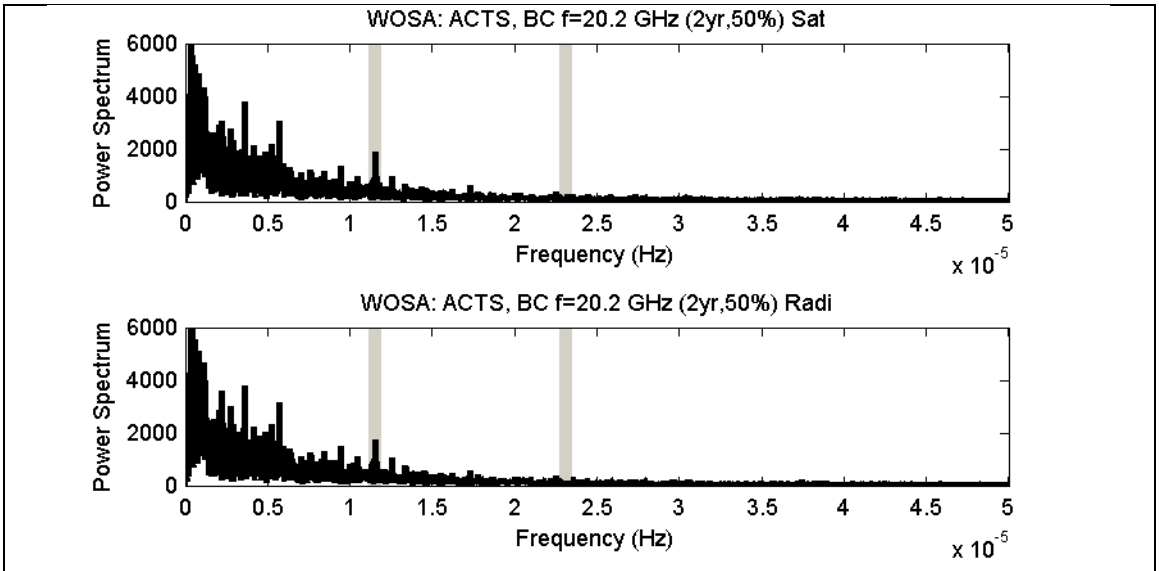

(a) The output from 0 to 4 harmonics of a solar day. Gray lines: solar cycle (L), 1st harmonic(R)

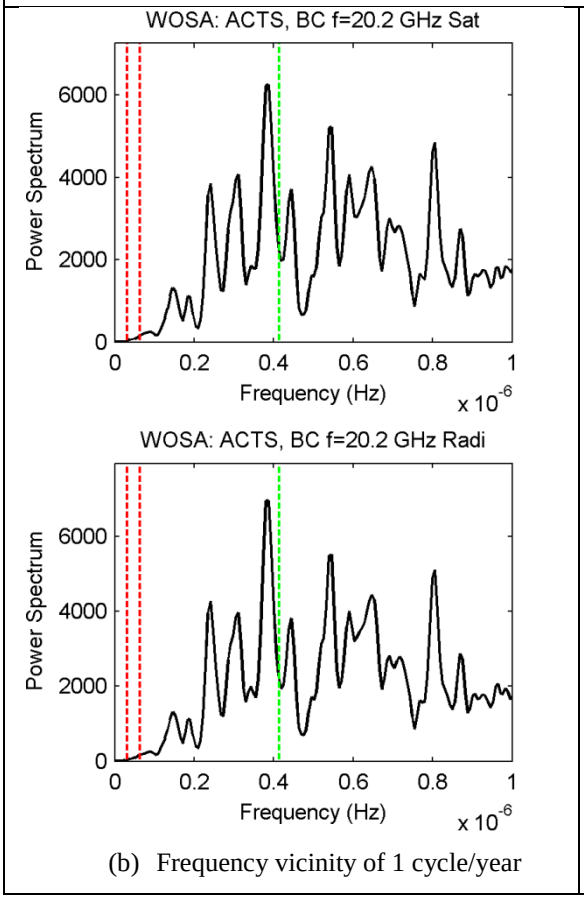

(b) Frequency vicinity of 1 cycle/year

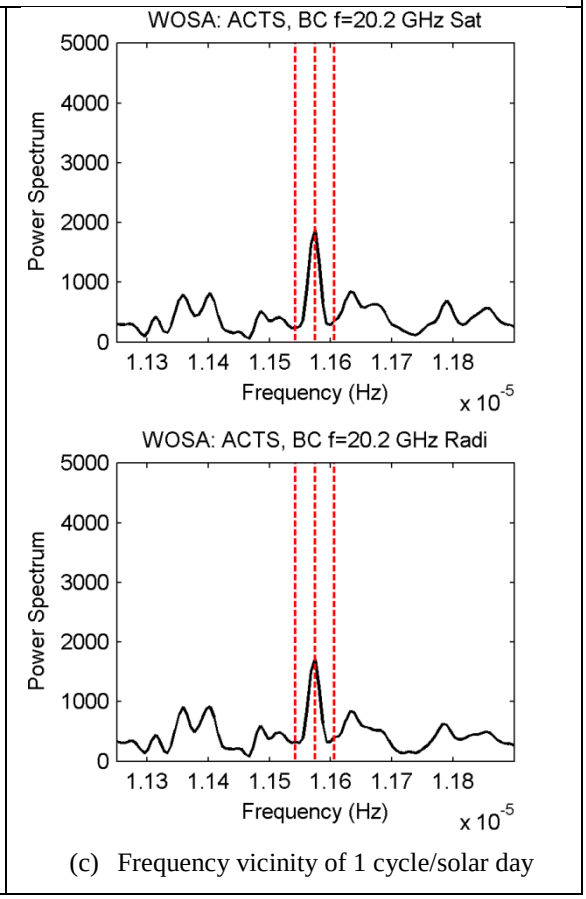

(c) Frequency vicinity of 1 cycle/solar day

Figure 4.24: Method 1 for ACTS 20.2GHz data in British Columbia

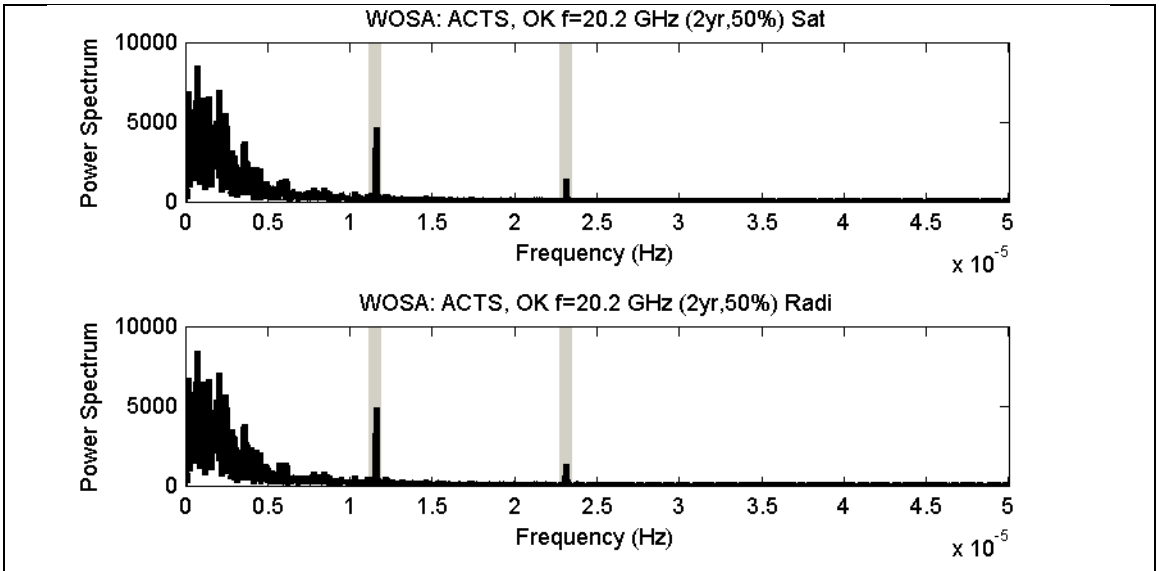

(a) The output from 0 to 4 harmonics of a solar day. Gray lines: solar cycle (L), 1st harmonic(R)

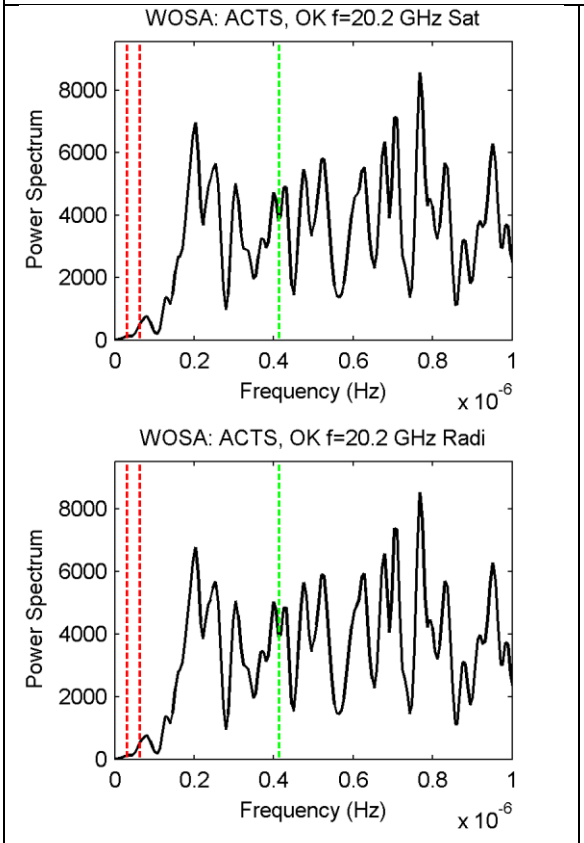

(b) Frequency vicinity of 1 cycle/year

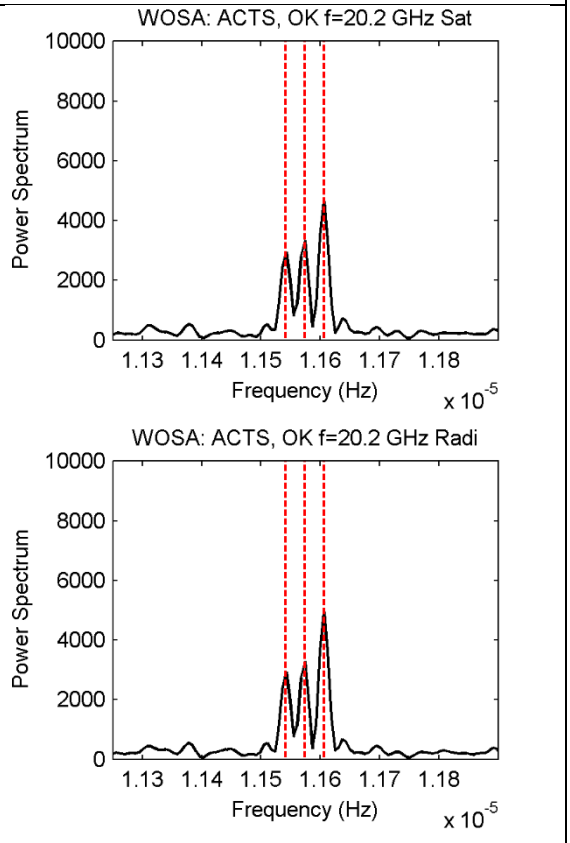

(c) Frequency vicinity of 1 cycle/solar day

Figure 4.25: Method 1 for ACTS 20.2GHz data in Oklahoma

The results show that the removal of the seasonal trend was successful. Peaks that were previously seen at the frequencies of 1 cycle and 2 cycles per year in previous raw periodograms are now suppressed, as shown in subfigure (b) in Figure 4.20 to Figure 4.25. In subfigure (a), with the removal of a dominant large peak, the presence of other smaller peaks, are more visible, particularly at 1 cycle of solar day which is of interest. The result of averaging saw a significant reduction in background noise.

Solar periodicity is now more significant in subfigures (c) of two more sites, New Mexico (Figure 4.22) and Oklahoma (Figure 4.25). Both previously had no solar peak detected in their raw periodograms. For the results in Florida (Figure 4.20), Colorado (Figure 4.21) and New Mexico, there is a reduction in the relative amplitudes of the sidereal and anti-sidereal peaks to the solar peak. The constant presence of a solar peak even after averaging exemplified its existance. In Alaska (Figure 4.23) however, the apparent lack of any solar day periodicity does not change with the seasonal trend removal.

The presence of a lunar cycle periodicity can be seen in Florida and Colorado but not significantly elsewhere.

4.3.3 Result with method 2

Figure 4.26 gives the result for method 2 using the capped input data given in Figure 4.8 for beacon, and in Figure 4.9 for radiometer. The red dotted horizontal lines mark the location of solar cycle on the x-axis. For each site, the beacon and radiometer spectrum is depicted next to each other. The result is the averaged spectrum of 60 non overlapping segments. The length of segment is 30 days data, with a spectrum resolution of $\frac{1/60}{30\times1440} = 3.859 \times 10^{-7} Hz$. This resolution however is not sufficient to show evidence of sidereal and anti-sidereal component, if any.

Comparing the result obtained using Method 2 with Method 1 the presence of a solar peak remains in Florida, Colorado, New Mexico and Oklahoma, but no longer in British Columbia. No solar periodicity is detected in Alaska.

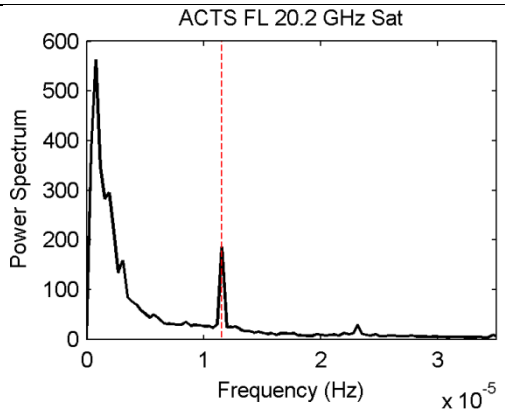

(a) Florida (beacon)

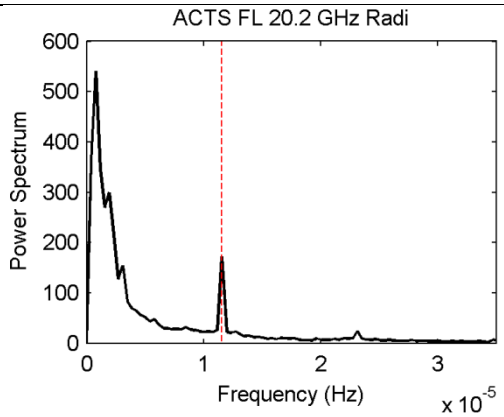

(b) Florida (radiometer)

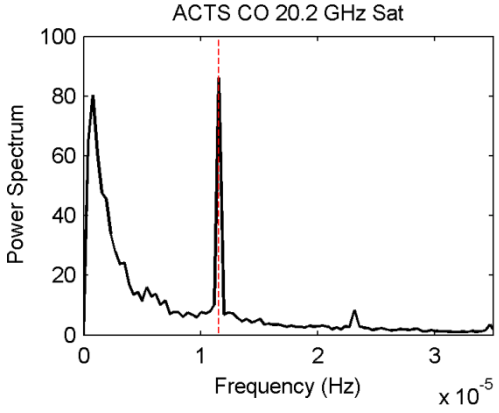

(c) Colorado (beacon)

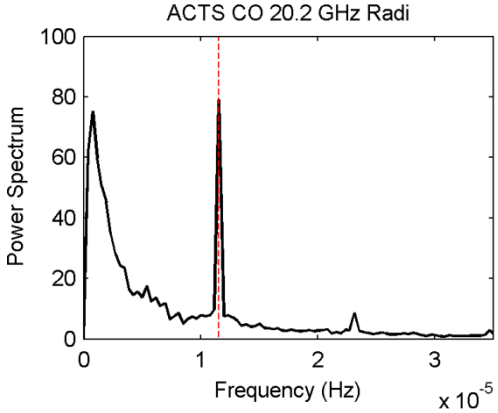

(d) Colorado (radiometer)

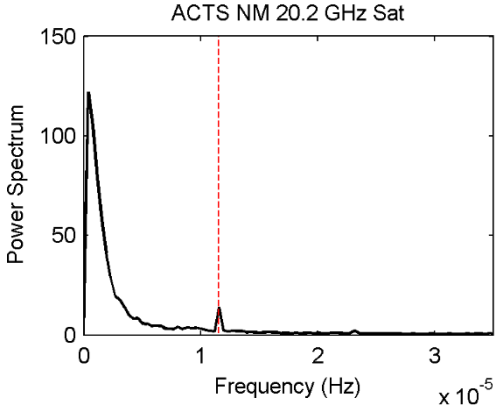

(e) New Mexico (beacon)

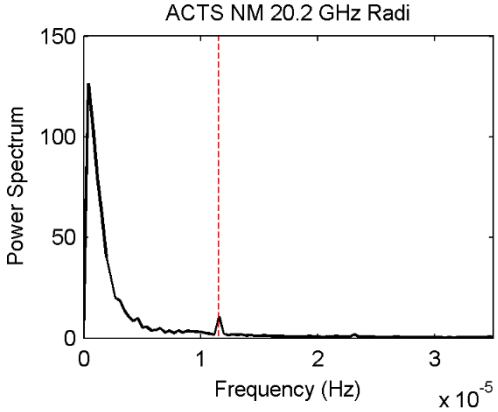

(f) New Mexico (radiometer)

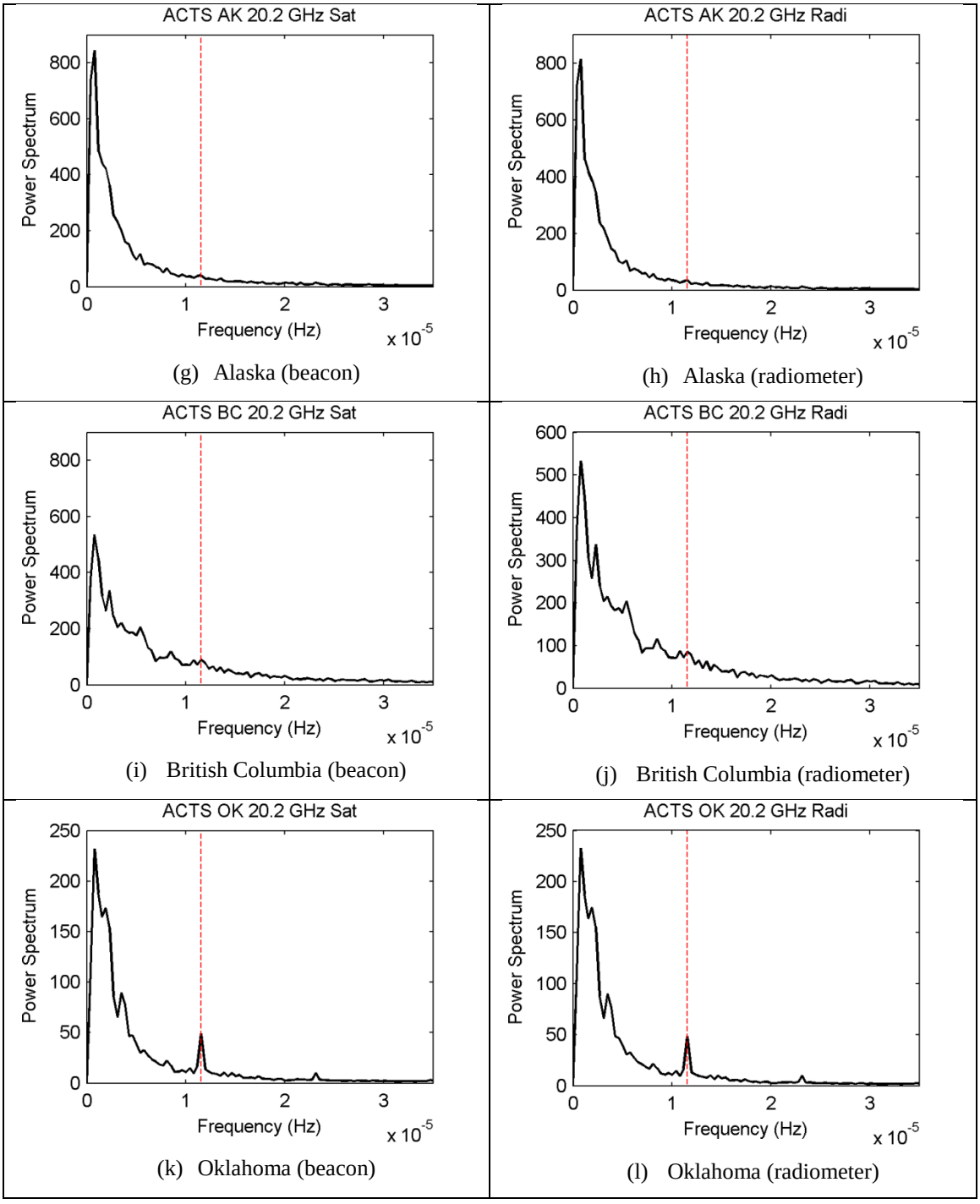

(g) Alaska (beacon)

(h) Alaska (radiometer)

(i) British Columbia (beacon)

(j) British Columbia (radiometer)

(k) Oklahoma (beacon)

(l) Oklahoma (radiometer)

Figure 4.26: Spectrum obtained using Method 2 onto ACTS 20.2 GHz data

4.3.4 Discussion

Result from the ACTS 20.2 GHz spectrum analysis confirms the advantage of removing any known dominant frequency component and outliers. Comparing subfigure (b) of the raw periodogram with its counterpart in Method 1, the seasonal trend removal was able to remove completely or partially the dominant frequency component at 1 cycle per year and its harmonic at 2 cycles per year. This gives prominence to relatively weaker frequency components that existed in the spectrum output. Comparing the result of Method 1 and 2, the averaging suppresses noise, producing a smoother background spectrum, at the expense of spectrum resolution.

The spectrum obtained are of mixed spectra, consisting of both (periodic or quasi periodic) oscillations that produce spectral peaks, as well as irregular fluctuations which account for a sloping spectral continuum. This can be clearly seen in the result of Method 2 as well as in all subfigures (a) of the raw periodogram and Method 1. The continuous spectra result from time series that exhibit some form of irregular fluctuations that occur at all scales of variation (which can be considered to be noise), though not necessarily with the same average amplitude (e.g. red noise) [46]. Red noise is a description given to a sloping spectrum that drops off towards high frequencies, compared to white noise that produces a flat spectral continuum. It is the background noise for climatic and climatic-proxy data [52]. Red noise occur in time series that is described as first order autoregressive (AR(1)). An autoregressive (AR) process indicates partial dependence of new values on previous values. For first-order AR process, only the immediately preceding value is influencing the current value.

Table 4.3: Summary of the spectrum estimation result for the ACTS 20.2 GHz data

Site	**Raw periodogram**	**Method 1**	**Method 2**
Florida	Significant presence of a peak at solar, sidereal and anti-sidereal frequencies, at relatively the same amplitude	Presence of solar, sidereal and anti-sidereal peaks remains but the side-peaks are at relatively lower amplitudes.	Solar frequency component detected
Colorado	A peak at the solar and anti-sidereal frequencies but no sidereal peak	Only solar peak detected.	Solar frequency component detected
New Mexico	Sidereal and anti-sidereal detected but no solar component.	Solar peak detected, with a possible anti-sidereal peak but no sidereal component.	Solar frequency component detected
Alaska	No solar, anti-sidereal and sidereal peak detected.	No solar, anti-sidereal & sidereal peak detected.	No solar frequency component detected
British Columbia	Spectrum contains higher background noise compared to other sites but a solar component is clearly seen.	Solar peak detected but not significantly higher than background noise.	No solar frequency component detected
Oklahoma	No significant solar, anti-sidereal and sidereal peak detected	Significant solar, sidereal and anti-sidereal component detected. Sidereal is relatively larger than the two peaks.	Solar frequency component detected

Table 4.3 gives a summary of the spectral estimation results obtained using all three methods, for both beacon and radiometer data. The presence of a solar periodicity is significant in Florida, Colorado, New Mexico and Oklahoma, but not in Alaska and British Columbia. In New Mexico and Oklahoma, a significant solar peak only emerged in Method 1 and 2, after the seasonal variations were removed. The detected peak is said to be ‘significant’ if its amplitude is considerably larger than the background level. The statistical significance of the peak detected at the solar frequency is covered in Chapter 5.

The presence of a solar day frequency component suggests the existence of diurnal variations in the beacon and radiometer attenuation levels.

Discussion on the differences seen between sites is given in Section 4.3.4 after the spectral estimation result for the ACTS 27.5 GHz data (Section 4.3.4).

4.4 ACTS 27.5 GHz data

This section presents the spectral estimation results using the raw periodogram, Method 1 and Method 2 for the ACTS 27.5 GHz beacon and radiometer attenuation data.

4.4.1 Time plot data

Figure 4.27 and Figure 4.28 gives the time data plot for the 27.5 GHz beacon and radiometer data, respectively. Similar to its 20.2 GHz counterpart, missing data files were replaced with those of similar dates from different years, while unreadable data points were interpolated from neighboring values. Both beacon and radiometer time series data are preprocessed to remove any outliers using the method outlined in Figure 4.10 of Section 4.2.1. Threshold values are given in Table 4.4. The minimum, maximum and mean data set used in removing outliers are in Figure 4.29 for beacon, and Figure 4.30 for radiometer data. Similar to the 20.2 GHz data, a seasonal variation can be detected in the mean line plot in all sites, except in British Columbia. The maximum line plot also appears more erratic compared to its counterpart in 20.2 GHz (Figure 4.6 and Figure 4.7).

The time series data with their outliers removed are given in Figure 4.31 and Figure 4.32 respectively. As before these data are referred to as capped data.

Table 4.4: Threshold values for removing outliers in 20.2GHz ACTS data

Site	Florida	Colorado	New Mexico	Alaska	British Columbia	Oklahoma
Threshold A_1	7.0	2.5	2.0	5.5	5.0	5.0
Threshold B_1	3.2	1.1	0.8	2.0	3.4	2.5
Threshold A_2	6.0	2.5	2.0	5.5	5.0	4.5
Threshold B_2	3.1	1.1	0.8	2.0	3.3	2.4

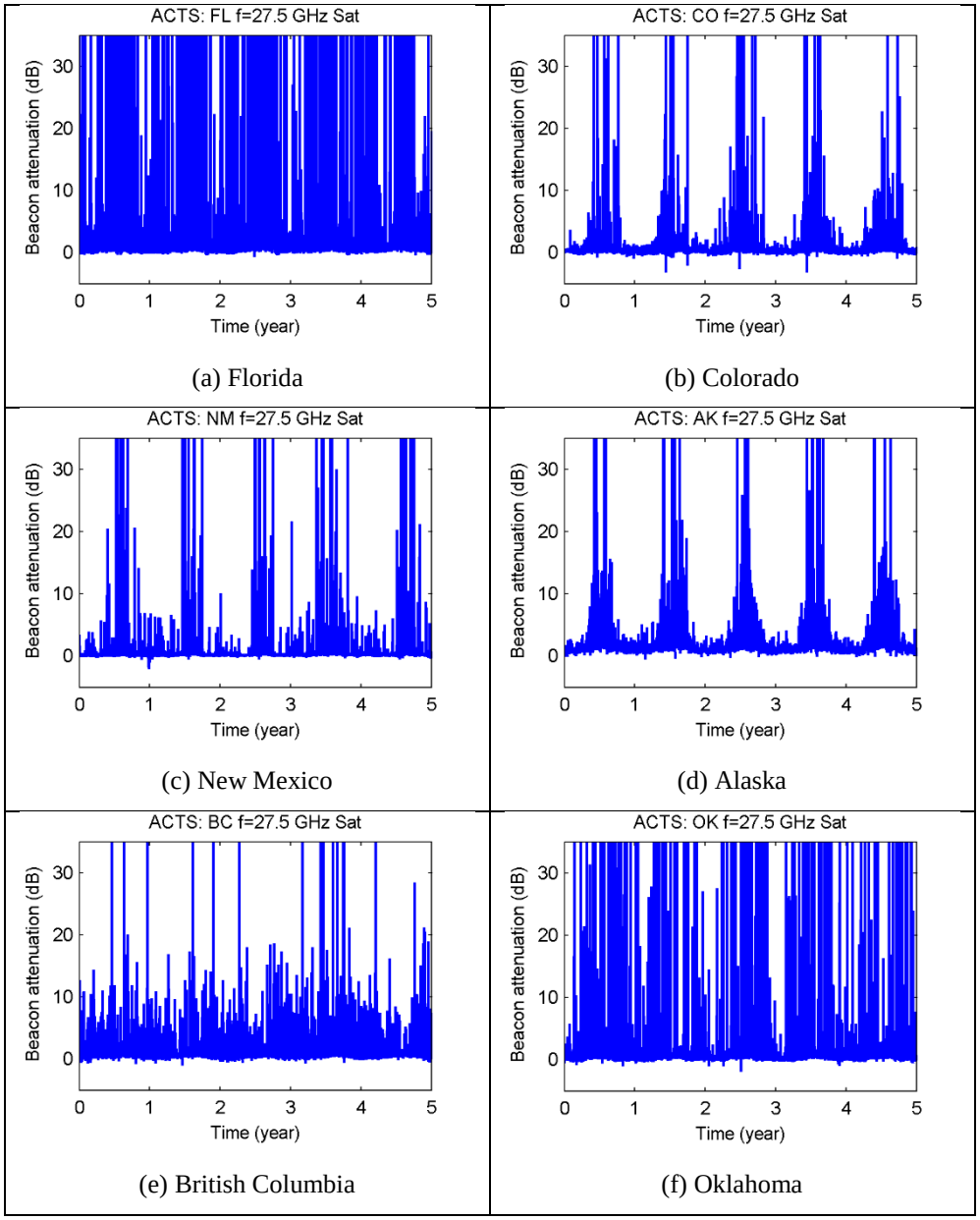

Figure 4.27: ACTS 27.5 GHz beacon attenuation data (raw data)

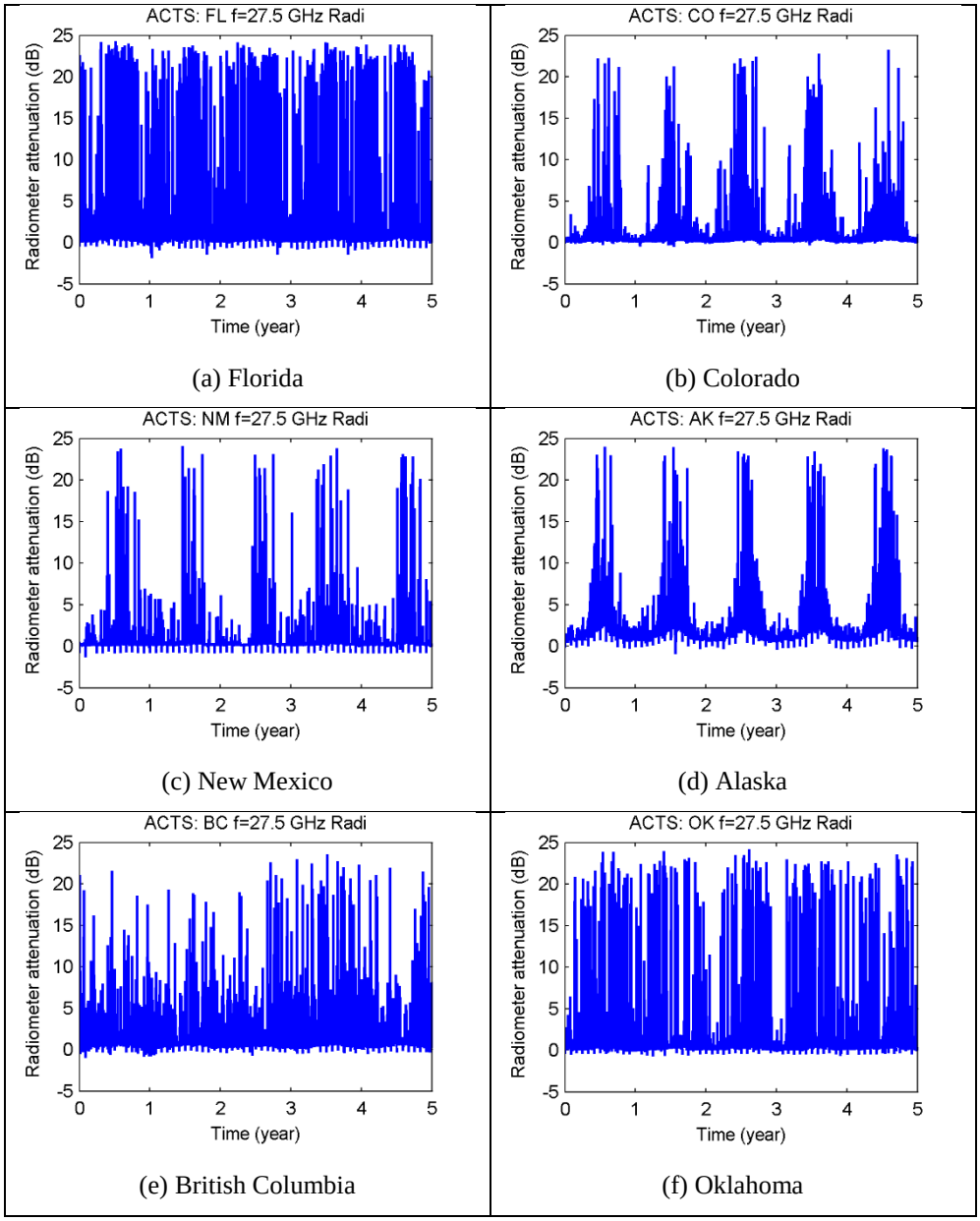

Figure 4.28: ACTS 27.5 GHz radiometer attenuation data (raw data)

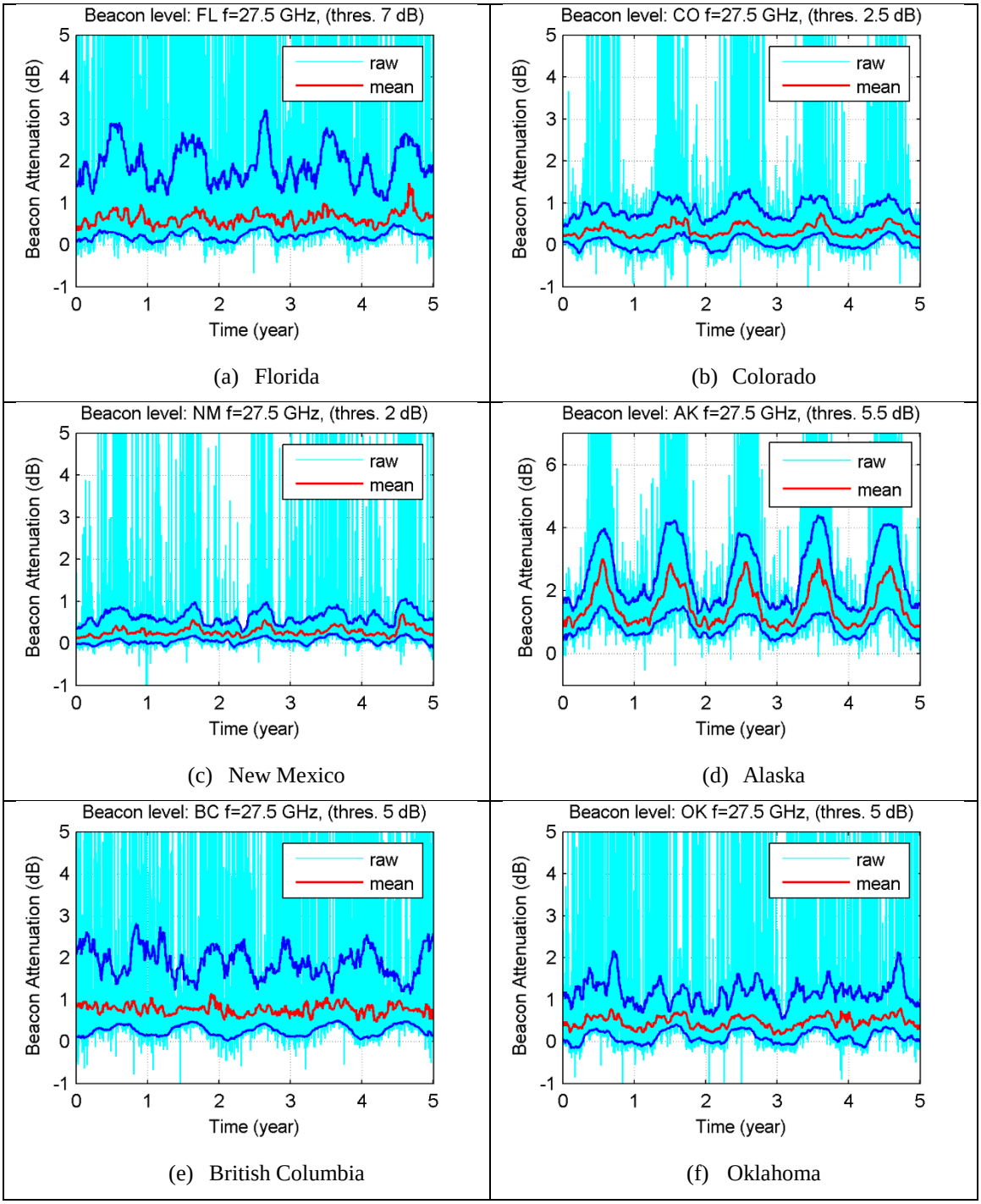

Figure 4.29: The max, min and mean line for ACTS 27.5 GHz beacon attenuation

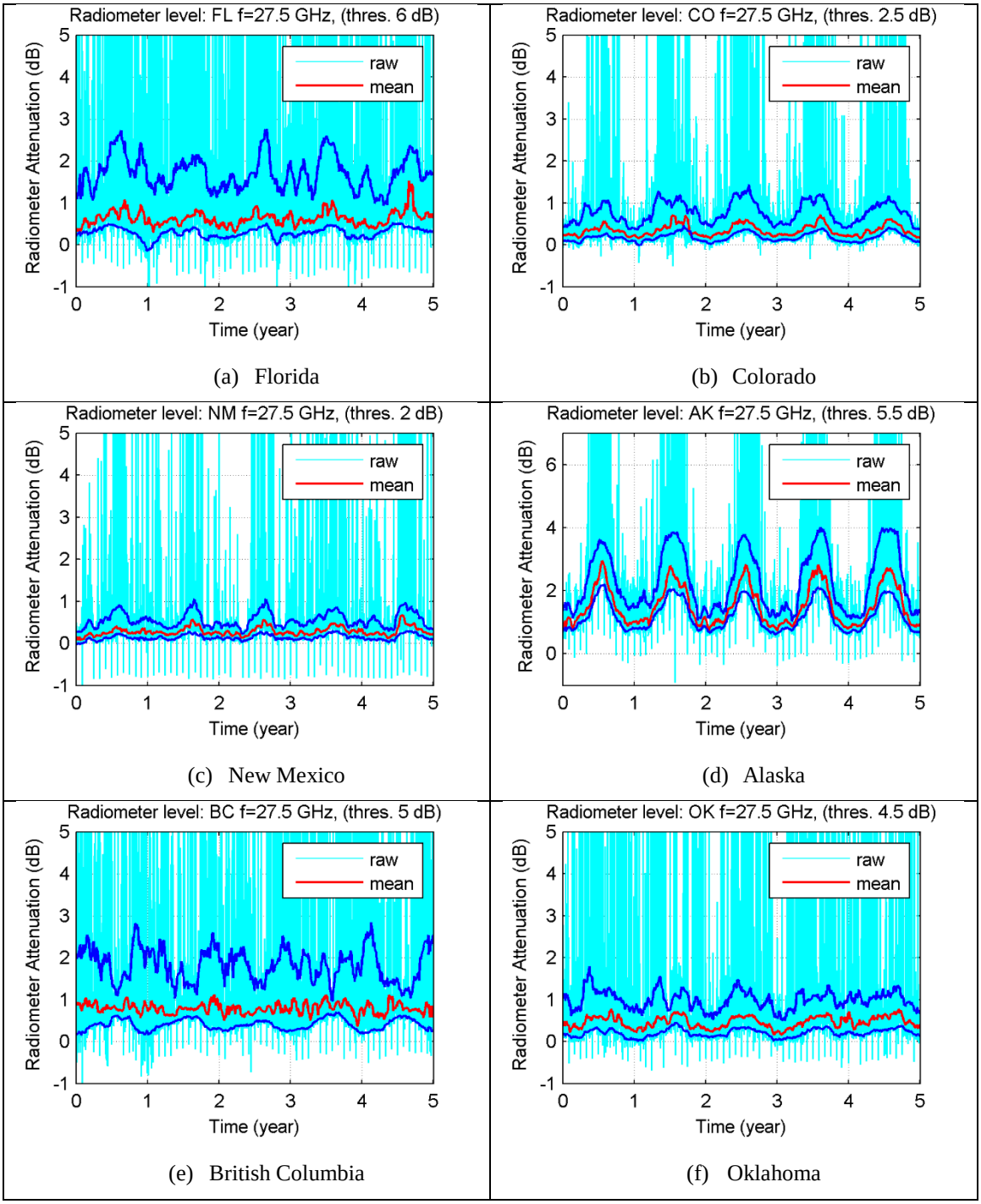

Figure 4.30: The max, min and mean line for ACTS 27.5 GHz radiometer attenuation

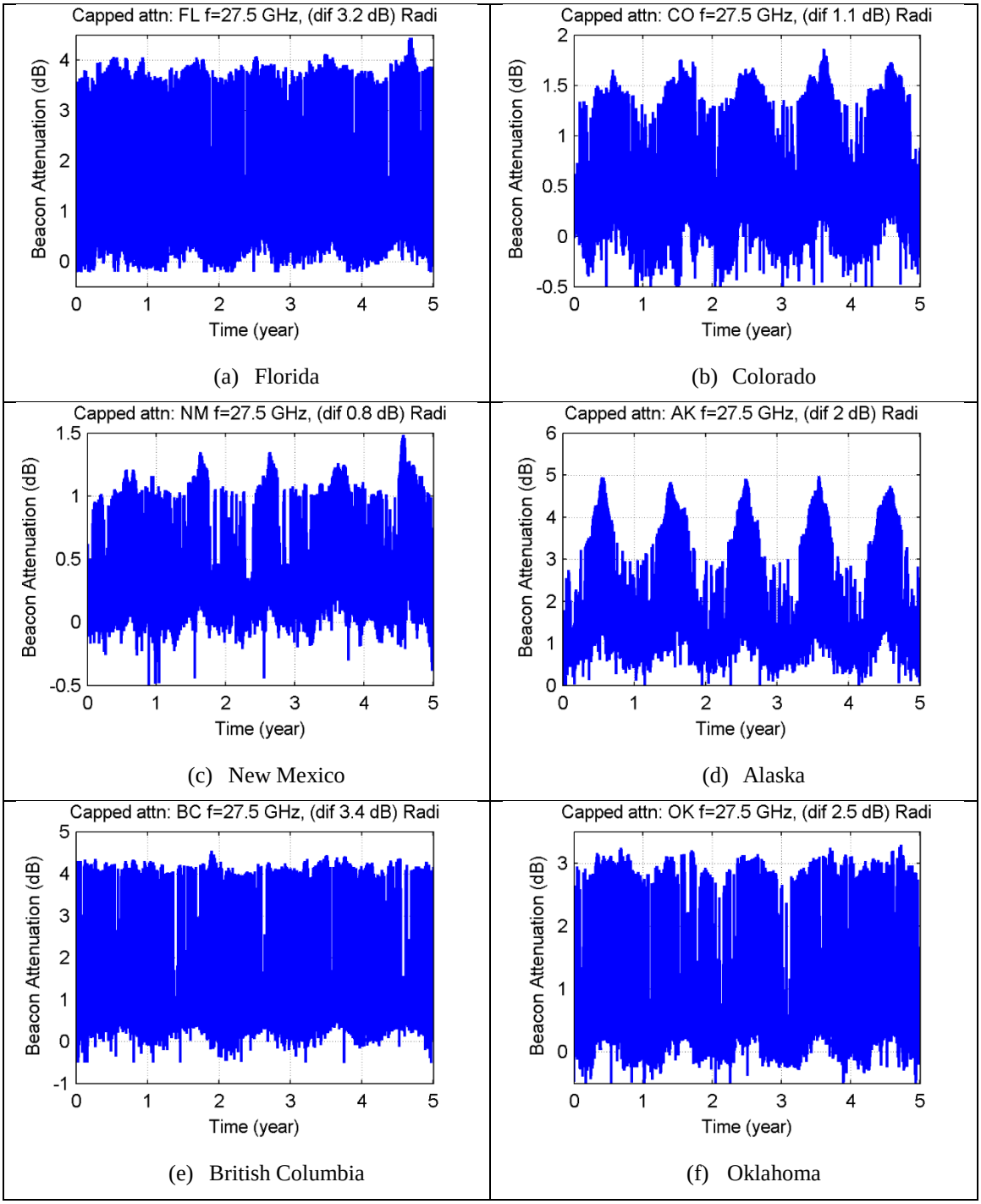

Figure 4.31: ACTS 27.5 GHz beacon attenuation after outliers removal (capped data)

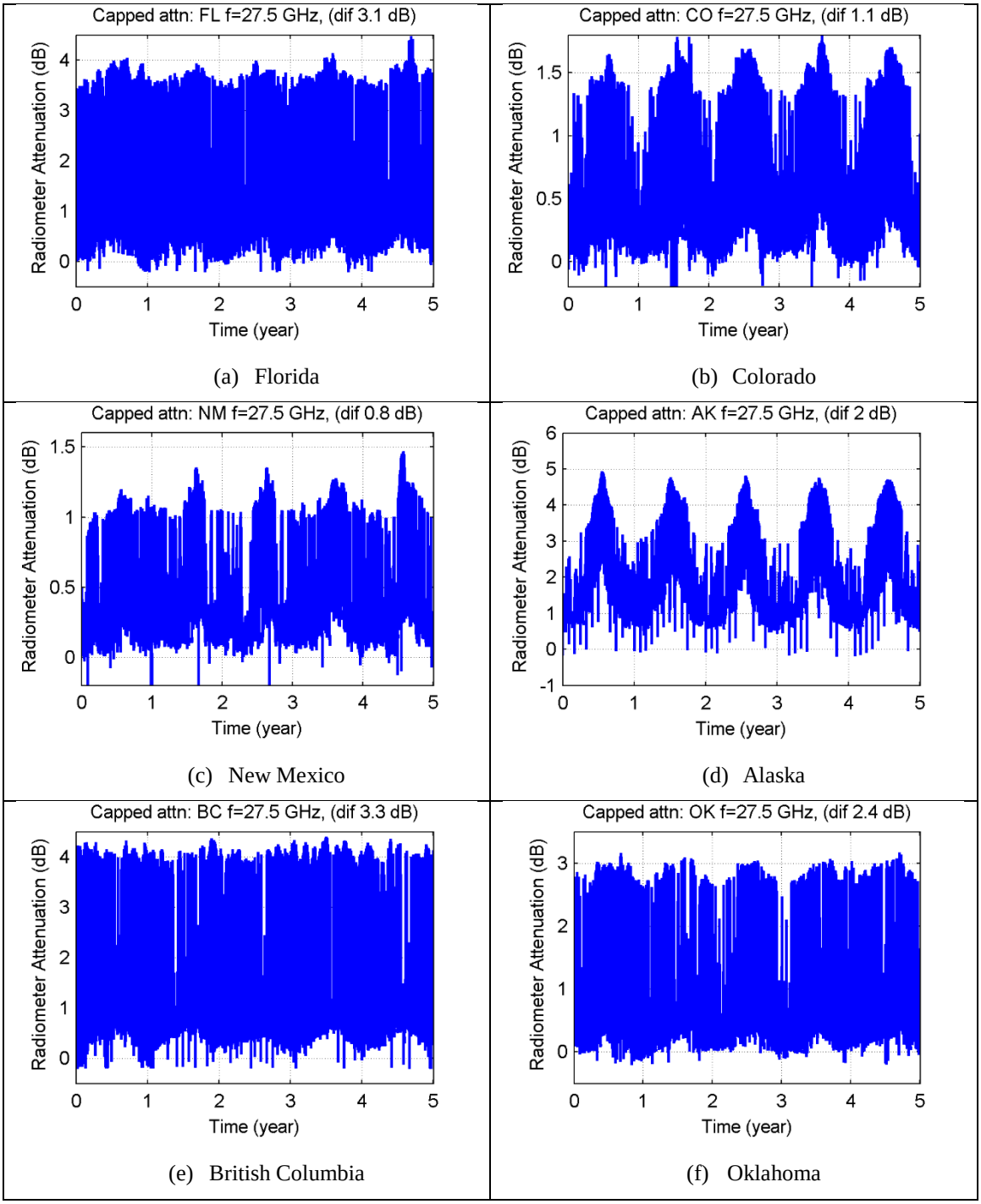

Figure 4.32: ACTS 27.5 GHz radiometer attenuation after outliers removal (capped data)

4.4.2 Raw periodogram

The raw periodogram uses the raw data as input (Figure 4.27 and Figure 4.28), and the result for each respective site is give in Figure 4.33 to Figure 4.38.

Comparing the result with similar analysis onto the 20.2 GHz data (Figure 4.11 to Figure 4.16), the solar peak and its' harmonics are more visible here. In New Mexico (Figure 4.35) and Oklahoma (Figure 4.38), a significant solar peak can be seen in the raw periodogram of the 27.5 GHz but not in the raw periodogram of its 20.2 GHz counterpart. However no specific pattern can be detected in terms of the presence of sidereal and anti-sidereal peaks. For example the sidereal and anti-sidereal peaks are relatively higher than the solar peak in the 20.2 GHz compared to the 27.5 GHz data for Florida (Figure 4.33). But in Oklahoma, the opposite is true.

The raw periodogram output for Colorado (Figure 4.34), Alaska (Figure 4.36) and British Columbia (Figure 4.37) are similar with their 20.2 GHz data.

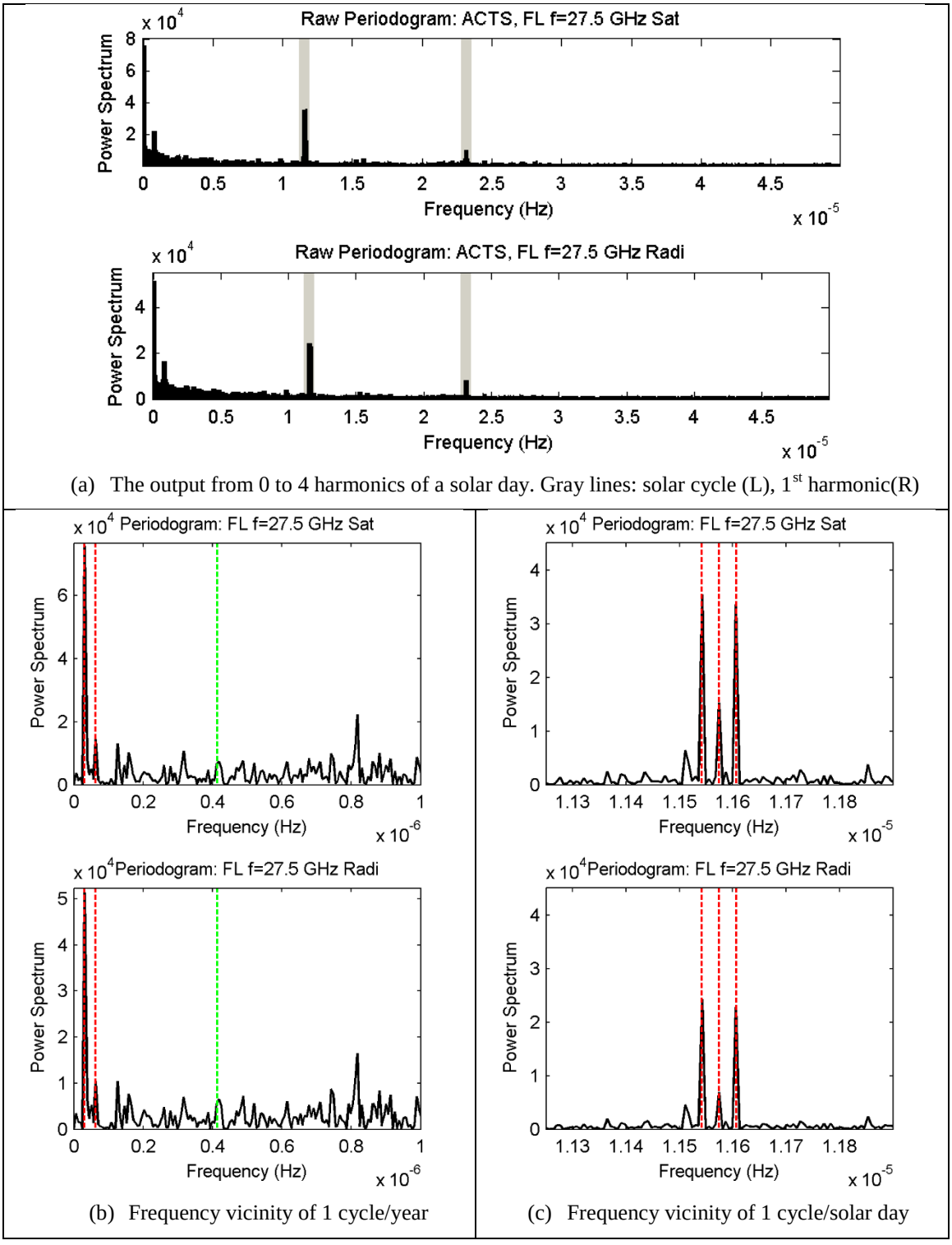

(a) The output from 0 to 4 harmonics of a solar day. Gray lines: solar cycle (L), 1st harmonic(R)

(b) Frequency vicinity of 1 cycle/year

(c) Frequency vicinity of 1 cycle/solar day

Figure 4.33: Raw periodogram for ACTS 27.5 GHz in Florida

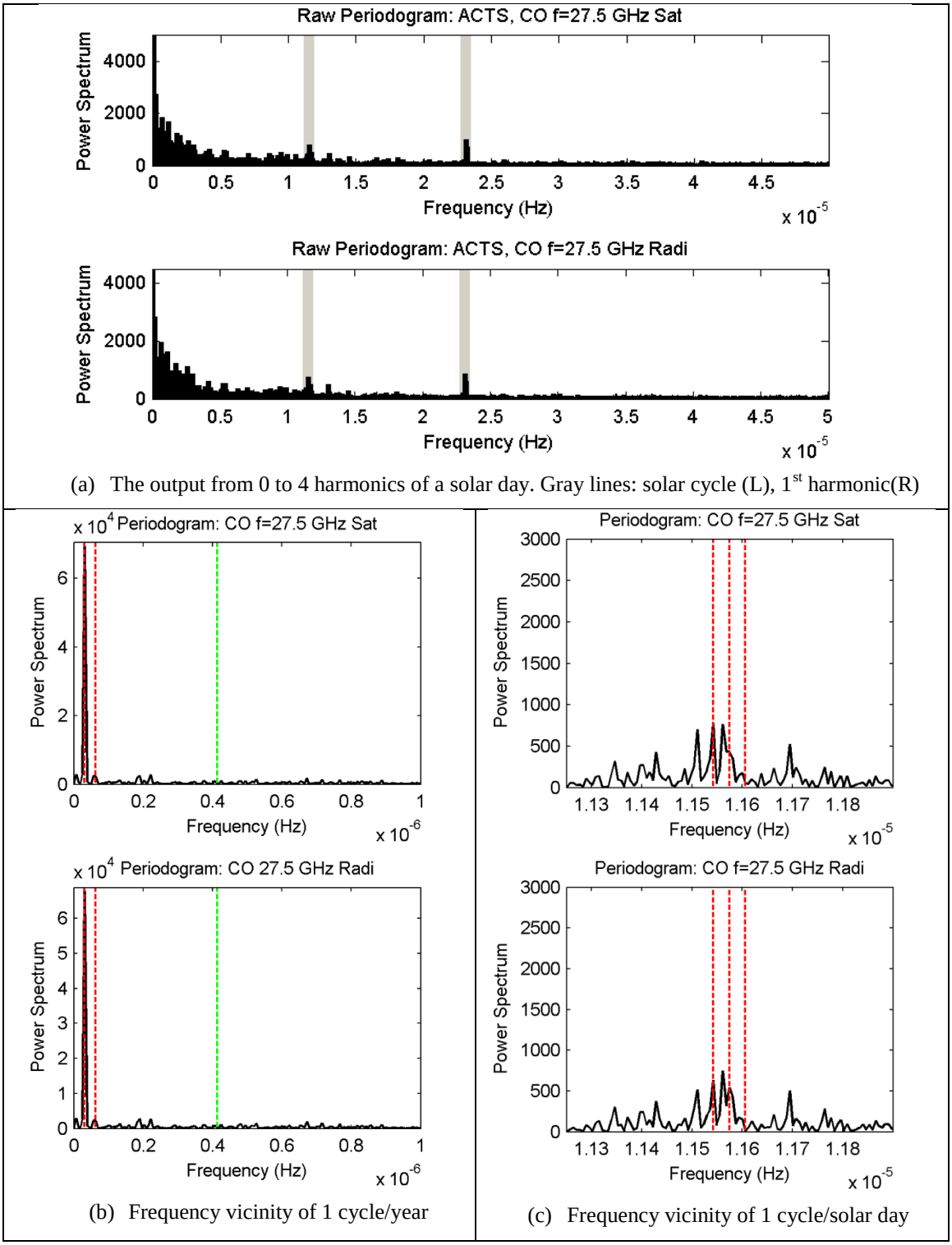

(a) The output from 0 to 4 harmonics of a solar day. Gray lines: solar cycle (L), 1st harmonic(R)

(b) Frequency vicinity of 1 cycle/year

(c) Frequency vicinity of 1 cycle/solar day

Figure 4.34: Raw periodogram for ACTS 27.5 GHz in Colorado

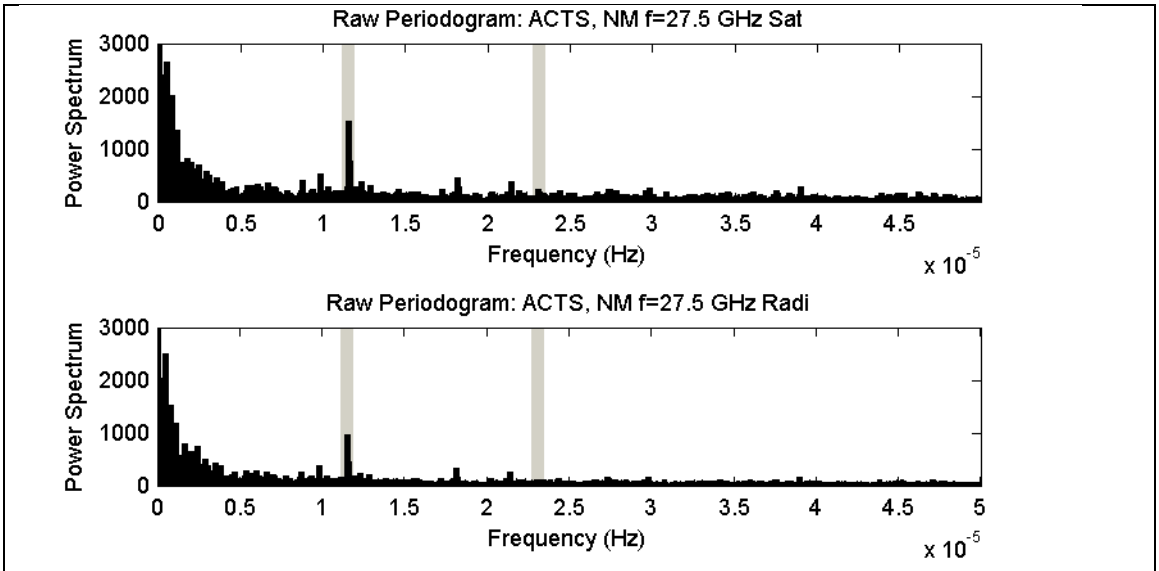

(a) The output from 0 to 4 harmonics of a solar day. Gray lines: solar cycle (L), 1st harmonic(R)

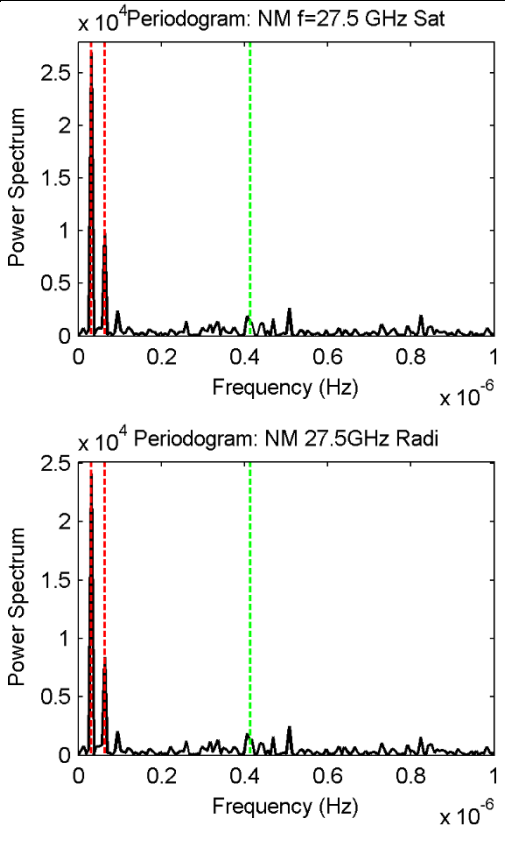

(b) Frequency vicinity of 1 cycle/year

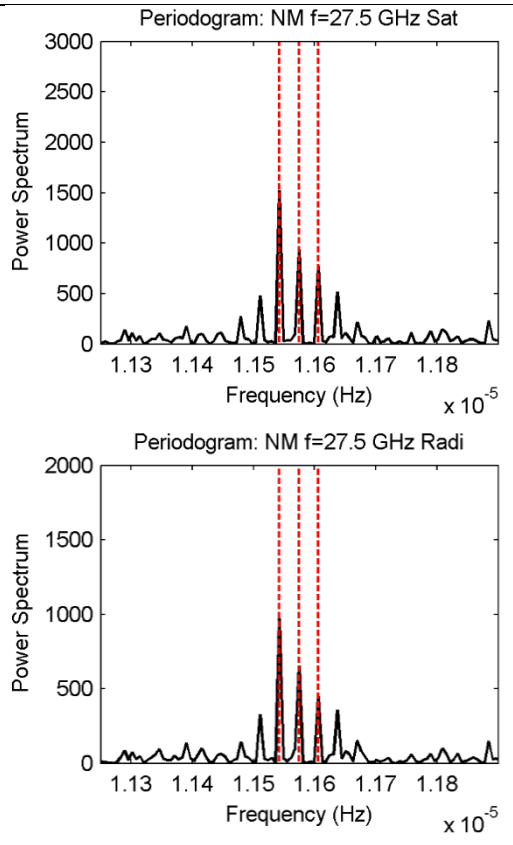

(c) Frequency vicinity of 1 cycle/solar day

Figure 4.35: Raw periodogram for ACTS 27.5 GHz in New Mexico

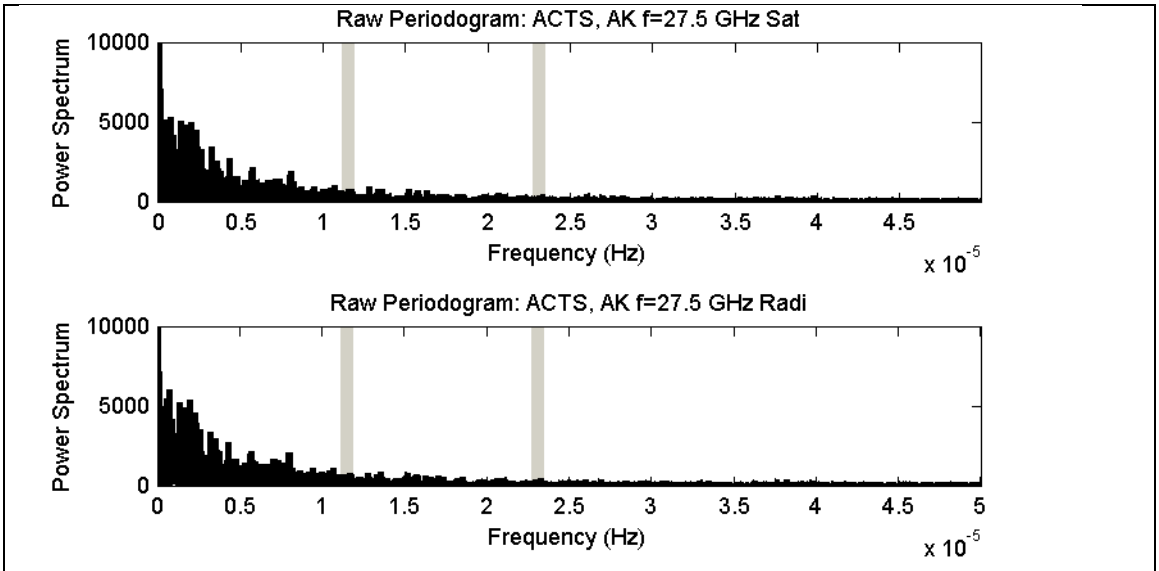

(a) The output from 0 to 4 harmonics of a solar day. Gray lines: solar cycle (L), 1st harmonic(R)

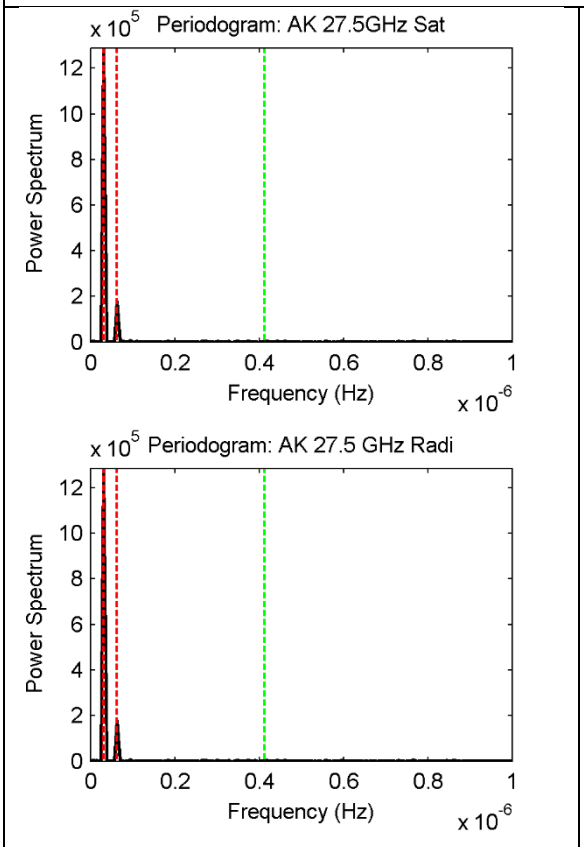

(b) Frequency vicinity of 1 cycle/year

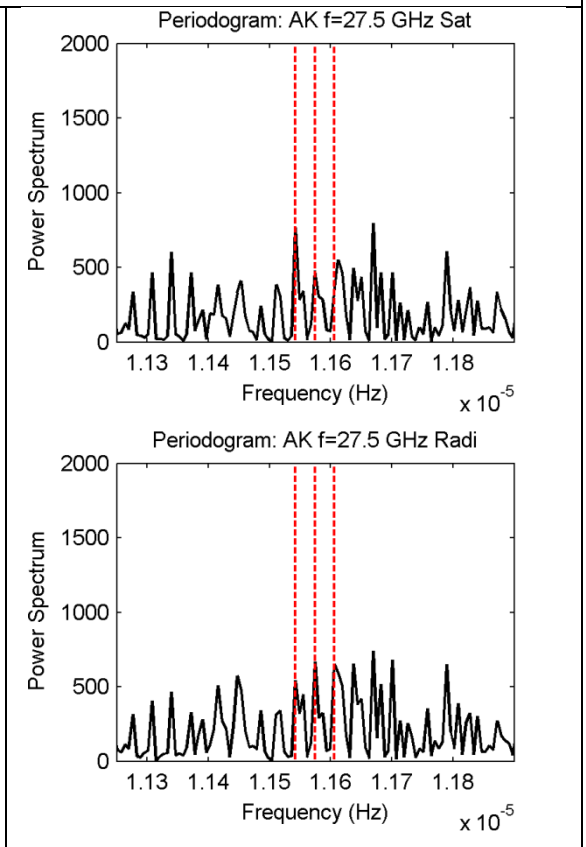

(c) Frequency vicinity of 1 cycle/solar day

Figure 4.36: Raw periodogram for ACTS 27.5 GHz in Alaska

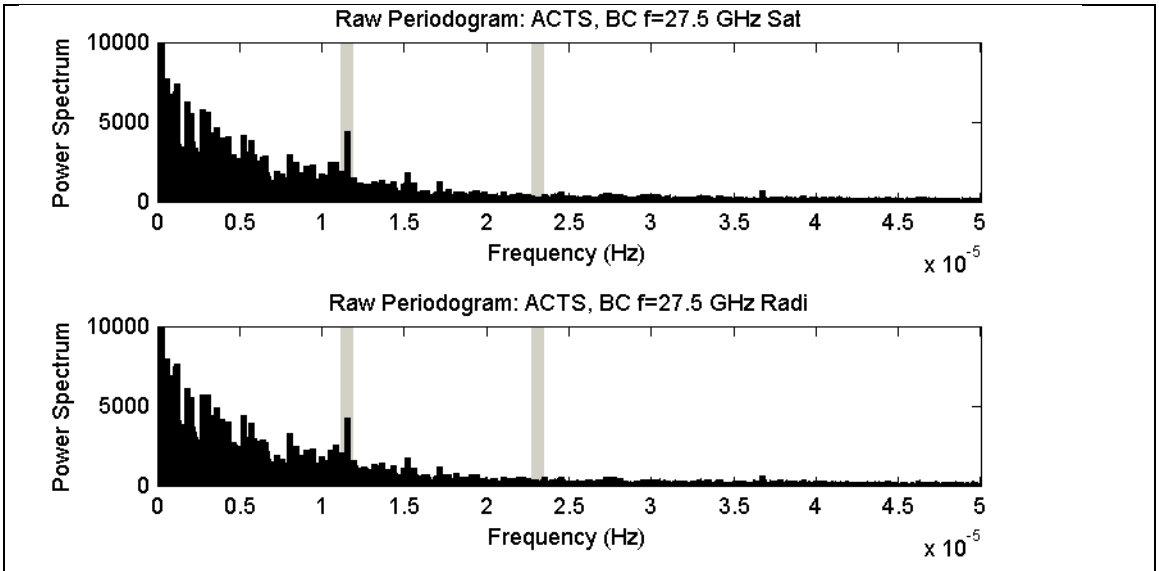

(a) The output from 0 to 4 harmonics of a solar day. Gray lines: solar cycle (L), 1st harmonic(R)

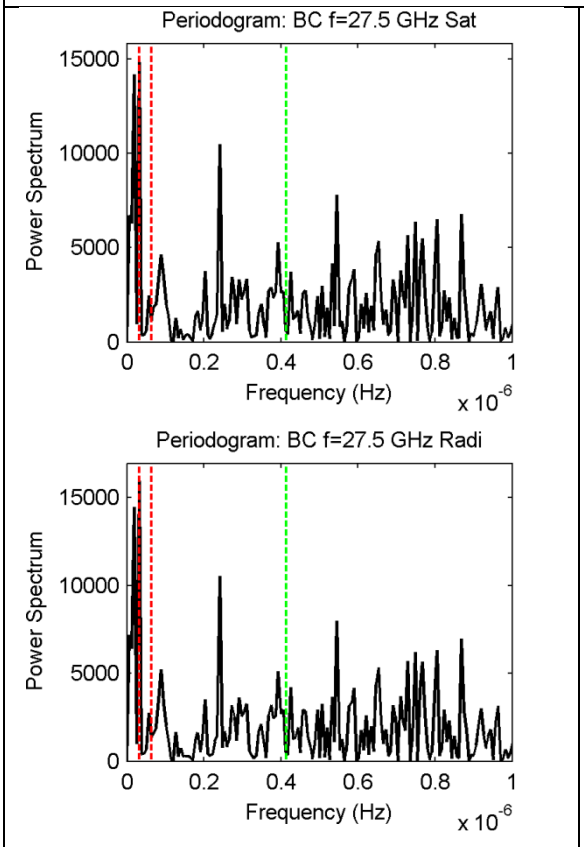

(b) Frequency vicinity of 1 cycle/year

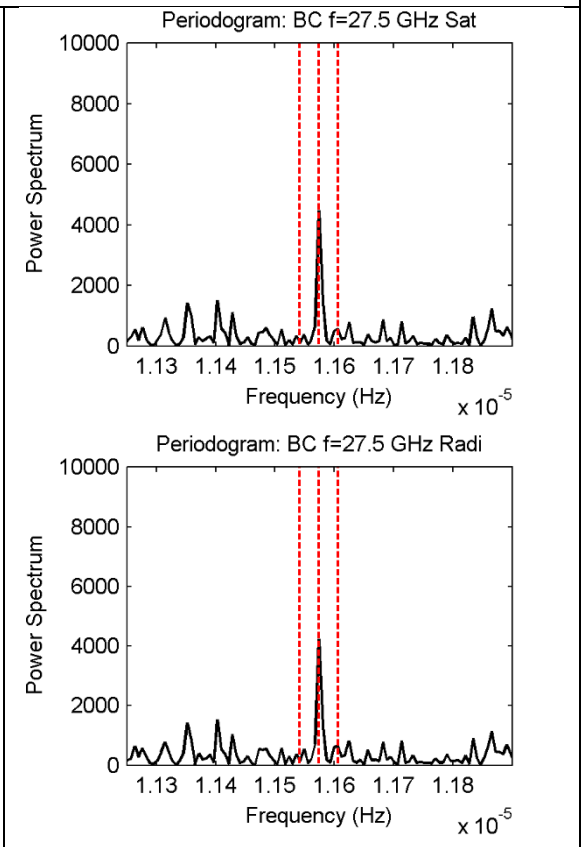

(c) Frequency vicinity of 1 cycle/solar day

Figure 4.37: Raw periodogram for ACTS 27.5 GHz in British Columbia

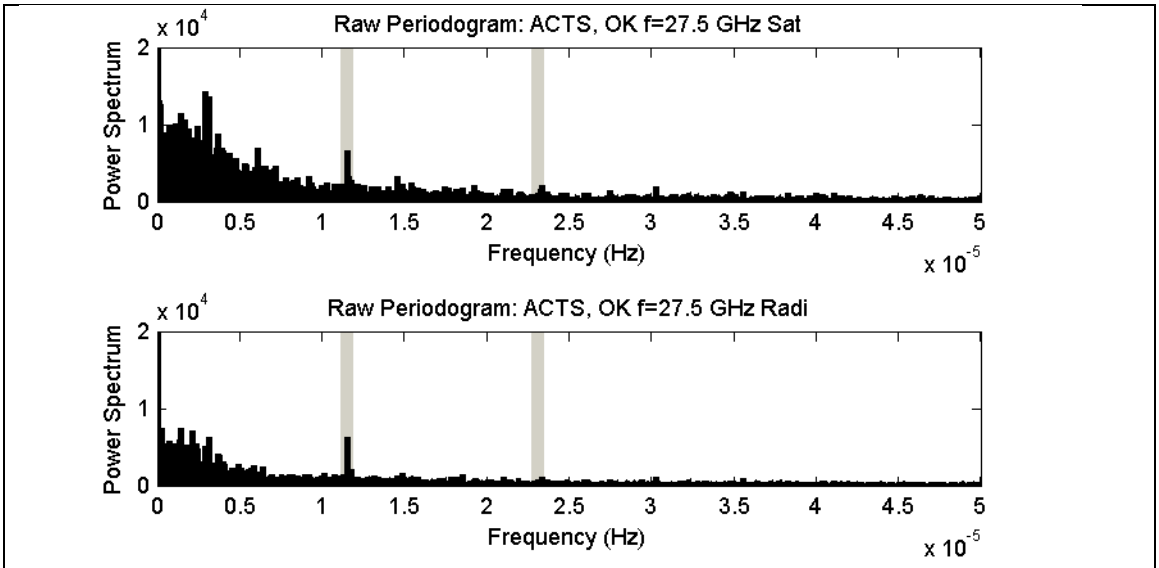

(a) The output from 0 to 4 harmonics of a solar day. Gray lines: solar cycle (L), 1st harmonic(R)

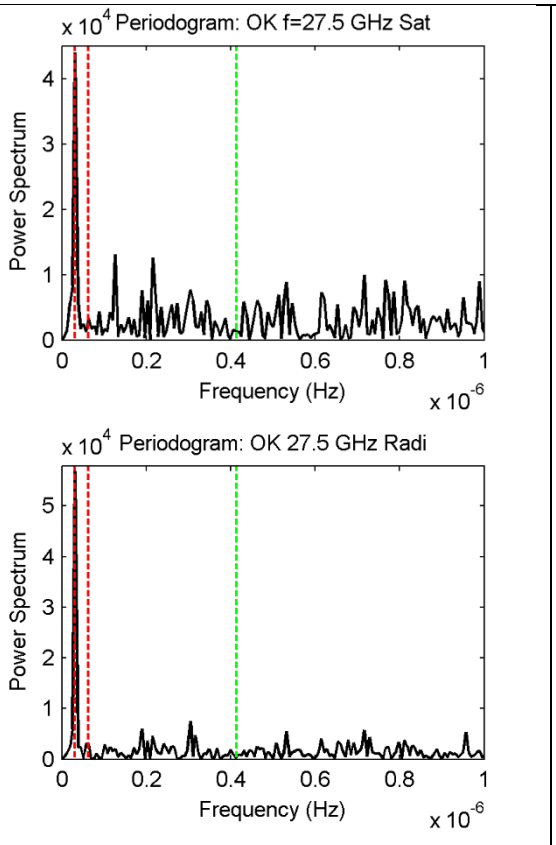

(b) Frequency vicinity of 1 cycle/year

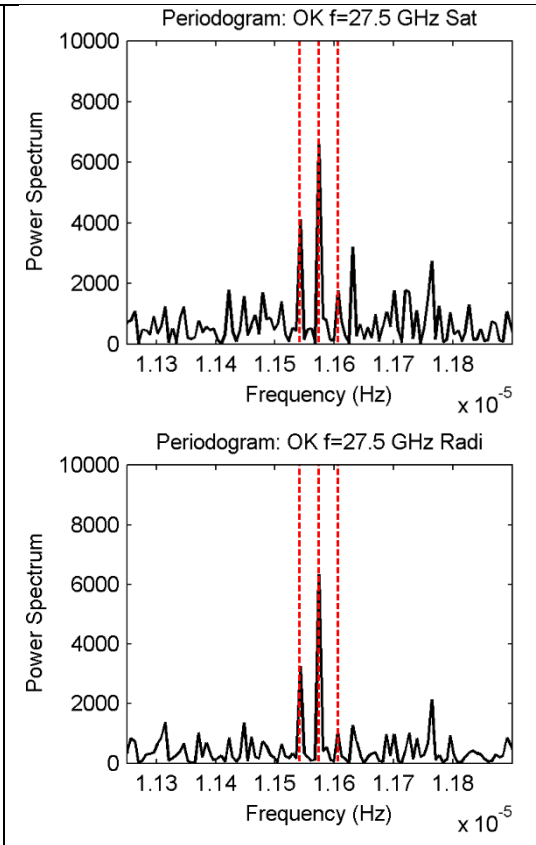

(c) Frequency vicinity of 1 cycle/solar day

Figure 4.38: Raw periodogram for ACTS 27.5 GHz in Oklahoma

4.4.3 Result with Method 1

Method 1 was implemented onto the normalized 27.5 GHz data. Figure 4.39 and Figure 4.40 below are the normalized data used as input. The resultant spectrum generated for each ACTS site is given in Figure 4.41 to Figure 4.46.

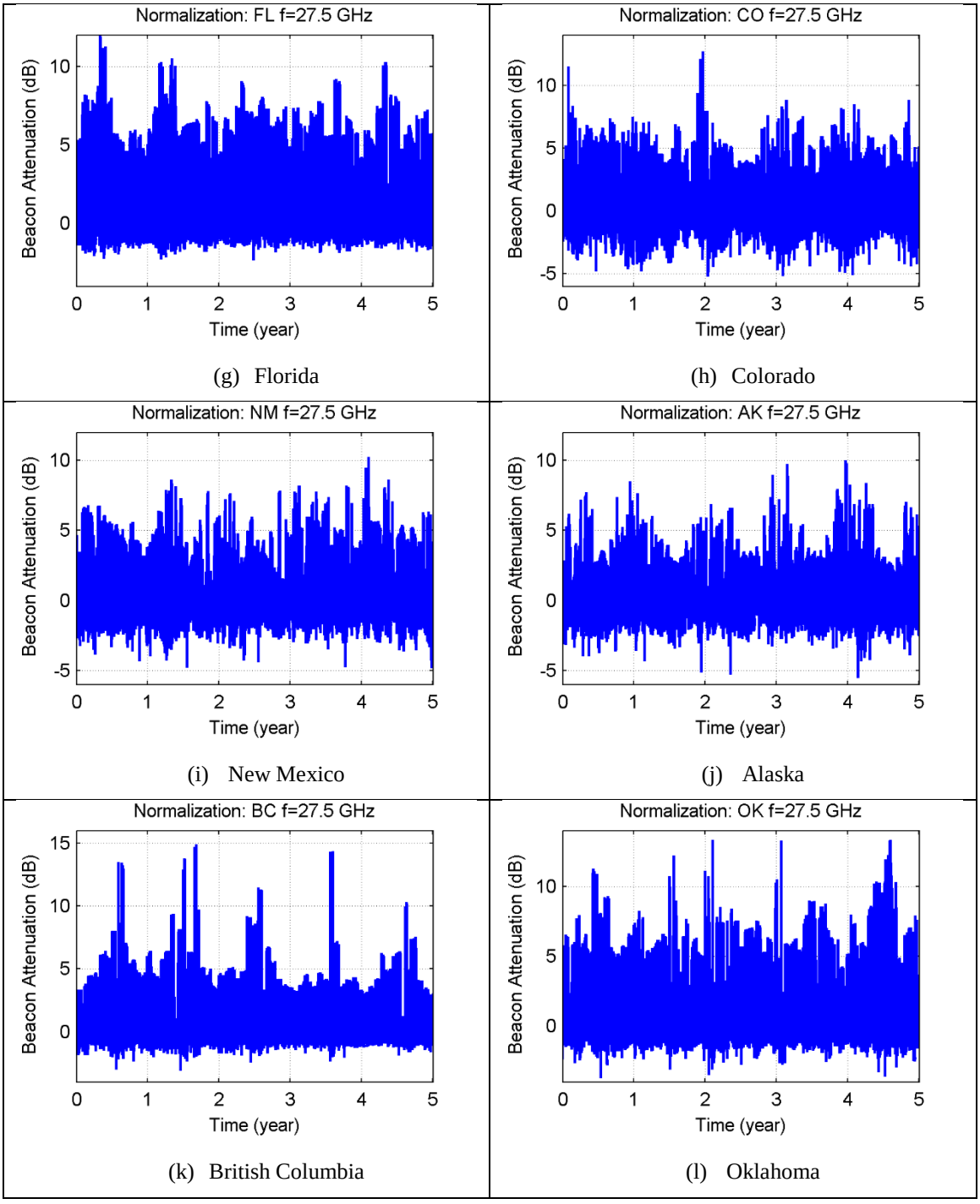

Figure 4.39: Normalized ACTS 27.5 GHz beacon data

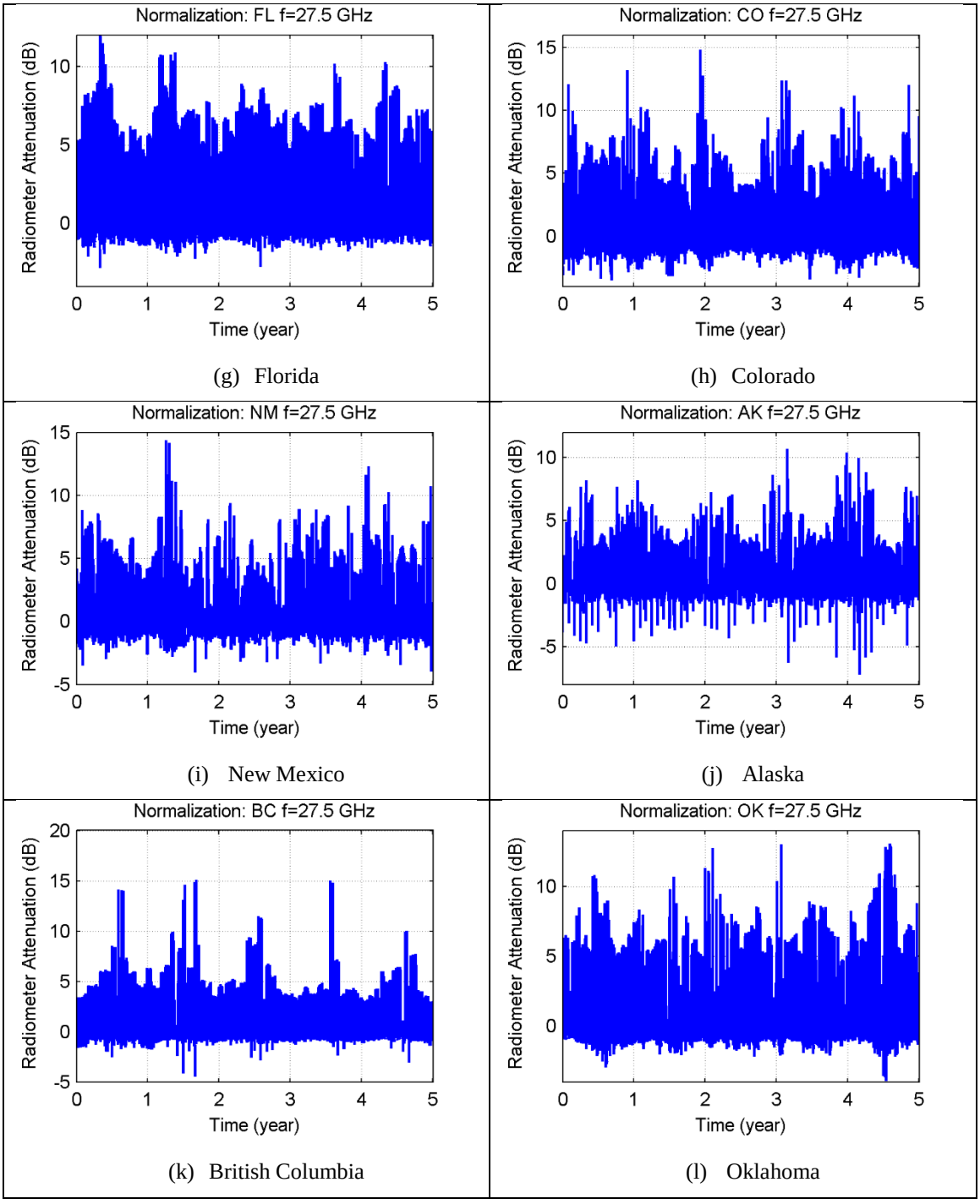

Figure 4.40: Normalized ACTS 27.5 GHz radiometer data

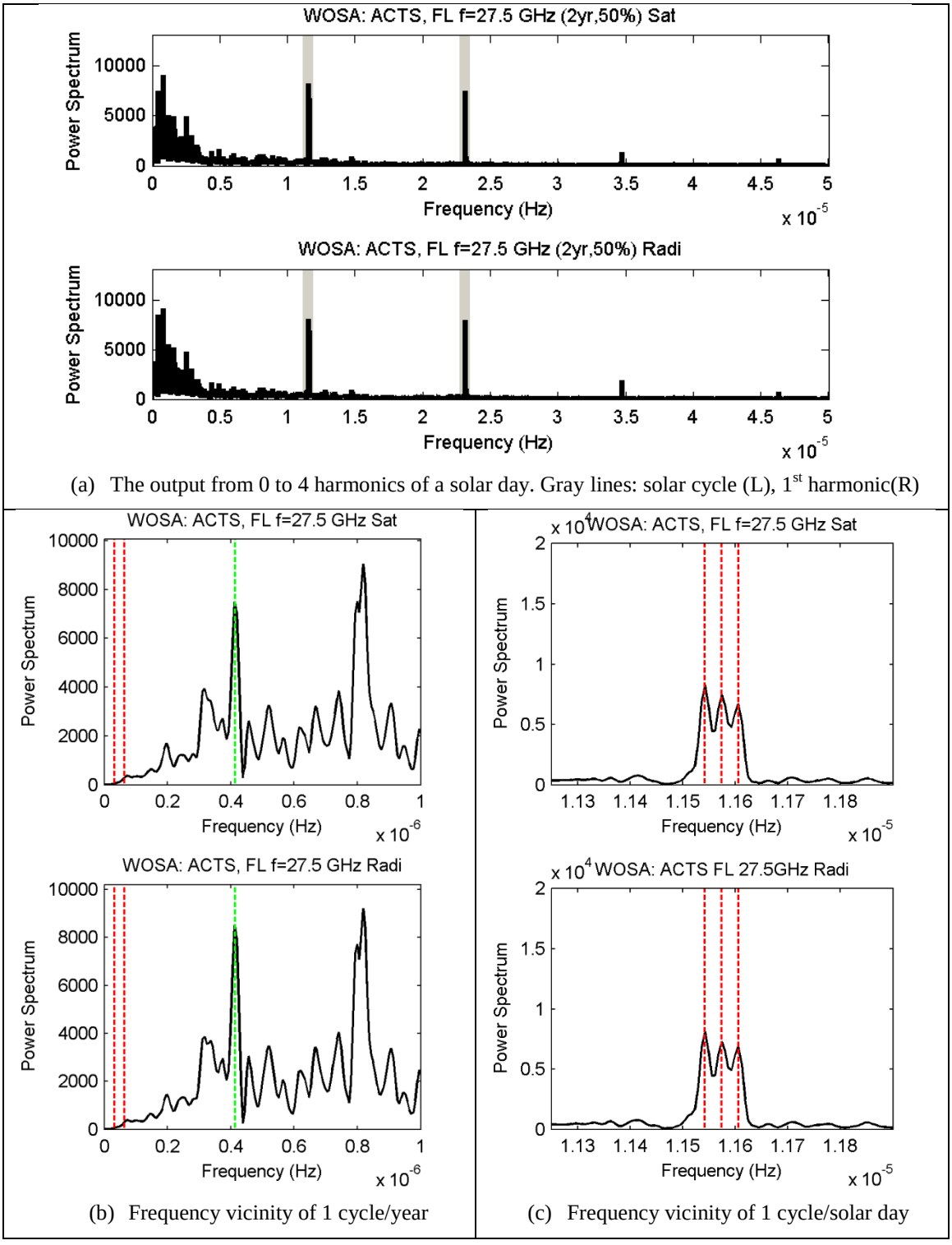

(a) The output from 0 to 4 harmonics of a solar day. Gray lines: solar cycle (L), 1st harmonic(R)

(b) Frequency vicinity of 1 cycle/year

(c) Frequency vicinity of 1 cycle/solar day

Figure 4.41: Method 1 for ACTS 27.5 GHz data in Florida

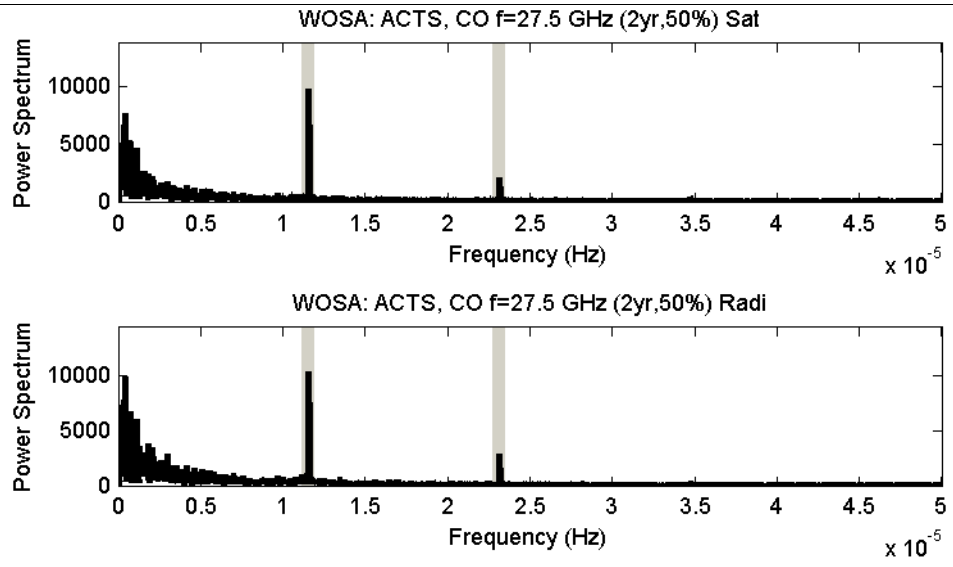

(a) The output from 0 to 4 harmonics of a solar day. Gray lines: solar cycle (L), 1st harmonic(R)

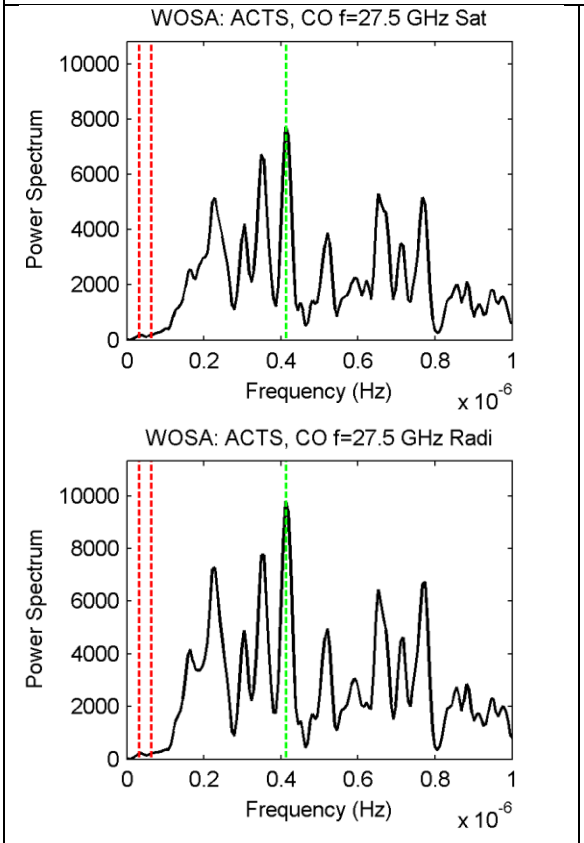

(b) Frequency vicinity of 1 cycle/year

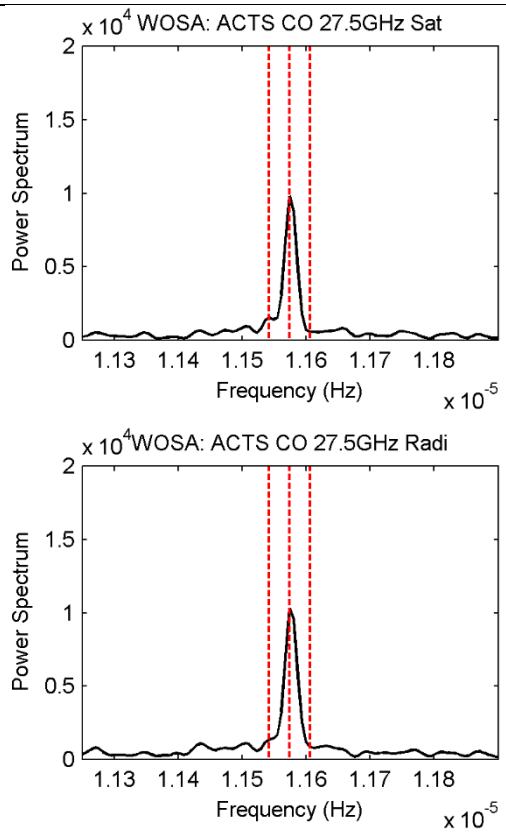

(c) Frequency vicinity of 1 cycle/solar day

Figure 4.42: Method 1 for ACTS 27.5 GHz data in Colorado

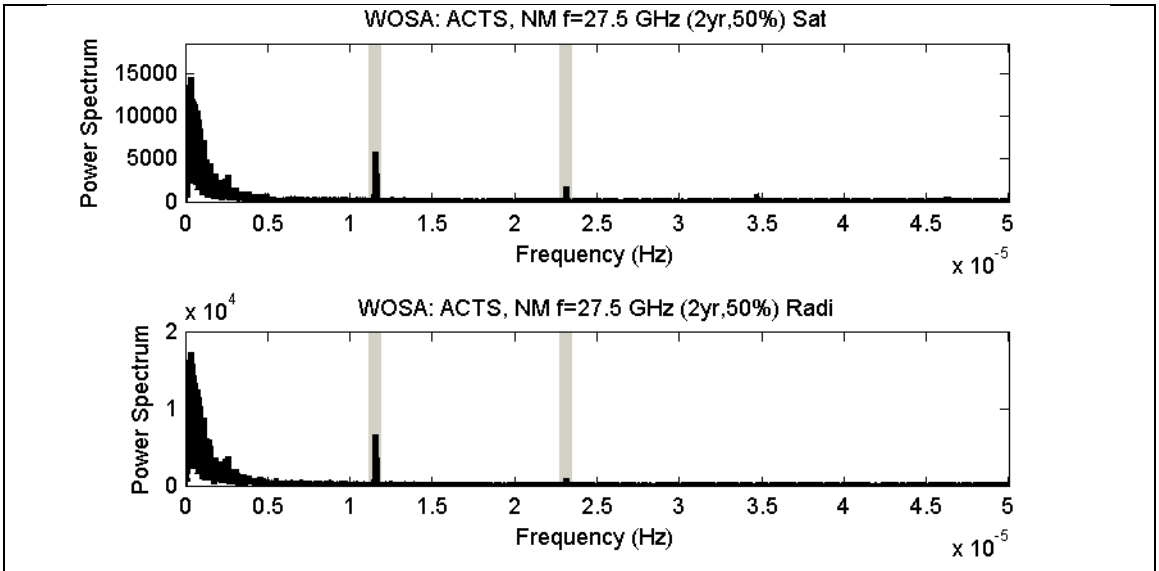

(a) The output from 0 to 4 harmonics of a solar day. Gray lines: solar cycle (L), 1st harmonic(R)

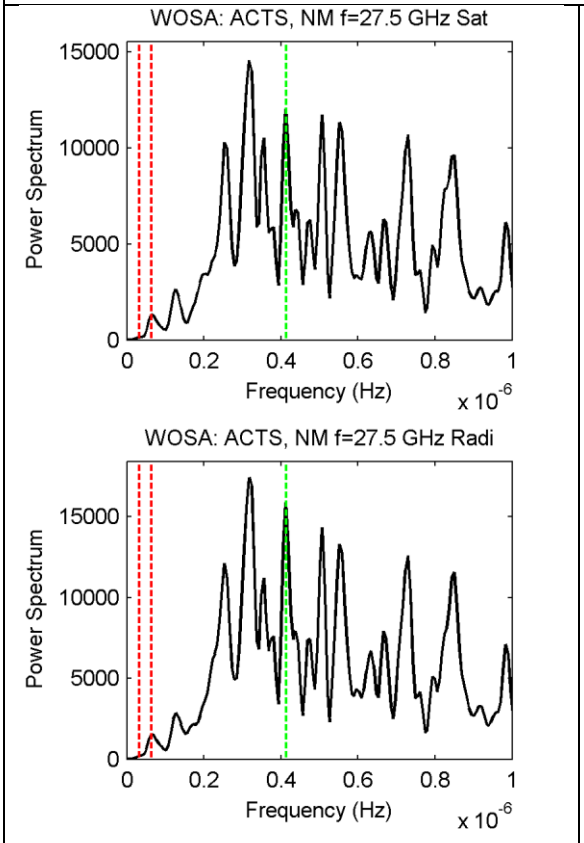

(b) Frequency vicinity of 1 cycle/year

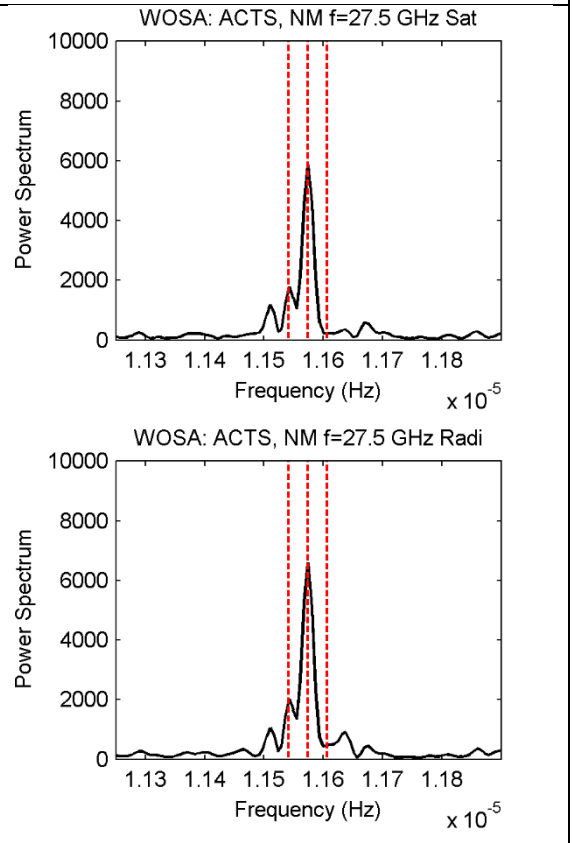

(c) Frequency vicinity of 1 cycle/solar day

Figure 4.43: Method 1 for ACTS 27.5 GHz data in New Mexico

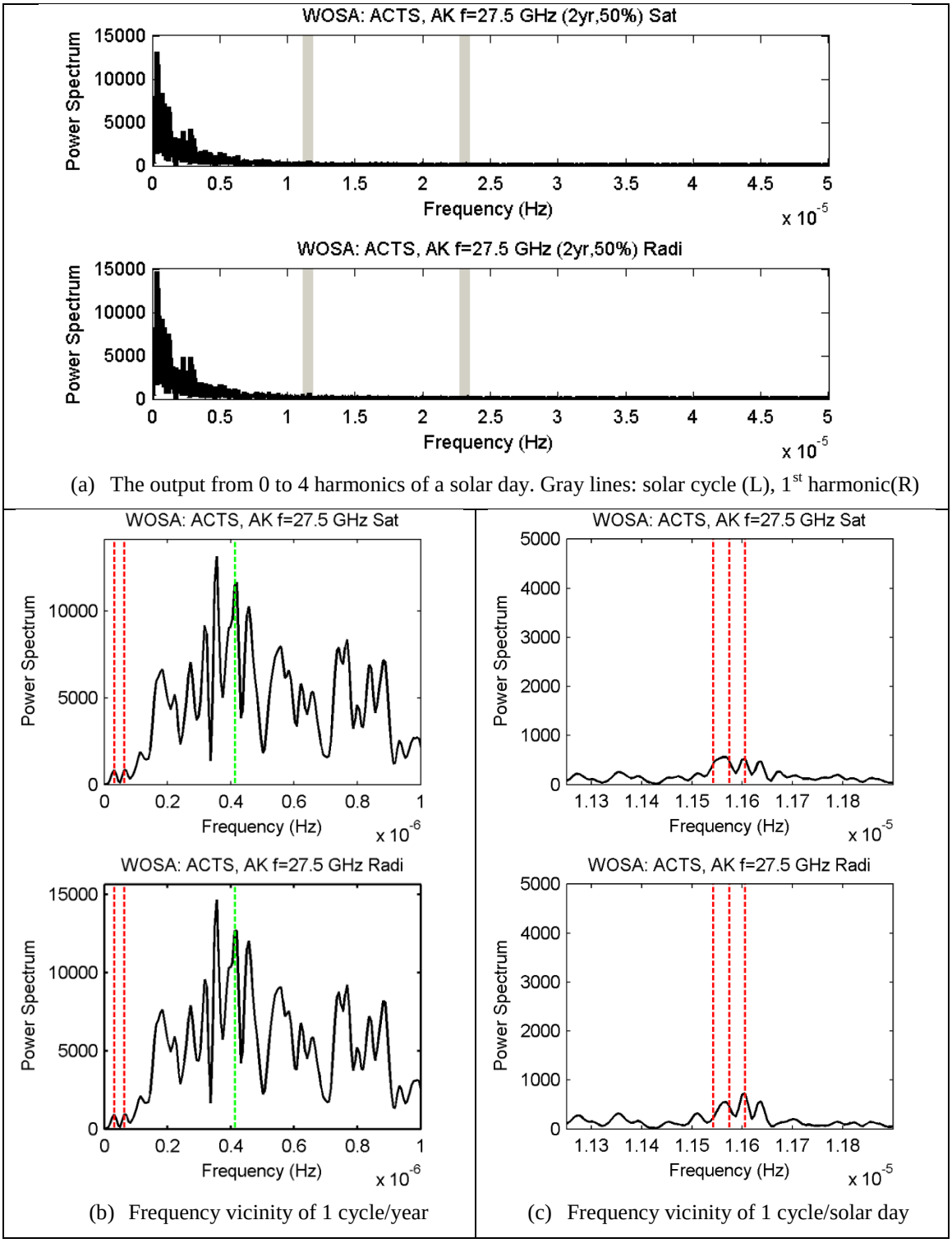

(a) The output from 0 to 4 harmonics of a solar day. Gray lines: solar cycle (L), 1st harmonic(R)

(b) Frequency vicinity of 1 cycle/year

(c) Frequency vicinity of 1 cycle/solar day

Figure 4.44: Method 1 for ACTS 27.5 GHz data in Alaska

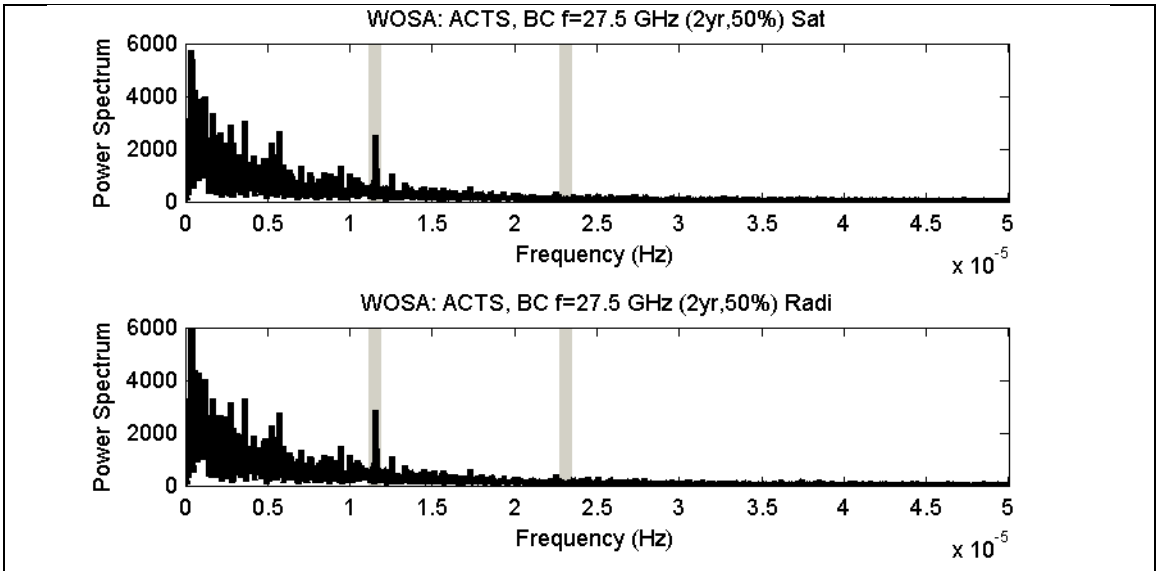

(a) The output from 0 to 4 harmonics of a solar day. Gray lines: solar cycle (L), 1st harmonic(R)

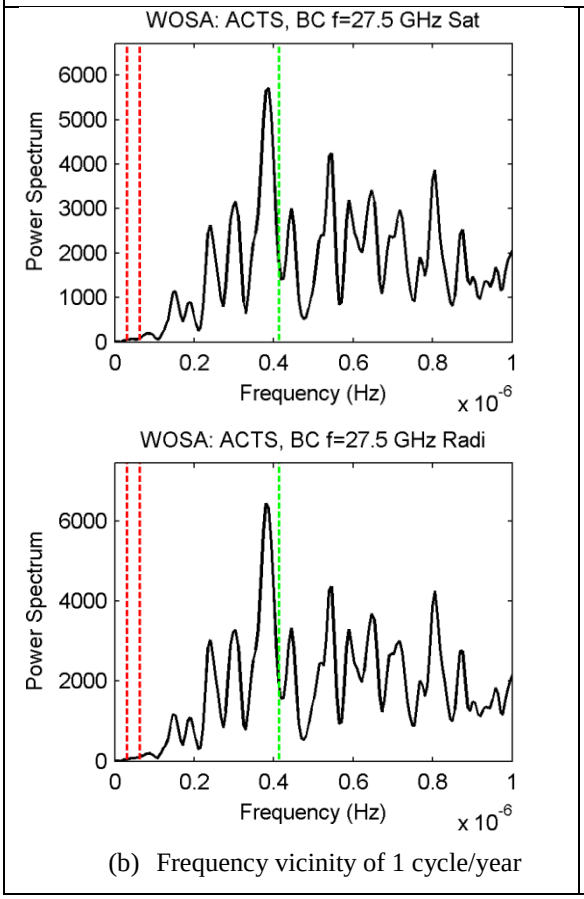

(b) Frequency vicinity of 1 cycle/year

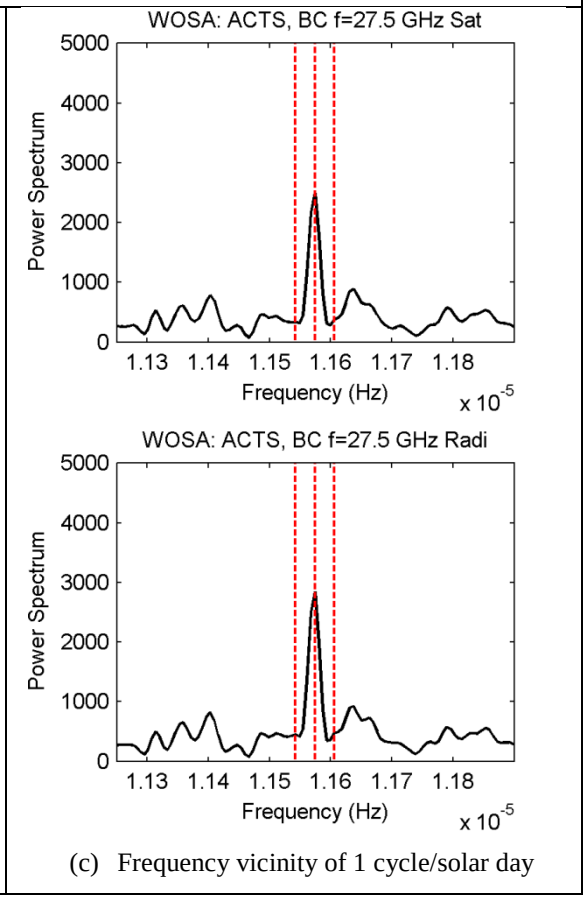

(c) Frequency vicinity of 1 cycle/solar day

Figure 4.45: Method 1 for ACTS 27.5 GHz data in British Columbia

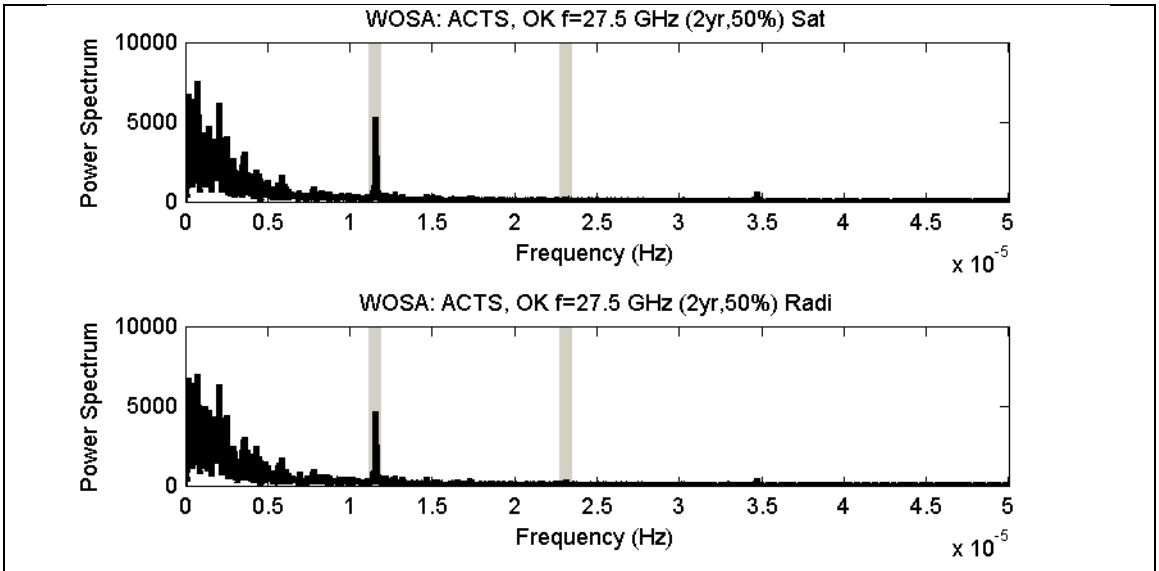

(a) The output from 0 to 4 harmonics of a solar day. Gray lines: solar cycle (L), 1st harmonic(R)

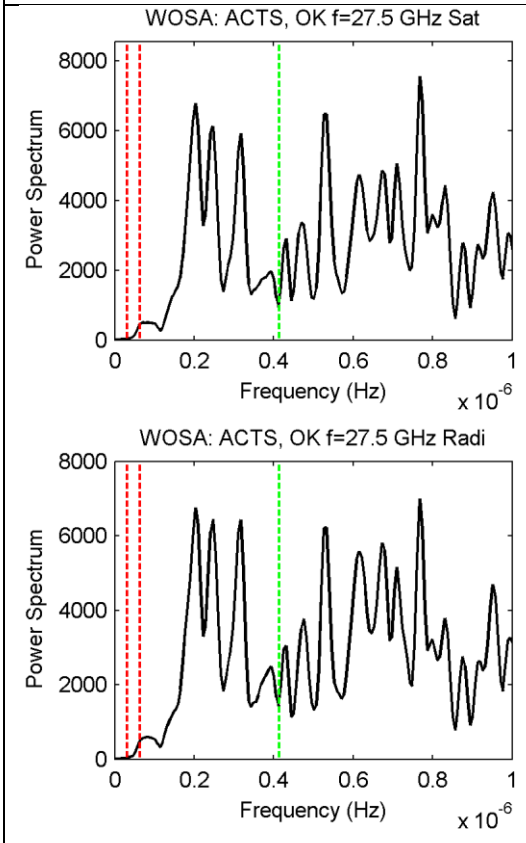

(b) Frequency vicinity of 1 cycle/year

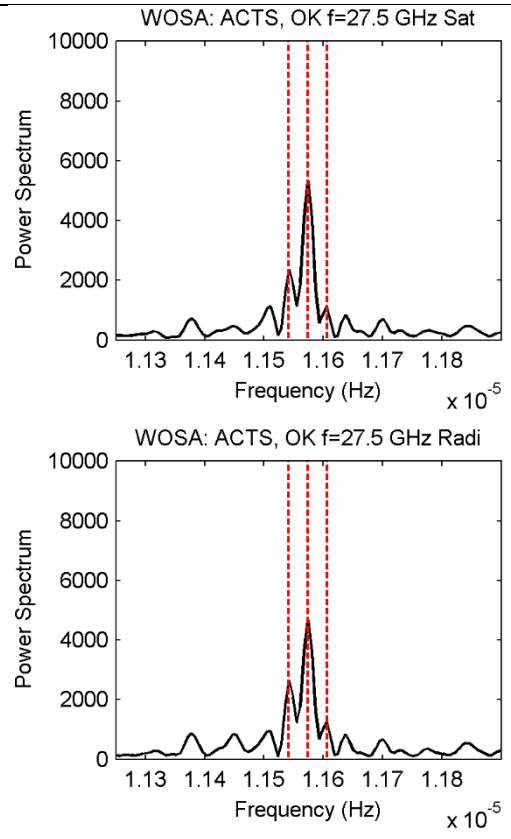

(c) Frequency vicinity of 1 cycle/solar day

Figure 4.46: Method 1 for ACTS 27.5 GHz data in Oklahoma

Comparing the spectral estimation generated using Method 1 with the raw periodogram, the result generated with Method 1 produces a more defined solar peak with a less erratic background noise. This is similar to the result obtained with the 20.2 GHz data. For the result in Colorado (Figure 4.42) and New Mexico (Figure 4.43), a more pronounce solar peak is detected, together with a relative reduction in the sidereal and anti-sidereal peaks, compared to their raw periodogram (Figure 4.34 for CO and Figure 4.35 for NM). A sidereal and anti-sidereal peak remains as pronounced in the result of Method 1 for Florida (Figure 4.41) and Oklahoma (Figure 4.46). However in Florida, the solar, sidereal and anti-sidereal peaks appear to be partially fused together. This was not seen in the spectrum obtained from the raw periodogram (Figure 4.33).

To investigate if the result seen in subfigure (c) of Figure 4.41 may be due to low resolution, we modified the WOSA parameters as follows. The segment size is increased from 2 to 3 years, the percentage of overlap is increased from 50% to 84% and the hamming window is replaced with a rectangular window, as suggested in [53]. This increases the resolution to $\frac{1/60}{3\times365\times1440} = 1.057 \times 10^{-8}\, Hz$, but maintains the number of averaging of 4. The modified WOSA for Method 1 was implemented onto the 27.5 GHz beacon and radiometer data in Florida, with the results given in Figure 4.47(a) and (b). Result shows that with better resolution, the solar, sidereal and anti-sidereal peaks are more defined, and no longer partially fused together.

Overall, a peak at the solar frequency is detected in all sites except for Alaska (Figure 4.44) and the presence of a lunar cycle periodicity can be seen in Florida and Colorado but not significantly elsewhere.

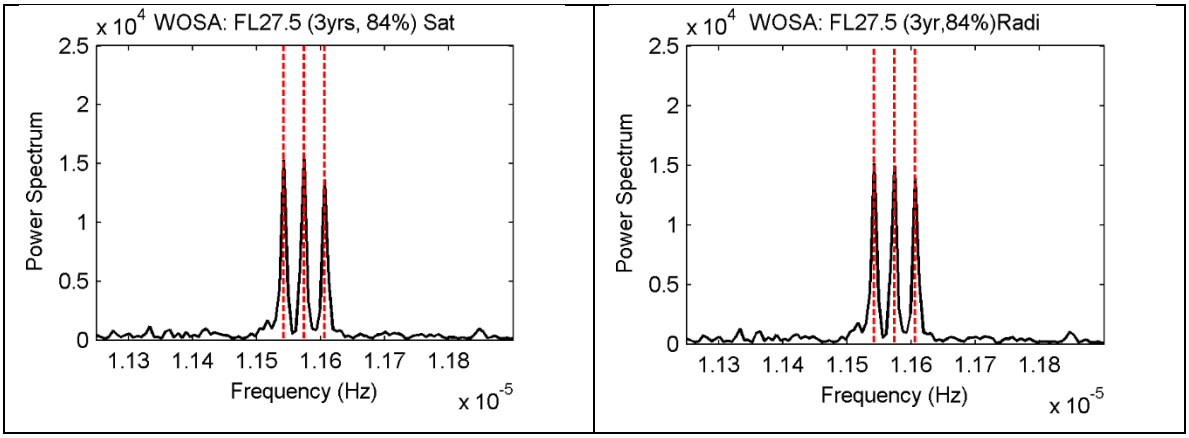

Figure 4.47: Method 1 for ACTS 27.5 GHz data in Florida (increased resolution)

4.4.4 Result with Method 2

Figure 4.48 below, gives the result of implementing Method 2 (Section 4.2.2, page 58) onto the raw data of the 27.5 GHz frequency. The red dotted horizontal line marks the location of the solar frequency.

Comparing the result obtained using Method 2 with Method 1 the presence of a solar peak remains in Florida, Colorado, New Mexico and Oklahoma, but no longer in British Columbia. No solar periodicity is detected in Alaska. These outcomes are similar to those obtained in Method 1 using the 20.2 GHz data (Section 4.3.3, page 81).

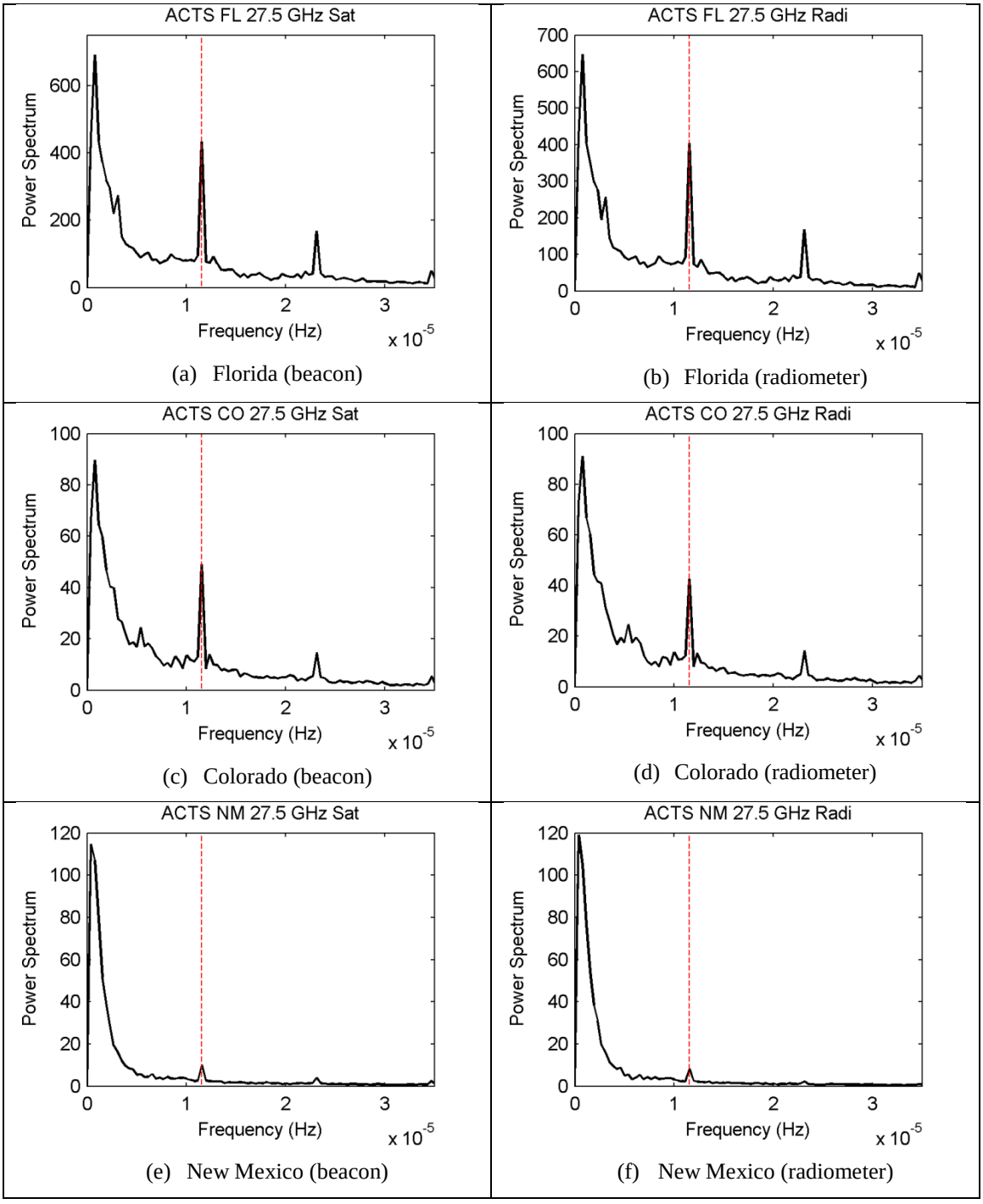

(a) Florida (beacon)

(b) Florida (radiometer)

(c) Colorado (beacon)

(d) Colorado (radiometer)

(e) New Mexico (beacon)

(f) New Mexico (radiometer)

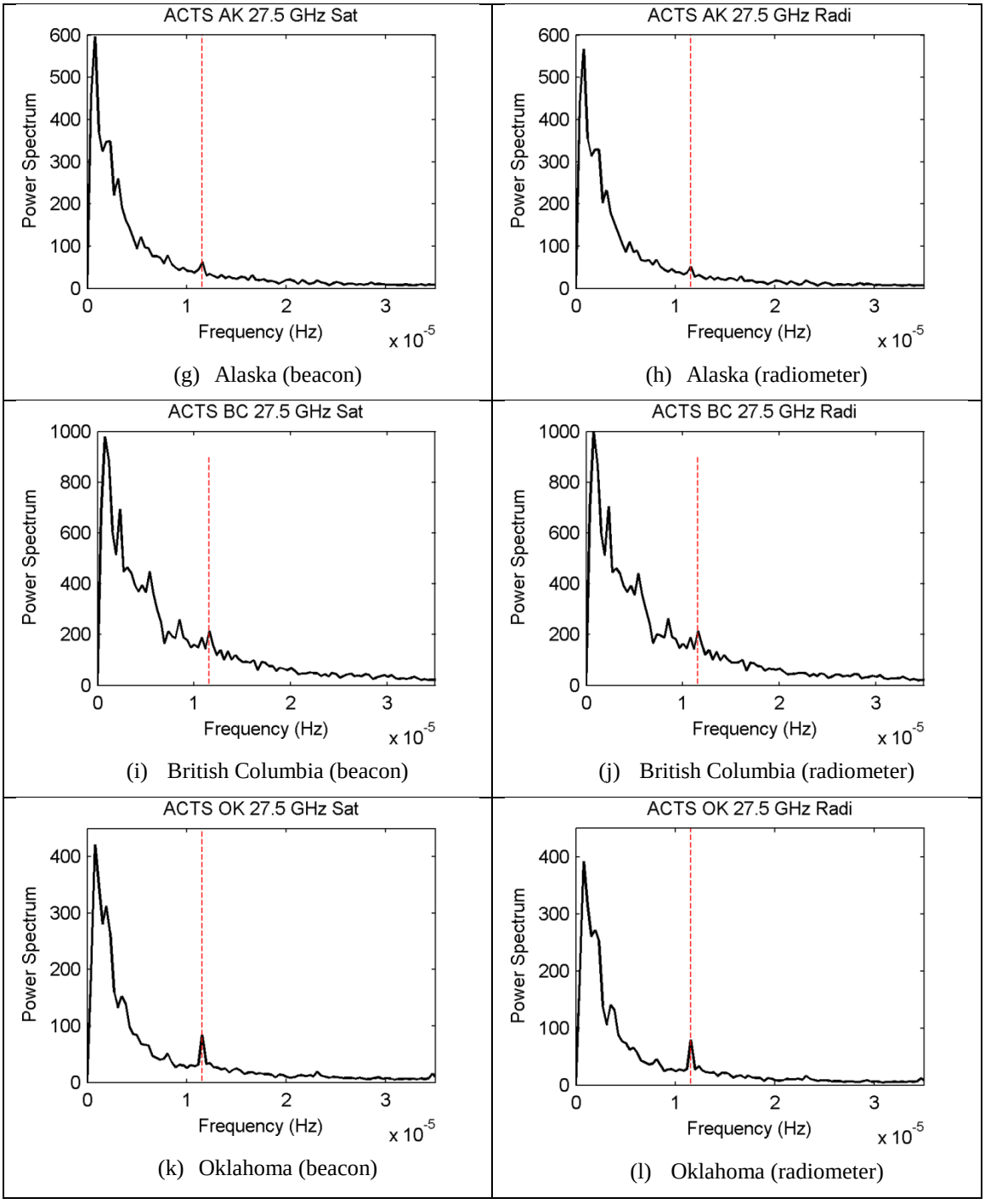

(g) Alaska (beacon)

(h) Alaska (radiometer)

(i) British Columbia (beacon)

(j) British Columbia (radiometer)

(k) Oklahoma (beacon)

(l) Oklahoma (radiometer)

Figure 4.48: Spectrum obtained using Method 2 onto ACTS 27.5 GHz data

4.4.5 Discussion

Table 4.5 gives a summary of the spectrum estimation result of the ACTS 27.5 GHz data using all three methods. The summary applies to both beacon and radiometer data.

Table 4.5: Summary of the spectrum estimation result for the ACTS 27.5 GHz data

Site	**Raw periodogram**	**Method 1**	**Method 2**
Florida	Significant presence of a peak at solar, sidereal and anti-sidereal frequencies. However compared to the 20.2 GHz, the amplitude of the solar peak is much lower than the sidepeaks.	Presence of solar, sidereal and anti-sidereal peaks remains but are not as clearly defined, and seem to be linked together.	Solar frequency component detected
Colorado	A peak at the solar and anti-sidereal frequencies is somewhat present.	Similar to the 20.2 GHz, significant peak at the solar frequency.	Solar frequency component detected
New Mexico	Significant presence of a peak at solar, sidereal and anti-sidereal frequencies. The anti-sidereal is the highest peak, decreasing with solar and then the sidereal. In the 20.2 GHz no solar component was detected.	Solar peak detected, with a possible anti-sidereal peak but no sidereal component. This is similar to the 20.2 GHz frequency data.	Solar frequency component detected
Alaska	Similar to the 20.2 GHz data, no significant solar, anti-sidereal and sidereal peak detected.	No solar, anti-sidereal and sidereal peak detected.	No solar frequency component detected
British Columbia	Similar to its 20.2 GHz, the spectrum contains higher background noise compared to other sites, but a much higher solar peak.	Solar peak detected and is relatively larger than the 20.2 GHz data.	No solar frequency component detected
Oklahoma	Significant solar and anti-sidereal peak detected. This was not detected in 20.2 GHz	Significant solar and anti-sidereal component detected. Compared to the 20.2 GHz, sidereal component less significant.	Solar frequency component detected

The background noise for the 27.5 GHz was found to be higher than its 20.2 GHz counterpart. However, the presence of solar periodicity in the spectrum estimation result of Method 1 and 2 remains consistent between the two frequencies, but with differences in the relative presence of the side-peaks, if any. Harmonics of the solar frequency are relatively more predominant in the 27.5 GHz data.

Evidence of the existence of diurnal variations in the beacon and radiometer attenuation levels were found in all of the ACTS sites for the 20.2 GHz and 27.5 GHz frequencies, except for in Alaska. The site without any significant evidence of diurnal variation of attenuation levels was the coldest and with the lowest elevation angle. Table 4.6 lists the climate information of each site based on the Köppen climate classification, together with their temperature and dew point information shown Figure 4.49, obtained from the National Climatic Data Center [54] and Canadian Climate Normals [55]. A low elevation angle will have a longer path which translate to more path attenuation, and a correspondingly higher incidence of depolarization and tropospheric scintillation. The result from British Columbia is excluded from further discussion due to reports of calibration errors [49].

The characteristics of the solar, sidereal and anti-sidereal components differ in all the sites. There appears to be a general trend of decreasing solar, sidereal and anti-sidereal component as the climate becomes less warm and humid. Both the Colorado and New Mexico sites are almost 1.5km above sea level and far from large tracts of open water. Greely Colorado experiences a very dry, semi-arid climate, with high temperatures (32°C) in summer and low temperatures (4°C) in winter. The diurnal temperature range is

usually rather wide, with a 10-degree (Celsius) difference between daytime high and nighttime low, especially in the spring and fall months. New Mexico also has a mild arid or semiarid, desert climate. It is mainly characterized by light precipitation totals, abundant sunshine, low relative humidity, and a relatively large annual and diurnal temperature range. Fairbanks' climate is usually classified as subarctic, with long, cold winters, and short, warm summers, in which much of the annual precipitation falls. Winter lasts from late September/early October until late April/early May.

Table 4.6: Climate information for the ACTS site

Site	**Elevation Angle (°)**	**Sea level height (m)**	**Climate zone (Köppen)**
Florida	52	50	Cfa: Humid subtropical. Hot and humid during summer, cool and humid during winter
Oklahoma	49.1	420	Cfa: humid subtropical Hot and humid during summer, cool and humid during winter
Colorado	43.1	1900	Bsk: Semi-arid, steppe Extremely dry, wide diurnal temperature, greater precipitation in the steppe than deserts
New Mexico	51.1	1460	Bwk: Mid-latitude Deserts Extremely dry, wide diurnal temperature, highest diurnal temperature ranges of all climates, highest daily maximum temperatures of all climate types.
Alaska	8.1	180	Dfc: subarctic Severe winter, short cool summer
British Columbia	29.3	110	Cfb: Marine west coast Mild summer, mild winter, snow melts quickly, no dry season

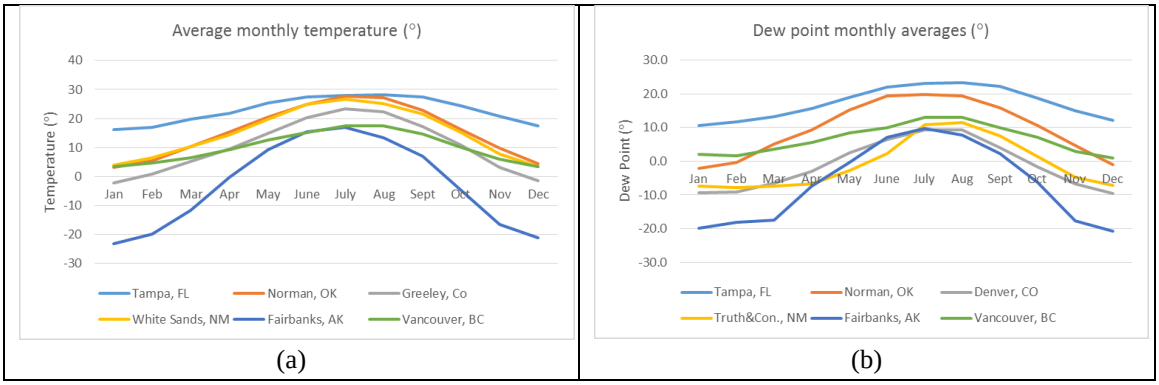

Figure 4.49: Monthly temperature (°C) and dew point (°C) averages for the ACTS sites.

No specific pattern was seen between the spectrum estimation result in 20.2 and 27.5 GHz. However, the existence or nonexistence of the solar component remains consistent between the two frequency data. The strength of a solar component and the solar and sidereal peaks do not seem to increase or decrease concurrently.

The gaseous absorption of the 20.2 GHz frequency is higher than the 27.5 GHz frequency during clear air for all six sites. This is because there is a strong water/water absorption line at 22 GHz, which is closer to the 20.2 GHz beacon frequency than the 27.5 GHz frequency. As soon as it started to rain, the 27.5 GHz absorption was higher than the 20.2 GHz frequency. The cumulative excess attenuation data at 20.2 GHz and 27.5 GHz measured by beacon receivers is shown in Figure 4.50. This agrees with a similar investigation in [56] which found the complementary cumulative distribution statistics of 30 GHz begins to be higher than the 20 GHz at 2% of the time and higher, on a 30 degree slant-path in the UK. It is speculated that the magnitude of the diurnal variation will increase with frequency, as does the attenuation due to atmospheric gasses.

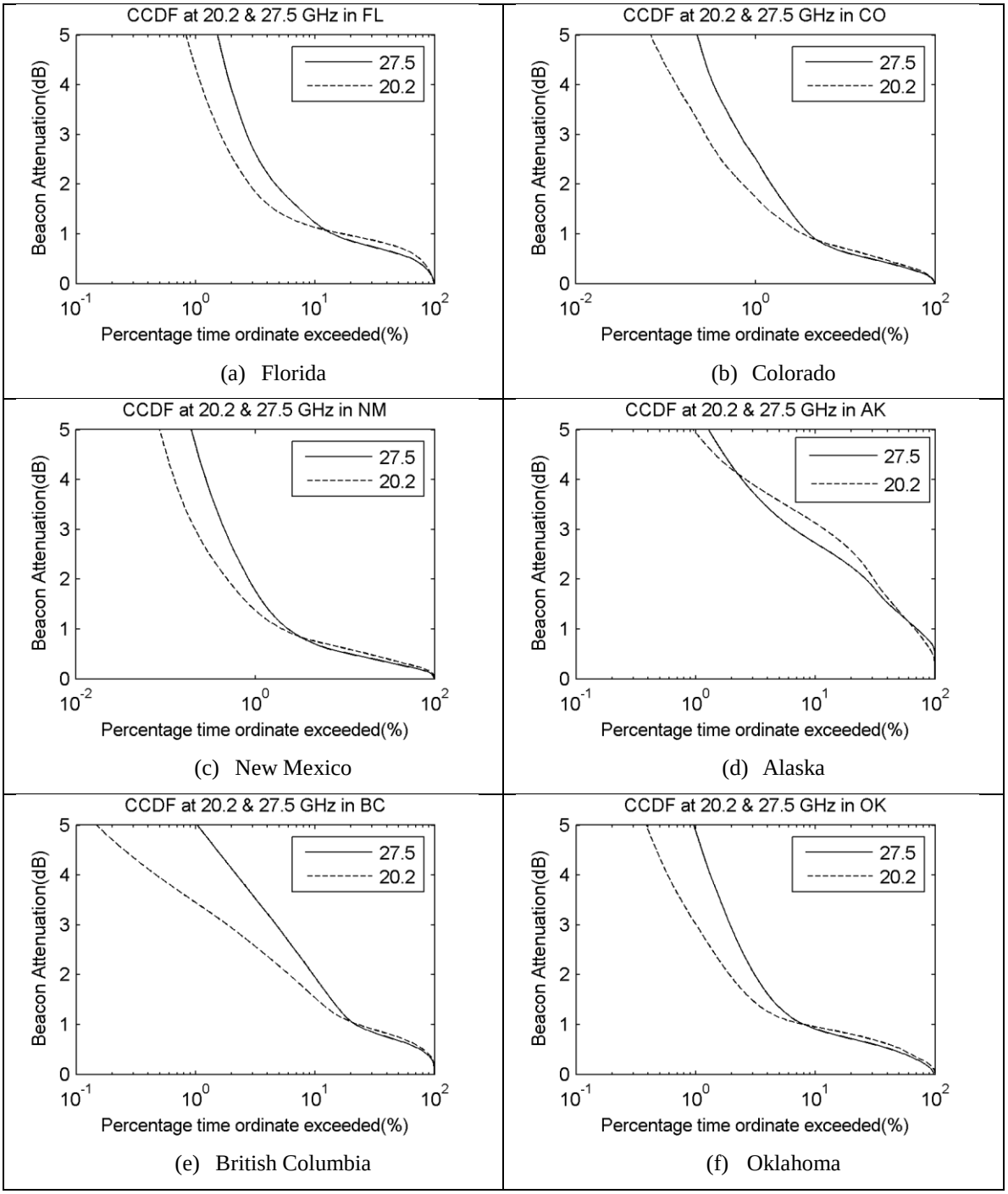

Figure 4.50: Cumulative excess attenuation plot of the ACTS beacon attenuation data

4.5 Texas database

The University of Texas at Austin conducted 8 years of simultaneous 11.2-GHz (Ku-band) beacon and radiometer observations in Austin, Texas, located at 30.39°N latitudes, 97.73°W longitudes, and at an altitude of 185m above mean sea level. The measurements were taken from an 11.198-GHz signal emitted from INTELSAT's type VA geostationary satellite (F-10) at 335.5°E, at an elevation angle of 5.8°. The propagation terminal incorporates a 2.4 m diameter receiving antenna feeding both a beacon receiver and a radiometer, with a tipping bucket rain gauge, and sensors for wind, relative humidity, and pressure close to the antenna. Table 4.7 below summarizes the path characteristic and the data collected. Data is sampled every 10s. The ratio between recorded to total data is very high, almost 100%

Table 4.7: Path characteristics and data statistics for Texas data

Coordinate	30.39°N, 97.73°W
Path elevation	5.8 °
Station height	185m
Frequency	11.2 GHz
Climate	humid subtropical
Period of recorded data	8 years (06/01/1988 – 05/31/96)
Ratio between recorded to total	99.9%

Quantities measured in addition to the beacon signal level and the sky temperature are the rain rate as well as meteorological variables such as ambient temperature, relative

humidity, wind speed, wind direction and barometric pressure. Data is extracted and then converted as outlined in the storage format memorandum [57] as follows:

$$Beacon\ data = \frac{Extracted\ data - 600}{100} \quad (dB) \tag{4.10}$$

$$Radiometer\ data = \frac{Extracted\ data}{10} \quad (K) \tag{4.11}$$

The beacon fade level in dB which is stored in the raw data files has been calculated from the measured detector voltage and is given relative to a 10 volt full scale, and adjusted to be 6 dB below saturation point [58]. As mentioned earlier in Section 3.4, data extracted from this database is the apparent beacon attenuation, prior to the diurnal variation removal.

4.5.1 Time data plot

The extracted beacon signal level (unit dB) and the antenna temperature (K) is then averaged to every one minute resulting in a total of 4,207,680 data points. Figure 4.51(a) and (b) show the graphical plot of the raw beacon and radiometer antenna temperature data respectively. This is after any corrupt data were removed and replaced with interpolated values.

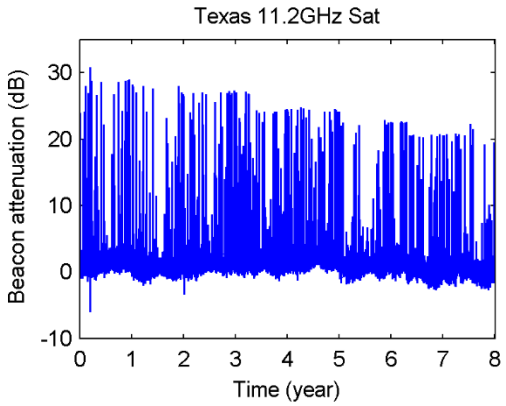

(a) Beacon data

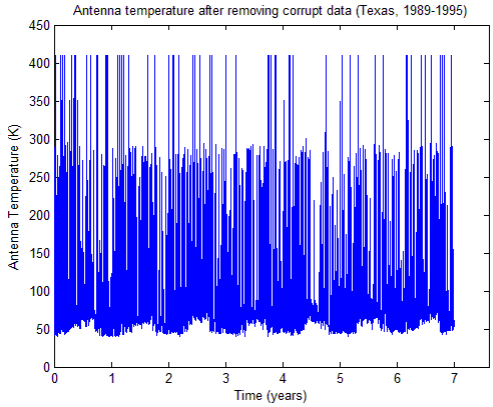

(b) Radiometer data

Figure 4.51: Raw beacon and radiometer data from the Texas database

The antenna temperature, T_{ant} is then converted to inferred attenuation using the following formula [24]: The value of the sky temperature is threshold to 90K to eliminate the rain fades effect as stated in the publication. A 6-minute running average is performed onto the beacon data to remove any scintillation effect.

$$T_{sky} = \left[\frac{T_{ant} - (1-h)T_{gnd}}{h}\right] \tag{4.12}$$

$$A_{gas} = 10log\left[\frac{T_m - T_c}{T_m - T_{sky}}\right] \tag{4.13}$$

Where

A_{gas} = Inferred gaseous attenuation from sky temperature

T_{sky} = Sky temperature

T_{gnd} = Average ground temperature (K) = 294K

T_c = Average cosmic background temperature (K) = 2.7K

T_m = Average medium temperature (K) = 273K

h = Coupling efficiency of the antenna to the sky = 0.98

Figure 4.52 gives the minimum, maximum and mean data set generated for (a) beacon data and (b) radiometrically inferred attenuation, A_{gas}.

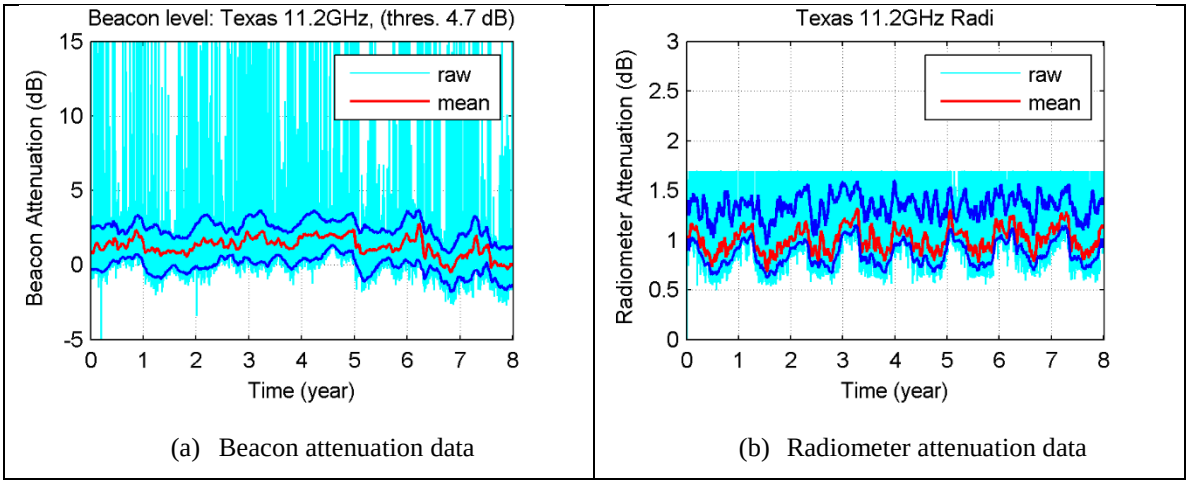

(a) Beacon attenuation data (b) Radiometer attenuation data

Figure 4.52: The max, min and mean line for Texas data

However, the outlier removal process are only applied onto the beacon data. This is because the sky temperature used to generate the radiometrically inferred attenuation,

is already capped to 90K. Figure 4.53 gives the capped data for beacon, and (b) radiometer attenuation data, and Table 4.8 records the threshold values used.

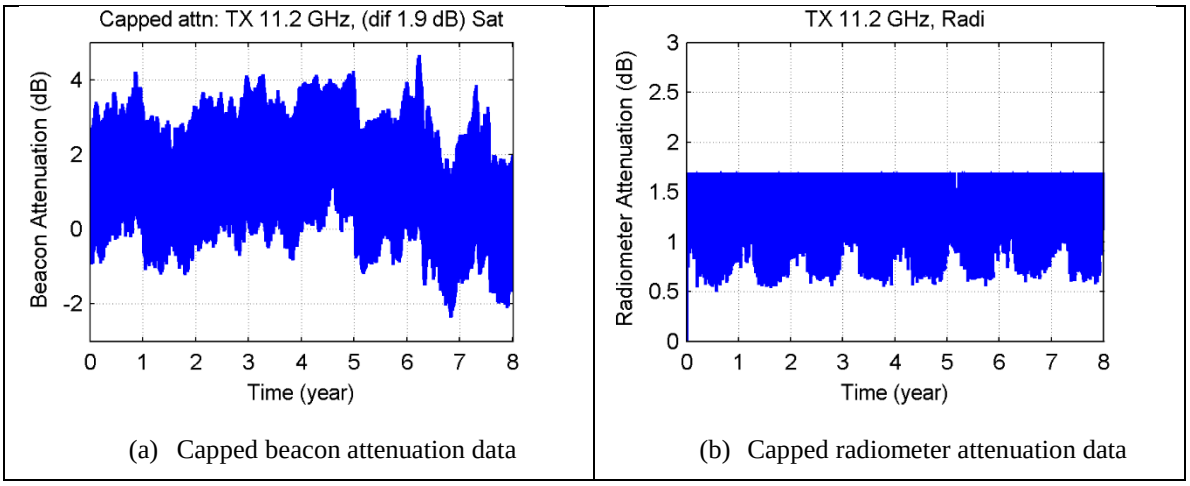

(a) Capped beacon attenuation data

(b) Capped radiometer attenuation data

Figure 4.53: Texas data after outliers removal (capped data)

Table 4.8: Threshold values for removing outliers in Texas

Parameter	Beacon data	Radiometer data
Threshold A	4.7	None
Threshold B	1.9	None

Similar spectral estimation methods were then conducted onto the raw beacon and radiometer attenuation data. The results are depicted in the following order:

i. The raw periodogram using raw data

ii. The spectral estimation result with Method 1 using normalized data.

iii. The spectral estimation result with Method 2 using capped data

4.5.2 Raw periodogram

Figure 4.54 gives the result of the raw periodogram. In subfigure (c) a solar peak is detected in both beacon and radiometer data, together with a relatively small anti-sidereal peak. Low frequency variation dominates the spectrum for the radiometer data, as seen in the plots in (b), which has a clear value of 1 cycle/year.

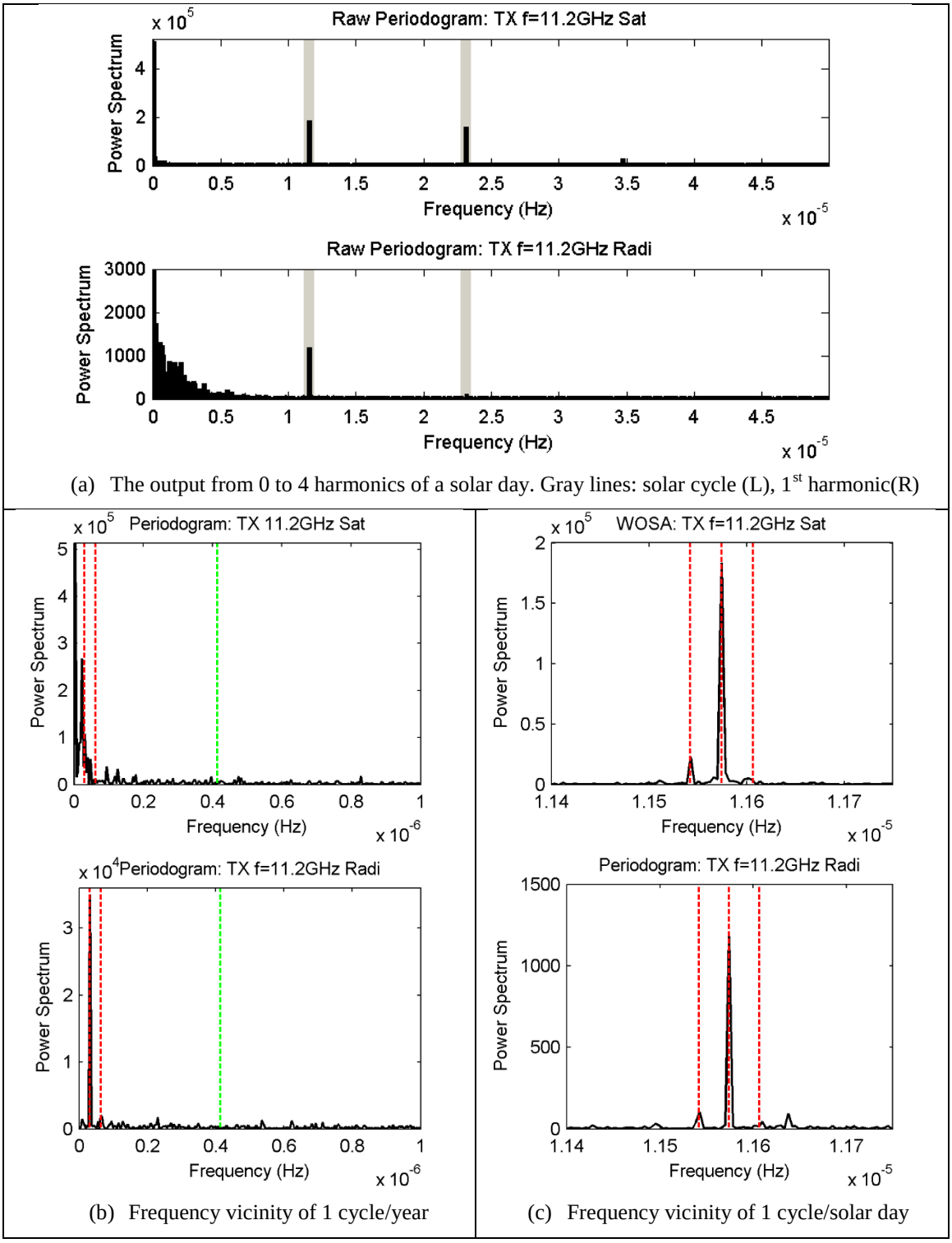

(a) The output from 0 to 4 harmonics of a solar day. Gray lines: solar cycle (L), 1st harmonic(R)

(b) Frequency vicinity of 1 cycle/year

(c) Frequency vicinity of 1 cycle/solar day

Figure 4.54: Raw periodogram Texas

4.5.3 Result with Method 1

Here the 8 years of normalized Texas data was partitioned into 3 year segments, with 50% overlap. This results in 5 segments, with a frequency resolution of $\frac{1/60}{3\times365\times1440} = 1.057 \times 10^{-8}\ Hz$. Figure 4.55 gives the normalized data used as input to Method 1.

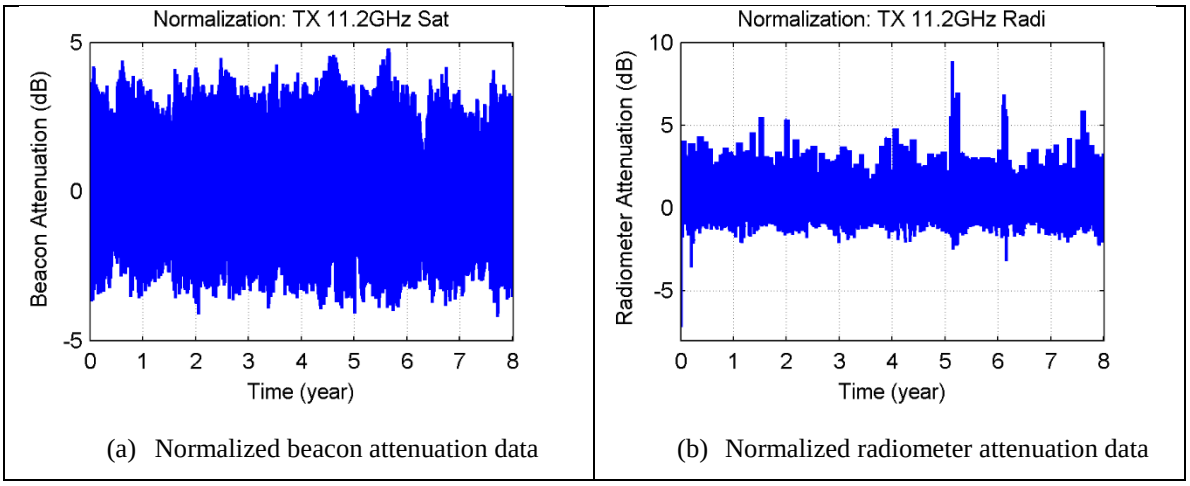

(a) Normalized beacon attenuation data

(b) Normalized radiometer attenuation data

Figure 4.55: Normalized Texas data

The Method 1 result is given in Figure 4.56 with the result for beacon attenuation data placed above the radiometer attenuation data for each section. In subfigure (a) the presence of a solar peak is strongly detected in both beacon and radiometer data. There are also large peaks at the 2nd and 3rd harmonics of the solar frequency, in the beacon data. Both data contain a relatively small anti-sidereal and sidereal side peaks, as depicted in subfigure (c). No significant lunar cycle can be detected in subfigure (b) for both beacon and radiometer result.

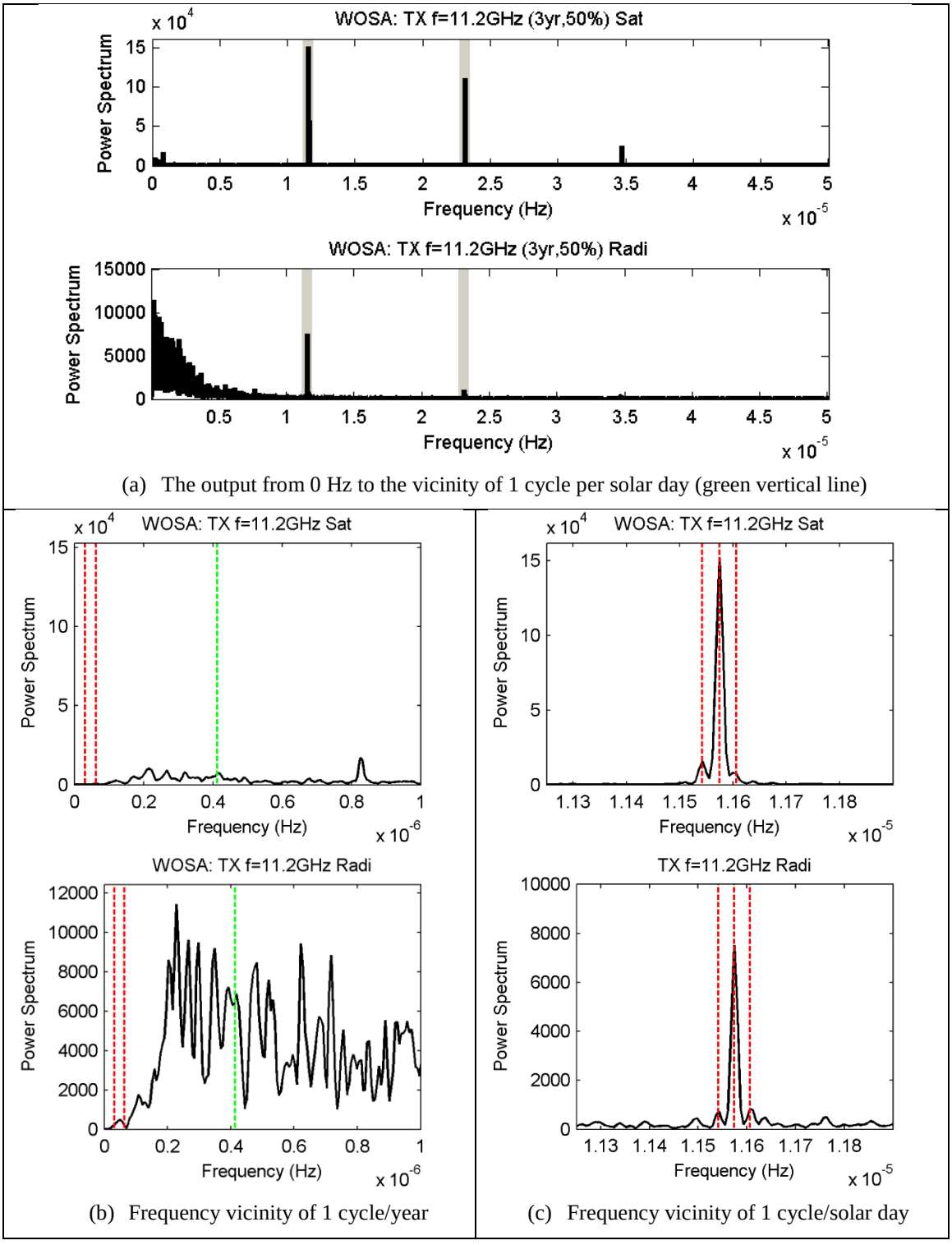

(a) The output from 0 Hz to the vicinity of 1 cycle per solar day (green vertical line)

(b) Frequency vicinity of 1 cycle/year

(c) Frequency vicinity of 1 cycle/solar day

Figure 4.56: Method 1 output for Texas

4.5.4 Result with Method 2

Figure 4.57 gives the result of Method 2 onto the capped (a) beacon and (b) radiometer data. The presence of a solar cycle can be seen in both result.

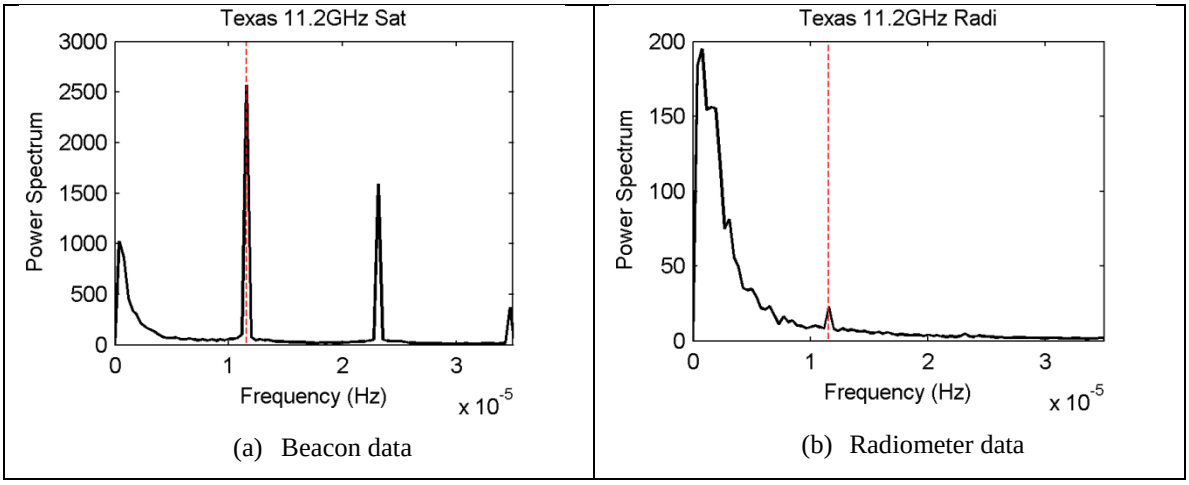

(a) Beacon data (b) Radiometer data

Figure 4.57: Spectrum obtained using Method 2 onto Texas data

The statistical significance test of the solar peak detected here is given in Section 5.2.2.

4.5.5 Discussion

The result in Texas produced a strong solar frequency presence in the spectrum of beacon as well as radiometer data. This proved that the diurnal variation is caused by the atmosphere and not caused by satellite motion as presumed in [24] and [58]. A presence of sidereal and anti-sidereal peak were detected in both, but is more predominant in the beacon data compared to the radiometer. The climate in Austin, Texas is humid subtropical, characterized by hot summers and mild winters.

4.6 Brazil database

Co-located beacon and radiometer propagation measurement data collected in Mosqueiro, Brazil were provided by Dr. Marcio Rodrigues and Dr. Martha Pudwell, former PhD students of Dr. Luiz da Silva Mello of Pontifical Catholic University of Rio de Janeiro, Brazil. Details of the site in Mosqueiro and its data statistics are given in Table 4.9 below. The receiver antenna has a diameter of 3m, and pointed towards INTELSAT 705, located at 50°W.

Table 4.9: Path characteristics and data statistics for Brazil data

Location (Lat. N, Long. W)	-1.11°, 311.57°	
Elevation angle (degree)	89°	
Station height (m)	24m	
Climate	Tropical rainforest	
Frequency	11.45 GHz	
	Beacon data	**Radiometer data**
Period of recorded data	22 months April 96 - Jan 98	31 months April 96 - Oct. 98
Ratio between recorded to total	82.3%	67.4%

Of the said duration of the recorded data, only 67% is available for radiometer and 82% for relative beacon power level. Missing data is either not found or corrupted. To obtain a continuous flow of data, these missing data files were replaced with data obtained from similar dates in other years.

4.6.1 Time data plot

The beacon data is of received power level at the receiver (dBm) and the radiometer data is of sky noise temperature (K). The sampling rate for the beacon and radiometer is 1 second, and 2 seconds respectively. Both were then averaged to one minute.

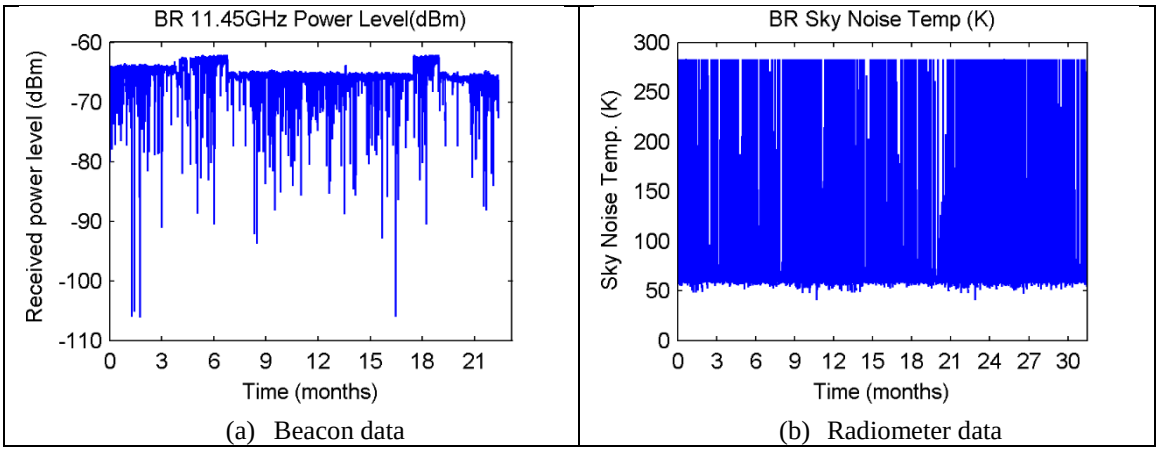

(a) Beacon data (b) Radiometer data

Figure 4.58: Raw beacon and radiometer data from the Brazil database

A jump in the beacon level is detected in the month of September to November 1996. This jump is seen repeated in parts of September to October of 1997 as the original data is not available and was replaced by those from 1996. No reference was found as to what was the cause of these changes.

With reference to the manual provided by the experimenters [59], the sky temperature is limited to a threshold of 283K, to eliminate the hydrometeor effect. It is then converted to inferred attenuation using Equation (4.13), with $T_c = 30K$ and $T_m = 285K$.

4.6.2 Raw periodogram

The raw periodogram output is given in Figure 4.59. For both beacon and radiometer data, a peak of 1 cycle/year is detected in subfigure (b), while a peak at 1 cycle/solar day is detected in subfigure (c). However, as higher resolution is not attainable, the presence of similar sidereal and anti-sidereal peaks are not verifiable.

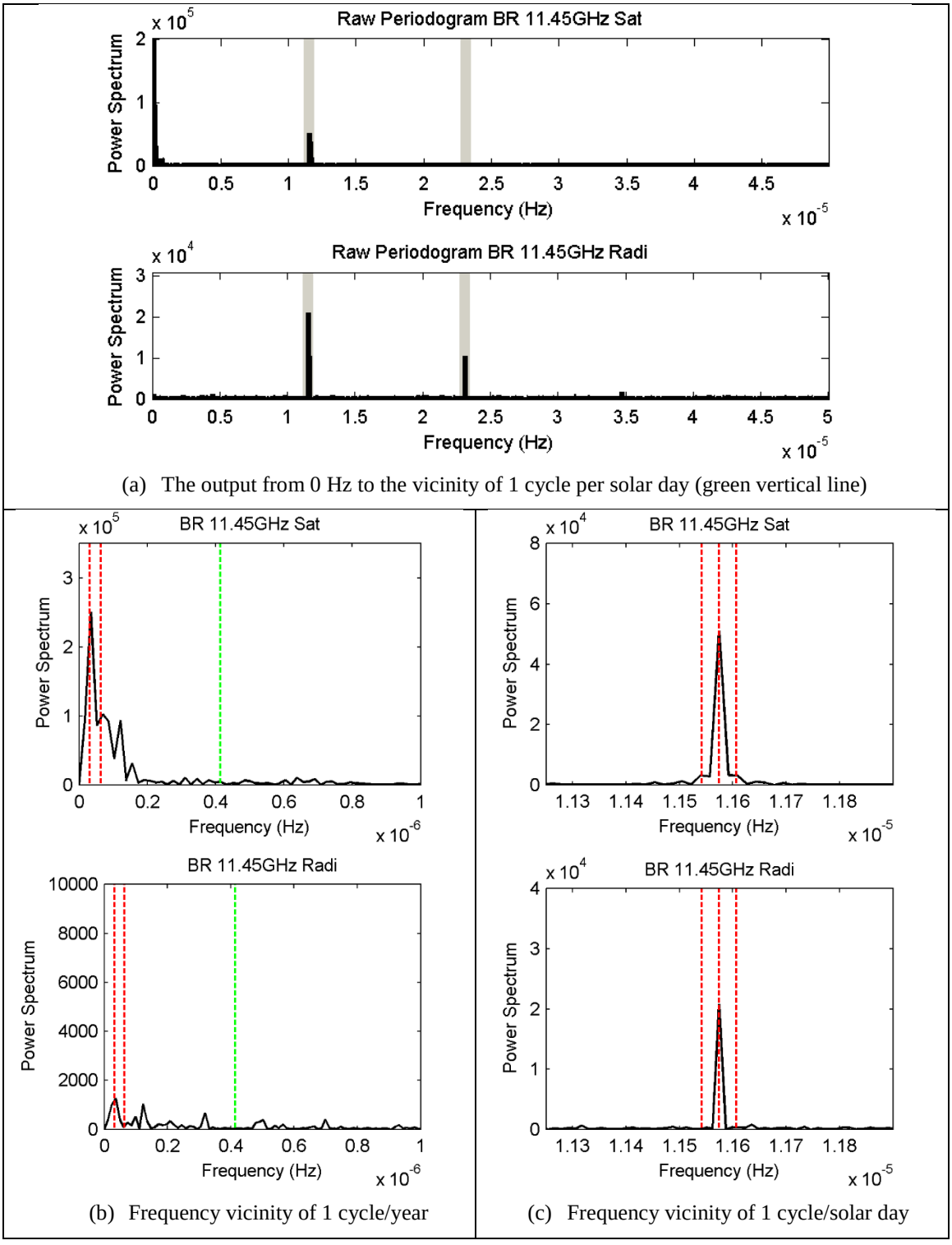

(a) The output from 0 Hz to the vicinity of 1 cycle per solar day (green vertical line)

(b) Frequency vicinity of 1 cycle/year

(c) Frequency vicinity of 1 cycle/solar day

Figure 4.59: Raw periodogram output for Brazil

4.6.3 Result with Method 2

Implementation of Method 1 was not possible due to the data set being limited to less than 2 years. The results for Method 2 is given in Figure 4.60, using raw data as input, instead of the capped data, as in the analysis of previous databases. Due to the 'jump' seen in the time series data, the procedure to remove any possible outliers prior is left out.

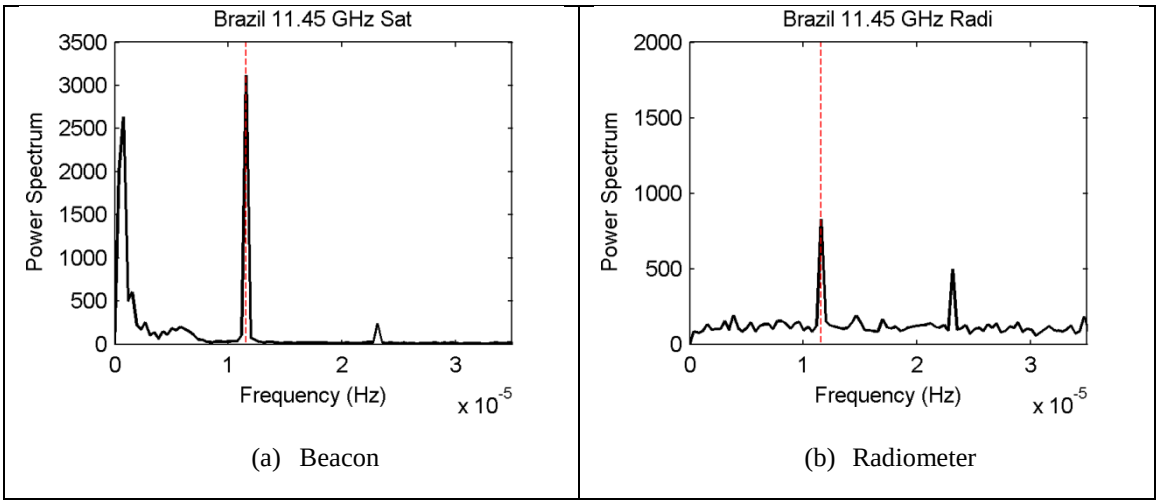

(a) Beacon (b) Radiometer

Figure 4.60: Spectrum obtained using Method 2 onto Brazil data

4.6.4 Discussion

The climate in Mosqueiro, Brazil is characterized as tropical rainforest. The experimental site receives significant rainfall throughout the year. Spectral estimation result reveal a solar day periodicity in the beacon as well as radiometer data variations.

However, due to significant discontinuities in the beacon time series plot and with only 68% of the original radiometer data available, further analyses with the Brazil database were not carried out.

4.7 Olympus database

Virginia Polytechnic Institute and State University (Virginia Tech) designed, constructed and performed a comprehensive set of propagation measurements using the Olympus satellite beacons at 12.5, 20 and 30 GHz. There were separate receiving terminals for each frequency, and each terminal contained a total-power radiometer, used to set the clear air reference level for each beacon and also to predict path attenuation. The Olympus satellite was launched on 12th of July 1989. However, it suffered a solar panel failure, had an unscheduled foray around the world, and once re-stabilized in its original orbital location in August 1991, the N-S stationkeeping had to be abandoned due to fuel shortage. Olympus was subsequently used in an inclined orbit from 1992-1993. Table 4.10 gives a summary of the path length characteristic. The satellite used a 3-axis stabilization and had an orbital position of 18.8°W. Although the ratio between recorded to total data is very high, it consist of portions of data extracted in 1991 and 1992 to form a complete year.

Table 4.10: Olympus path characteristic and data statistic

Earth receiver location	37.2°N, 80.42°W	
Path elevation/azimuth	14° / 105°	
Station height	634m	
Period of recorded data	12 months (Jan-May'91, June-Aug.'92, Sept.-Dec.'91)	
Ratio between recorded to total	**Beacon data**	**Radiometer data**
f = 12.5 GHz (referred as 12 GHz)	82.8%	95.6%
f = 19.77 GHz (referred as 20 GHz)	90.9%	97.9%
f = 29.66 GHz (referred as 30 GHz)	90.5%	94.9%

4.7.1 Time data plot

Figure 4.61 gives raw beacon and sky temperature data extracted from the *E-file* folders of the Olympus data CD. Data stored in the *E-files* has been corrected for discontinuities and bad data, but prior to any diurnal variation correction due to satellite proper motion. The beacon data is of relative signal power (dB) and the radiometer is of sky temperature (K). Based on the database manuals [60], the data is extracted as follows:

$$Beacon\ data = \frac{Extracted\ data - 7200}{100} \quad (dB) \tag{4.14}$$

$$Sky\ temperature = \frac{Extracted\ data}{10} \quad (K) \tag{4.15}$$

The sampling rate for the beacon and radiometer data is 0.1 second, and 1 second respectively. Both were then averaged to one minute. A very distinct change in the beacon and radiometer data level can be detected during the month of June, where the collection year skipped from 1991 to 1992. Control of the Olympus spacecraft was lost on May 29, 1991 and was regained 76 days later.

The sky temperature is then converted to radiometric attenuation using Equation (4.13), with $T_m = 275K$ and $T_c = 2\,K$. The hydrometeor effect is removed from the radiometric attenuation by only considering T_{sky} below a certain threshold. This threshold is set to 60K at 12 GHz and 110K at both 20 GHz and 30 GHz [61].

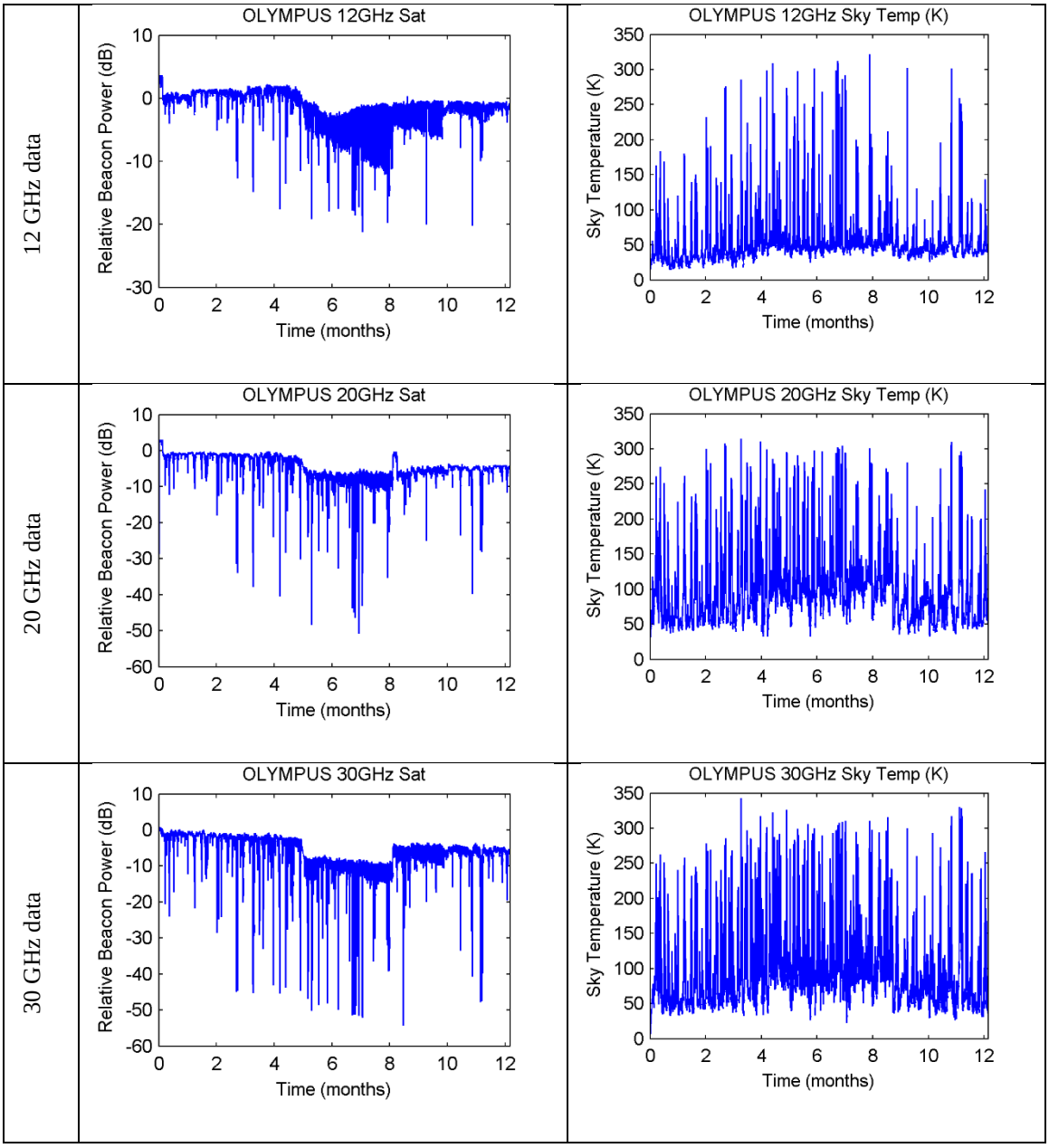

Figure 4.61: Raw beacon and sky temperature data from Olympus

4.7.2 Raw periodogram

Similar spectral estimation methods for Brazil data were conducted onto Olympus. Prior to that, a 6-minute running average was performed onto the beacon data to remove any scintillation effect [61]. The periodogram output for 12, 20 and 30 GHz are given in Figure 4.62, Figure 4.63 and Figure 4.64, respectively.

The presence of a solar day periodicity in the radiometer section is not detected in their respective beacon counterpart. The varied position of the peak detected in the top portion of subfigure (c) may definitely be the effect of eliminating the satellite's N-S stationkeeping, which causes the satellite to wobble in its position (nutation).

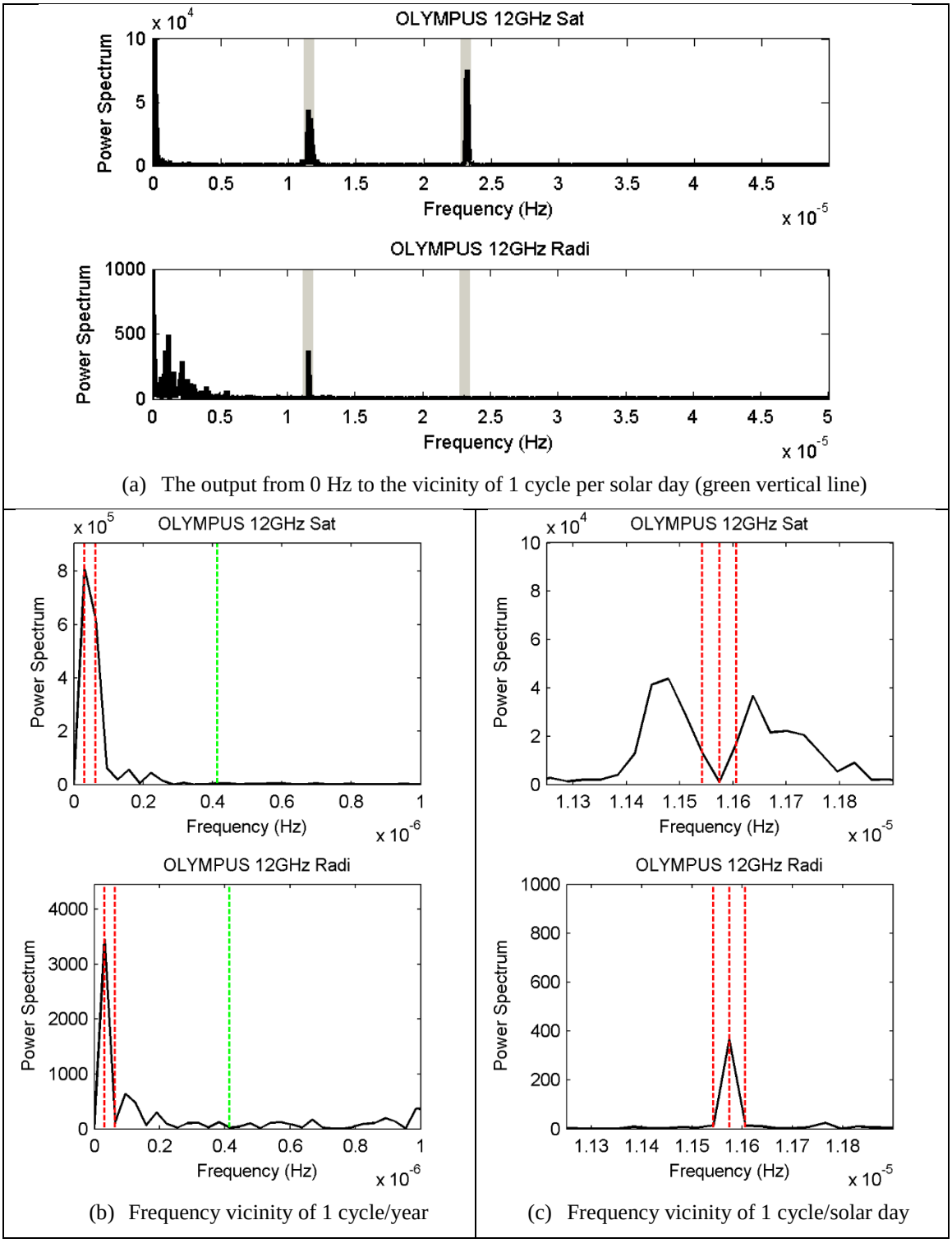

(a) The output from 0 Hz to the vicinity of 1 cycle per solar day (green vertical line)

(b) Frequency vicinity of 1 cycle/year

(c) Frequency vicinity of 1 cycle/solar day

Figure 4.62: Raw periodogram for 12 GHz Olympus.

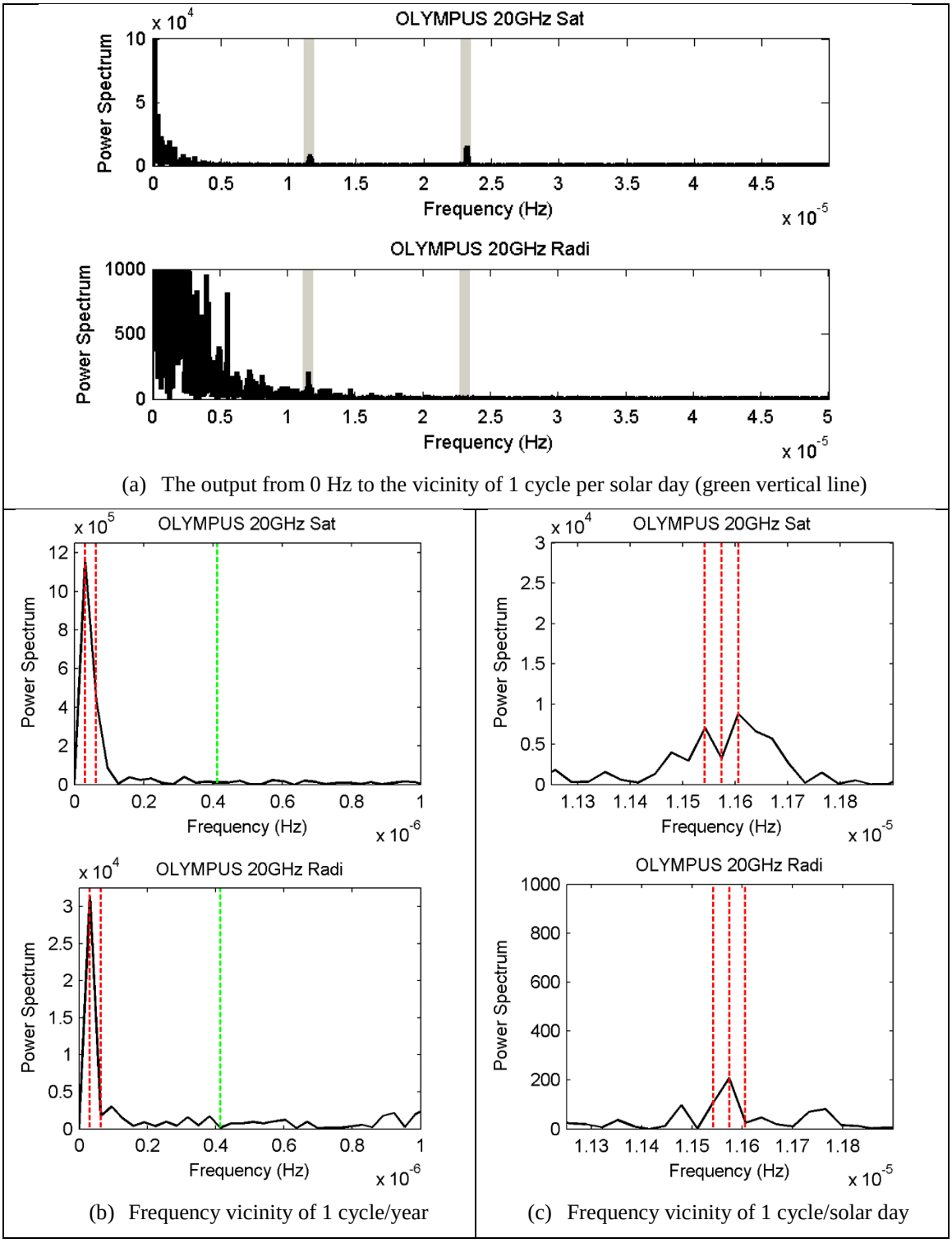

(a) The output from 0 Hz to the vicinity of 1 cycle per solar day (green vertical line)

(b) Frequency vicinity of 1 cycle/year

(c) Frequency vicinity of 1 cycle/solar day

Figure 4.63: Raw periodogram for 20 GHz Olympus.

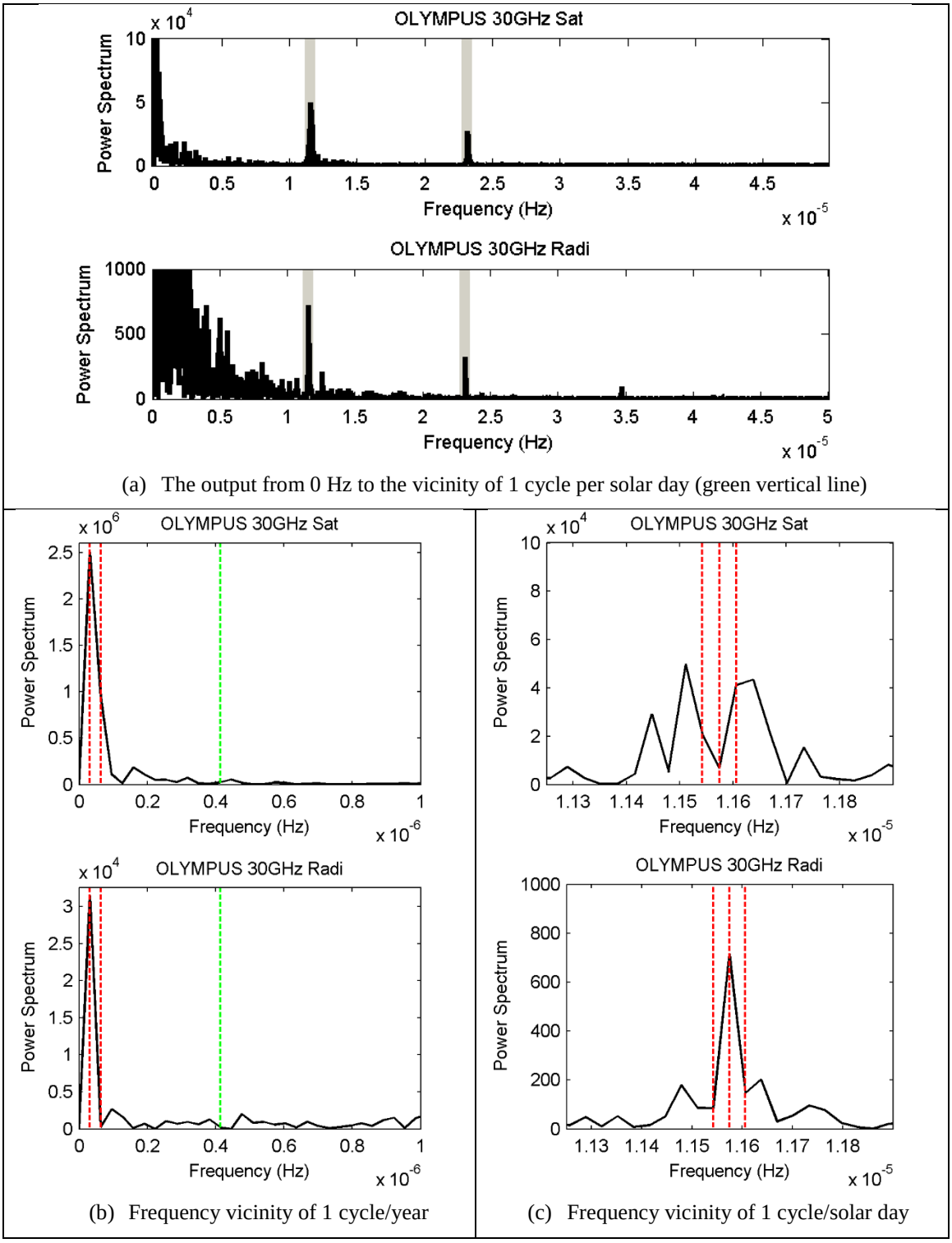

(a) The output from 0 Hz to the vicinity of 1 cycle per solar day (green vertical line)

(b) Frequency vicinity of 1 cycle/year

(c) Frequency vicinity of 1 cycle/solar day

Figure 4.64: Raw periodogram in 30 GHz Olympus

4.7.3 Result with Method 2

Result of Method 2 using the 12, 20 and 30 GHz Olympus data are given in Figure 4.65 for both beacon and radiometer data.

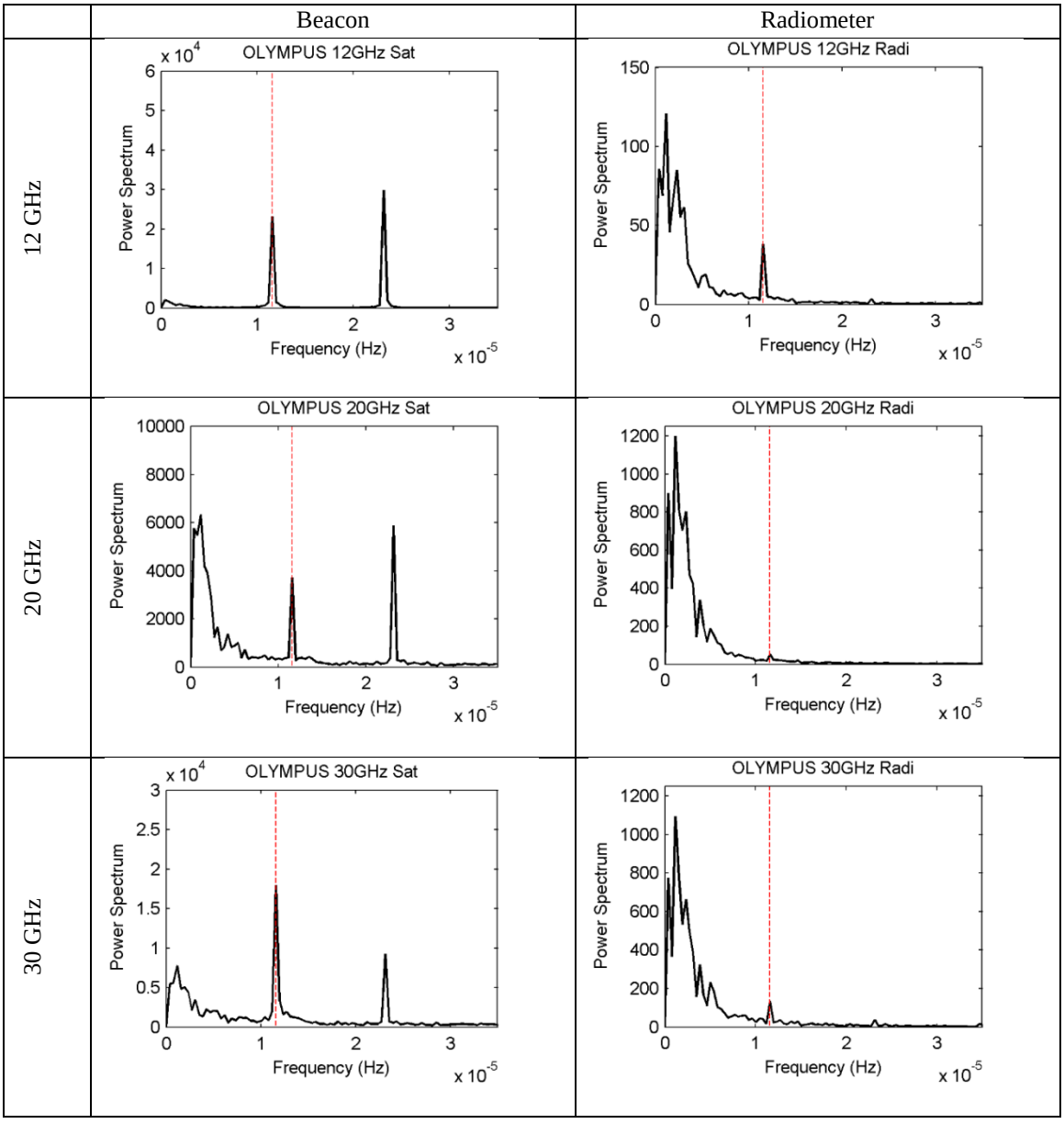

Figure 4.65: WOSA (30 days) output for Olympus

4.7.4 Discussion

The Olympus data was collected from terminals located in Blacksburg Virginia. Due to its elevation above sea level, the climate is humid continental, with warm and humid summers and cool winters. The Olympus data length is limited to a year, thus no seasonal variation pattern can be detected in the beacon or radiometer data, nor is the resolution high enough to discern between a sidereal and anti-sidereal peak, if any existed.

From the periodogram output in Figure 4.62 to Figure 4.64, the radiometer contained a consistent peak at a solar day in the 12, 20 and 30 GHz frequency. The spectrum analysis on the beacon data however contains several strong peak at the vicinity, but none exactly at a solar day frequency. The inexistence of similar peaks at their respective radiometer's frequency spectrum indicates that the cause of the variation seen in the beacon data is not an atmospheric effect, but caused by the unstable Olympus satellite. This effect coincide with reports of an unstable Olympus satellite. A satellite without any N-S stationkeeping will wobble in its position. This causes the earth station receiver to be in contact with different section of the main beam at different times, producing variations in the strength of the signal detected. It was reported that the Olympus data collection was terminated in August of 1992 due to the failure of the 30 GHz beacon system and the daily variations of several dB in the signals detected, due to its large inclination angle. It is not certain why the position of the peaks differs in the 12, 20 and 30 GHz. However the fact that the 30 GHz beacon system had suddenly fail in

August of 1992 could indicate that the 30 GHz beacon was experiencing problems that are not affecting the other two beacon frequencies.

Due to the short period of data collection of 1 year, and the problem caused by the unstable satellite, further analysis with the Olympus database were not completed.

CHAPTER 5: STATISTICAL ANALYSIS

In the mixed spectra obtained, there is a need to distinguish spectral peaks related to the erratic fluctuations of the spectral background, from peaks due to significant regular cyclicity. In this chapter, the significance of solar frequency peak detected in the spectrum obtained using Method 2 is tested. The spectrum generated from Method 2 is selected as this method incorporated the highest number of averaging, and the detected solar cycle peak in its resulting spectrum is relatively smaller compared to those obtained using Method 1. The greater the number of averaging, the less the spectral estimates are spread erratically around the spectral background.

The spectral background is set as the null continuum. Testing significance of a peak can generally be classified via the following two approaches [46].

In the first approach, the confidence level of the spectrum background is estimated. A peak is significant if it is above a predetermined confidence level. A variety of methods have been proposed in the estimation of the spectral background. For example using a quadratic fit to the spectrum plot of log power versus frequency, increasing the number of smoothing/averaging so that lesser peaks or troughs appear in the background, or fitting a suitable noise model to the data, for example [52] proposes an autoregressive model as the noise model that can be generated using the lag-1 autocorrelation obtained from a particular type of time series data that is influenced by the climate.

In the second approach, the confidence interval of the spectral peak of interest is estimated. If the range of uncertainty of a particular spectral peak value does not overlap with the continuum spectrum, that peak can be considered to be statistically distinguishable from the background. In this approach the spectral background is not identified.

Another related method is to test the significances of the cycles in the spectrum by comparing them to randomly derived cycles using the resampling approach. This method, used in [62], iteratively and randomly resample (permute) the time series using the Rohde and Muller's Markov chain Monte Carlo methods [63] (MCMC), before applying Fourier decomposition to produce the null continuum. This eliminates any possibility of the peak occurring by chance or a result of an artifact.

In this exercise, the second approach was adapted. The steps used in the significant test are as follows. The confidence interval of the solar peak is estimated using bootstrap, and the vicinity of the solar peak (referred as $f_{solar} \pm \Delta$) is used as an estimate of the spectral background. The solar peak is deemed significant if its lower confidence level do not include the amplitude level detected at $f_{solar} \pm \Delta$.

5.1 Generating confidence interval using the bootstrap method

For a spectra generated by the Fourier transform, the confidence interval (CI) of the spectrum can be estimated using a χ^2 (chi-squared) distribution [64]. However this technically only applies to uncorrelated data that has a standard normal distribution, and the determination of the degrees of freedom depends on the type of spectral estimation method, the type of tapering used and the degree of zero-padding [65].

Bootstrap resampling is an approach to construct error bars and CIs, without any prior knowledge of the distribution of the parameter. The idea is to draw random resamples from the data and calculate error bars and CIs from repeated estimations on the resamples. Here the original bootstrap [66], of resampling individual observation, is modified to resample blocks of 30 days data.

In Method 2 (Section 4.2.2), the time series data was divided into N_b blocks of nonoverlaping sequences of 30 days. The periodogram of each block is generated, and the average of N_b periodogram is the final estimated power spectrum. To generate the confidence interval of the estimated power spectrum using the bootstrap method, N_b blocks are randomly resampled, but with replacement. Thus of the N_b blocks resampled, some blocks may appear more than once, and some not selected. A set of randomly selected N_b blocks is a *resample*. The *estimator*, which is the average periodogram, is applied to each resample and stored. A simple example is given in Figure 5.1. The resample is repeated 1999 times (a total 2000 parameter estimation, together with the original), following the recommendation of Efron and Tibshirani [67]. Figure 5.2 gives

the diagram of the bootstrap principle used for constructing confidence interval, with B=1999.

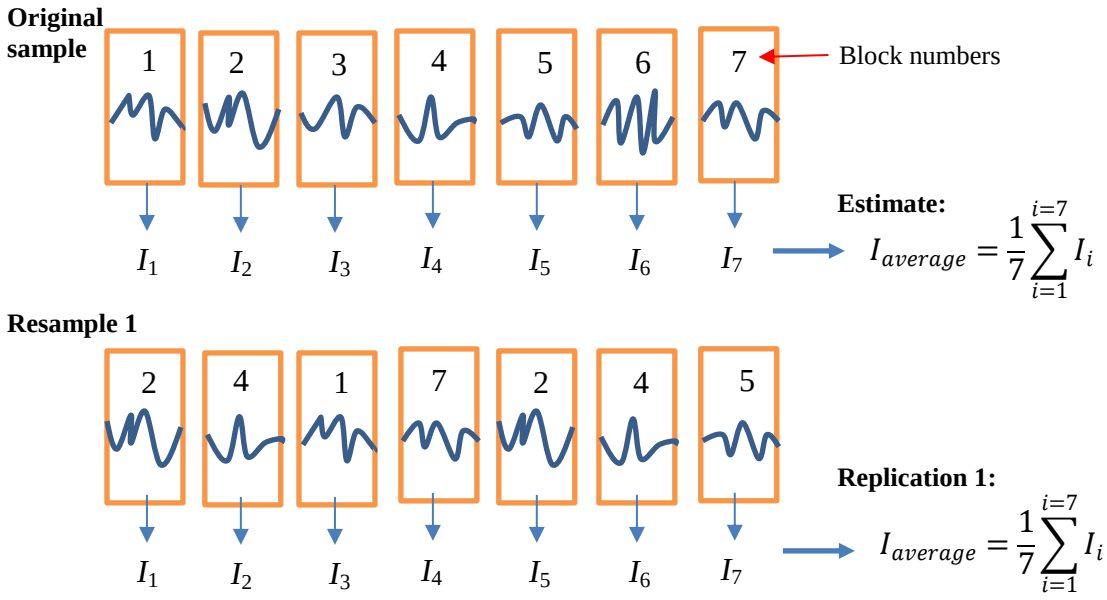

Figure 5.1: Random resampling of block data with replacement

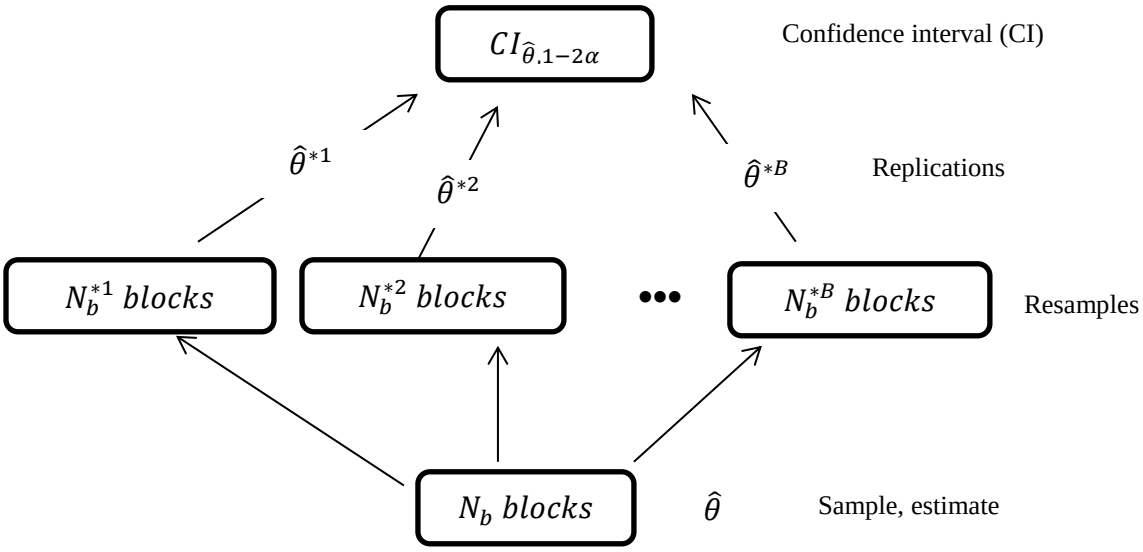

Figure 5.2: The block bootstrap method to generate confidence interval

5.2 Statistical significant of the solar peak

The hypothesis test for the statistical significant of the solar peak is a one tailed test, designed as follows:

Null hypothesis, H_0:

The peaks at f_{solar} are not significantly larger than the peaks at $f_{solar+\Delta}$ and $f_{solar-\Delta}$.

Alternative hypothesis, H_1:

The peaks at f_{solar} are significantly larger than the peaks at $f_{solar+\Delta}$ and $f_{solar-\Delta}$.

The test statistic is the average periodogram peak obtained at f_{solar} from Method 2. The separation, Δ, is selected to be one frequency bin away from f_{solar}, which is equal to the resolution (Eq. (4.4)). Thus $\Delta = \frac{1/60}{30\times1440} = 3.858 \times 10^{-7}$. The null hypothesis is rejected if the lower confidence level does include the amplitude level detected at $f_{solar} \pm \Delta$.

The p-value is the probability of obtaining a more extreme value that what was observed, under the null distribution. Thus, $p - value = Prob(peak \geq A_{slr}|H_0)$, with A_{slr} the power spectrum amplitude detected at f_{solar}. The significance level is set to α = 0.05.

5.2.1 ACTS 20.2 GHz and 27.5 GHz data

Figure 5.3 to Figure 5.8 below gives the result for all 6 sites. In each site, the 20.2 GHz and 27.5 GHz beacon attenuation data results are presented in subfigure (a) and (b) respectively. In each subfigure (a) or (b), the top refers to the spectrum at the vicinity of f_{solar} and its' 90% confidence interval, generated using the bootstrap method in Section 5.1. The three red circle marks the position for the power spectrum amplitude detected at $f_{solar-\Delta}$, f_{solar} and $f_{solar+\Delta}$. The bottom figures are three histograms for the power spectrum amplitude, obtained at the frequency of $f_{solar-\Delta}$, f_{solar} and $f_{solar+\Delta}$. The result for the radiometer data is almost similar to its beacon counterpart, and thus not shown for brevity.

For the result in Florida, Colorado, New Mexico and Oklahoma, H_0 is rejected at the significant level of 0.05%, all with extremely small p-value of less than 0.001. A very small p-values shows that it would be very rare for the peak to occur under the null distribution. As inference, the solar peak detected in both beacon and radiometer data of both 20.2 GHz and 27.5 GHz frequencies in these 4 sites are significant, and not similar to random fluctuation of the background spectrum.

The result of the hypothesis test also failed to reject the null hypothesis for the result in British Columbia and Alaska, at the significant level of 0.05%. Thus no solar periodicity was detected in these two sites, for both beacon and radiometer data in the 20.2 GHz, as well as 27.5 GHz frequencies.

This implies that the diurnal variation seen in the beacon and radiometer data collected from the sites in Florida, Colorado, New Mexico and Oklahoma, exhibits a

strong periodic behavior with a frequency of a solar day. This however is not detected in the data from the site in Alaska and British Columbia.

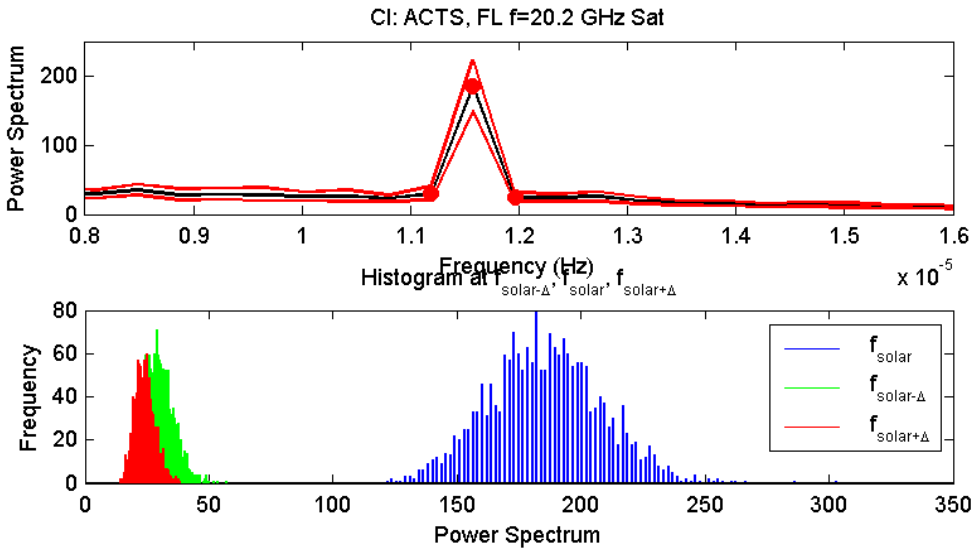

(a) 20.2GHz Beacon data: Reject H_0 at the significance level of $\alpha = 0.05$, with p-value<0.001

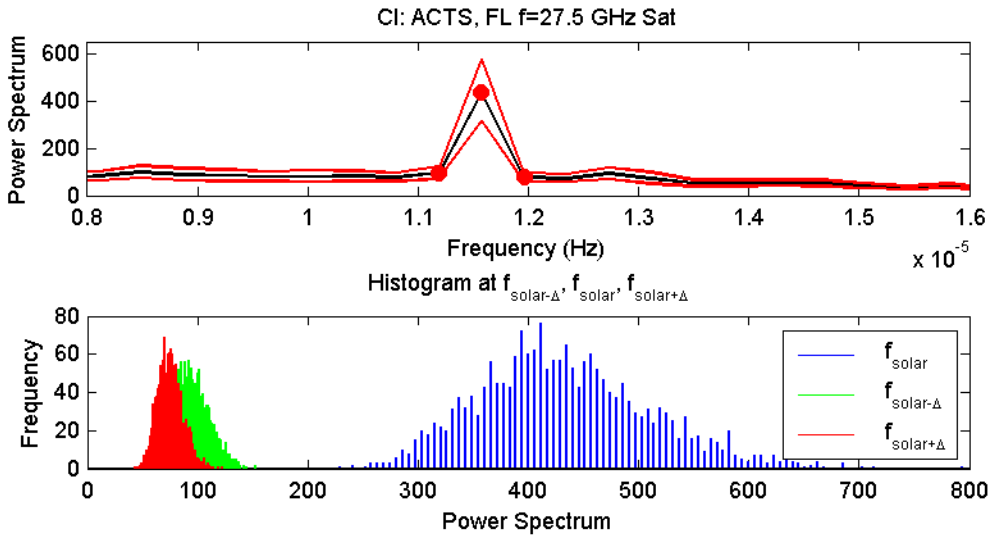

(b) 27.5GHz Beacon data: Reject H_0 at the significance level of $\alpha = 0.05$, with p-value<0.001

Figure 5.3: Significance test for the solar peak detected in Florida

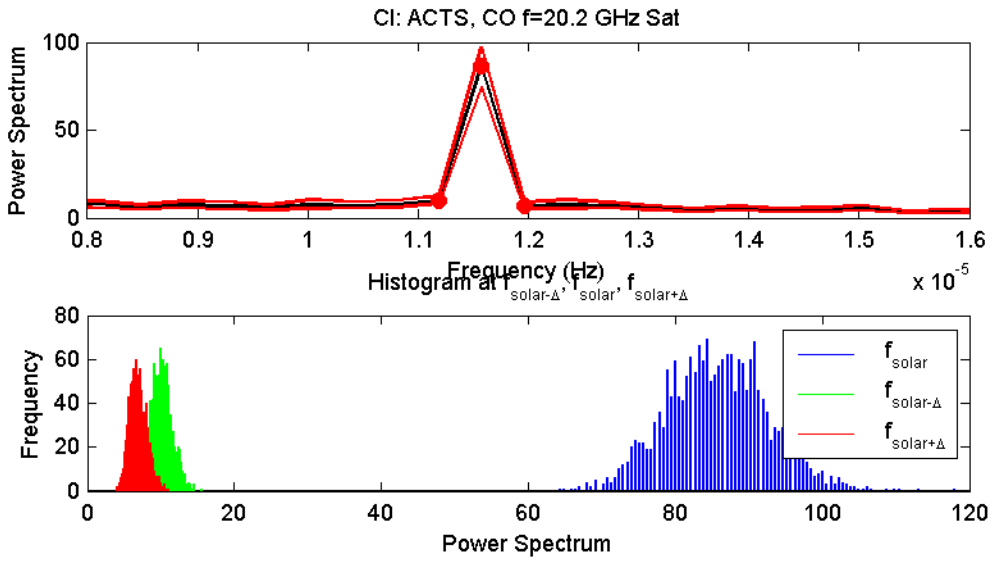

(a) 20.2 GHz Beacon data: Reject H_0 at the significance level of $\alpha = 0.05$, with p-value<0.001

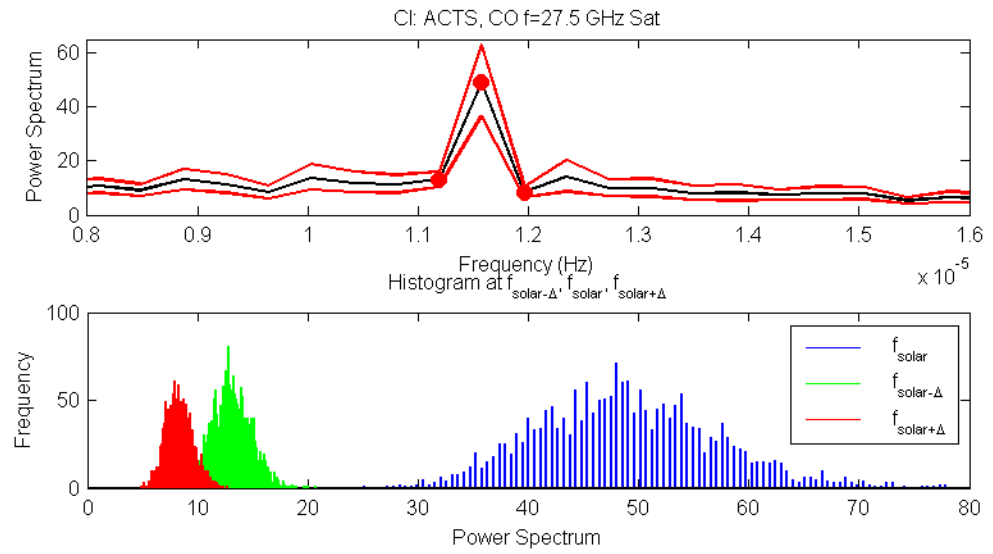

(b) 27.5GHz Beacon data: Reject H_0 at the significance level of $\alpha = 0.05$, with p-value<0.001

Figure 5.4: Significance test for the solar peak detected in Colorado

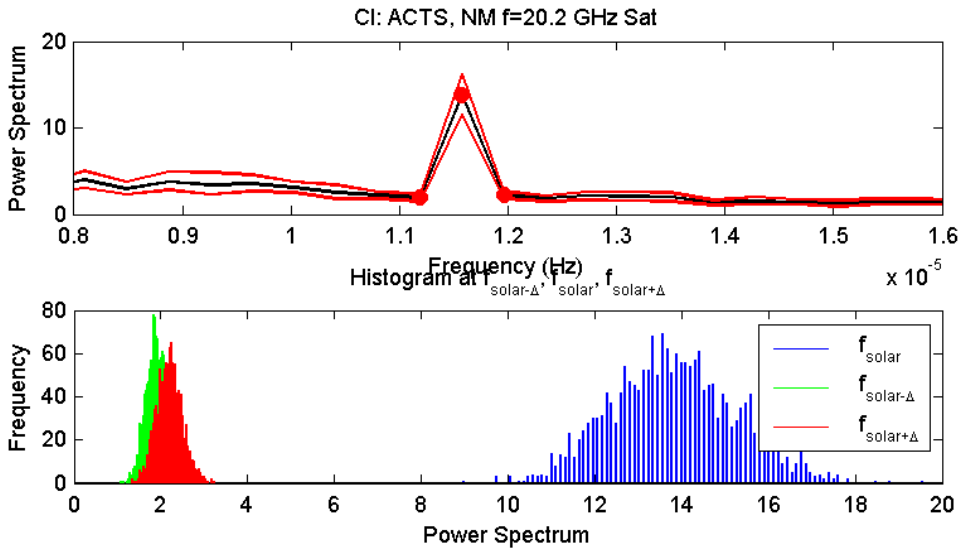

(a) 20.2 GHz beacon data: Reject H_0 at the significance level of $\alpha = 0.05$, with p-value<0.001

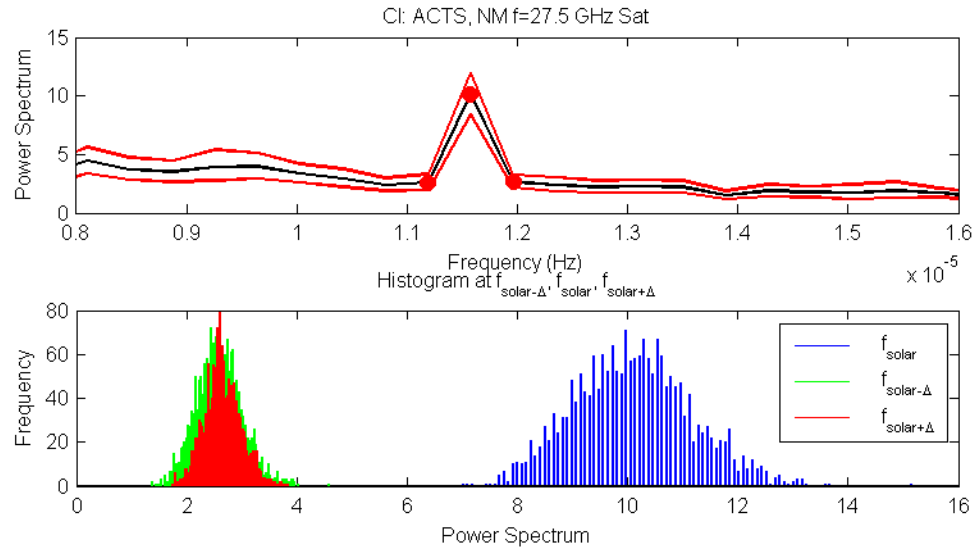

(b) 27.5GHz beacon data: Reject H_0 at the significance level of $\alpha = 0.05$, with p-value<0.001

Figure 5.5: Significance test for the solar peak detected in New Mexico

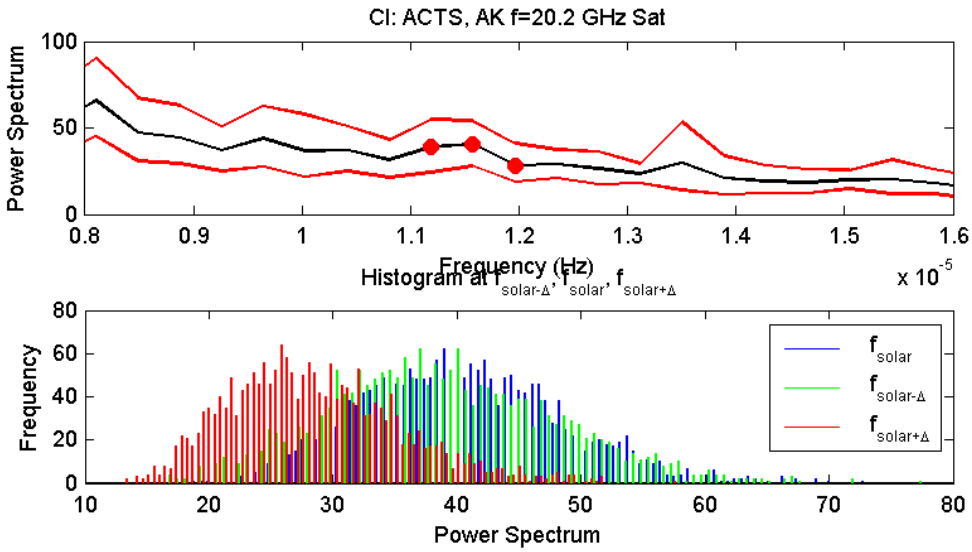

(a) 20.2 GHz beacon data: Fail to reject H_0 at the significance level of $\alpha = 0.05$.

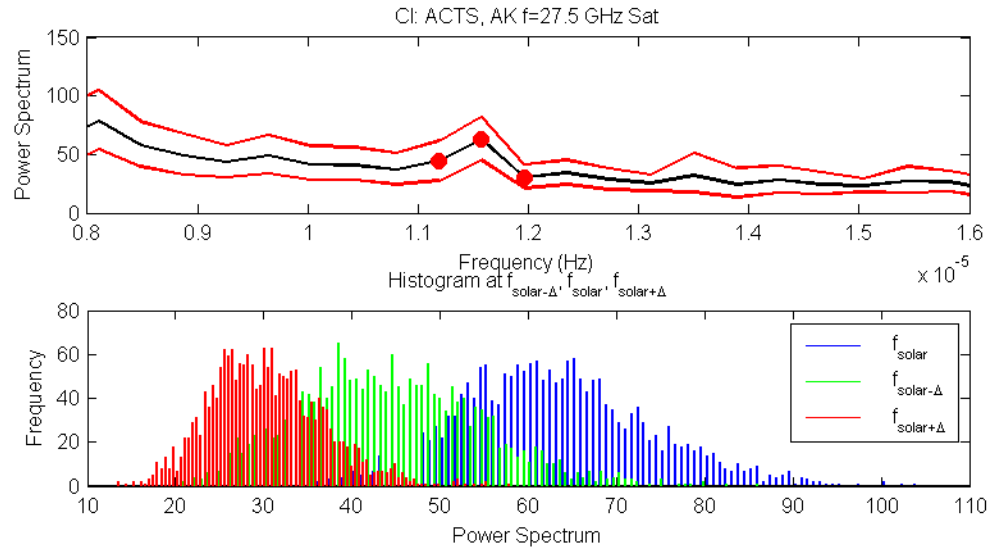

(b) 27.5GHz beacon data: Fail to reject H_0 at the significance level of $\alpha = 0.05$.

Figure 5.6: Significance test for the solar peak detected in Alaska

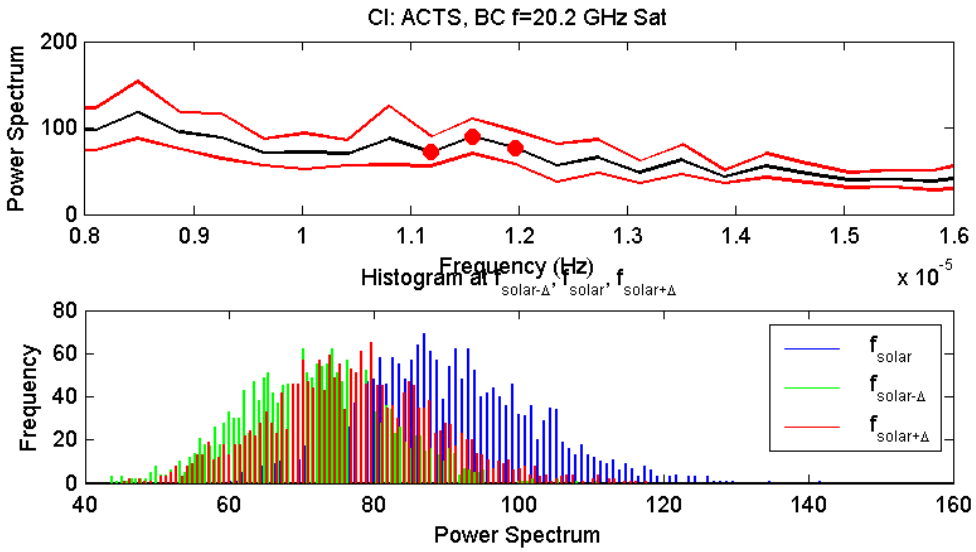

(a) 20.2 GHz beacon data: Fail to reject H_0 at the significance level of $\alpha = 0.05$.

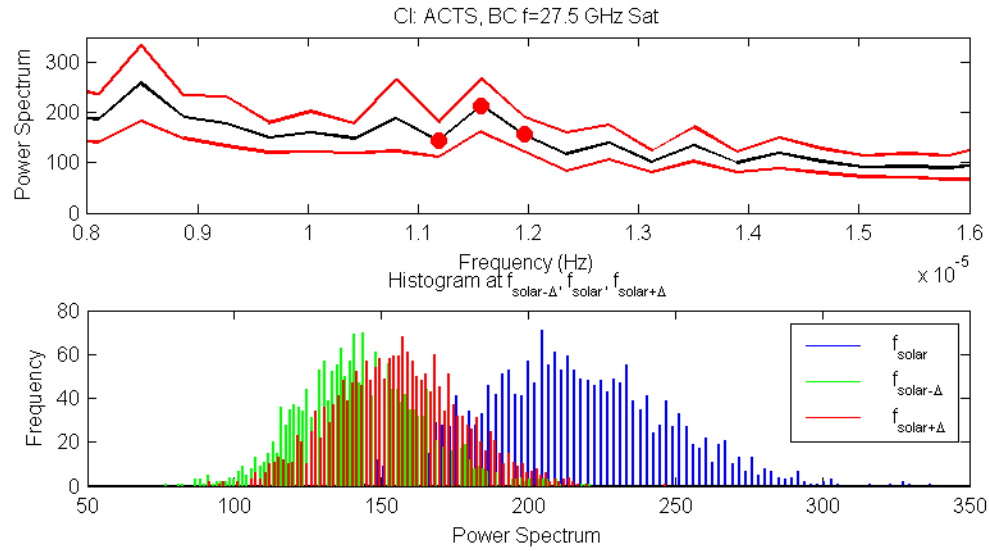

(b) 27.5GHz beacon data: Fail to reject H_0 at the significance level of $\alpha = 0.05$.

Figure 5.7: Significance test for the solar peak detected in British Columbia

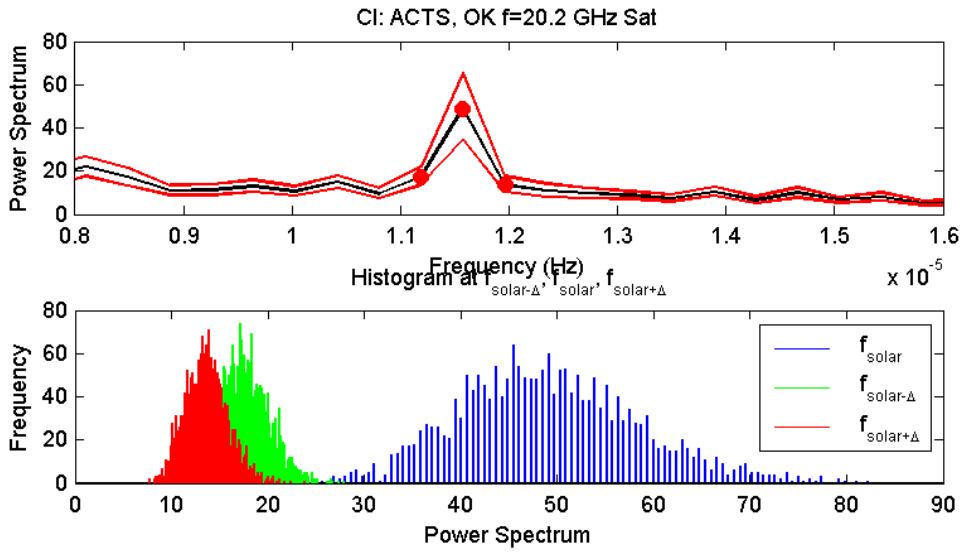

(a) 20.2 GHz beacon data: Reject H_0 at the significance level of $\alpha = 0.05$, with p-value<0.001

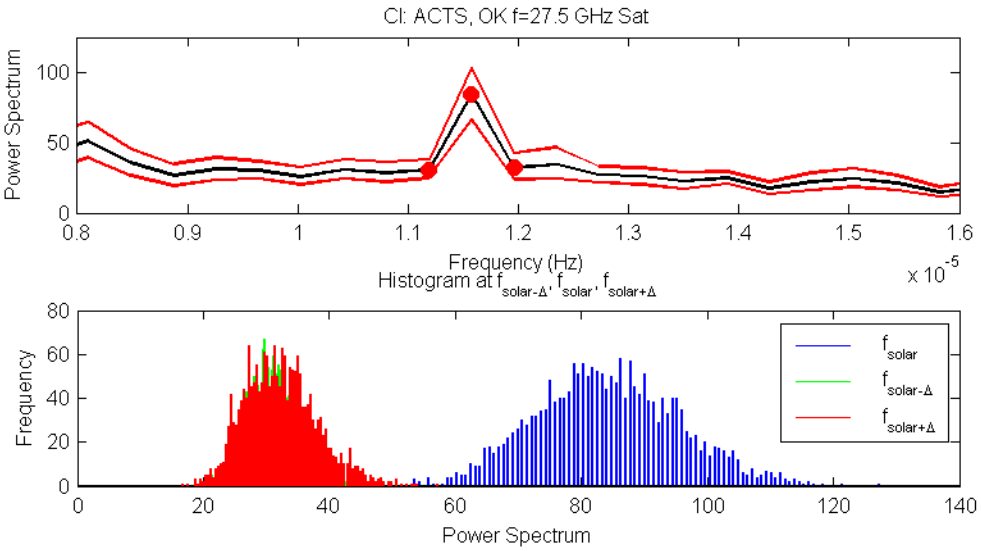

(b) 27.5GHz beacon data: Reject H_0 at the significance level of $\alpha = 0.05$, with p-value<0.001

Figure 5.8: Significance test for the solar peak detected in Oklahoma

5.2.2 Texas

A similar hypothesis test is conducted onto the solar peak obtained from Method 2 in Texas. The result is given in Figure 5.9, with (a) beacon attenuation data and (b) radiometrically inferred attenuation data.

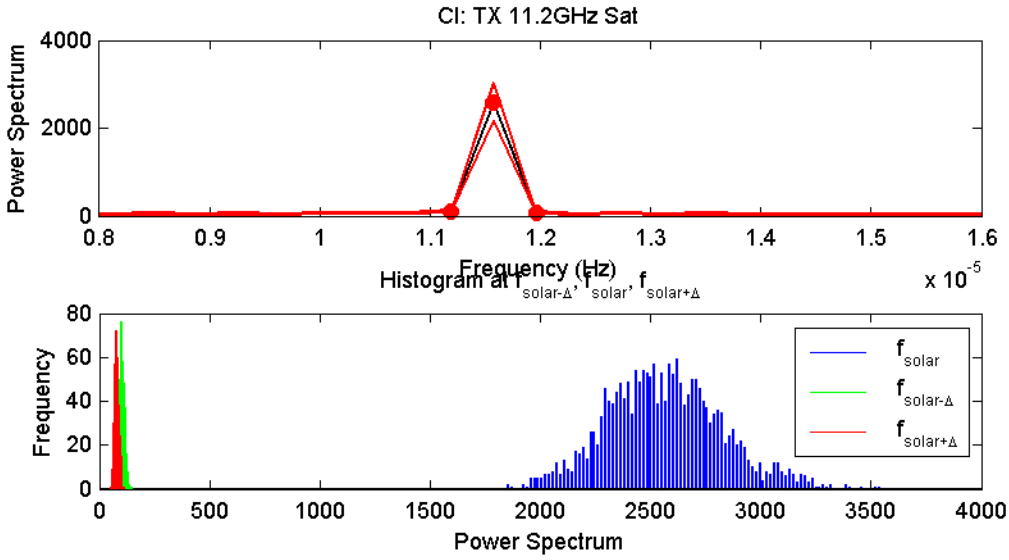

(a) Beacon data: Reject H_0 at the significance level of $\alpha = 0.05$, with p-value<0.001

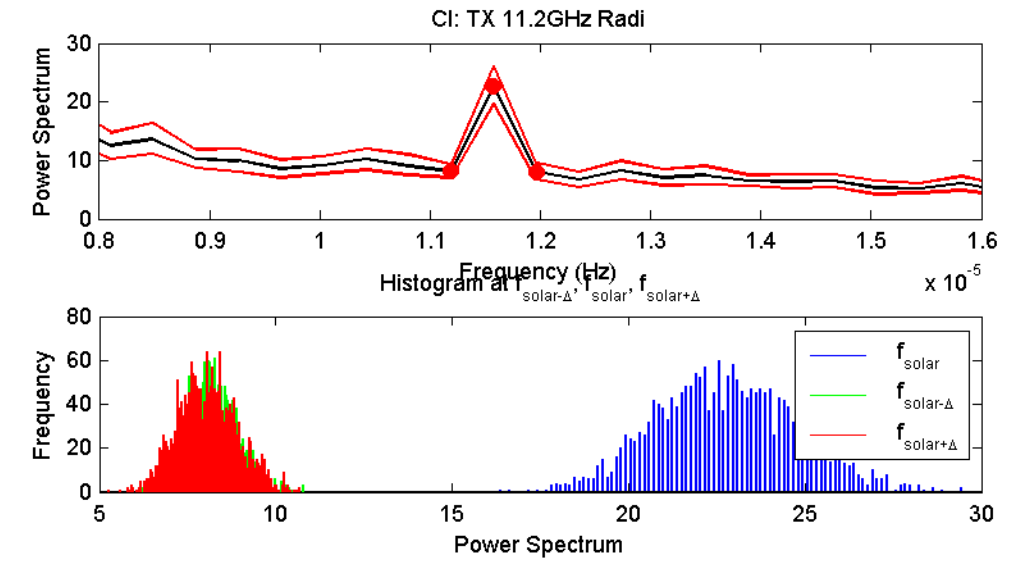

(b) Radiometer data: Reject H_0 at the significance level of $\alpha = 0.05$, with p-value<0.001

Figure 5.9: Significance test for the solar peak detected in Texas

5.2.3 Discussion

The result of the significant test showed that there is a strong periodic behavior with a frequency of a solar day in the ACTS beacon and radiometer data from the site in Florida, Colorado, New Mexico and Oklahoma, as well as from the Texas database. No periodic variation is detected in both beacon and radiometer data from the ACTS site of Alaska and British Columbia.

5.3 Cumulative excess attenuation

Cumulative excess attenuation is the complementary cumulative distribution function (CCDF) of attenuation. It is the probability $P_{A_{tot}}(x)$ that at an arbitrary time instant, t_0, total attenuation exceeds *x* dB.

$$P_{A_{tot}} = P\{A_{tot}(t_0) > x\} \tag{5.1}$$

Cumulative excess attenuation in clear sky conditioned to the hours of the day, or to different season, could assist in investigating the different margin needed to operate a system in clear sky for different hours/month, and their respective probability. They provide quantitative information to evaluate the impact on low margin systems, of changes in clear sky level.

For the ACTS, the cumulative excess attenuation or CCDF was obtained for the time series data of total attenuation A_{tot}, i.e. the attenuation with respect to the absence of atmosphere that is essentially due to oxygen, water vapor, clouds, rain, and tropospheric turbulence. The CCDF at high time percentages is essentially due to clear sky. To find a general limit to indicate the time percentages for which above it is due to clear sky, and below is due to water droplets in the atmosphere, the CCDF result of Figure 4.50 is used as reference. The gaseous absorption of the 20.2 GHz frequency is higher than the 27.5 GHz frequency during clear air, and when it begins to rain, the gaseous absorption of the

27.5 GHz will be higher than 20.2 GHz. The time percentage for which this transition occurs is used as a boundary marker between clear sky and not.

5.3.1 Seasonal variations

Figure 5.10 and Figure 5.11 gives the CCDF of total attenuation, for the 20.2 and 27.5 GHz respectively. The CCDF of total attenuation are generated for all the years, as well as conditioned to the four meteorological seasons. Winter consist of complete months of December, January, and February; spring consists of March, April, and May; summer consists of June, July and August; and fall consists of September, October and December. The horizontal red dotted line marks the time percentage for which above it is attenuation due to clear sky. It is taken as an 'average' guide used for all seasons. As it rains more in summer, it would be reasonable to expect that the time percentage for which above it is clear-sky, is slightly lower in winter than summer. The legend for some of the subfigures had to be remove so as to not obscure the data plot. However, the legend for all subfigures in Figure 5.10 and Figure 5.11 are the same.

Generally, winter months provide significantly less total attenuation than summer months due to the lower vapor gas content in the atmosphere. The results for 20.2 GHz and 27.5 GHz are almost similar. A clear seasonal difference can be seen in the Alaska, then less so in Colorado and New Mexico. In Alaska, during summer, the total attenuation exceeds 4 dB at 10% of the time, but it winter it only exceeds 1.2 dB; a difference of more than 3 dB. Compared to the average annual distribution, at 10% of the time the attenuation distribution for summer is almost 1 dB above the annual distribution;

in winter it is 2 dB below the annual distribution. Seasonal variations are significantly different than annual ones.

In Colorado, the difference between winter and summer is clear, while spring and fall are almost identical, close to the annual distribution, and lay between winter and summer. For New Mexico however, the distribution for spring is almost similar to winter, while fall is closer to summer. The climate and geographical location for the site in Colorado and New Mexico too are most similar.

For Oklahoma a clear difference can be seen during winter compared to the other 3 seasons, but not between summer, fall and spring. The climate in Florida and Oklahoma are both humid subtropical, and contain the least seasonal difference in the distribution amongst the rest.

The site in British Columbia has a maritime climate, with strong orographic influences. Heavy rain is infrequent but drizzle is widespread. The seasonal statistics for Vancouver do not show important inter-seasonal variability. However due to reports of calibration error here, it is difficult to analyze the CCDF result.

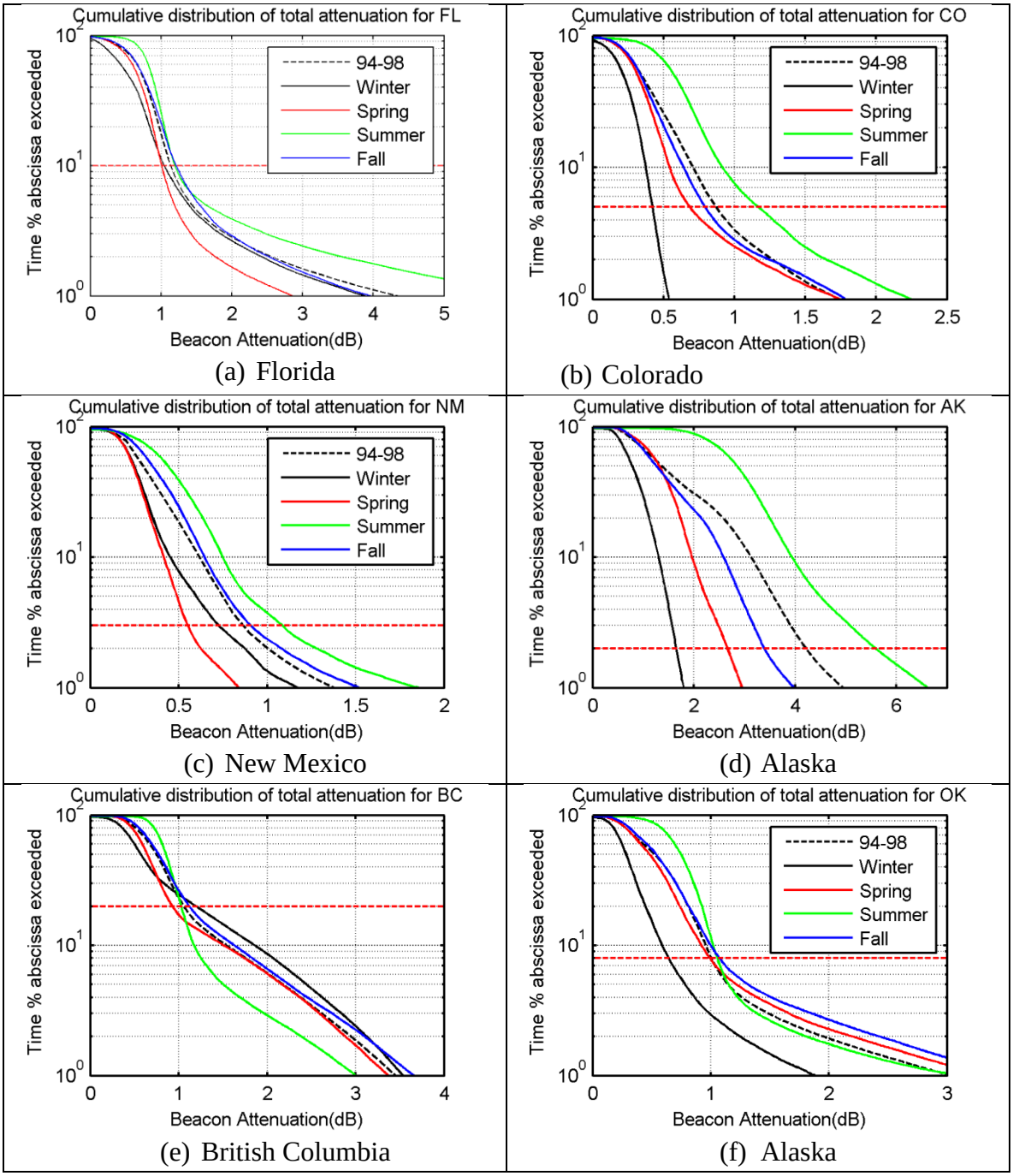

Figure 5.10: The CCDF of attenuation condition on season for 20.2 GHz ACTS

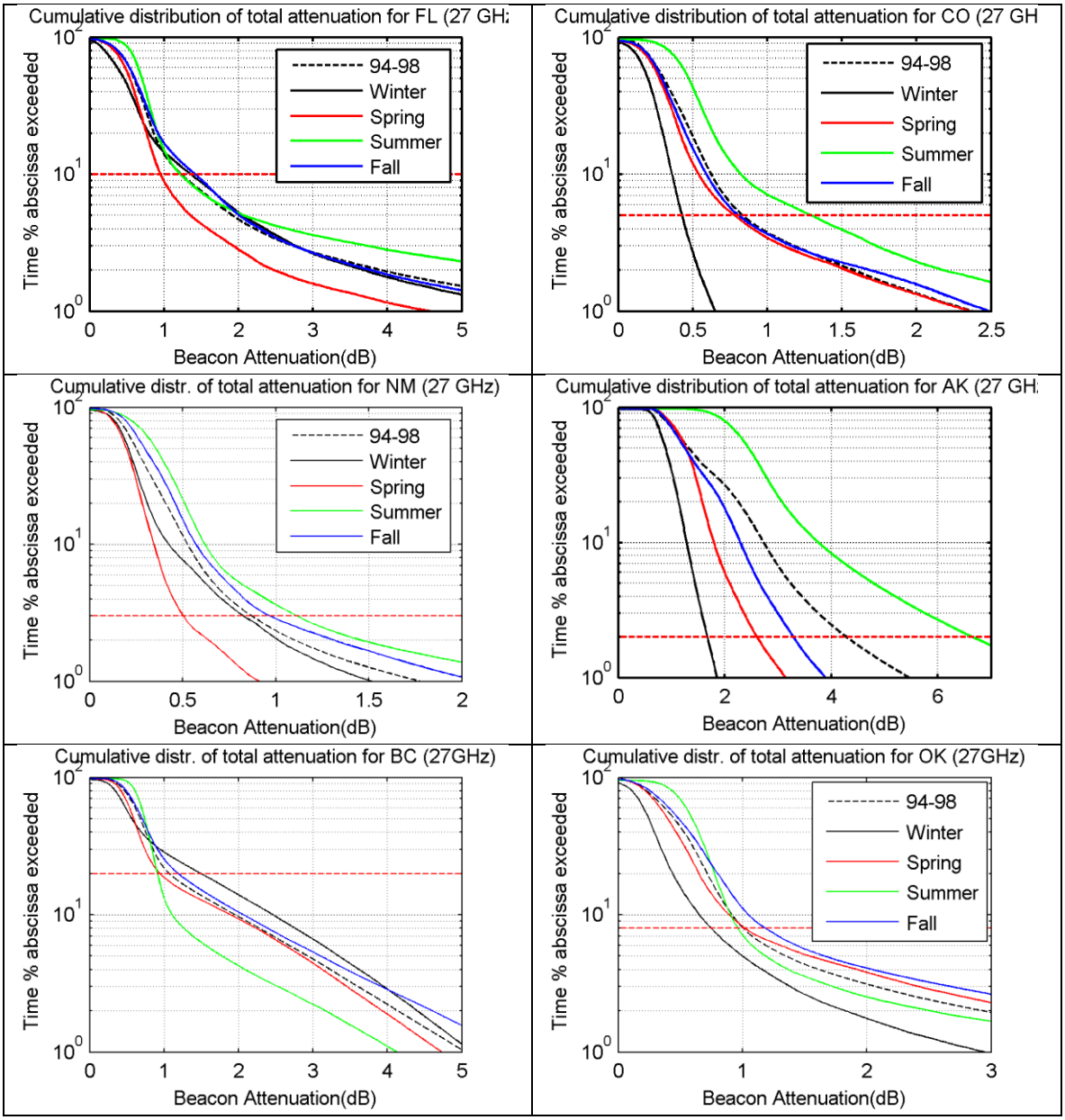

Figure 5.11: The CCDF of attenuation condition on season for 27.5 GHz ACTS

For Texas, the CCDF was obtained for the beacon attenuation time series data. Compared to the previous analysis reported on the ACTS data, similar method used to estimate the boundary for clear sky attenuation was not possible. However, the CCDF at time percentages higher than 6% to 8% can be considered to be due to clear sky. From Figure 5.12 a clear difference can be seen during winter compared to the other 3 seasons, but not between summer, fall and spring. Winter sees lower attenuation compared to other seasons as well as the average year. However all these differences are less than 1 dB.

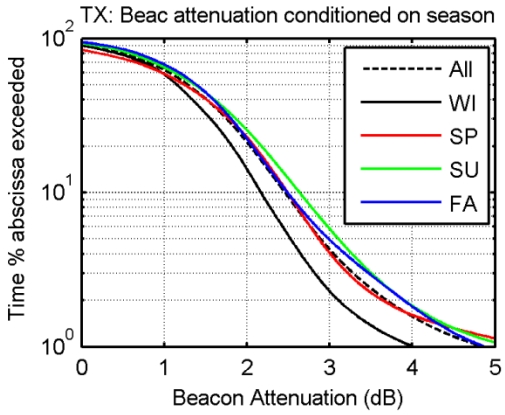

Figure 5.12: The CCDF of attenuation condition on season for Texas

5.3.2 Diurnal variations

For the CCDF conditioned on time, the day is divided into four period of 6 hours each (local time); 00:00-6:00, 6:00-12:00, 12:00-18:00, and 18:00-24:00. Results are given in Figure 5.13 and Figure 5.14, for the 20.2 and 27.5 GHz, respectively. Similarly

the horizontal red line is an estimate of the time percentages for which above it is due to clear sky, and below is due to water droplets in the atmosphere. The biggest diurnal difference is detected in Florida and Oklahoma, and lesser in Colorado and New Mexico. No significant difference in attenuation among the four periods is observed in Alaska and British Columbia.

There are some differences is detected between the result of the 20.2 GHz and the 27.5 GHz. For 20.2 GHz in Florida and Oklahoma, the 18:00-24:00 indicate the highest attenuation than the rest. However for 27.5 GHz in Florida and Oklahoma, the highest attenuation is during 06:00-12:00.

Compared to the result on the seasonal variation statistics, the diurnal variation are not significantly further away than the average annual variation, with minor differences between the different time slots.

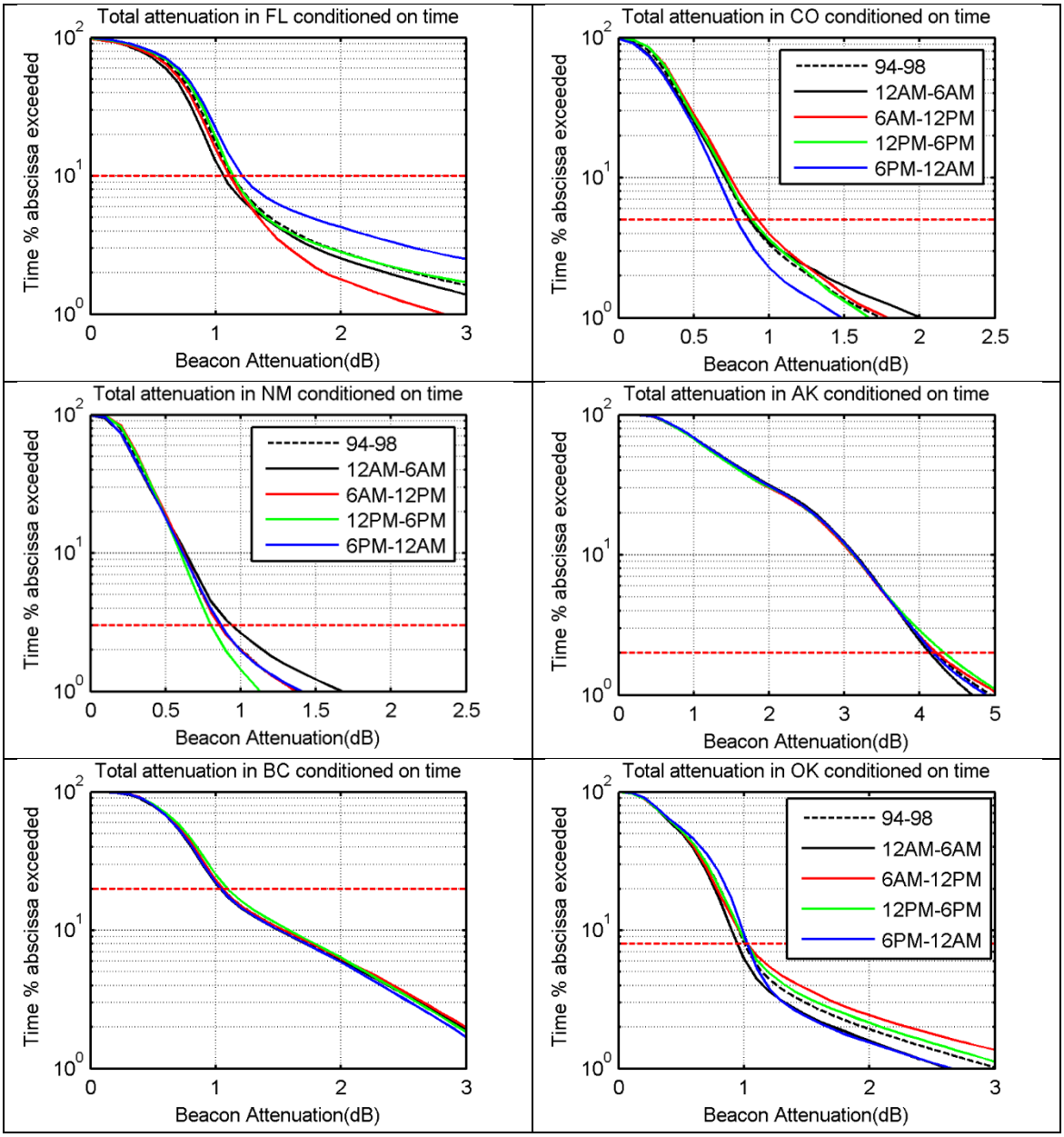

Figure 5.13: CCDF of total attenuation conditioned on time for ACTS 20.2 GHz

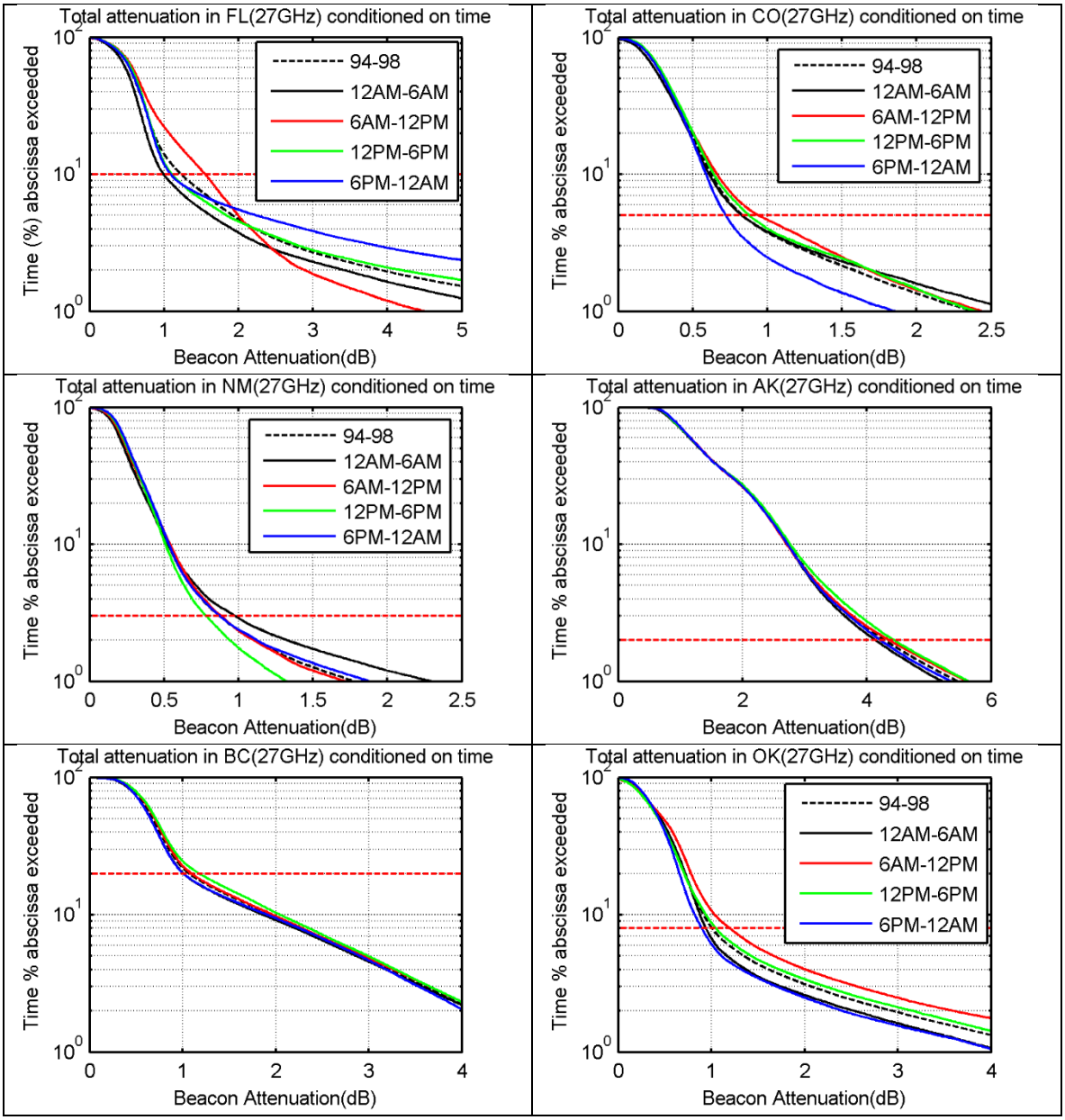

Figure 5.14: CCDF of total attenuation conditioned on time for ACTS 27.5 GHz

Figure 5.15 shows the CCDF conditioned on time for Texas. The 12:00AM-06:00AM indicate the highest attenuation than the rest. However these differences are minor and very much less than 0.5 dB.

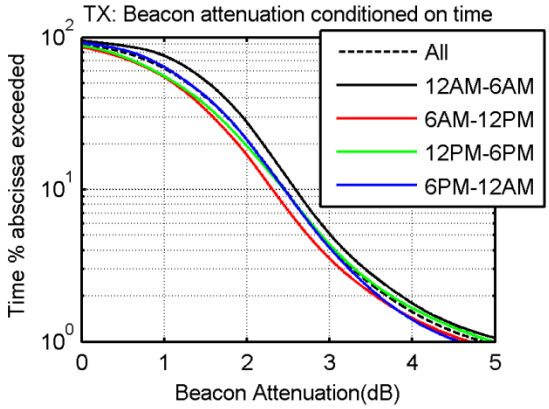

Figure 5.15: CCDF of total attenuation conditioned on time for Texas

5.3.3 Discussion

The statistics of seasonal and diurnal variations in the total attenuation time series of the ACTS and Texas data, indicate a climatic dependence, and their result is in agreement with those obtained from the spectral analysis of beacon and radiometer attenuation time series. The CCDF of attenuation for Alaska has the highest seasonal variation, but no diurnal variation detected. The diurnal variation in Florida, Oklahoma and Texas is most visible compared to the other sites, and each site has different time duration that indicates the highest attenuation. The seasonal variation statistics shows significant departure from its annual average statistic compared to its diurnal variation counterpart.

CHAPTER 6: SOURCE OF THE OBSERVED DIURNAL VARIATION

This chapter discusses some of the other possible causes that may produce a solar day variation in the beacon and radiometer data, namely the receiving equipment's front end instability as well as contribution from the radiometer side-lobe. The definition of the solar, sidereal and anti-sidereal time is given. The sidereal and anti-sidereal frequencies are sidebands that are produced when daily solar variation is amplitude modulated by seasonal variation of one cycle/year. The sidebands of the sidereal and anti-sidereal frequencies are produced on the right and left side of the solar frequency, respectively.

6.1 Front end instability

Diurnal variations may arise at least from three different origins: Fluctuations of the satellite EIRP due to the satellite orbit, changes in the atmospheric attenuation and gain variations in the receiver due to residual thermal instabilities.

Based on the spectrum estimation result in Chapter 4, it is clear that the diurnal variations observed in Figure 4.4 (a) to (c) are not caused by the interaction of the spacecraft proper motion and earth-terminal receiver. If the effect had been due to a satellite phenomenon there would have been two different results from those observed. First, the variation would have been on a sidereal day basis and not a solar day. Second, the radiometer would not have detected the effect.

In ACTS, both the radiometer and antenna share a common low noise amplifier (LNA) at the front-end of the terminal. After the LNA, the input was divided into the radiometer section and the satellite beacon section. As the radiometer measurements were not carried out by an independent instrument, an argument might arise that these simultaneous diurnal variations in the beacon and radiometer data were not the result of atmospheric effect, but due to heating effects in the shared receiver front-end, producing gain instabilities that effected both sets of equipment. However the assertion in the paragraphs below that the temperature of the front-end was kept stable, and that the effect of any front-end gain instabilities would produce an adverse effect, rebut the argument.

The Satellite Communications Group at Virginia Polytechnic Institute and State University designed and constructed a prototype of the ACTS Propagation Terminals (APT). The prototype system description, specification and performance results were detailed in the final report produced by them in [68].

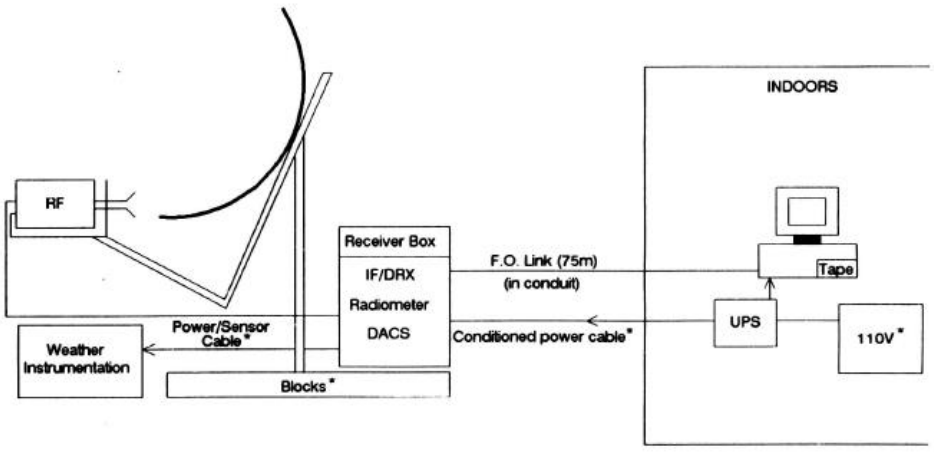

Figure 6.1: Physical diagram of the ACTS propagation terminal

The physical diagram for the complete ACTS propagation terminal (APT) package is shown in Figure 6.1, extracted from [68]. It consist of five physical units: the antenna; the RF enclosure which contains all RF front end and down conversion with output at 70 MHz; the receiver enclosure which houses the radiometer chain, the beacon IF and digital receiver, and the data acquisition and collection systems (DACS); the weather instrumentation; the indoor equipment consisting of a computer, cassette tape unit, and a UPS (uninterruptable power supply). Final processing occurs in the digital receiver. The system monitors power failure, receiver lock, PLL, outside temperature, RF enclosure temperature and IF enclosure temperature. Standard bench tests, as well as testing on actual satellite signals, were conducted onto a receiver prototype. All operations objectives were successfully achieved. The use of the small antenna with a shared beacon/total power radiometer RF front end proved out very well when the enclosure temperature is carefully controlled. In an email communication with Dr. Dennis Sweeney, one of the engineers who designed the ACTS propagation terminals, there was a large heat sink (a thick metal plate) onto which the LNA was bolted, and a Peltier Effect cooler that regulated the temperature of the heat sink, providing temperature stability of the frond end [69].

In Texas [24] and Olympus [22] too, the radiometers shared the same antenna and RF front end on each terminal system, and were housed in a temperature-controlled environment to keep gain constant.

A poor temperature stability in the front end however, would have an opposite effect on the radiometer and the satellite beacon receiver [69]. If the temperature stability

was poor and the gain of the amplifier went up, the received beacon signal and the perceived sky noise temperature would both be stronger. An increase in the received beacon signal will record a signal enhancement, while if the perceived sky noise went up, a perceive attenuation event would be recorded.

The two measurements therefore move in opposite directions, while a result in Figure 4.4 showed a concomitant beacon and inferred path attenuation. The two went in-step. All this provides justification that the observed diurnal variations were not the result of gain variations in the receiver due to thermal instabilities in the shared front end LNA.

When diurnal variations in signal level were observed on satellite beacon experiments, they were often ascribed to changes in satellite antenna beam pointing due to orbital motion and/or variations in pointing due to diurnal heating effects on the satellite antenna, and not to the atmosphere itself [24], [27] and [70]. Only when radiometers and satellite beacon receivers were co-located and looked along the same azimuth and elevation angle paths, did it become clear that the effect was not solely due to satellite-induced effects.

6.2 Radiometer side lobe contribution

A radiometer is a device for measuring the variation in noise power or brightness temperature of a source. When co-located with the beacon receiver, a radiometer provides a measure of the inferred attenuation of the signal that is obtained based on the noise temperature that is detected along the path. It is a non-coherent detector and so it integrates all of the sky-noise detected within the antenna beam. A beacon receiver, on the other hand, is a coherent detector and so will detect attenuation mainly within the first

Fresnel zone along the path to a satellite. For this reason, a radiometer tends to underestimate rain attenuation when compared with that of a collocated beacon receiver unless the rain is close to the two measuring devices. A radiometer also has an inferred attenuation range limited to about 10 dB. However, on a statistical basis, a radiometer provides a good estimate of the beacon attenuation, particularly in low attenuation events and clear air.

When a radiometer measures antenna noise temperature, T_{ant}, it is a summation of all contributions of energy entering the antenna from any direction. The noise temperature contributions entering the radiometer antenna will be from three sources, (a) the cosmic background temperature, (b) contributions entering the side lobes of the antenna from structures around the radiometer and from the ground, and (c) constituents along the path, primarily atmospheric emission by rain, clouds and gases.

The cosmic background temperature is permanent and does not have a cyclic periodicity [7]. Noise contributions from the ground, could have a solar periodicity as the ground heats and cools in a like manner to the path to the satellite. However the effect will only be seen through the side lobes and not the main lobe, and thus will amount to much less than changes along the path. With knowledge of the fraction of power received by the main beam, *H*, the side lobe contribution is integrated out to determine the actual sky temperature.

$$T_a = HT_s + (1 - H)T_g \quad (K) \tag{6.1}$$

$$T_{s=}\frac{T_a-(1-H)T_g}{H}\quad(K) \tag{6.2}$$

H is also known as the antenna integration factor and is usually in the order of 0.9. T_a, T_s and T_g are the antenna temperature, sky brightness temperature and ground brightness temperature, respectively. The brightness temperature range of the ground is approximately between 260 K and 290 K.

Assuming the side lobe factor was not extracted out from the inferred attenuation calculation, and was the cause of the diurnal variation detected in the radiometer inferred attenuation data, the maximum probable side lobe contribution is estimated, with the value H = 0.9, and a hypothetical diurnal change in the ground temperature from 260 to 290 K (-13 to 17°C), the perceived ground temperature contribution will change from 10% of 260 to 10% of 290 K. This amounts to a change of 3 K in the ground temperature contribution. For a medium temperature of 273 K, cosmic background temperature of 2 K, and using the radiative transfer formula given in (3.1), this gives a change in inferred path attenuation of about 0.03 dB. The changes seen in Figure 4.4 however were almost 0.25 dB for Florida.

For the ACTS experiment, an extensive documentation of the radiometer calibration can be found in [71]. The radiometer system calibration was established by comparing the sky brightness temperatures observed by the radiometer to those predicted theoretically based on simultaneously measured vertical profiles of atmospheric temperature and relative humidity. The comparison between the attenuation estimates derived from the radiometer measurements and the gaseous absorption estimates showed

a good match, with a small variability of less than 0.05 dB. To maintain stability, automatic calibration was executed every 15 minutes by inserting known power level changes into the radiometer receiver and the receiver output is corrected to match these changes. The system calibration is also continuously monitored by comparing the radiometer attenuation values with the gaseous absorption estimates for the minutes of observations in each day when the standard deviation of the radiometer attenuation is less than an elevation-angle-dependent threshold value.

The propagation data from Texas used a conical horn-reflector type antenna, with low-noise properties and very low side lobes [72], well suited for measurements at low elevation angle. Its measured antenna integration factor, *H* is 0.98, and was included in the radiometer inferred attenuation calculation [24].

6.3 Solar, sidereal and anti-sidereal time

Solar time is measured by the apparent diurnal motion of the Sun, and local noon in solar time is defined as the moment when the Sun is at its highest point in the sky (exactly due south or north depending on the observer's latitude and the season). The average time taken for the Sun to return to its highest point is 24 h. It has a cycle of 365.25days/year.

Sidereal time is time measured with respect to the apparent motion of the 'fixed' stars in the sky due to the Earth's rotation. While the Earth is rotating on its axis it is also moving along its orbit around the Sun. Over the course of a day the Earth moves about one degree along its orbit (360 degrees in a full orbit divided by 365.25 days in a year is about one degree). Therefore, from our perspective, the Sun moves about one degree

from west to east with respect to the 'fixed' stars. 1° corresponds to 4 minutes, and so the mean solar day is about 4 minutes longer than the sidereal day. The sidereal time has 366.25cycles/year. Figure 6.2 below gives an illustration of this time difference [73].

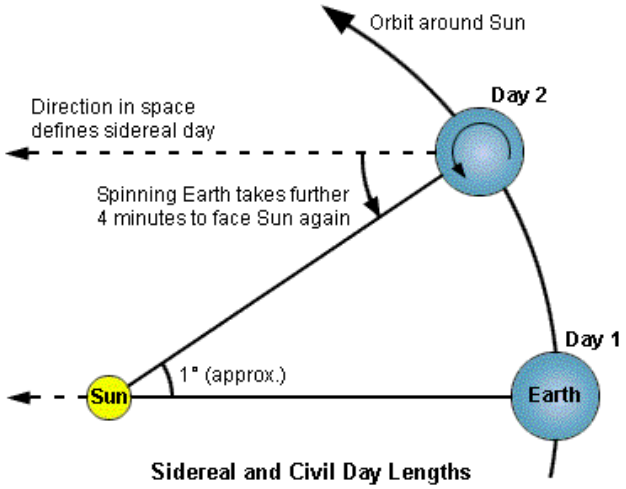

Figure 6.2: Sidereal and mean solar day description

Anti-sidereal time has a cycle of 364.25/year. However it corresponds to no physical viewpoints. In cosmic ray research, it is used as an artificial time standard to analyze the daily variation in the number of cosmic rays received on Earth. Cosmic rays are high energy radiation which strikes Earth from space. Some cosmic ray can have ultrahigh energies in the range of 100 – 1000 TeV. The peak of the energy distribution is at about 0.3 GeV. It is generally believed that the radiation below 10^{16} to 10^{17} eV is of galactic origin, while beyond about 10^{18}eV it is thought to be of extragalactic origin. A very small portion of the cosmic ray flux (1%) at low level of energy (few hundred GeV) is caused by the Sun.

It is known that when a daily solar variation is amplitude modulated by a seasonal variation of one cycle/year, it produces sidebands at the sidereal and anti-sidereal frequencies, on the right and left side of the solar frequency, respectively [74]. Similarly, an annual amplitude modulation of one cycle/year on the sidereal frequency of 366.25 cycles/year, produces sidebands of 365.25 cycles/year and 367.25 cycles/year (an extended-sidereal time). Extended sidereal time is also considered as an artificial time standard. Analysis done on the $3x10^8$ extensive air-shower events recorded at Auckland found that the sidereal variation observed is a genuine sidereal effect, and not only a residuum due to season changes. Interestingly correcting for the seasonal effect was found to increase rather than decrease the sidereal variation and to alter its phase [74].

Temporal variation of cosmic ray radiation has been studied in solar and in sidereal time. Observations on the intensity of low energy cosmic radiation ($E<10^{12}$eV), found evidence of time variation, attributed to the solar magnetic field, solar activity and to variations of the geomagnetic field. Diurnal modulation effects (day and night) were discovered, partly due to atmospheric and meteorological change [75]. Experiments on the development of air showers initiated by cosmic rays at energies of 10^{18}eV and higher, found evidence of seasonal and diurnal modulation on the rate of events. Atmospheric parameters such as pressure, affects the longitudinal development of air showers, while the density was found to affect the lateral distribution of the shower particles [76]. Variation of the incident radiation due to solar perturbation decreases with increasing energy and becomes negligible in the multi-TeV range, but atmospheric effects remain as the major factor of disturbance

The following shows a simple simulation how amplitude modulating a solar day variation produces sidebands on the sidereal and anti-sidereal frequencies. In Amplitude Modulation (AM), the carrier signal, $c(t) = Asin(\omega_c t + \theta_c)$, has its amplitude A, modulated in proportion to the message bearing (lower frequency) signal m(t).

The message signal m(t) is represented here by an arbitrary waveform with a single audio tone, $m(t) = Mcos(\omega_m t + \theta_m)$. It is assumed that $\omega_m \ll \omega_c$ and that $\min[m(t)] = -M$.

The modulated signal y(t) is formed by the product

$$y(t) = [1 + m(t)] \cdot c(t) = A[1 + \text{Mcos}(\omega_m t + \varphi_m)] \cdot \sin(\omega_c t + \varphi_c) \tag{6.3}$$

$$\begin{aligned} y(t) = A\sin(\omega_c t + \varphi_c) + \frac{AM}{2}\left[sin\big((\omega_c + \omega_m)t + (\varphi_c + \varphi_m)\big)\right] \\ + \frac{AM}{2}\left[sin\big((\omega_c - \omega_m)t + (\varphi_c - \varphi_m)\big)\right] \end{aligned} \tag{6.4}$$

The modulated signal has three components: a carrier wave at the frequency ω_c, and two sinusoidal waves (known as sidebands), whose frequencies are slightly above and below ω_c, at $\omega_c + \omega_m$ and $\omega_c - \omega_m$. Using the solar frequency of 1 cycle/solar day, we have the carrier frequency as $f_c = \frac{1}{24\times60\times60} Hz$. The frequency of the message signal is of 1 cycle/year, $f_m = \frac{1}{365.25\times24\times60\times60} Hz$

We then obtain the sidebands at:

$f_c - f_m = \frac{364.25}{365.25 \times 24 \times 60 \times 60} Hz$, a frequency of anti-sidereal day

and

$f_c + f_m = \frac{366.25}{365.25 \times 24 \times 60 \times 60} Hz$, a frequency of a sidereal day

Solar, sidereal and anti-sidereal frequency refers to the reciprocal of their respective time periods. Figure 6.3 below gives the spectrum of an AM modulated signal generated with the above carrier and message signal frequencies. From Equation (6.4), both AM sidebands should be of equal height

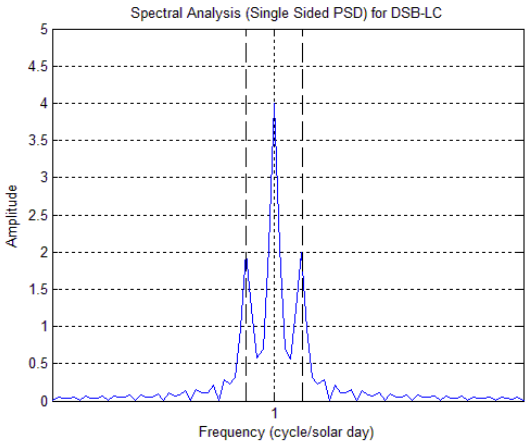

Figure 6.3: The simulated AM spectrum

The spectrum of the AM signal above has lower sidebands than the carrier. This is similar to the spectrum estimation output of the 20.2 GHz beacon and radiometer data in Florida. The results in Oklahoma also contained a strong presence of sidereal and anti-

sidereal sidebands, but both heights were not equal. The sidereal is comparatively higher in the 20.2 GHz and shorter in the 27.5 GHz compared to its anti-sidereal counterpart.

The result of this simple AM simulation showed that the sidereal and anti-sidereal peaks are the result of a combination of daily periodicity and seasonal variation, and do not exist independently. Further investigation would be required to determine why the presence of sidereal and anti-sidereal component is not seen in the spectral estimation result from some site, as well as the reason that in some instances, the height of the sidereal and anti-sidereal peaks are not equal. Most of the time, it is the anti-sidereal peak that is slightly larger than the sidereal peak, despite the fact that the anti-sidereal time corresponds to no physical viewpoints, unlike the sidereal time.

6.4 The sun and energy

The Sun is the main source of energy on Earth. It emits a nearly constant amount of electromagnetic radiation towards Earth but the amount of radiation received varies in each season. Earth's orbit around the Sun and its orientation with respect to incoming radiation influence the seasonal and latitudinal receipt of incoming solar radiation, called insolation.

Insolation is the measure of solar radiation energy received on a given surface area and recorded during a given time. From day to day, the local heating effectiveness of this solar energy – the solar insolation – depends upon both latitude and time. The altitude of the Sun determines over what area a given amount of radiation is spread. For example, in Figure 6.4, if a unit of energy falls upon area X when the Sun is at zenith, the same amount of energy is spread upon the area X/sinθ when the Sun's altitude is at angle θ. The heating efficiency decreases as θ decreases due to beam spreading. More direct illumination causes a more intense amount of heating.

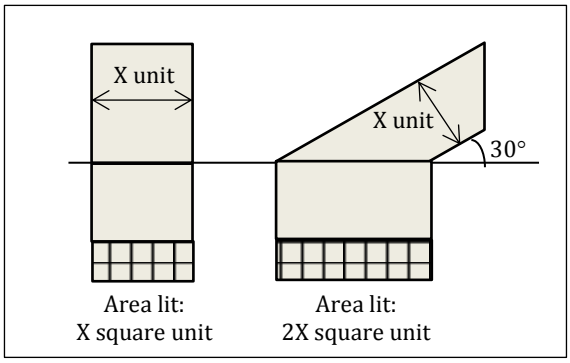

Figure 6.4: Effect of the Sun's altitude on the amount of energy received

6.4.1 Daily and annual temperature variations

At solar noon, the Sun achieves its greatest angle above the horizon but noon is not the warmest time of the day. The maximum air temperature is likely to occur at least a couple of hours afterwards. Typically, the cooling rate is much slower than the previous warming, largely because as the surface becomes colder than the ground beneath, heat is conducted upward. This slows the decrease in temperature.

The amplitude of the daily temperature pattern is reduced under overcast conditions. During the day the cloud cover can greatly reduce the daytime input of solar radiation and likewise reduce the net longwave radiation loss over the entire 24-hour period. The overall effect is to lower the daytime maximum temperature while keeping nighttime temperatures somewhat higher than they would be on a clear night.

Strong winds also moderate daily temperature ranges. When turbulence increases, the enhanced vertical movement causes any small parcel of air immediately in contact with the ground to be quickly displaced upward and replaced by another parcel. This reduces the increase in air temperature near the surface as the heat transferred from the ground is distributed to a greater mass of air. The same process works at night to inhibit cooling. No parcel of air will remain in contact with the chilled surface long enough to undergo substantial cooling.

The Earth's seasons – spring, summer, fall and winter – arise because the Earth's equatorial plane is inclined about 23.5deg to the ecliptic plane as it moves around the Sun. The rotation axis points in the same direction as Earth orbits the sun. This result in a variation of the angle at which sunlight strikes the Earth, its duration (daylight hours) and

the length of the path a beam of radiation must take through the atmosphere before reaching the surface. The change in noon time solar angle over the course of a year causes significant differences in the intensity of sunlight hitting the surface due to this beam spreading.

6.4.2 Temperature: Geographical influences on its pattern

Certain geographical factors combine to influence temperature patterns across the globe. These factors include latitude, altitude, atmospheric circulation patterns, continentally, ocean current characteristics along coastal location and local conditions.

The tilt of the Earth's axis influences the amount of solar radiation available at any latitude on any particular day. The availability of incoming radiation (and therefore temperature) is more variable as distance from the equator increases.

Temperatures in the troposphere typically decrease with altitude above sea level. This occurs because the surface is the primary source of direct heating for the troposphere, and increased altitude implies greater distance from the energy source. Sparse atmosphere above grounds of higher elevation have lower ability to absorb the outgoing radiation from the surface, thus the daytime temperature is slightly cooler and during nighttime, temperature drops rapidly.

An organized pattern of mean atmospheric pressure and air flow across the globe strongly influences the movement of warm and cold air, with a direct effect on temperature. These large-scale circulation patterns also influences the development of cloud cover, which has an indirect effect on temperature. Clouds reflect sunlight off their top side, while they absorb and redirect downward thermal radiation from the Earth's

surface. It also reflects down thermal heating. Thus its presence lowers daytime maximum temperature and increases nighttime temperature producing less diurnal temperature variances.

Oceans take longer to warm and cool when subject to comparable energy gains and losses. Thus coastal areas compared to inland locations of the same latitude experience smaller changes in temperature diurnally as well as seasonally.

A number of site-specific factors, such as slope orientation and steepness, can influence the local temperature characteristic of an area. In the Northern Hemisphere, slopes that are south-facing receive midday sunlight at a more direct angle than do those oriented in other directions thereby increasing their surface temperature. Densely wooded areas also have different temperature regimes than areas devoid of vegetation cover.

The amount of energy obtained by the Earth system is not equal at all latitudes. Areas near the equator receive a surplus of energy, while more pole ward regions have an energy deficit. The energy surplus at low latitudes is offset by the horizontal movement, or advection, of heat pole ward. This transfer is accomplished primarily by the global wind systems (75%) and secondarily by oceanic currents (25%) [77].

6.4.3 Heating of the atmosphere

Of the 342 Wm^{-2} of solar radiation reaching the top of the atmosphere, about 168 Wm^{-2} are absorbed by the earth's surface and 67 Wm^{-2} are absorbed by the atmosphere (43 Wm^{-2} by water vapor, 14 Wm^{-2} by ozone, 7 Wm^{-2} by clouds, and 3 Wm^{-2} by O_2 and CO_2) [78]. This atmospheric solar heating, combined with upward eddy conduction of heat from the ground, generates waves in the atmosphere at periods of the integral

fractions of a solar day, primarily at the diurnal (24 h) and semidiurnal (12 h) periods. These waves cause regular oscillations in atmospheric wind, temperature, and pressure fields, which are often referred to as atmospheric tides [79].

Solar heating is the primary driver of atmospheric tides. Gravitationally driven atmospheric tides, analogous to ocean tides, are about 20 times weaker than thermally driven atmospheric tides. The gravitational tides are primarily driven by the moon and appear in harmonics of a lunar day. The lunar diurnal tidal period is about 24.8 h, while the lunar semidiurnal period is 12.4 h.

At ground level, atmospheric tides can be detected as regular but small oscillations in surface pressure with periods of 24 (diurnal) and 12 hours (semidiurnal). Tidal oscillations tend to increase in amplitude with height and become major components of the total meteorology above about 50 km [80]. Solar tides can be separated into two components: **migrating** and **non-migrating**.

The primary source of migrating solar tides is the radiation absorption by the atmosphere that varies longitudinally. This absorption varies diurnally, due to the rotation of the Earth, and propagate west ward with the apparent motion of the Sun, from the perspective of an observer on the ground. Seasonal variation of the tides occurs as the Earth tilts relative to the Sun. The migrating diurnal tide originates primarily in the troposphere. Although tropospheric semidiurnal forcing is not negligible, there is comparatively more semidiurnal forcing in the middle atmosphere.

Non-migrating tides do not follow the apparent motion of the Sun but have the same periods as the migrating tides. They exist due to longitudinal differences in

topography, land-sea contrast and surface interaction that produce zonal variations in the local time behavior of the atmosphere.

6.4.4 Temperature: Effect on propagation path attenuation variation

A radiowave propagating through the Earth's atmosphere experiences a reduction in its signal level, when it interacts with gaseous components in the transmission path, mainly oxygen and water vapor. The level of signal degradation can be minor or severe, depending on frequency, temperature, pressure, water vapor concentration and freezing level height.

The clear linkage between changes in beacon level and sky noise temperature from the co-located receiver and radiometer, respectively, shows that it is an atmospheric effect. The presence of a diurnal variation component in the beacon and radiometer data, as well the differences detected in each site can be linked to the water vapor concentration at the respective site.

Oxygen is categorized as a permanent gas, while water vapor as a variable gas. Permanent gases constitute 99% of the atmosphere (the largest being nitrogen 78%, oxygen 21%) and the remaining 1% is of variable gases (water vapor, carbon dioxide and ozone). Despite their scarcity, variable gases profoundly affect the behavior of the atmosphere. Oxygen is found everywhere in nearly the same proportion (21%), whereas the distribution of water vapor in the atmosphere is uneven in both time and space. As water vapor content increases, the other gases decrease proportionately.

Near the Earth's surface, the water vapor content ranges from just a fraction of 1% of total atmosphere over deserts and the polar regions to about 4% in the tropics.

Sites that are close to open tracts of water have higher water vapor content. For example in North America, the amount of water vapor generally decreases with distance from the Gulf of Mexico towards the north and the Great Plains, and from the Pacific Coast to the Rocky Mountains. The rapid reduction from the coast to the Rocky Mountains is due to the local mountains blocking off moisture from inland areas. At higher altitudes, water vapor is even rarer.

Temperature largely determines the maximum amount of water vapor air can hold. Warm air can hold more water vapor than cool air. Dew point temperature (dew point) is the temperature at which saturation occurs. It is always equal to or less than the air temperature. If air is cooled to the dew point temperature, it becomes saturated and any further cooling leads to the removal of water vapor by condensation. The dew point is a valuable indicator of the moisture content; when the dew point is high, abundant water vapor is in the air. Figure 6.5 below gives the average dew point for sites in Florida, Oklahoma, Texas, Colorado, New Mexico and Alaska.

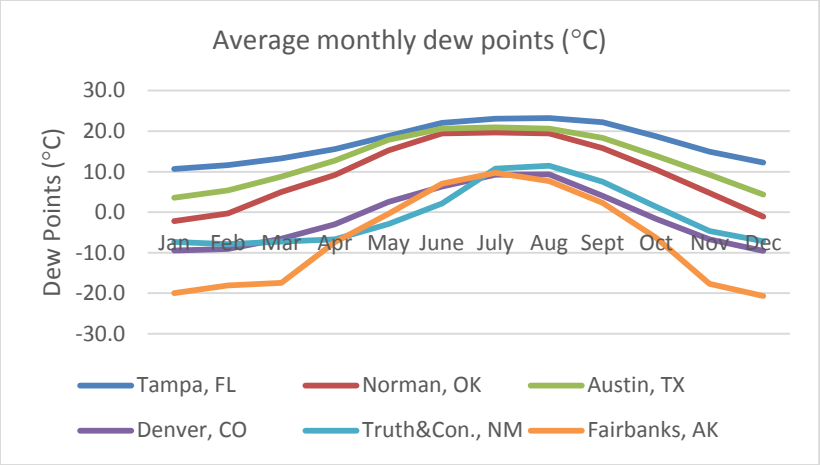

Figure 6.5: Average monthly dew points for sites close to the ACTS site and in Texas

There is a substantial increase in the amount of water vapor in the air for the summer months than during winter. Lower winter temperature prevents the existence of high water vapor content. The site in Colorado and New Mexico are both on a higher altitude, and have a desert like climate. Thus the lower dew point averages. Fairbanks Alaska has a subarctic climate, with the driest climate especially during the long cold winter months.

The diurnal and seasonal changes in the temperature effect the amount of water vapor along a given satellite path, and hence there is a positive relationship between temperature variation and attenuation. The content of water vapor is less at higher elevations above sea level as well as in extreme cold temperature, hence the lack of diurnal effect seen in the sites in Colorado, New Mexico and even more so in Alaska, compared to Oklahoma, Florida and Texas.

The height of the freezing level (the free air 0° isotherm) is the altitude in which the temperature is 0°C. It is up to this height where most of the atmospheric attenuation occurs. Figure 6.6 shows how the height is influenced by solar heating effect, extracted from Fig. 4.60 of Ref. [7]. Regions close to the equator have a higher probability of a higher freezing level height than temperate regions. Temperate regions with a sub-tropical climate also have a higher freezing level height than other regions at the same latitude. The higher the freezing level, the higher the gaseous attenuation effect as the propagation path affected by gaseous absorption increases. The seasonal variation in the freezing level height will also produce seasonal variation in the gaseous absorption.

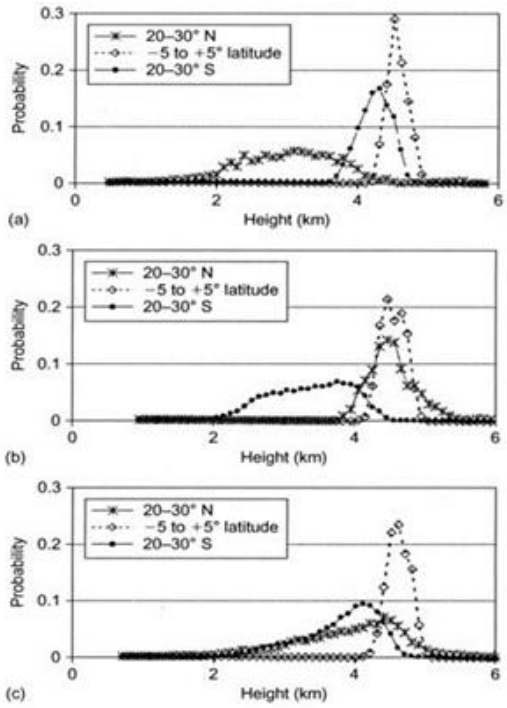

Figure 6.6: Probability distribution of freezing (melting) level heights: (a) December, January, February; (b) June, July and August; (c) Annual.

CHAPTER 7: CLEAR SKY ATTENUATION AND MODELING

In this chapter the seasonal and diurnal variation detected in the mean clear sky beacon attenuation is modelled.

Research in South Africa [81], Canada [82], Germany and Italy [83], found seasonal variations in the onset time of heavy rains (having low time percentages) that cause satellite signal outages. No seasonal variations were detected in their resultant CCDF of attenuation, for high time percentages (clear sky), albeit it was difficult to discern as the figures were focused to show the result during the low time percentages. Analysis of diurnal variations in the attenuation, were also reported in [82] and [83]. Diurnal variations of heavy rain show definite trends to those parts of the day when there is significant heating from the sun (i.e. late afternoon/evening, and possibly just after midnight).

However, all of the above experiments were focused on establishing the required link margin for 99.9% availability or more, which occurs in a rain event, and not during clear sky. Their result showed that the required link margin for 99.9% availability or more, varies seasonally as well as diurnally, depending on the frequency of rain in each site specific season, as well the most common time of day for it to rain.

7.1 Analysis of seasonal variation

Seasonal variations were detected in Figure 4.6 and Figure 4.29 for the ACTS beacon attenuation data as well as in Figure 4.7 and Figure 4.30 for radiometer data. There was a concomitant variation over longer periods that track the solar heating cycle on an annual basis. The site in Alaska has the largest variation, almost 3 dB from the highest to the lowest peak. This is then followed by Oklahoma, Florida, and then by Colorado and New Mexico. The result in British Columbia did not conform to others, probably due to the calibration error reported previously.

As described in Section 3.3 and 6.4.4, a radiowave propagating through the Earth atmosphere will experience a reduction in signal level due to the gaseous components present in the transmission path. Attenuation due to atmospheric gases is the major source of signal degradation during clear sky, and this is suspected to be the source of these variations. The ITU-R provides a procedure to estimate the gaseous attenuation based on frequency, temperature, pressure and water vapor concentration information. Two prediction methods are given in Recommendation ITU-R 676-9 [29]; 1) a detailed line-by-line summation of the spectral lines of water vapor and oxygen, and 2) a simplified approximation method based on curve fitting to the line-by-line calculation. The simplified method can be found in Annex 2 of the documentation, is valid for sites located at sea level to an altitude of 10 km, and agrees with the more accurate calculations to within an average of about 10% at frequencies away from the centers of major absorption lines.

This simplified method is used in an attempt to quantify the attenuation experienced by the satellite during clear sky, using surface meteorological data of temperature, pressure and water vapor concentration collected in each site. The procedure selected for use from Annex 2 is duplicated below except for the equation number. It can be summarized into 3 basic steps.

The first step is to find the specific attenuation of the gaseous atmosphere (excluding water droplets, ice and pollutants) which is made up of two components: that due to oxygen γ_0 and that due to water vapor γ_w. The specific attenuation for dry air, γ_0 (dB/km), is determined based on the frequency of operation.

$$\gamma_0 = \left[\frac{7.2r_t^{2.8}}{f^2 + 0.34r_p^2 r_t^{1.6}} + \frac{0.62\xi_3}{(54-f)^{1.16\xi_1} + 0.83\xi_2}\right] f^2 r_p^2 \times 10^{-3} \quad (7.1)$$

With

$$\xi_1 = \varphi\left(r_p, r_t, 0.0717, -1.8132, 0.0156, -1.6515\right) \quad (7.2)$$

$$\xi_2 = \varphi\left(r_p, r_t, 0.5146, -4.6368, -0.1921, -5.7416\right) \quad (7.3)$$

$$\xi_2 = \varphi\left(r_p, r_t, 0.5146, -4.6368, -0.1921, -5.7416\right) \quad (7.4)$$

$$\xi_3 = \varphi\left(r_p, r_t, 0.3414, -6.5851, 0.2130, -8.5854\right) \quad (7.5)$$

$$\varphi(r_p, r_t, a, b, c, d) = r_p^a r_t^b exp[c(1 - r_p) + d(1 - r_t)] \tag{7.6}$$

Where

f: frequency (GHz)

r_p = $p_{tot}/1013$, where p_{tot} represents total air pressure

r_t = 288/(273 + t)

p : pressure (hPa)

t : temperature (°C)

The specific attenuation for water vapor, γ_w (dB/km) is given by

$$\begin{aligned}\gamma_w = \Bigg\{ & \frac{3.98\eta_1 exp[2.23(1 - r_t)]}{(f - 22.235)^2 + 9.42\eta_1^2} g(f, 22) + \frac{11.96\eta_1 exp[0.7(1 - r_t)]}{(f - 183.31)^2 + 11.14\eta_1^2} \\ & + \frac{0.081\eta_1 exp[6.44(1 - r_t)]}{(f - 321.226)^2 + 6.29\eta_1^2} + \frac{3.66\eta_1 exp[1.6(1 - r_t)]}{(f - 325.153)^2 + 9.22\eta_1^2} \\ & + \frac{25.37\eta_1 exp[1.09(1 - r_t)]}{(f - 380)^2} + \frac{17.4\eta_1 exp[1.46(1 - r_t)]}{(f - 448)^2} \\ & + \frac{844.6\eta_1 exp[0.17(1 - r_t)]}{(f - 557)^2} g(f, 557) \\ & + \frac{290\eta_1 exp[0.41(1 - r_t)]}{(f - 752)^2} g(f, 752) \\ & + \frac{8.3328 \times 10^4 \eta_2 exp[0.99(1 - r_t)]}{(f - 1780)^2} g(f, 1780) \Bigg\} f^2 r_t^{2.5} \rho \\ & \times 10^{-4}\end{aligned} \tag{7.7}$$

With

$$\eta_1 = 0.955 r_p r_t^{0.68} + 0.006\rho \tag{7.8}$$

$$\eta_2 = 0.735 r_p r_t^{0.5} + 0.0353 r_t^4 \rho \tag{7.9}$$

$$g(f, f_i) = 1 + \left(\frac{f - f_i}{f + f_i}\right)^2 \tag{7.10}$$

where ρ is the water-vapor density (g/m^3).

The second step is to find the equivalent heights for dry air and water vapor. The total gaseous attenuation will be determined by application of equivalent heights in the atmosphere for dry air and water vapor. For dry air, the equivalent height is given by:

$$h_0 = \frac{6.1}{1 + 0.17 r_p^{-1.1}} (1 + t_1 + t_2 + t_3) \tag{7.11}$$

Where

$$t_1 = \frac{4.64}{1 + 0.066 r_p^{-2.3}} exp\left[-\left(\frac{f - 59.7}{2.87 + 12.4 exp(-7.9 r_p)}\right)^2\right] \tag{7.12}$$

$$t_2 = \frac{0.14 exp(2.12 r^p)}{(f - 118.75)^2 + 0.031 exp(2.2 r_p)} \tag{7.13}$$

$$t_3 = \frac{0.0114}{1 + 0.14 r_p^{-2.6}} f \frac{-0.0247 + 0.0001f + 1.61 \times 10^{-6} f^2}{1 - 0.0169f + 4.1 \times 10^{-5} f^2 + 3.2 \times 10^{-7} f^3} \tag{7.14}$$

with the constraint that:

$$h_0 \leq 10.7 r_p^{0.3} \text{ , when } f < 70\ GHz$$

And for water vapor, the equivalent height for $f \leq 350\ GHz$ is:

$$h_w = 1.66 \left(1 + \frac{1.39\sigma_w}{(f - 22.235)^2 + 2.56\sigma_w} + \frac{3.37\sigma_w}{(f - 183.31)^2 + 4.96\sigma_w} + \frac{1.58\sigma_w}{(f - 325.1)^2 + 2.89\sigma_w}\right) \tag{7.15}$$

$$\sigma_w = \frac{1.013}{1 + exp\left[-8.6\left(r_p - 0.57\right)\right]} \tag{7.16}$$

The third step is finding the total zenith (elevation angle = 90°) attenuation, listed as:

$$A = \gamma_0 h_0 + \gamma_w h_w\ dB \tag{7.17}$$

The final step is finding the total gaseous attenuation for the earth-satellite slant path using the site's elevation angle φ into the cosecant law, as follows:

$$A = \frac{A_0 + A_w}{sin\ \varphi}\ dB \tag{7.18}$$

Where $A_0 = h_0\gamma_0$ and $A_w = h_w\gamma_w$. This is valid for φ between 5° and 90°.

7.1.1 ACTS database

The ACTS database contains minute by minute surface meteorological data collected from each site. This data was used to produce time series data of gaseous attenuation estimation plotted in Figure 7.1 (red line plot), simultaneously with the actual recorded attenuation (turquoise plot) and mean (solid line plot). The mean line plot was produced using the method described in the flowchart of Figure 4.10, but with a higher running average window size of 200, to produce a smoother line plot. The gaseous attenuation estimation values only consider losses during clear sky while the actual recorded total attenuation includes other losses such as those due to rain events, clouds and fogs; hence the gaseous attenuation estimation are lower than the actual recorded data. While a comparison between estimated gaseous losses vs. measured beacon attenuation showed reasonable correlation for the site in Florida, Colorado, New Mexico and Oklahoma, a significant difference was found for Alaska and British Columbia. The site in Alaska is the coldest and with the lowest elevation path compared to the others. Low elevation angle path experience additional attenuation and sky noise increase from heavy clouds.

An inspection of meteorological data [84] showed that the Alaska site had significant cloud cover for a large percentage of a year compared to the other ACTS sites, with as high as 80% average cloud coverage during the months of August, September and October. Figure 7.3 gives a comparison of average cloud cover amongst all the ACTS sites, obtained from an independent meteorological website [85]. The Olympus experimenters also reported that clouds and scintillations produced more than 3 dB of attenuation at 30GHz on a low elevation angle path of 14°, and could be present for a large percentage of the time [27].

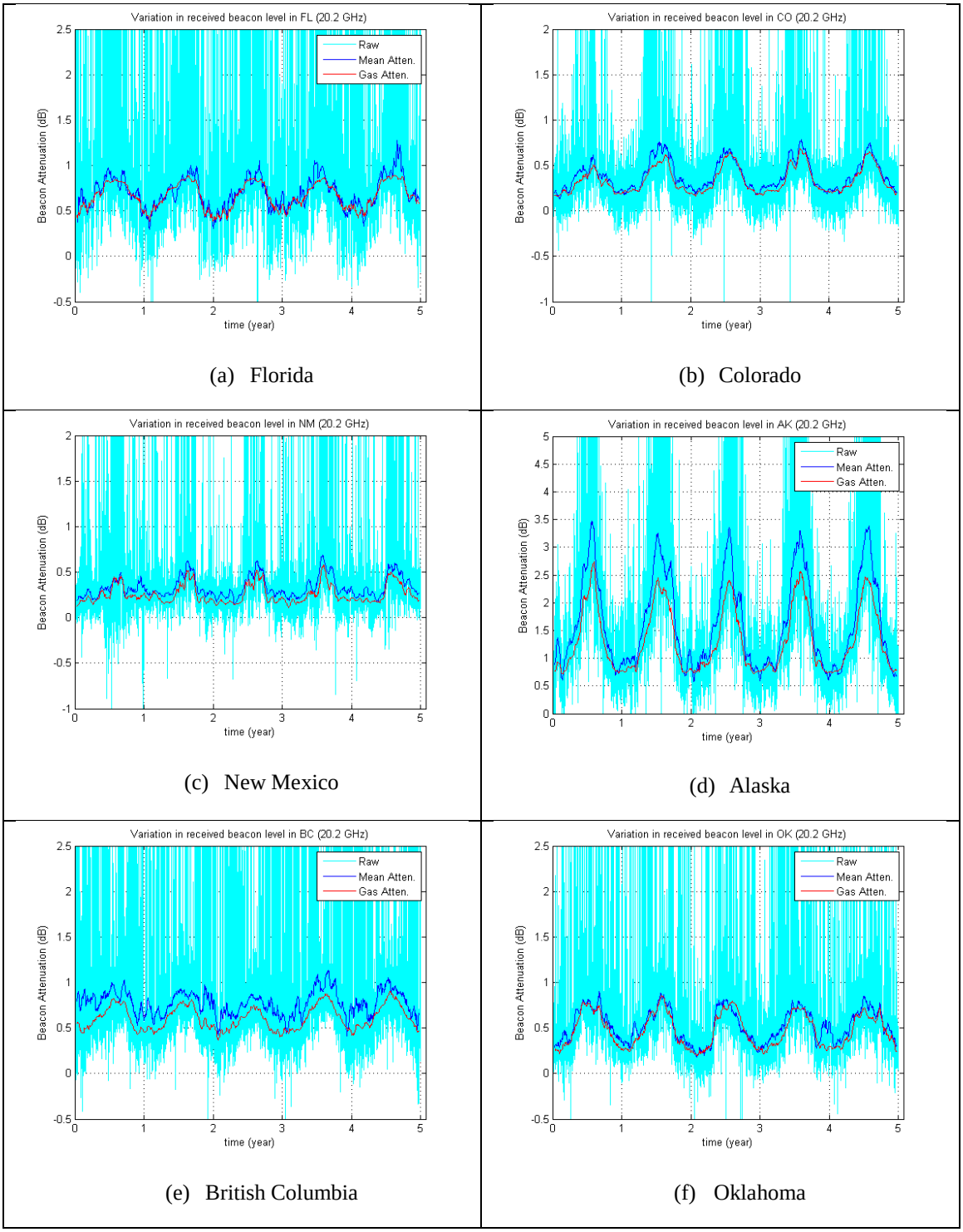

Figure 7.1: Variations in the received beacon attenuation in comparison with the simulated gaseous attenuation values for the 20.2 GHz frequency

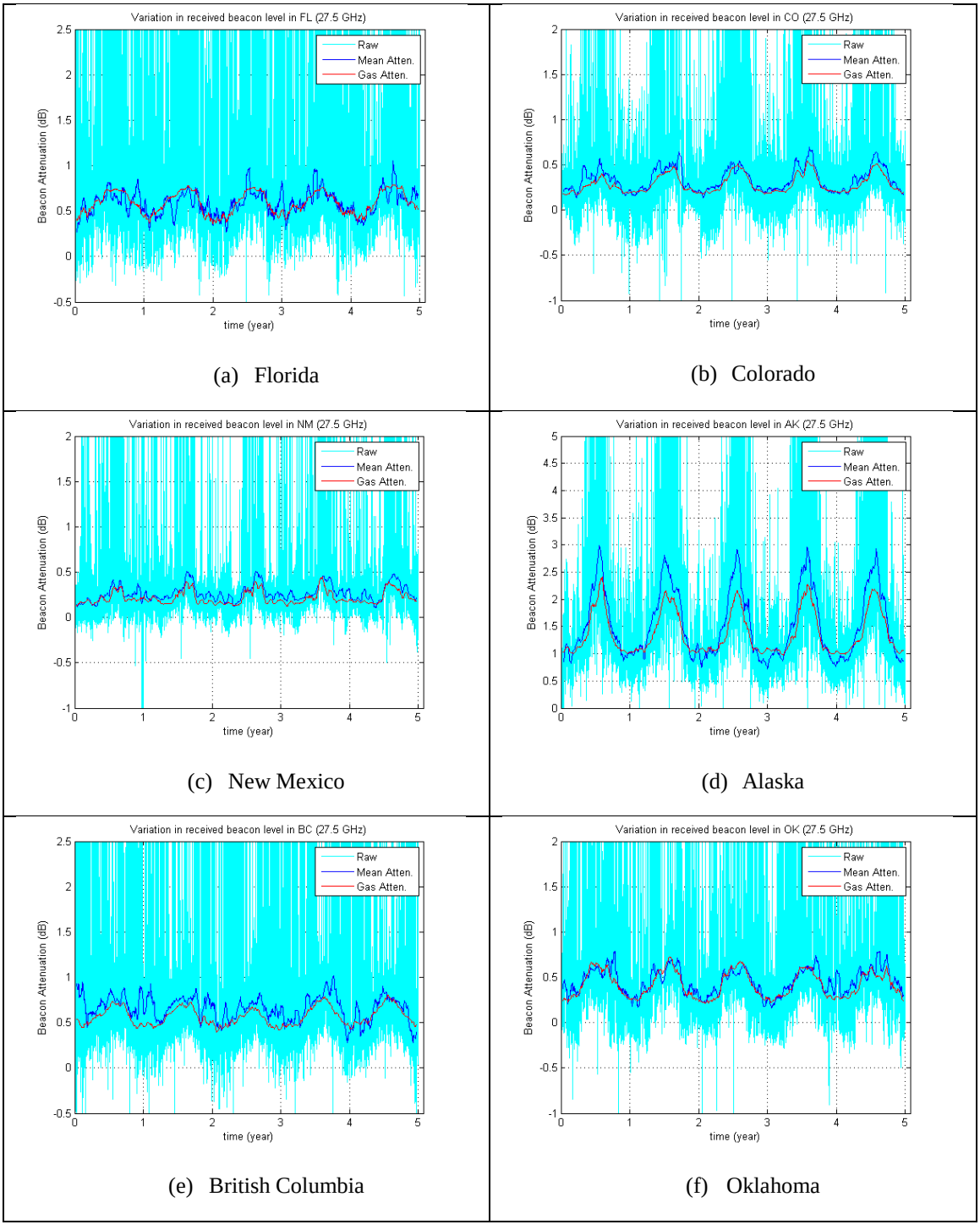

Figure 7.2: Variations in the received beacon attenuation in comparison with the simulated gaseous attenuation values for the 27.5 GHz frequency

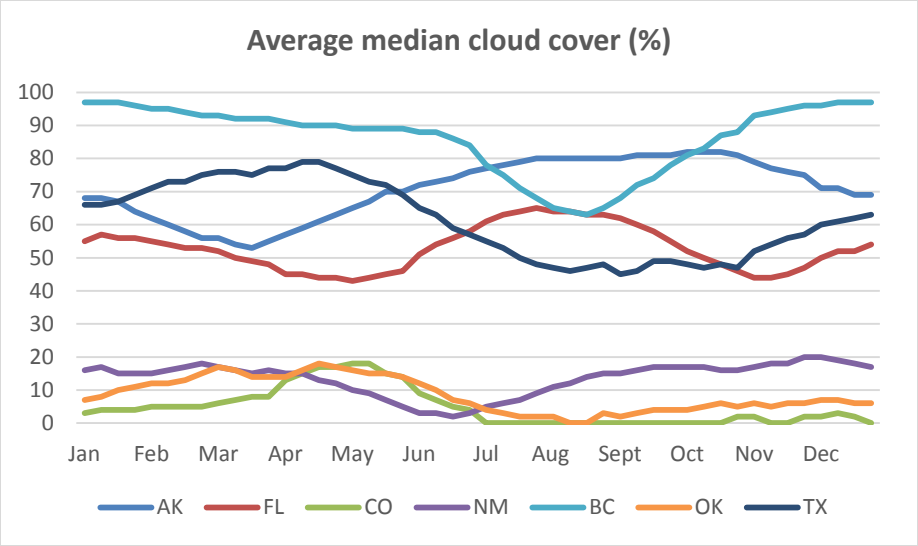

Figure 7.3: Cloud cover plot for the ACTS sites and in Texas

The ITU-R Recommendation 840-3 [86] provides a procedure to calculate the attenuation due to clouds for a given probability that uses the total columnar content of liquid water L (kg/m^2) in the atmosphere above the earth station location. The monthly values of total columnar content of reduced cloud liquid water, L (kg/m^2), exceeded for 1, 2, 3, 5, 10, 20, 30, 50, 60, 70, 80, 90, 95 and 99% of each average month are available in the form of digital maps, an integral part of this Recommendation. The procedures used for calculating cloud attenuation in Alaska are copied here.

Calculate the specific attenuation coefficient, K_l:

$$K_l = \frac{0.819f}{\varepsilon''(1+\eta^2)} \quad (dB/km)/(g/m^3) \tag{7.19}$$

Where *f* is the frequency (GHz), and where

$$\eta = \frac{2 + \varepsilon'}{\varepsilon"} \tag{7.20}$$

The complex dielectric permittivity of water, ε is given by:

$$\varepsilon"(f) = \frac{f(\varepsilon_0 - \varepsilon_1)}{f_p\left[1 + \left(f/f_p\right)^2\right]} + \frac{f(\varepsilon_1 - \varepsilon_2)}{f_s\left[1 + \left(f/f_s\right)^2\right]} \tag{7.21}$$

$$\varepsilon'(f) = \frac{(\varepsilon_0 - \varepsilon_1)}{\left[1 + \left(f/f_p\right)^2\right]} + \frac{(\varepsilon_1 - \varepsilon_2)}{\left[1 + \left(f/f_s\right)^2\right]} + \varepsilon_2 \tag{7.22}$$

$$\varepsilon_0 = 77.66 + 103.3(\theta - 1) \tag{7.23}$$

$$\varepsilon_1 = 0.0671\varepsilon_0 \tag{7.24}$$

$$\varepsilon_2 = 3.52 \tag{7.25}$$

$$\theta = 300/T \tag{7.26}$$

With *T* the temperature (K).

The principal and secondary relaxation frequencies are:

$$f_p = 20.20 - 146(\theta - 1) + 316(\theta - 1)^2 \quad GHz \tag{7.27}$$

$$f_s = 39.8 f_p \quad GHz \tag{7.28}$$

Cloud attenuation along slant paths are obtained as

$$A = \frac{LK_l}{sin\theta} \quad dB, for\ 90° \geq \theta \geq 5° \tag{7.29}$$

Where θ is the elevation angle and K_l is calculated from equations (7.19) to (7.28) for a water temperature of 0°C. The following Figure 7.4 shows the difference between estimated loss and actual loss can be reduced by incorporating the loss due to gaseous and cloud cover in the estimated loss.

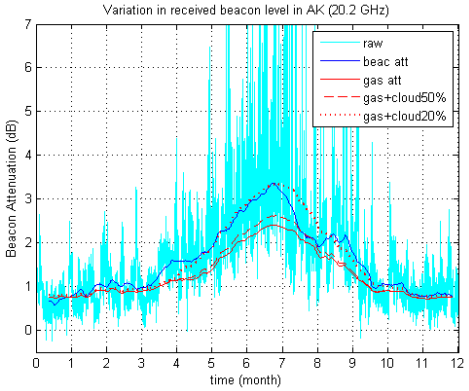

(a) 20.2 GHz

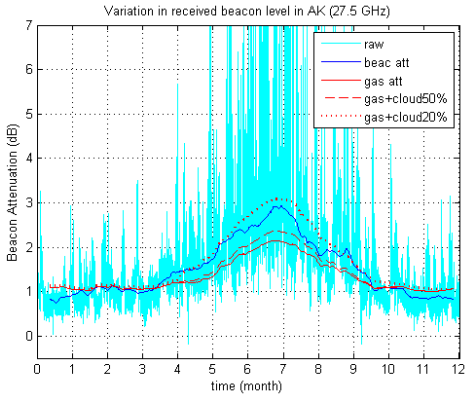

(b) 27.5 GHz

Figure 7.4 Variations in the received beacon attenuation in comparison with the simulated gaseous attenuation and cloud cover attenuation in Fairbanks Alaska

7.1.2 Texas database

Unlike the ACTS database, it is not possible to estimate the gaseous attenuation concomitantly as the minute by minute meteorological data was not extracted. Figure 7.5(a) gives the variation in the received beacon level, with the mean line produced using the same method as described in Figure 4.10, using the parameter values given in Table 4.8, but with the moving average window size for the mean data set to 400 (approximately 45 days averaging), for a smoother line effect. Using average monthly meteorological information from [87], collected recently (2013-2014) at a site nearest to the receiver's location, the gaseous attenuation is estimated and compared to the average beacon attenuation obtained from the 7 year data.

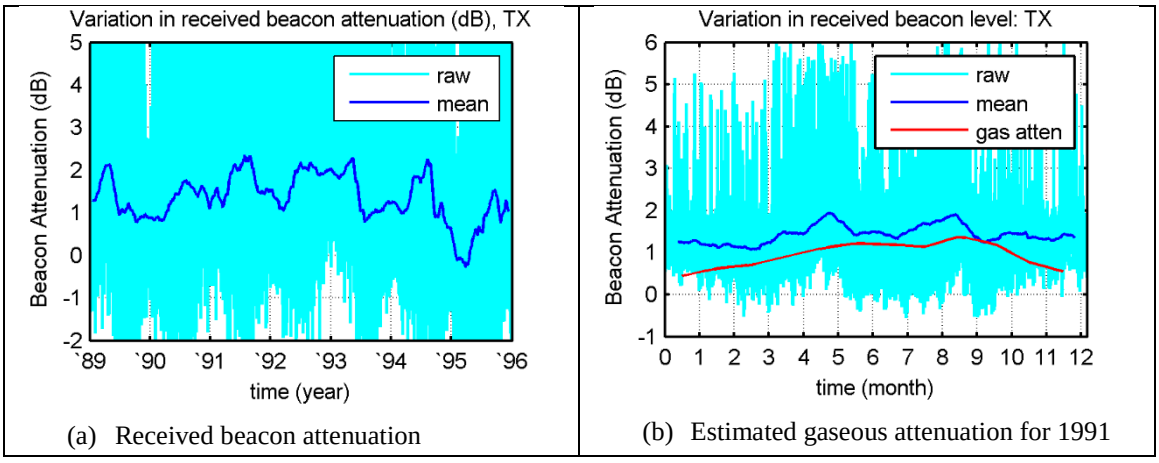

(a) Received beacon attenuation

(b) Estimated gaseous attenuation for 1991

Figure 7.5: Recorded beacon attenuation and estimated gaseous attenuation in Texas

The gaseous attenuation gives a close estimation, considering that the meteorological data was obtained recently and from external sources, and that cloud

coverage is more that 60% during the month of January till June and November till December in Austin, Texas (Figure 7.3).

The site in Austin, Texas uses an even lower elevation angle than Alaska, but its climate is significantly warmer than Alaska. The seasonal changes will therefore not be as significant as those detected in Alaska.

7.2 Analysis of diurnal variation

This section describe the attempt to model the diurnal variation seen in the beacon attenuation using a sinusoidal signal, with a frequency of a solar day cycle, and its parameter value generated using surface meteorological data. The model is referred to as the cosine clear sky model, and this exercise is limited to the ACTS database as the minute-by-minute meteorological data collected on site was successfully extracted.

To identify any seasonal effect in the diurnal variation of the received beacon level, the spectral content is investigated for each season. The ACTS data is divided into season based on the date of collection. The grouping is made as follows, winter (Dec. to Feb.), spring (Mar. to May), summer (June – Aug.) and fall (Sept. to Nov.). The WOSA technique (Section 4.2) is implemented in each season group, using a segment size of 30 days with an overlap of 50%, without executing any prior outlier removal methods. The final result given in Figure 7.6 and Figure 7.7 below is obtained by averaging the result obtained in the respective season of each year, from 1994 to 1998. The presence of a diurnal variation in the signal level is significant during summer compared to other season, and in terms of its' shape and magnitude, is most predominant in Florida for both

20.2 and 27.5 GHz frequencies. The horizontal lines in both figures mark the position of the solar cycle.

With a small segment size of 30 days, the resolution here is not enough to differentiate between the closely spaced sidereal and anti-sidereal frequencies as seen in previous result using a segment size of 3 years. However the approximate shape of the spectrum output agrees with those obtained previously in Section 4.3.3 and Section 4.4.4.

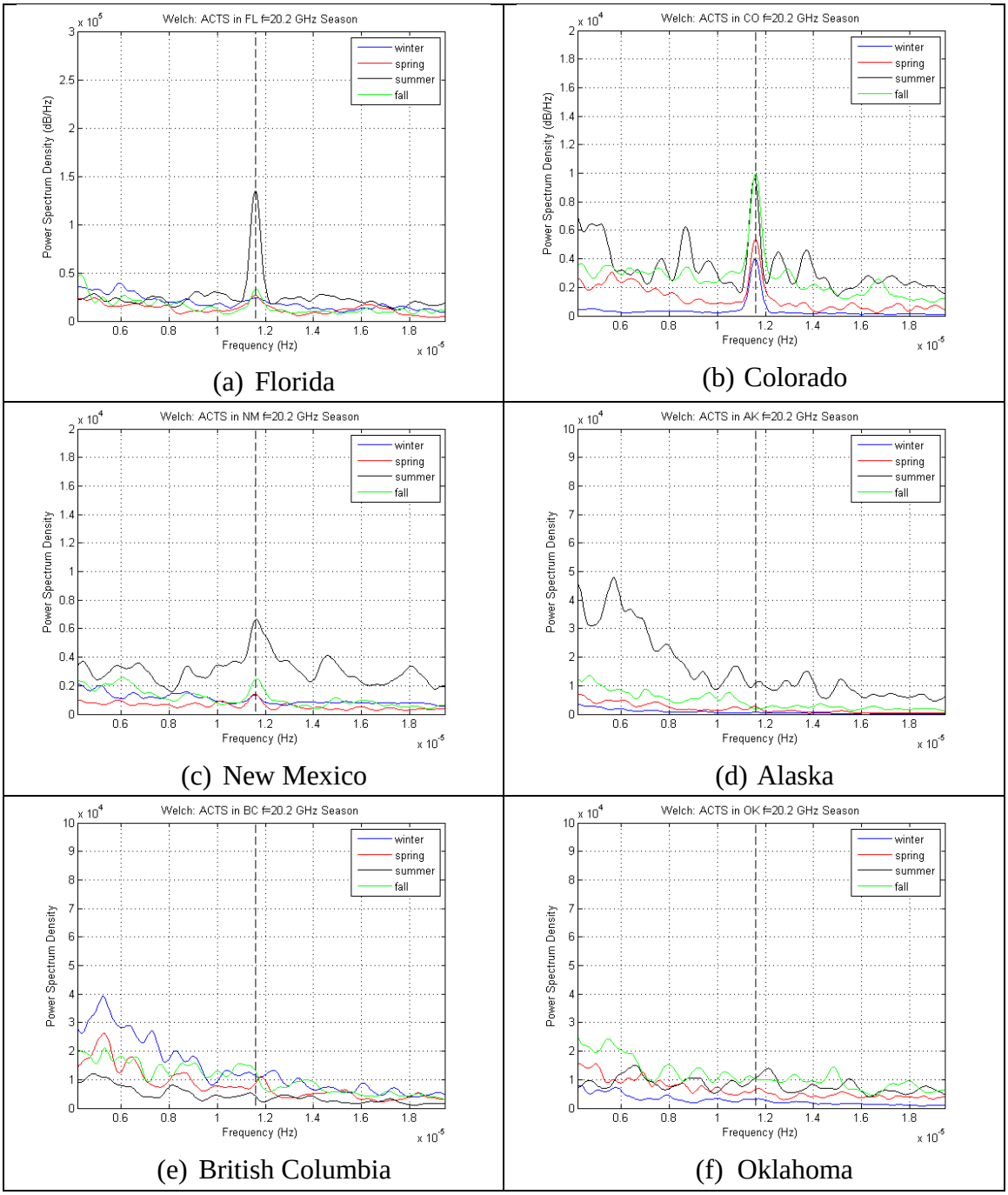

Figure 7.6: Spectrum content based on season for 20.2 GHz ACTS data

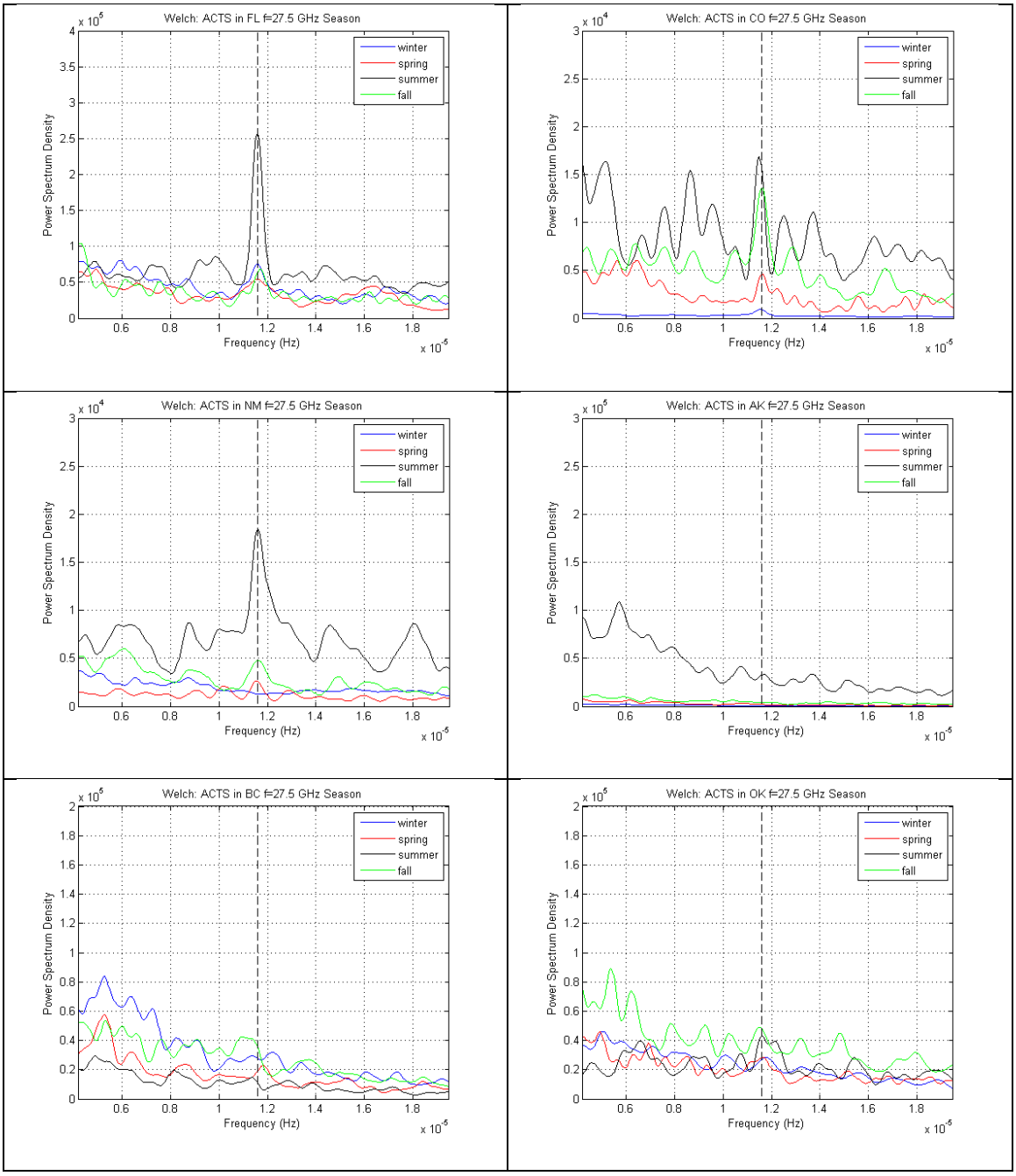

Figure 7.7: Spectrum content based on season for 27.5 GHz ACTS data

Based on the results obtained here as well as in Section 4.3 and 4.4, we limit our modeling exercise to only four of the ACTS sites that show strong presence of a solar day diurnal variation. They are Florida, Colorado, New Mexico and Oklahoma.

The cosine clear sky model is generated using a simple cosine formula,

$$y = \mathrm{A}\cos\big(2\pi f(t - B)\big) + DC \tag{7.30}$$

Where f is the signal frequency, given the value of a reciprocal of a solar day period of 24 hours, A is the amplitude, B is the time shift, and DC is a constant added to the sinusoidal amplitude variation. Figure 7.8 below gives a graphical representation of the cosine model

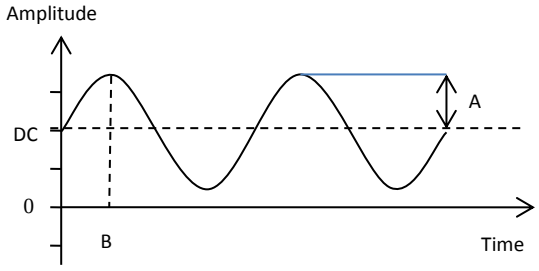

Figure 7.8: The cosine clear sky model

For a particular day, the magnitude of *A*, *B* and *DC* is estimated using the time series meteorological information together with the beacon attenuation values observed, described as follows:

- *A* is estimated by the difference between maximum estimated gaseous attenuation, and the minimum beacon attenuation (above a threshold). The gaseous attenuation is calculated based on the ITU-R formula given in Equation (7.1) to (7.18).
- *DC* is estimated by the average beacon attenuation value, amongst values that do not exceed a threshold. The threshold is set to exclude attenuation due to factors other than gaseous absorption.
- *B* is given an initial value of the time of maximum temperature detected for that day as this is when the clear sky variation is anticipated to peak. Using the aforementioned parameters, the initial cosine wave is generated. The value *B* is then varied, which is analogous to sliding the cosine model back and forth, to obtain the best possible fit with the observed beacon attenuation values.

The fit with the least root mean squared error (RMSE) is selected as the model, and is then extended for the next 6 consecutive days, as a prediction of the diurnal variation. The following Figure 7.9 till Figure 7.12 depict two samples each of the cosine clear sky model generated in Florida, Colorado, New Mexico and Oklahoma, for a period of 7 consecutive days. Each sample consists of 4 subplots. The top three consist of the beacon attenuation compared to concurrent temperature variation, estimated gaseous absorption, and the third with the cosine clear sky model. The last subfigure is the

absolute difference between the actual beacon attenuation and the cosine clear sky model, and between the actual beacon attenuation and the constant clear sky model. The constant clear sky model has a value that is the average estimated gaseous absorption of the first day. The horizontal axis is marked by the day's date.

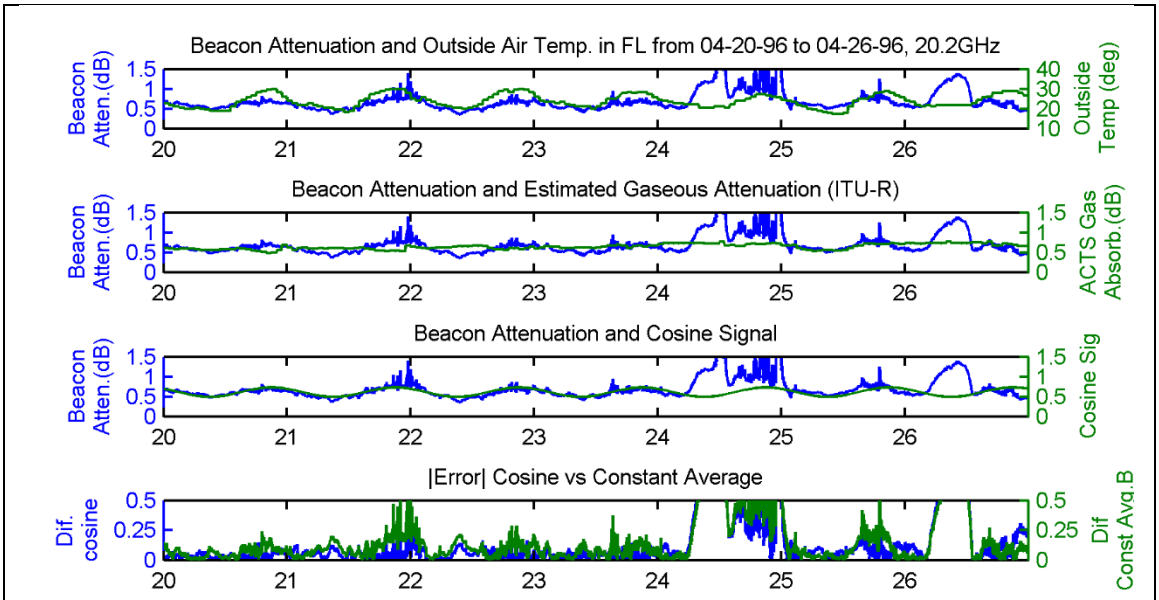

(a) Florida, 04/20/1996 to 04/26/1996

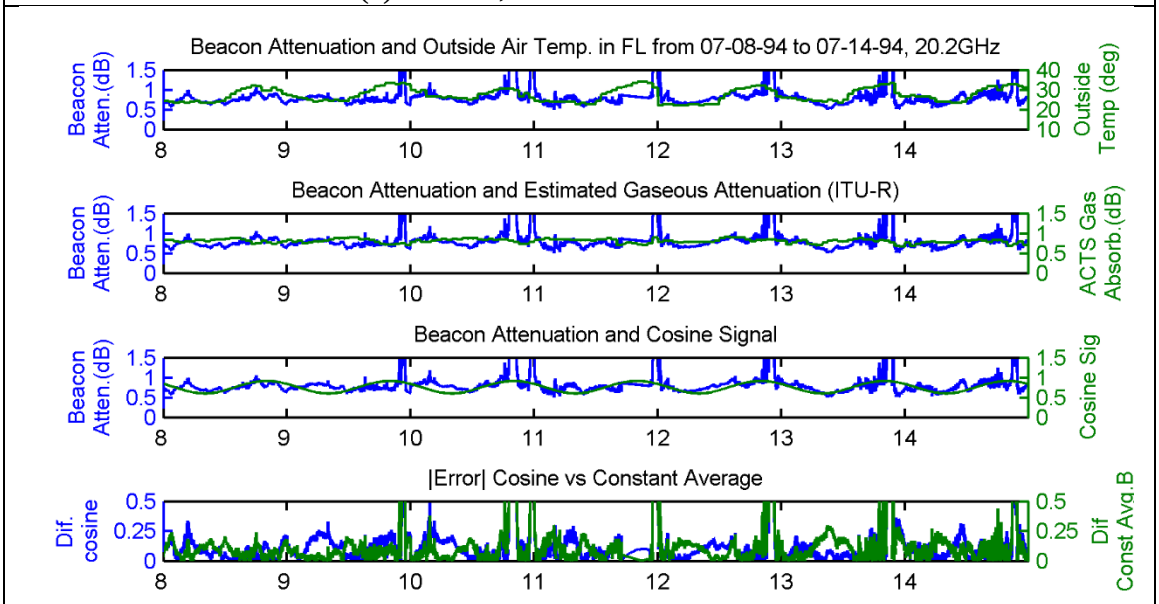

(b) Florida, 07/08/1994 to 07/14/1994

Figure 7.9: Cosine clear sky model sample in Florida

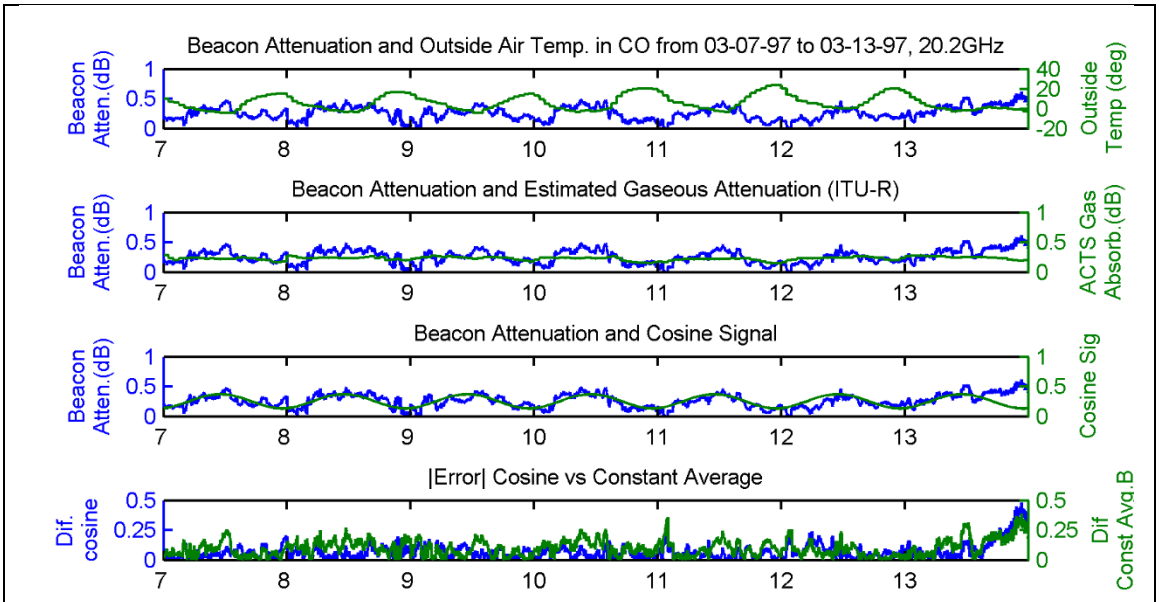

(a) 7 days set: 03/07/1997 to 03/13/1997

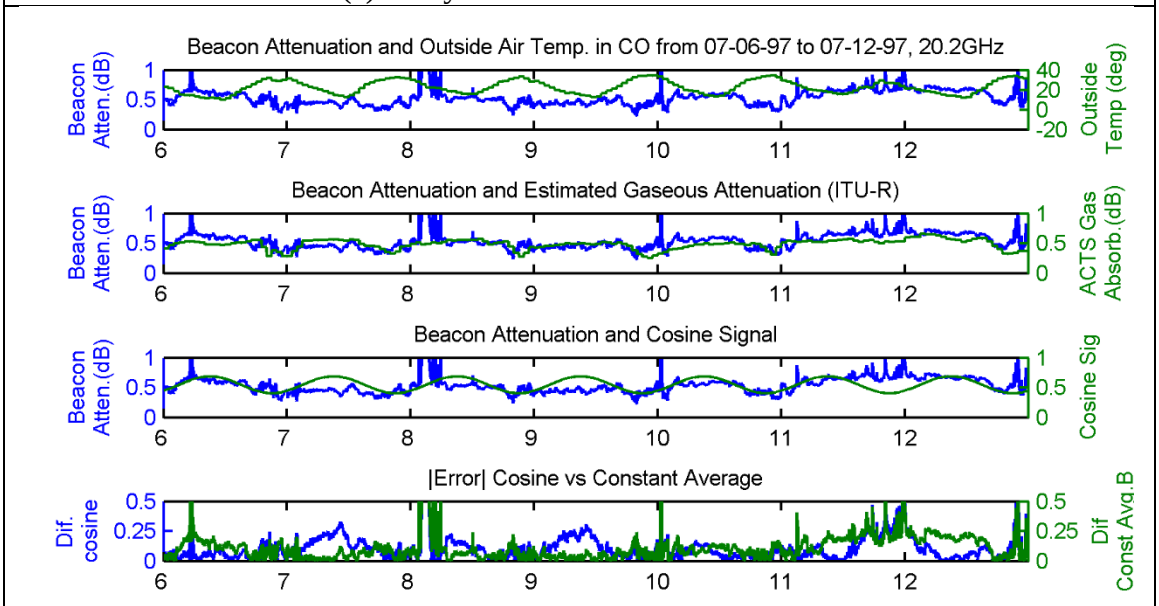

(b) 7 days set: 07/06/1997 to 07/12/1997

Figure 7.10: Cosine clear sky model sample in Colorado

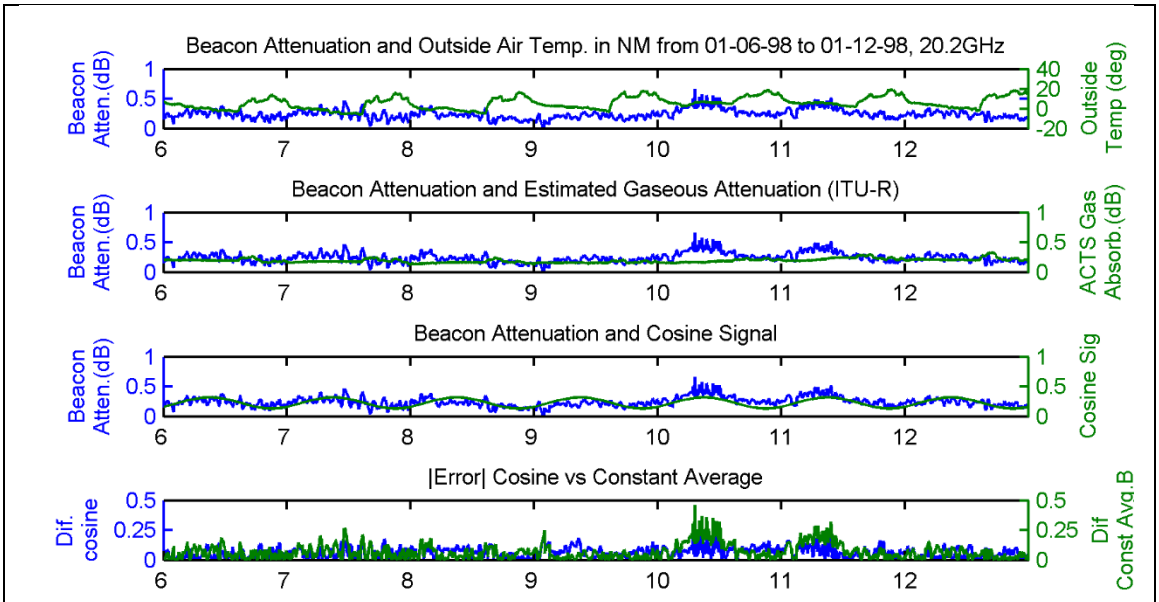

(a) 7 days set: 01/06/1998 to 01/12/1998

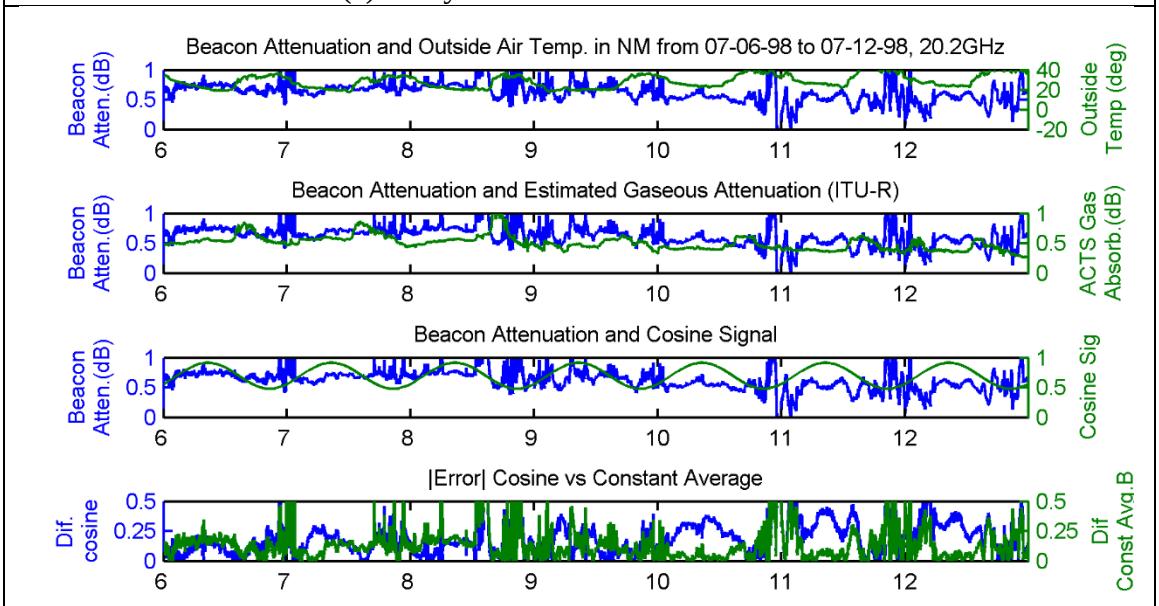

(b) 7 days set: 07/06/1998 to 07/12/1998

Figure 7.11: Cosine clear sky model sample in New Mexico

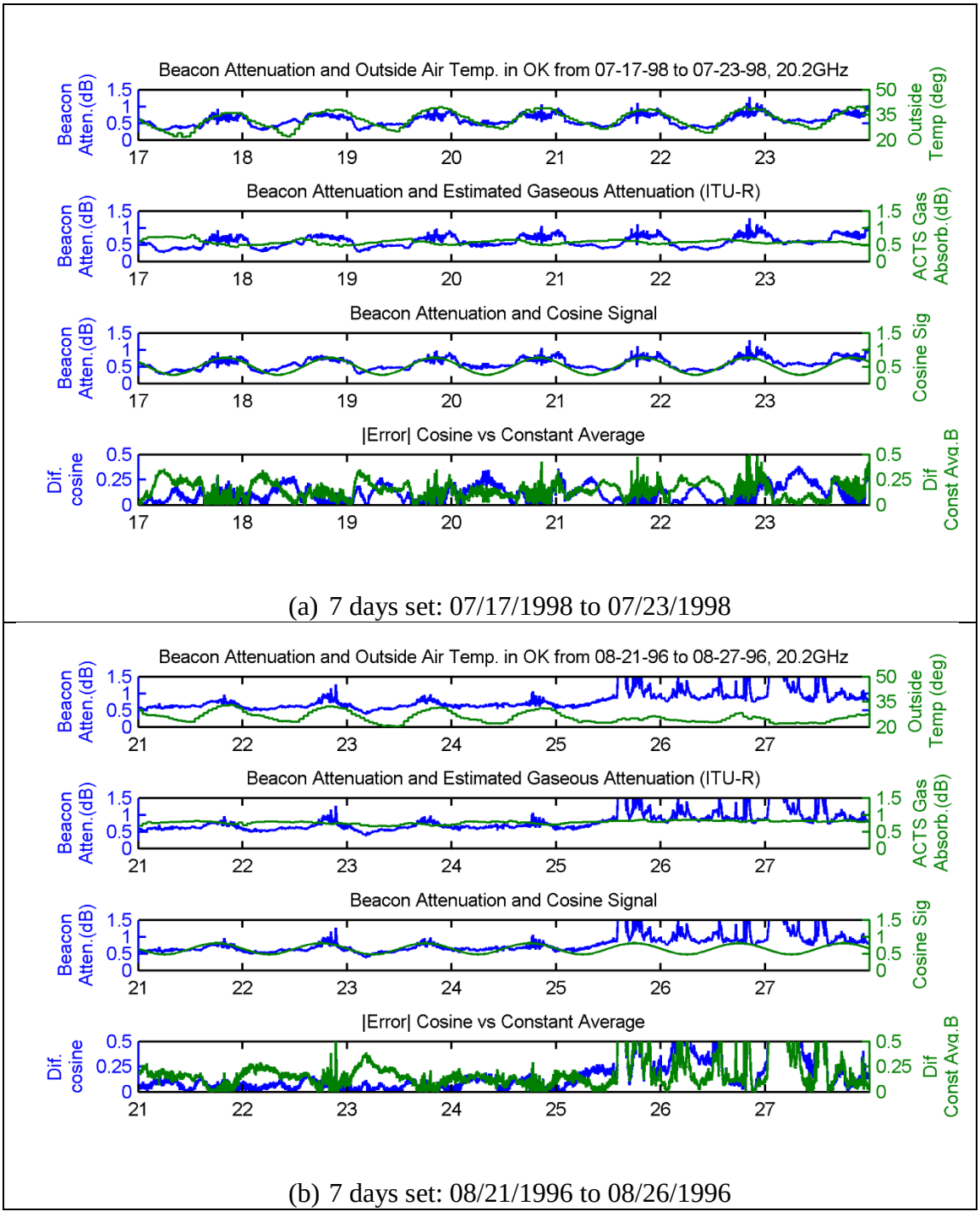

(a) 7 days set: 07/17/1998 to 07/23/1998

(b) 7 days set: 08/21/1996 to 08/26/1996

Figure 7.12: Cosine clear sky model sample in Oklahoma

7.2.1 Model evaluation

To evaluate the sinusoidal clear sky model, data from several sets of 7 continuous days with limited rain event were collected. The root mean squared error (RMSE) is used to measure the differences between values predicted by the model and the values observed. RMSE also represents the sample standard deviation of the differences between predicted and observed values. The RMSE formula is as follows

$$RMSE = \sqrt{\frac{\sum_{t=1}^{n}\left(X_{obs,t} - X_{model,t}\right)^2}{n}} \tag{7.31}$$

Where $X_{model,t}$ is the predicted value for time *t*, $X_{obs,t}$ is the actual observed value for time *t* and n is the total number of observations.

For comparison, an RMSE is also calculated if the mean clear sky level is a constant. The constant clear sky model is generated based on the average value of the estimated gaseous attenuation obtained from day 1 of each set. Table 7.1 below gives the RMSE between the cosine clear sky model and actual beacon attenuation data, and between a constant clear sky model and the actual 20 GHz beacon attenuation data, for each site. A graphical representation of Table 7.1 is given in Figure 7.13.

Table 7.1: RMSE of cosine and constant clear sky model for ACTS 20.2 GHz

	Florida		Colorado		New Mexico		Oklahoma	
Day	RMSE cosine	RMSE constant	RMSE cosine	RMSE constant	RMSE cosine	RMSE constant	RMSE cosine	RMSE constant
1	0.2112	0.2661	0.0832	0.1202	0.1169	0.1483	0.0859	0.1262
2	0.3292	0.3438	0.1097	0.1205	0.1000	0.1017	0.1397	0.1438
3	0.4790	0.4751	0.1615	0.1597	0.1167	0.1148	0.3009	0.2959
4	0.3724	0.3613	0.1581	0.1564	0.1788	0.1761	0.2513	0.2400
5	0.8920	0.8771	0.1902	0.1797	0.2060	0.2035	0.2562	0.2383
6	0.7861	0.7631	0.2218	0.2065	0.2321	0.2423	0.3277	0.3202
7	0.6231	0.5980	0.1659	0.1479	0.2669	0.2778	0.5658	0.5591

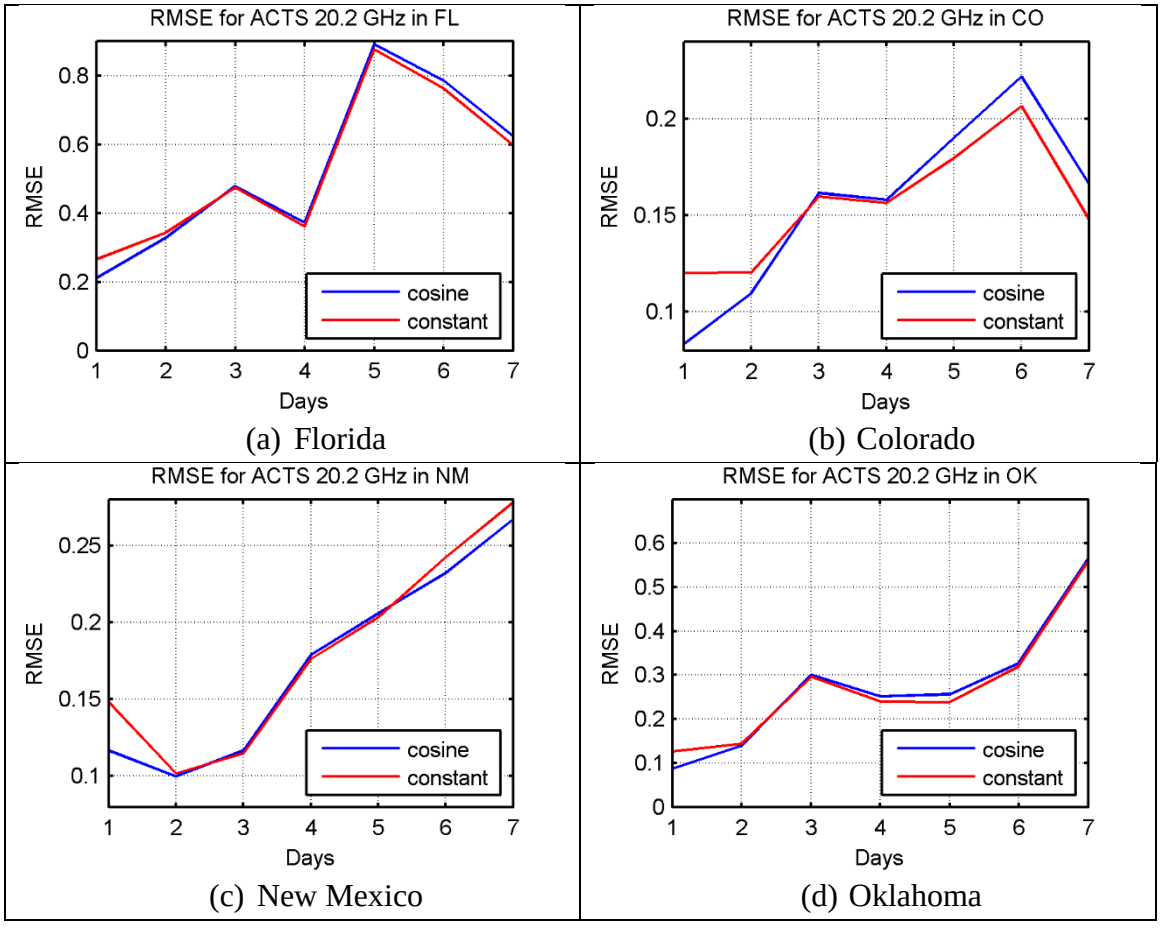

Figure 7.13: RMSE for the 20.2 GHz ACTS data

Referring to Figure 7.13, the lower RMSE for the cosine (blue plot) compared to the constant clear sky model (red plot) at Day 1 in all four sites showed that the algorithm is successful in modeling the diurnal variation using parameter obtained from that day. If this cosine model is then extended to predict the clear sky variation of the next day, the error increases, and at the 3rd day, it is slightly more than the error generated by the constant clear sky model.

Table 7.2 is the corresponding RMSE result for the 27.5 GHz ACTS data, with their graphical representation for each site given in Figure 7.14 below. The trend is similar, better performance for the initial day and for predicting the mean clear sky level for the next couple of days. However, the RMSE is higher for both cosine and constant clear sky model in the 27.5 GHz data.

Table 7.2: RMSE of cosine and constant clear sky model for ACTS 27.5 GHz

	Florida		**Colorado**		**New Mexico**		**Oklahoma**	
Day	RMSE cosine	RMSE constant	RMSE cosine	RMSE constant	RMSE cosine	RMSE constant	RMSE cosine	RMSE constant
1	0.4982	0.5360	0.1015	0.1175	0.1747	0.1964	0.1334	0.1515
2	0.4709	0.4770	0.1780	0.1792	0.1188	0.1212	0.1922	0.1895
3	0.8820	0.8708	0.1339	0.1279	0.2429	0.2439	0.3655	0.3452
4	0.8503	0.8286	0.1607	0.1490	0.2359	0.2361	0.3123	0.2891
5	1.4263	1.4096	0.2367	0.2327	0.2961	0.2995	0.3328	0.2988
6	1.3529	1.3195	0.2970	0.2892	0.2974	0.3071	0.4186	0.3903
7	1.0085	0.9683	0.2793	0.2702	0.3788	0.3893	0.8666	0.8469

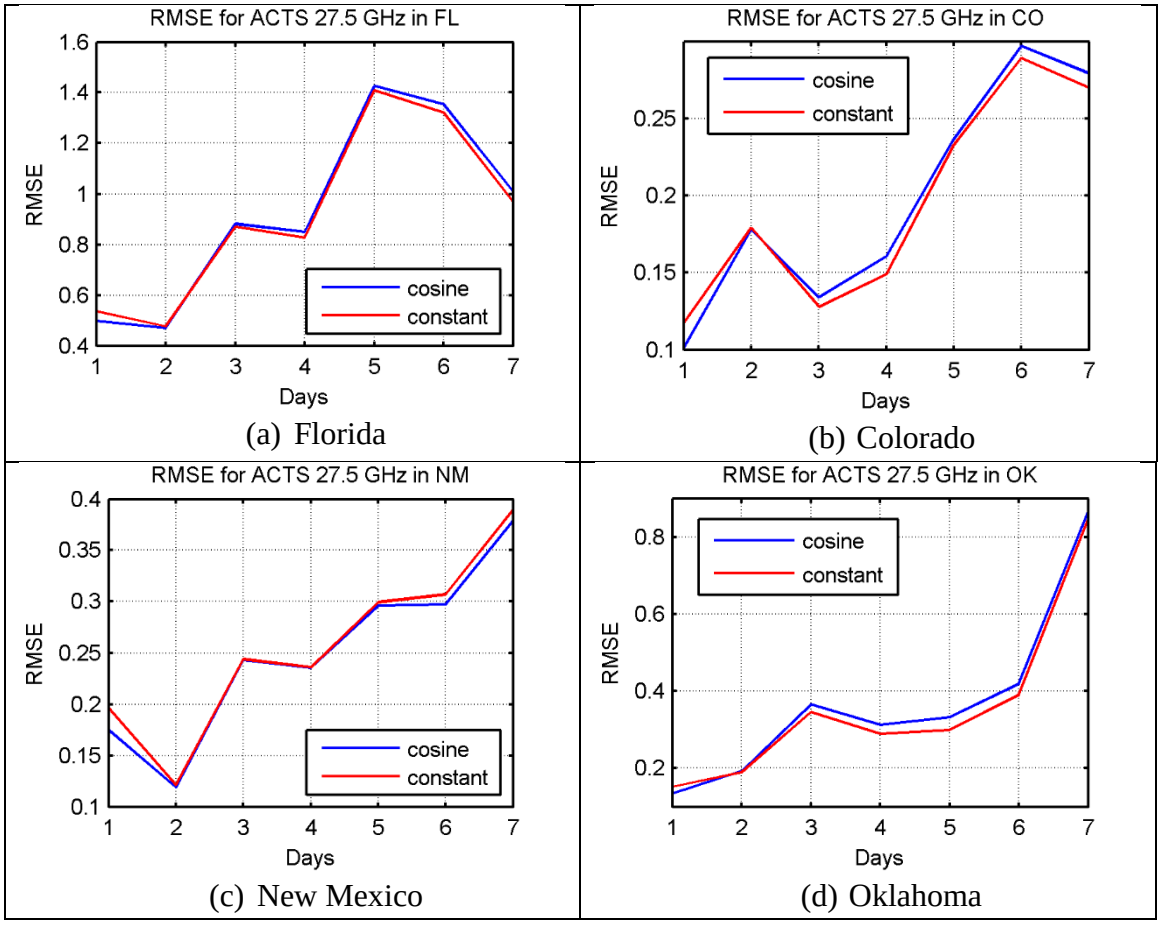

Figure 7.14: RMSE for the 27.5 GHz ACTS data

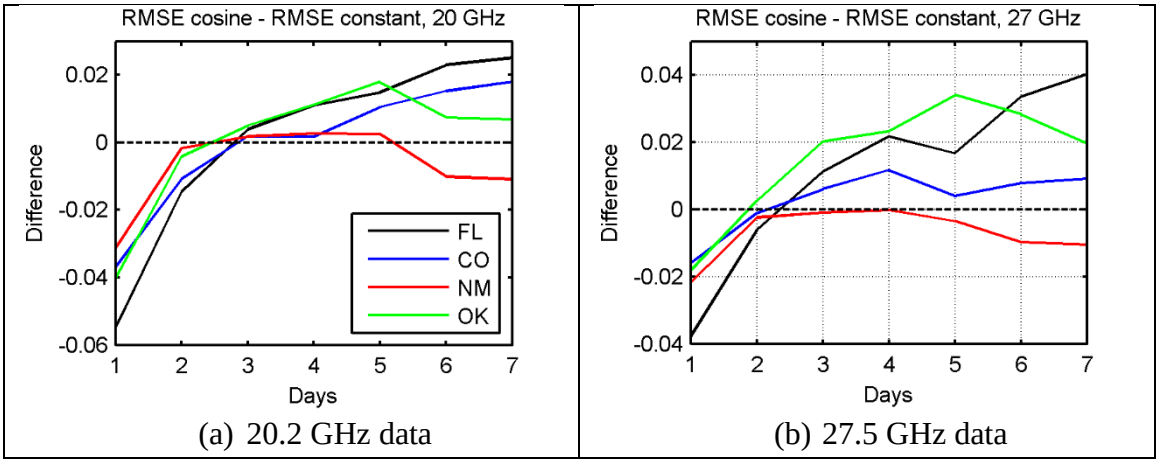

(a) 20.2 GHz data (b) 27.5 GHz data

Figure 7.15: Difference between RMSE cosine and constant clear sky model

Figure 7.15 gives a plot of the difference between RMSE for the cosine clear sky model and RMSE for constant clear sky model for a better interpretation of Figure 7.13 and Figure 7.14. The times when the differences are negative showed that the cosine is better than the constant clear sky model. For both frequencies, the cosine clear sky model is most beneficial to Florida. Thus for significant improvement, the cosine clear sky model here is more suitable for sites with a warm climate, or only implemented during the warm season. It can be used to predict the variation of the next 2 days with reasonable accuracy, in comparison to a constant clear sky mean level. Between the two frequencies, the model performs better in the 20.2 GHz database. It models and predicts the diurnal variation better, as seen by the larger negative value of the '*RMSE difference*' in Figure 7.15 (a).

For a better model, a more dynamic algorithm for determining model parameters can be employed, and other factors that contribute to the clear sky variation, such as cloud cover, can be taken into consideration.

The average value of the cosine clear sky model parameters of *A, B* and *DC* were collected and tabled according to season in Table 7.3 and Table 7.4, for the 20.2 and 27.5 GHz respectively.

Table 7.3: Average parameter values of the 20.2 GHz cosine clear sky model

Season	Florida			Colorado			New Mexico			Oklahoma		
	A	B	DC	A	B	DC	A	B	DC	A	B	DC
Spring	0.17	0.85	0.53	0.11	-7.38	0.29	0.06	-8.59	0.21	0.10	-0.31	0.37
Summer	0.16	0.36	0.78	0.18	-10.00	0.55	0.14	-6.55	0.43	0.12	-0.91	0.71
Fall	0.19	-0.78	0.64	0.12	-9.57	0.29	0.09	-7.67	0.29	0.12	1.00	0.41
Winter	0.15	-4.00	0.57	0.11	-9.27	0.22	0.07	-10.82	0.23	0.08	-2.25	0.31
Total set of 7 days	63			65			63			66		

The parameters of the cosine clear sky model for the 20 GHz show a distinctive pattern with the climate of each site. For example, in temperate climate such as Colorado and New Mexico, the amplitude variation (*A*), and the constant increment to the mean level (*DC*), are largest during summer. The average value of *A* showed that the amplitude of the variation in New Mexico is smallest compared to other sites, thus also having the least improvement as showed by the RMSE difference in Figure 7.15(a).

B gives the time shift needed from the time temperature is maximum, to obtain a maximum fit between the cosine clear sky model and the actual beacon attenuation. For tropical/subtropical climate such as Florida and Oklahoma, the required time shift is ±1hour, and this increases during winter. For Colorado and New Mexico, the required time shift is between 7 to 10 hours prior to the time temperature is maximum, with no apparent differences in season. Both Colorado and New Mexico are at a higher elevation above sea level, and have low humidity. All meteorological data were collected by sensors provided at the propagation terminals to record data continuously from the surface.

Table 7.4: Average parameter values of the 27.5 GHz cosine clear sky model

Season	Florida			Colorado			New Mexico			Oklahoma		
	A	B	DC	A	B	DC	A	B	DC	A	B	DC
Spring	0.18	0.36	0.49	0.10	-8.00	0.25	0.08	-3.39	0.18	0.14	-2.19	0.33
Summer	0.19	-1.32	0.63	0.10	-4.29	0.42	0.10	-5.05	0.36	0.18	-10.39	0.58
Fall	0.22	0.70	0.46	0.12	-5.30	0.30	0.09	-5.19	0.27	0.16	-4.25	0.40
Winter	0.19	-6.83	0.47	0.09	-6.00	0.23	0.08	-3.83	0.19	0.13	-1.93	0.22
Total set of 7 days	52			44			67			66		

As noted earlier, the performance of the cosine clear sky model for the 27 GHz was poorer than the 20 GHz. Comparing the set of parameter values for the two frequency databases, there are considerable differences detected in Colorado, for values set for parameter B, the time shift.

Figure 7.16 to Figure 7.19 gives samples of cosine clear sky model in the 20.2 GHz and 27.5 GHz for similar dates. The 27.5 GHz beacon attenuation data seems to be experiencing higher instabilities, such as sudden peak and jitters, compared to its 20.2 GHz counterpart, which caused errors in establishing the cosine clear sky model.

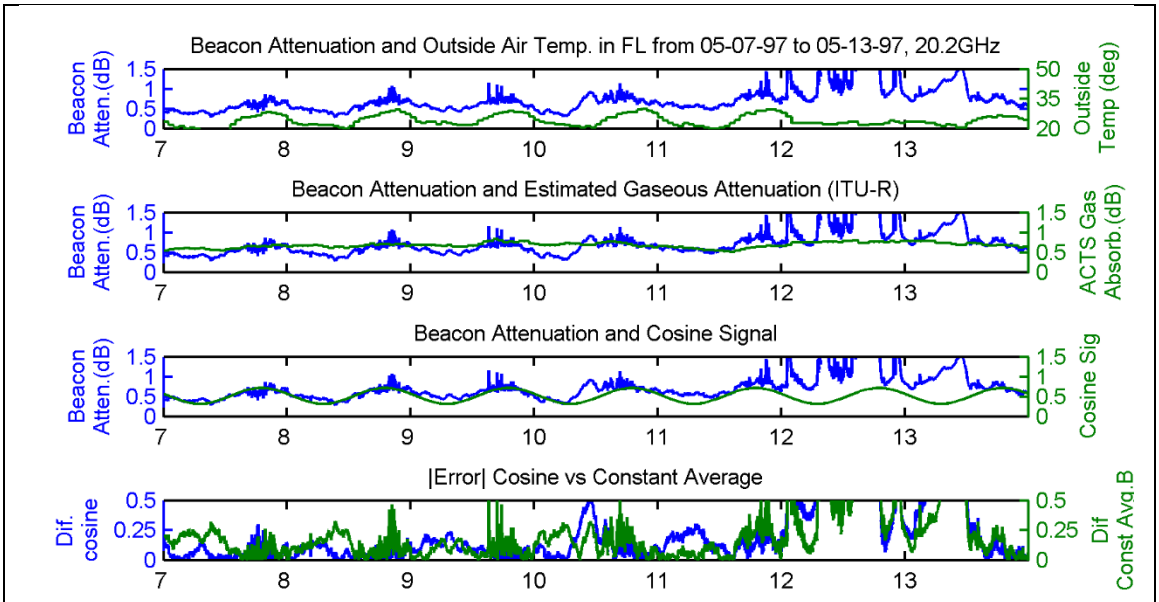

(a) 20 GHz Florida

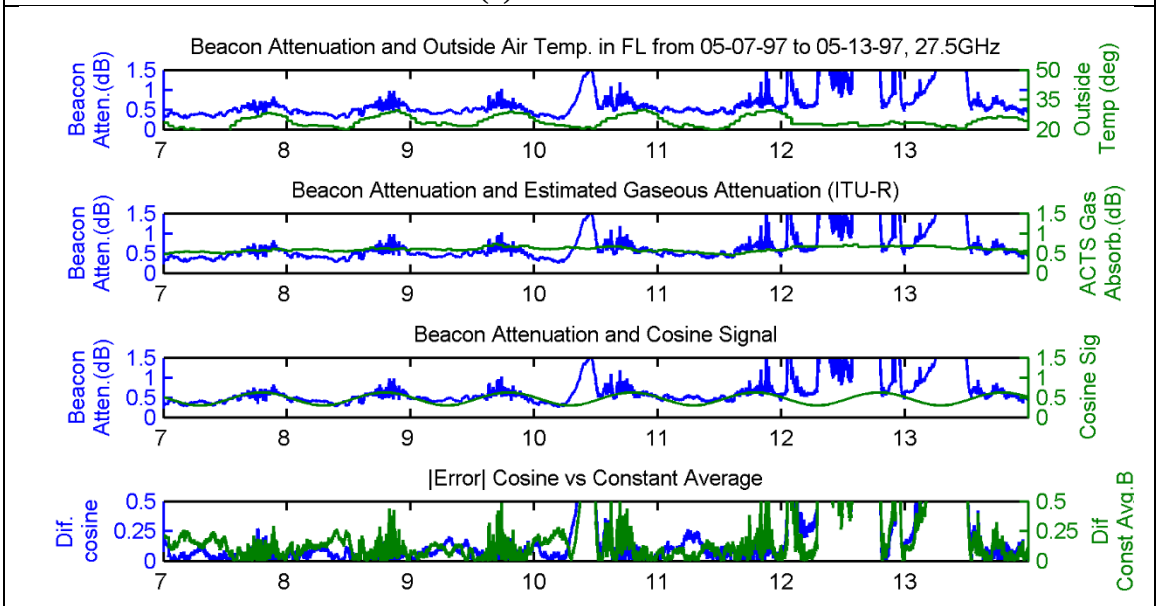

(b) 27.5 GHz Florida

Figure 7.16: Cosine clear sky model comparison in Florida for 20.2 and 27.5 GHz

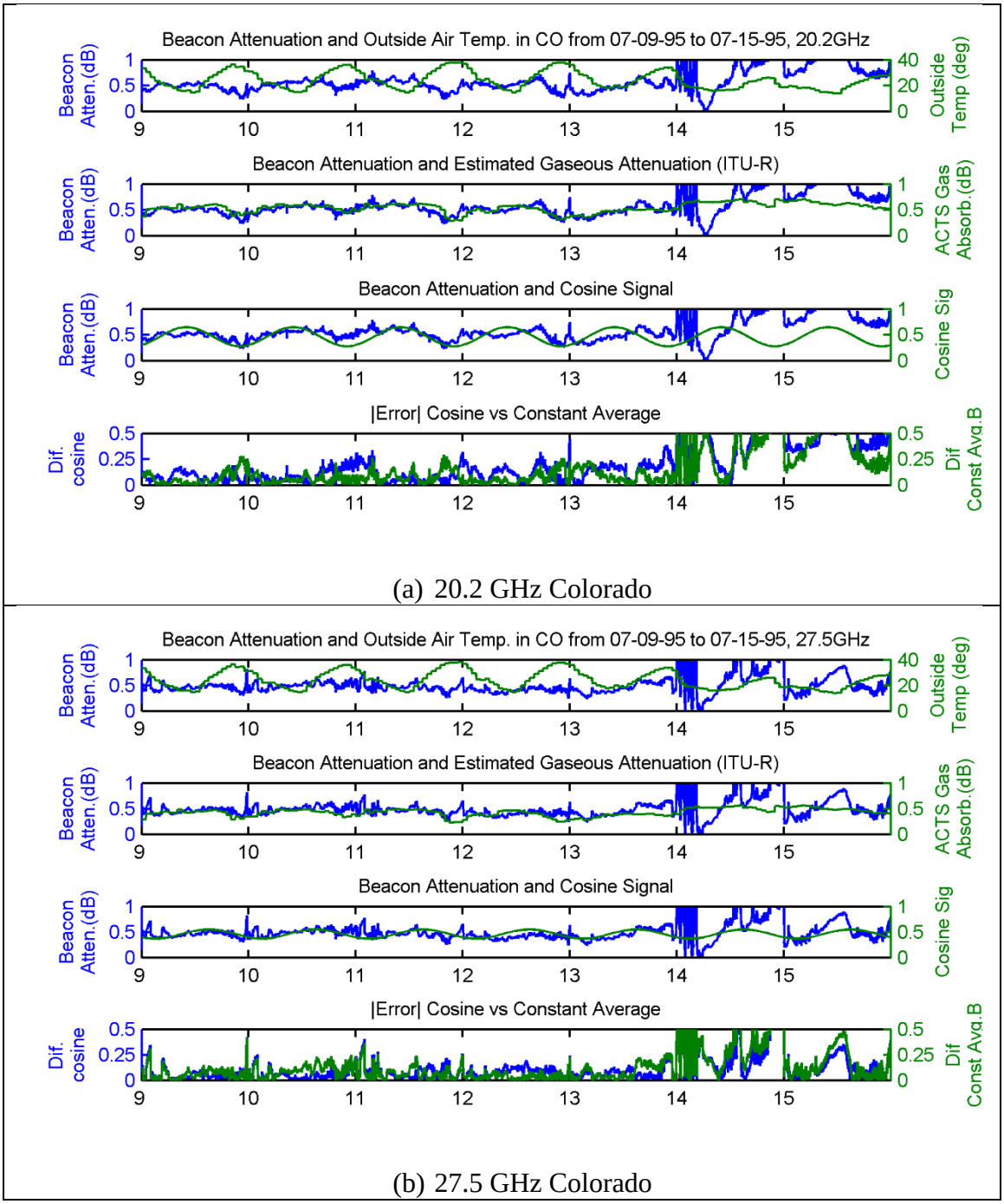

Figure 7.17: Cosine clear sky model comparison in Colorado for 20.2 and 27.5 GHz

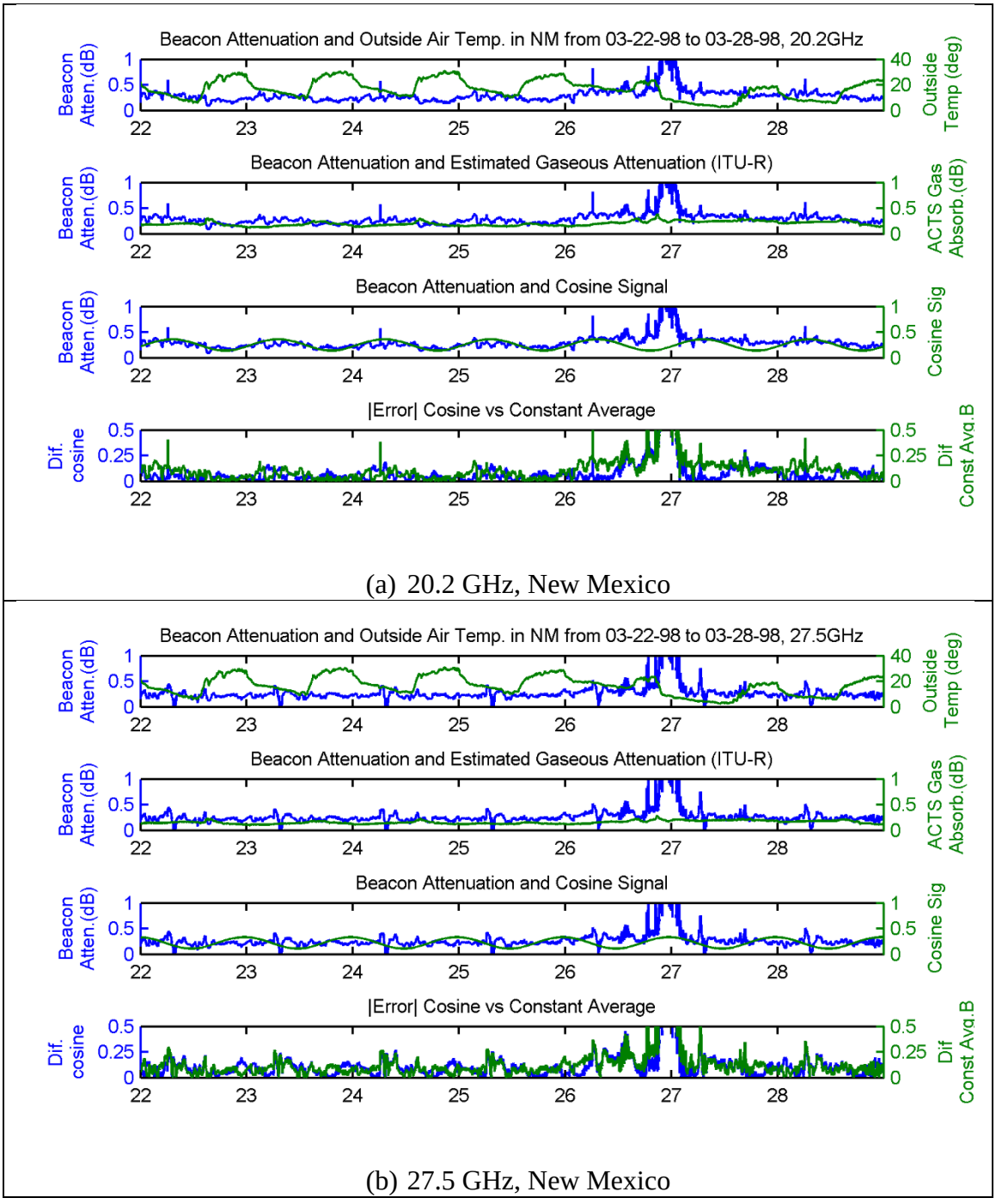

Figure 7.18: Cosine clear sky model comparison in NM for 20.2 and 27.5 GHz

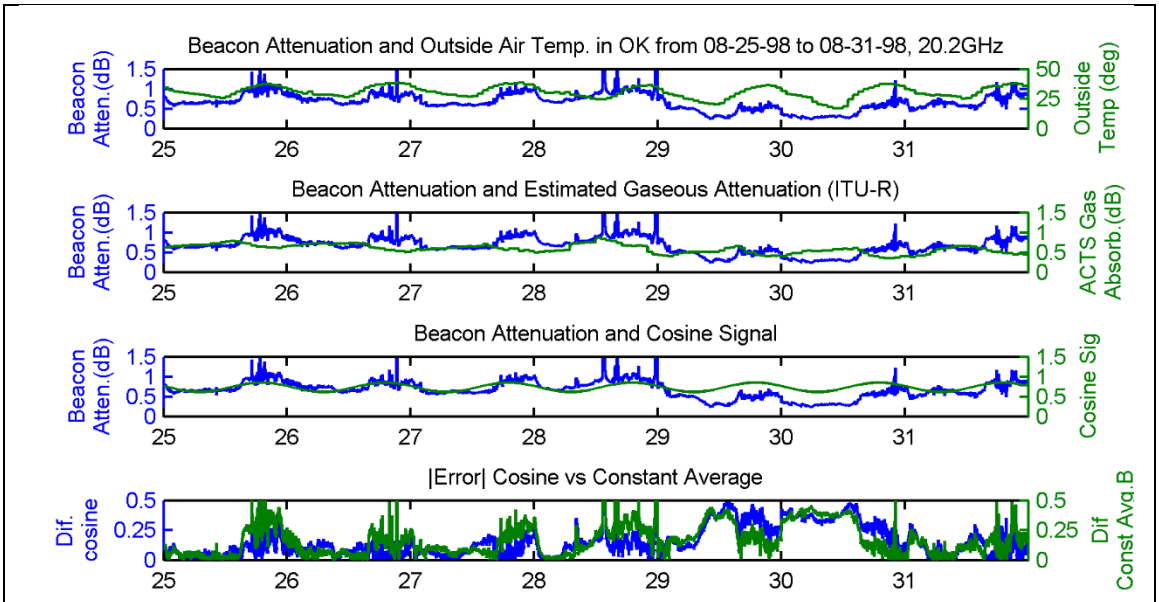

(a) 20.2 GHz, Oklahoma

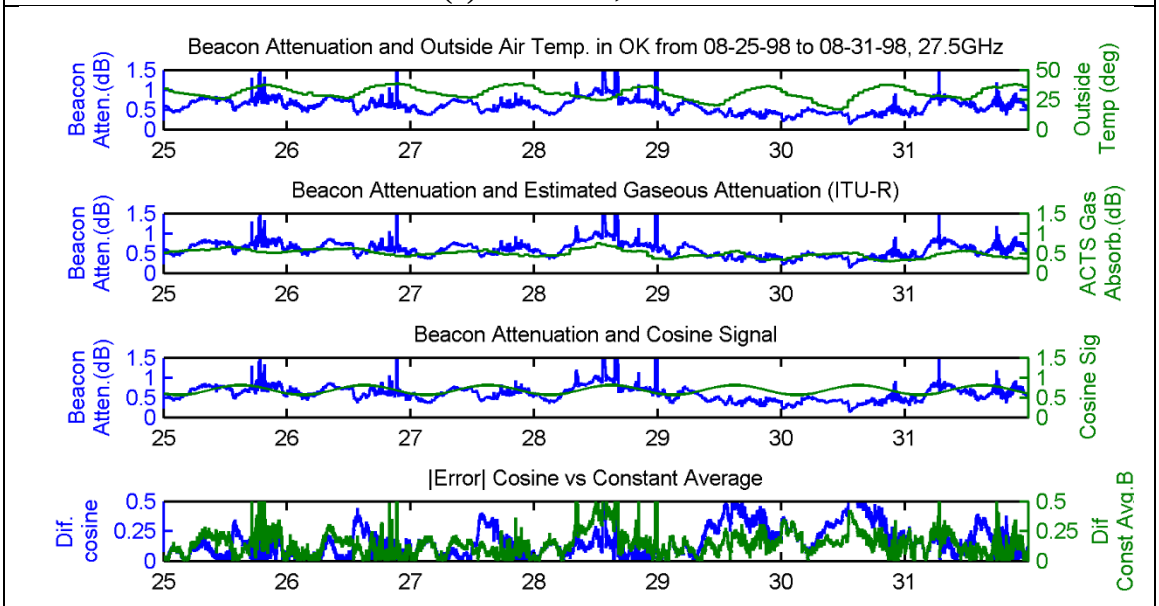

(b) 27.5 GHz, Oklahoma

Figure 7.19: Cosine clear sky model comparison in Oklahoma for 20.2 and 27.5 GHz

7.3 Discussion

The seasonal variation detected in the ACTS and Texas database can be closely estimated using the gaseous attenuation model provided in the ITU recommendation P676-9. The seasonal variation was highest in Alaska, with more than a 3dB difference between the maximum detected in summer and minimum detected during winter.

It was also possible to model the mean clear sky level using a cosine formula, with a period of 24 hours and its other parameters such as amplitude, vertical and horizontal shift estimated from the meteorological data together with the observed average beacon attenuation. The cosine clear sky model gives a good prediction if the model is estimated using parameters obtained from the previous day or two, and used only on sites that have significant presence of a diurnal variation in its received signal level.

In the references for the Olympus propagation experiment [27], the diurnal variation of the received signal are mostly attributed to the interaction of the spacecraft proper motion with the earth-terminal antenna pattern, with clear-air absorption introducing a constant loss, together with a slowly varying loss that depends on the local weather. A sixth order polynomial interpolation technique was used to remove diurnal variation caused by the satellite orbit. This technique allowed them to handle most rainy periods without using previous- or following-day data. The signal both provides the diurnal fluctuation and is used to set the absolute reference level. The method was reported to work very well during clear days and for as long as 30 hours.

The Texas experiment also suggested that the diurnal variation were due to satellite motion [58]. It uses six min averaged data points to establish the clear air absorption, and using a seasonal decomposition algorithm on seven days of data to reveal a diurnal (due to satellite motion) and a slowly varying aperiodic component (due to satellite drift) with occasional jumps (due to satellite maneuvers) [24].

CHAPTER 8: CONCLUSION AND FUTURE WORK

We have shown that *atmospheric tides,* first noticed in an experiment in a tropical, very wet country, is not just an equatorial phenomenon. To do this, we have successfully extracted satellite propagation data from four different databases. These databases contain time series data of the received signal level from geostationary satellite beacons together with inferred attenuation from co-located radiometer directed along the same path. Some databases also contain meteorological time series data collected at or near the receiver.

Upon investigation, the time data plot of the received beacon signal level and inferred attenuation from the radiometer contained concomitant seasonal as well as diurnal variations. Results from three different spectral estimation techniques showed that the diurnal variation detected in the beacon and radiometer were both of a solar day periodicity. This showed that solar heating effects are driving the diurnal variation observed, and that they are not satellite induced. There is also a general trend of decreasing solar tidal effect as the climate becomes less warm and humid. The only site that did not show evidence of a solar day variation was in Fairbanks, Alaska. This site is both the coldest, and has the lowest elevation angle. Other possible causes of variations in received beacon level such as front end instabilities, as well as a possible noise contribution from the antenna side lobes, were found to be untenable.

In some warmer and more humid sites, a sidereal and anti-sidereal peak was also detected to the right and left of the solar peak, respectively. These side peaks are found mainly in cosmic ray research. They are generated when a daily solar variation is amplitude modulated by a seasonal variation of one cycle/year, producing sidebands at the sidereal and anti-sidereal frequencies.

The seasonal variation detected in both the ACTS and Texas database were closely estimated using the gaseous attenuation model provided in the ITU recommendation P676-9. This calculation uses meteorological values such as averages of pressure, temperature and humidity together with the earth station's elevation angle with respect to the satellite, to calculate attenuation along the path in clear sky. From the result of the simulation we were able to identify as well as quantify the sources of the mean clear sky variation. The seasonal variation was highest in Alaska, with more than a 3dB difference between the maximum detected in summer and minimum detected during winter.

It was also possible to model the mean clear sky level using a cosine formula, with a period of 24 hours and its other parameters such as amplitude, vertical and horizontal shift estimated from the meteorological data together with the observed average beacon attenuation. The cosine clear sky model gives a better prediction than a constant clear sky value if the model is estimated using parameters obtained from the previous day or two, and used only on sites that have significant presence of a diurnal variation in its received signal level.

8.1 Contribution and recommendation

In short, the contribution of this dissertation can be listed as:

- The diurnal variation seen in both satellite beacon and co-located radiometer data were confirmed as solar heating effect and not caused by satellite instabilities. This variation has a solar day period of 24 hours.
- The sidereal and anti-sidereal components are also detected in the spectrum estimation result of both beacon and radiometer data from warm climate sites. They can be reproduced with amplitude modulation of a daily solar variation by a seasonal variation of one cycle/year.
- The source of the seasonal and diurnal variations were identified as heating effects in the atmosphere. Both variations were found to be tractable to modeling.

From the result of this investigation, it is recommended that:

- The seasonal and diurnal variation of the mean clear sky level are considered in link budget determination. This produces a more accurate fade margin description to establish performance and availability criteria in systems with limited link operating margins.
- The cosine clear sky model is applied to assist in evaluating the true rain fade level as the radiometer will not be able to assist in the removal of any signal variations due to the atmosphere.

8.2 Future work

Solar and sidereal effects are well known phenomena in atmospheric physics, but they have been largely ignored in communication satellite research. It is interesting to

note that the sidereal and anti-sidereal spectra required many years' worth of data to become apparent. Examination on the spectral content of the specific attenuation due to dry air (γ_0) and water vapor (γ_w) for each site showed that the water vapor absorption is the main contributor to the sidereal component, while the oxygen absorption produces a solar variation effect [88]. Both γ_0 and γ_w were estimated using the approximate method found in Annex 2 of ITU-R 676-9 (2012) using meteorological data stored in the ACTS database. The results for Florida at the frequency of 20.2 GHz were given in Figure 8.1.

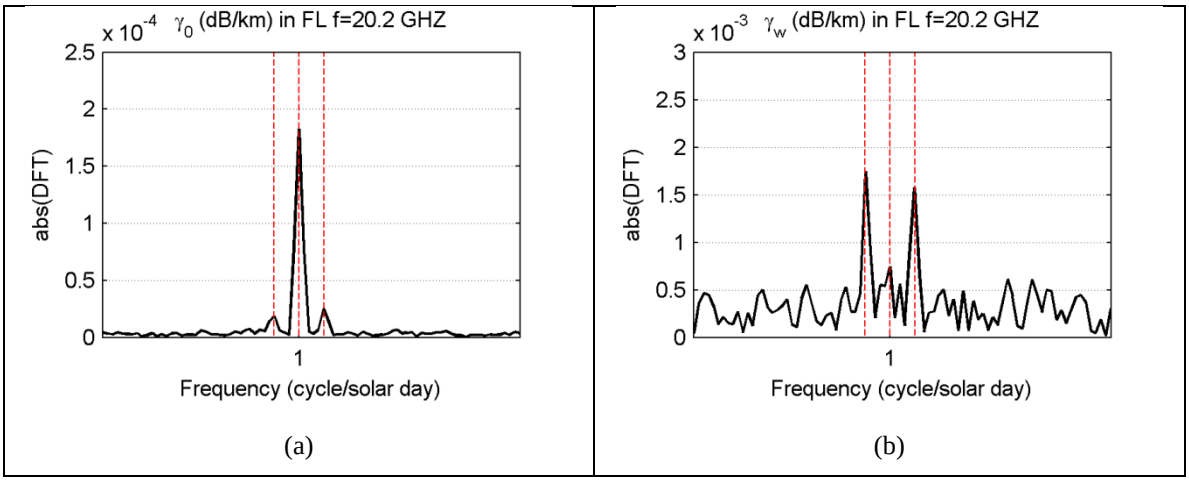

Figure 8.1: Spectrum content of (a) $\gamma_0$and (b) γ_w in Florida at 20.2GHz

Further investigation can be made to find out why the presence of sidereal and anti-sidereal component is not seen in all of the spectral estimation results and if there is any relationship with the frequency of the transmitting beacon. Another observation is that, the anti-sidereal peak and the sidereal peak were frequently not of a similar amplitude level. Most of the time, it is the anti-sidereal peak that is slightly larger than

the sidereal peak, despite the fact that the anti-sidereal time corresponds to no physical viewpoints, unlike the sidereal time.

A lunar cycle was also detected in the ACTS beacon and radiometer signal variation for the site in Florida and Colorado. It would also be interesting to find out what affect the moon has on the beacon signal variation.

A lot can be improved on the simple mean clear sky cosine model presented here. Other factors that contribute to the clear sky variation, such as the cloud cover for example, can also be taken into consideration.

Investigation of potential atmospheric tide effects in the communications frequency bands above Ka-band is also another area that requires further research.

REFERENCES

[1] F. Barbaliscia, M. Boumis, and A. Martell, "Characterization of Atmospheric Attenuation in the Absence of Rain in Europe in SHF/EHF Bands for VSAT Satcom Systems Applications," presented at the Ka Band Conference, Sorrento, Italy, 1997, pp. 293–298.

[2] Q. W. Pan, J. E. Allnutt, and C. Tsui, "Evidence of atmospheric tides from satellite beacon experiment," *Electron. Lett.*, vol. 42, no. 12, p. 706, 2006.

[3] G. Maral, *Satellite communications systems: systems, techniques and technology*, 5th ed. Chichester, West Sussex, U.K: John Wiley, 2009.

[4] J. E. Allnutt and D. V. Rogers, "Low-fade-margin system: propagation considerations and implementation approaches," presented at the Antennas and Propagation, 1989. ICAP 89., Sixth International Conference on (Conf. Publ. No.301), 1989, pp. 6 –9 vol.2.

[5] INTELSAT Earth Station Standards (IESS), "Document IESS-207 (Rev.4): Antenna and Wideband RF Performance Characteristics of C-Band Earth Stations Accessing the INTELSAT Space Segment." INTELSAT, 07-Oct-2012.

[6] INTELSAT Earth Station Standards (IESS), "Document IESS-208 (Rev.6): Antennal and Wideband RF Performance Characteristics of Ku-Band Earth stations Accessing The INTELSAT Space Segment for Standard Services." INTELSAT, 07-Oct-2012.

[7] J. E. Allnutt, *Satellite-to-ground radiowave propagation*. London: Institution of Engineering and Technology, 2011.

[8] G. Brussaard and D. V. Rogers, "Propagation considerations in satellite communication systems," *Proc. IEEE*, vol. 78, no. 7, pp. 1275 –1282, Jul. 1990.

[9] "The INTELSAT propagation measurements program," presented at the International Conference on Antennas and Propagation (ICAP 81), 1981, pp. 118–123.

[10] D. Chakraborty, F. Davarian, and W. L. Stutzman, "The Ka-band propagation measurements campaign at JPL," *IEEE Antennas Propag. Mag.*, vol. 35, no. 1, pp. 7 –13, Feb. 1993.

[11] J. W. Kiebler, "ACTS propagation experiments," presented at the Telesystems Conference, 1992. NTC-92., National, 1992, pp. 5/1 –5/6.

[12] X. Boulanger, G. Carrie, L. Castanet, L. Casadebaig, and B. Gabard, "Statistics of total attenuation and fade dynamics from measurements in Toulouse of the 19.7 GHz beacon of Eutelsat Hot Bird 6," presented at the 2012 6th European Conference on Antennas and Propagation (EUCAP), 2012, pp. 81 –85.

[13] C. Amaya, T. Nguyen, A. Rocha, J. M. Riera, A. Benarroch, P. Garcia-del-Pino, J. M. Garcia-Rubia, G. Carrie, and L. Castanet, "Joint results of 20 GHz recent earth-space propagation experiments in Canada and europe," presented at the Proceedings of the 5th European Conference on Antennas and Propagation (EUCAP), 2011, pp. 3384 –3388.
[14] Y. Karasawa and Y. Maekawa, "Ka-band Earth-space propagation research in Japan," *Proc. IEEE*, vol. 85, no. 6, pp. 821 –842, Jun. 1997.
[15] L. J. Ippolito, R. D. Kaul, and R. G. Wallace, *Propagation effects handbook for satellite systems design : A summary of propagation impairments on 10 to 100 GHz satellite links with techniques for system design*. Washington, DC, USA: National Aeronautics and Space Administration, 1983.
[16] *OPEX (Olympus Propagation Experimenters), Second Workshop of the Olympus Propagation Experimenters*, vol. 1–4. Noordwijk, The Netherlands: ESA WPP, 1994.
[17] "COST 205 Final Report: Influence of the atmosphere on radiopropagation on satellite-earth paths at frequencies above 10 GHz," Commission of the European Communities, EUR 9923 EN, 1985.
[18] "COST 255 Final Report: Radiowave propagation modeling for new sitcom services at Ku-band and above," ESA Publications Division, SP-1252, 2002.
[19] A. Dissanayake, J. Allnutt, and F. Haidara, "A prediction model that combines rain attenuation and other propagation impairments along Earth-satellite paths," *IEEE Trans. Antennas Propag.*, vol. 45, no. 10, pp. 1546 –1558, Oct. 1997.
[20] W. L. Stutzman, "Prediction of rain effects on earth-space communication links operating in the 10 to 35 GHZ frequency range," *Int. J. Satell. Commun.*, vol. 7, no. 1, pp. 37–45, 1989.
[21] L. J. Ippolito, *Satellite communications systems engineering: atmospheric effects, satellite link design and system performance*. Chichester, England: Wiley, 2008.
[22] W. L. Stutzman, T. Pratt, A. Safaai-Jazi, P. W. Remaklus, J. Laster, B. Nelson, and H. Ajaz, "Results from the Virginia Tech propagation experiment using the Olympus satellite 12, 20 and 30 GHz beacons," *IEEE Trans. Antennas Propag.*, vol. 43, no. 1, pp. 54 –62, Jan. 1995.
[23] R. K. Crane, X. Wang, D. B. Westenhaver, and W. J. Vogel, "ACTS propagation experiment: experiment design, calibration, and data preparation and archival," *Proc. IEEE*, vol. 85, no. 6, pp. 863 –878, Jun. 1997.
[24] W. J. Vogel, G. W. Torrence, and J. E. Allnutt, "Rain fades on low elevation angle Earth-satellite paths: comparative assessment of the Austin, Texas, 11.2 GHz experiment," *Proc. IEEE*, vol. 81, no. 6, pp. 885 –896, Jun. 1993.
[25] N. Mohamed Shah and J. Allnutt, "Additional evidence of atmospheric tides on satellite-to-ground paths," presented at the 2012 Symposium & Wireless Summer School, Virginia Tech, 2012.
[26] J. Koller, G. Diermaier, and F. Murr, "Software Requirements Document, Part 1, Data Processing Software." ESA Contr. 7609, Nov-1988.

[27] W. L. Stutzman, F. Haidara, and P. W. Remaklus, “Correction of satellite beacon propagation data using radiometer measurements,” *Microw. Antennas Propag. IEE Proc.*, vol. 141, no. 1, pp. 62 –64, Feb. 1994.
[28] R. M. Allnutt, T. Pratt, W. L. Stutzman, and J. B. Snider, “Use of radiometers in atmospheric attenuation measurements,” *Microw. Antennas Propag. IEE Proc.*, vol. 141, no. 5, pp. 428 –432, Oct. 1994.
[29] ITU-R Rec. P.676-9, “Attenuation by atmospheric gases.” International Telecommunication Union, Geneva, Feb-2012.
[30] ITU-R Rec. P.618-10, “Propagation data and prediction methods required for the design of Earth-space telecommunication systems.” International Telecommunication Union, Geneva, Oct-2009.
[31] Scott A. Borgsmiller, “Effects of Atmospheric Scintillation in Ka-band Satellite Communications,” Georgia Institute of Technology, Georgia, USA, 1998.
[32] Laurent Castanet, “Fade Mitigation Techniques for new SatCom systems operating at Ka and V bands,” PhD of SUPAERO, Toulouse, France, 2001.
[33] W. J. Vogel, G. W. Torrence, and J. E. Allnutt, “Scintillation fading on a low elevation angle satellite path: assessing the Austin experiment at 11.2 GHz,” presented at the Eight International Conference on Antennas and Propagation, 1993, vol. 1, pp. 48–51.
[34] E. Couto de Miranda, M. S. Pontes, L. A. R. da Silva Mello, and M. P. de Almeida, “Choice of standard medium temperature for tropical and equatorial climates: Comparison between radiometric and satellite beacon attenuation data on two 12 GHz links in Brazil,” *Electron. Lett.*, vol. 34, no. 21, p. 2002, 1998.
[35] L. J. Ippolito, “Propagation effects and system performance considerations for satellite communications above 10 GHz,” presented at the , IEEE Global Telecommunications Conference, 1990, and Exhibition. “Communications: Connecting the Future”, GLOBECOM ’90, 1990, pp. 89 –91 vol.1.
[36] M.-S. Alouini, S. A. Borgsmiller, and P. G. Steffes, “Channel characterization and modeling for Ka-band very small aperture terminals,” *Proc. IEEE*, vol. 85, no. 6, pp. 981 –997, Jun. 1997.
[37] J. E. Allnutt, “Recent developments in propagation counter-measures for VSAT services,” presented at the , Eighth International Conference on Antennas and Propagation, 1993, 1993, pp. 198 –201 vol.1.
[38] R. G. Lyons, *Understanding digital signal processing*, 2nd ed. Upper Saddle River, NJ: Prentice Hall PIR, 2004.
[39] C. W. Therrien, *Discrete random signals and statistical signal processing*. Englewood Cliffs, NJ: Prentice Hall, 1992.
[40] P. D. Welch, “The use of fast Fourier transform for the estimation of power spectra: A method based on time averaging over short, modified periodograms,” *IEEE Trans. Audio Electroacoustics*, vol. 15, no. 2, pp. 70–73, Jun. 1967.
[41] F. J. Harris, “On the use of windows for harmonic analysis with the discrete Fourier transform,” *Proc. IEEE*, vol. 66, no. 1, pp. 51–83, Jan. 1978.
[42] S. W. Smith, *Digital signal processing: a practical guide for engineers and scientists*. Amsterdam ; Boston: Newnes, 2003.

[43] J. Smith and X. Serra, "PARSHL: An Analysis/Synthesis Program for Non-Harmonic Sounds Based on a Sinusoidal Representation." [Online]. Available: https://ccrma.stanford.edu/~jos/parshl/Analysis_Window_Step_1.html.
[44] C. Chatfield, *The analysis of time series: an introduction*. London: Chapman and Hall, 1996.
[45] C. E. Duchon, *Time series analysis in meteorology and climatology: an introduction*. Chichester, WestSussex, UK ; Hoboken, NJ: Wiley-Blackwell, 2012.
[46] G. P. Weedon, *Time-series analysis and cyclostratigraphy: examining stratigraphic records of environmental cycles*. Cambridge, U.K.; New York: Cambridge University Press, 2005.
[47] M. B. Priestley, *Spectral analysis and time series. Vol. 1 Vol. 1*. London: Academic Press, 1984.
[48] D. S. Wilks, *Statistical methods in the atmospheric sciences*, 3rd ed. Amsterdam ; Boston: Elsevier/Academic Press, 2011.
[49] R. K. Crane and A. W. Dissanayake, "ACTS propagation experiment: attenuation distribution observations and prediction model comparisons," *Proc. IEEE,* vol. 85, no. 6, pp. 879–892, Jun. 1997.
[50] F. J. M. Farley and J. R. Storey, "Time Variations of Extensive Air Showers," *Proc. Phys. Soc. Sect. B*, vol. 70, no. 9, pp. 840–844, Sep. 1957.
[51] P. Billoir and A. Letessier-Selvon, "A coverage independent method to analyze large scale anisotropies," *Astropart. Phys.*, vol. 29, no. 1, pp. 14–19, Feb. 2008.
[52] M. E. Mann and J. M. Lees, "Robust estimation of background noise and signal detection in climatic time series," *Clim. Change*, vol. 33, no. 3, pp. 409–445, Jul. 1996.
[53] G. Heinzel, A. Rudiger, and R. Schilling, "Spectrum and Spectral Density Estimation by the Discrete Fourier Transform(DFT), Including a Comprehensive List of Window Functions and Some New At-Top Windows," Albert-Einstein-Institut, Hannover, Germany, Technical Report 395068, 2002.
[54] National Oceanic and Atmospheric Administration (NOAA), "National climatic data center," 29-Sep-2013. [Online]. Available: http://www.ncdc.noaa.gov/data-access/land-based-station-data/land-based-datasets/climate-normals.
[55] Government of Canada, "Canadian Climate Normals 1971-2000 Station Data," *http://climate.weather.gc.ca/climate_normals/results_e.html?stnID=889,* 29-Sep-2013. .
[56] R. W. Thorn, "Long term attenuation statistics at 12, 14, 20 and 30 GHz on a 30deg slant-path in the UK." British Telecom Research Laboratories, 1984.
[57] "INTEL-540B data storage format (INTELFOR)," Electrical Engineering Researach Laboratory, The University of Texas at Austin, Jun. 1988.
[58] "INTEL-540B Data Analysis (INTANALY)," Electrical Engineering Researach Laboratory, The University of Texas at Austin, Jun. 1988.
[59] M. Rodrigues and M. Pudwell, "Mosqueiro data manual." Center of Telecommunication Studies of Pontifical Catholic University of Rio de Janeiro.
[60] Virginia Tech, "OLYMPUS CD-ROM data manual." Sep-1994.

[61] W. L. Stutzman, "Correction of satellite beacon propagation data using radiometer measurements," *IEE Proc. - Microw. Antennas Propag.*, vol. 141, no. 1, p. 62, 1994.
[62] J. B. Bjorn-Gustaf, "Earth Scientist's Guide to Discrete-Time Power Spectrum Analysis," in *Fourier Transforms - New Analytical Approaches and FTIR Strategies*, G. Nikolic, Ed. InTech, 2011.
[63] R. A. Rohde and R. A. Muller, "Cycles in fossil diversity," *Nature*, vol. 434, no. 7030, pp. 208–210, Mar. 2005.
[64] D. B. Percival, *Spectral analysis for physical applications: multitaper and conventional univariate techniques*. Cambridge ; New York, NY, USA: Cambridge University Press, 1993.
[65] P. Bloomfield, *Fourier analysis of time series: an introduction*, 2nd ed. New York: Wiley, 2000.
[66] B. Efron, "Bootstrap Methods: Another Look at the Jackknife," *Ann. Stat.*, vol. 7, no. 1, pp. 1–26, Jan. 1979.
[67] B. Efron, *An introduction to the bootstrap*. New York: Chapman & Hall, 1993.
[68] W. Stutzman, T. Pratt, C. Nunnally, P. Remaklus, B. Sylvester, A. Predoehl, and D. Graff, "Final report on design and construction of a prototype ACTS propagation terminal," Virginia Polytechnic Institute and State University, Blacksburg, Virginia, EE SATCOM 93-5, Apr. 1993.
[69] J. E. Allnutt and D. Sweeney, "ACTS terminal," 19-May-2013.
[70] W. J. Vogel, G. W. Torrence, and J. E. Allnutt, "Measured radiometric satellite link attenuation estimation error statistics at 11.2 GHz," *Electron. Lett.*, vol. 26, no. 18, p. 1503, 1990.
[71] R. K. Crane, X. Wang, and D. Westenhaver, "ACTS propagation experiment: Preprocessing software user's manual," in *Proceedings of the Twentieth NASA Propagation Experimenters Meeting and Advanced Communication Technology Satellite (ACTS) Propagation Studies Miniworkshop*, Fairbanks, Alaska, 1996, pp. 9–40.
[72] J. N. Hines, T. Li, and R. H. Turrin, "The electrical characteristics of the conical horn-reflector antenna," *Bell Syst. Tech. J.*, vol. 42, no. 7, pp. 1187–1211, 1963.
[73] C. Mihos, "Astronomical Coordinates," 27-Oct-2014. [Online]. Available: http://burro.cwru.edu/Academics/Astr306/Coords/coords.html.
[74] F. J. M. Farley and J. R. Storey, "Time Variations of Extensive Air Showers," *Proc. Phys. Soc. Sect. B*, vol. 70, no. 9, pp. 840–844, Sep. 1957.
[75] P. K. F. Grieder, *Extensive air showers: high energy phenomena and astrophysical aspects: a tutorial reference manual and data book*. Heidelberg ; New York: Springer, 2010.
[76] J. Abraham and et al, "Atmospheric effects on extensive air showers observed with the surface detector of the Pierre Auger observatory," *Astropart. Phys.*, vol. 32, no. 2, pp. 89–99, Sep. 2009.
[77] E. Aguado and J. E. Burt, *Understanding weather and climate*. Boston: Pearson, 2013.

[78] J. T. Kiehl and K. E. Trenberth, “Earth’s Annual Global Mean Energy Budget,” *Bull. Am. Meteorol. Soc.*, vol. 78, no. 2, pp. 197–208, Feb. 1997.
[79] S. Chapman and R. S. Lindzen, *Atmospheric Tides: Thermal and Gravitational*. Netherlands: D. Reidel Publishing Company, 1970.
[80] R. S. Lindzen, “Atmospheric Tides,” *McGraw-Hill Concise Encyclopedia of Science and Technology*. The McGraw-Hill Companies, Inc., 2006.
[81] A. A. Alonge and T. J. Afullo, “Seasonal analysis and predictioin of rain fall effects in Eastern South Africa at microwave frequencies,” *Prog. Electromagn. Res. B*, vol. 40, pp. 279–303, 2012.
[82] C. Amaya and D. Rogers, “Characteristics of earth-space propagation in continental and pacific maritime locations based on multiyear Ku and Ka band measurements,” presented at the XXVIIth General Assembly of the International Union of Radio Science, Maastricht, Netherlands.
[83] U.-C. Fiebig and C. Riva, “Impact of Seasonal and Diurnal Variations on Satellite System Design in V Band,” *IEEE Trans. Antennas Propag.*, vol. 52, no. 4, pp. 923–932, Apr. 2004.
[84] D. Dissing and G. Wendler, “Solar Radiation Climatology of Alaska,” *Theor. Appl. Climatol.*, vol. 61, no. 3–4, pp. 161–175, Dec. 1998.
[85] Cedar Lake Ventures Inc, “WeatherSpark,” 20-Apr-2014. [Online]. Available: https://weatherspark.com/. [Accessed: 20-Apr-2014].
[86] ITU-R Rec. P.840-5, “Attenuation due to clouds and fog.” International Telecommunication Union, Geneva, Feb-2012.
[87] “Average monthly climate and weather indicators in Austin Texas,” *climate zone*. [Online]. Available: http://www.climate-zone.com/climate/united-states/texas/austin/. [Accessed: 02-Jun-2014].
[88] N. Mohamed Shah and J. E. Allnutt, “A short note on the variation of path loss in the atmosphere,” *J. Atmospheric Sol.-Terr. Phys.*, vol. 110–111, pp. 58–62, Apr. 2014.

BIOGRAPHY

Noraisyah Mohamed Shah is an international student from Malaysia. She received her Bachelor of Engineering (Telecommunications) from University of Malaya, Malaysia in 1999. She was employed as a lecturer in University of Malaya, Malaysia since 1999 and received her Masters of Engineering from Oita University, Japan in 2002. Her education in George Mason University was funded by University Malaya under the lecturer training scheme.